Imperial College London
Department of Mechanical Engineering

Embedded Blade Row Flutter

Fanzhou Zhao

October 2016

Submitted in part fulfilment of the requirements for the degree of
Doctor of Philosophy in Mechanical Engineering of Imperial College London
and the Diploma of Imperial College London

Abstract

Modern gas turbine design continues to drive towards improved performance, reduced weight and reduced cost. This trend of aero-engine design results in thinned blade aerofoils which are more prone to aeroelastic problems such as flutter. Whilst extensive work has been conducted to study the flutter of isolated turbomachinery blades, the number of research concerning the unsteady interactions between the blade vibration, the resulting acoustic reflections and flutter is very limited. In this thesis, the flutter of such embedded blade rows is studied so as to gain understanding as for why and how such interactions can result in flutter. It is shown that this type of flutter instability can occur for single stage fan blades and multi-stage core compressors.

Unsteady CFD computations are carried out to study the influence of acoustic reflections from the intake on flutter of a fan blade. It is shown that the accurate prediction of flutter boundary for a fan blade requires modelling of the intake. Different intakes can produce different flutter boundaries for the same fan blade and the resulting flutter boundary is a function of the intake geometry in front of it. The above finding, which has also been demonstrated experimentally, is a result of acoustic reflections from the intake. Through in-depth post-processing of the results obtained from wave-splitting of the unsteady CFD solutions, the relationship between the phase and amplitude of the reflected acoustic waves and flutter stability of the blade is established. By using an analytical approach to calculate the propagation and reflection of acoustic waves in the intake, a novel low-fidelity model capable of evaluating the susceptibility of a fan blade to flutter is proposed. The proposed model works in a similar fashion to the Campbell diagram, which allows one to identify the region (in compressor map) where flutter is likely to occur at early design stages of an engine.

In the second part of this thesis, the influence of acoustic reflections from adjacent blade rows on flutter stability of an embedded rotor in a multi-

stage compressor is studied using unsteady CFD computations. It is shown that reflections of acoustic waves, generated by the rotor blade vibration, from the adjacent blade rows have a significant impact on the flutter stability of the embedded rotor, and the computations using the isolated rotor can lead to a significant over-optimistic predictions of the flutter boundary. Based on the understanding gained, an alternative strategy, aiming to reduce the computational cost, for the flutter analysis of such embedded blades is proposed. The method works by modelling the propagation and reflection of acoustic waves at the adjacent blade rows using an analytical method, whereby flutter computations of the embedded rotor can be performed in an isolated fashion by imposing the calculated reflected waves as unsteady plane sources. Computations using the proposed model can lead to two orders of magnitude reduction in computational cost compared with time domain full annulus multi-row computations. The computed results using the developed low-fidelity model show good correlation with the results obtained using full annulus multi-row models.

Declaration of Originality

I herewith certify that all material in this thesis which is not my own work has been properly acknowledged. No part of the work presented here has been submitted to any other University or Institution for any other qualification.

Fanzhou Zhao

Oct 2016

Copyright Declaration

The copyright of this thesis rests with the author and is made available under a Creative Commons Attribution Non-Commercial No Derivatives licence. Researchers are free to copy, distribute or transmit the thesis on the condition that they attribute it, that they do not use it for commercial purposes and that they do not alter, transform or build upon it. For any reuse or redistribution, researchers must make clear to others the licence terms of this work.

Acknowledgements

I would like to express my sincere gratitude to my supervisor Dr Mehdi Vahdati for introducing this fascinating PhD project to me, for providing continuous support throughout my PhD and for the organisation of many fun and relaxing social events. I am grateful for his invaluable guidance and advice in all the time of the research, and for his kind patience in helping me with the writing of research papers and this thesis.

I would also like to thank my supervisor Professor Norbert Hoffmann for his encouragement and support. Many thanks go to all my colleagues at the Vibration UTC at Imperial College, for providing such a friendly and pleasant environment for my PhD study. Among them I would like to specially thank S. Stapelfeldt, F. Wang and Z. Zachariadis for their kind help at the start of my PhD, J. Dodds for his insightful advice in compressor aerodynamics, and P. Sureshkumar for many constructive discussions in acoustics during the later stages of my PhD and also his kind help in the technical and English writing of this thesis.

I would like to gratefully acknowledge Rolls-Royce plc. for both sponsoring this PhD and allowing the publication of research papers. I would also like to acknowledge B. Mueck, J. Nipkau, N. Smith, J. Green and M. Wilson at Rolls-Royce plc. for their support during this PhD.

Last but not the least, I would like to express my greatest gratitude to my parents who have kindly supported me, both financially and spiritually, throughout my PhD.

Nomenclature

Coordinate System

x	Axial coordinate (engine axis)
y	Transverse coordinate
r	Radius
θ	Angular coordinate
t	Time

Geometry

N_b	Blade count
r_h	Hub radius
r_t	Tip radius
h	Hub/tip ratio
θ_s	Stagger angle
c	Chord length
c_{ax}	Axial chord length
c/s	Solidity (chord/space ratio)
c_t	Covered passage parameter
A_d	Duct throat area
L	Intake length
D	Intake diameter
r_{lip}	Radius of intake lip
$\boldsymbol{n}$	Local unit normal vector on the blade surface
S	Surface area of blade

Aerodynamics

α_s	Flow incidence
W	Flow velocity (mean)
M	Flow Mach number (mean)
M_x	Axial flow Mach number (mean)
M_θ	Tangential flow Mach number (mean)
a	Speed of sound

p Static pressure (perturbation)

p_0 Stagnation pressure (mean)

T_0 Stagnation temperature (mean)

c_p Specific heat capacity

$\dot{m}$ Mass flow rate

$\bar{m}$ Non-dimensional mass flow rate

m_{ref} Ratio of non-dimensional mass flow rates ($\bar{m}/\bar{m}_{wl}$)

l Aerodynamic lift (perturbation)

$\boldsymbol{s}$ Unit vector normal to the mean flow

$C_L^{'}$ Slope of lift coefficient with respect to the incidence

C Coefficient for unsteady lift

Ω Shaft speed

$\bar{\Omega}$ Non-dimension shaft speed (blade tip Mach number)

Aeroelasticity

h_B Blade displacement (plunge motion)

θ_T Blade rotation (twist motion)

γ Percentage of twist component in flap mode

$\boldsymbol{v}$ Blade velocity vector

v_0 Initial vibration velocity

T Period of vibration

f_r Reduced frequency

ω Angular vibration frequency (relative frame)

$\bar{\omega}$ Normalised angular vibration frequency (stationary frame)

δ_d Logarithmic decrement

w Aerodynamic work

ζ Aerodynamic damping

τ 'Flutter index'

Acoustics

m Circumferential order

n Radial order

J Bessel function of the first kind

Y Bessel function of the first kind

χ Coefficient for eigenfunction of acoustic modes

A Amplitude of acoustic waves

ϕ Phase of acoustic waves

k Free stream wavenumber

k_x Axial wavenumber

k_y Transverse wavenumber

$k_{r\theta}$ Radial-circumferential wavenumber

λ Axial wavelength

ω^c Cut-on frequency

σ Cut-on ratio

α Mode angle with respect to the engine axis

η^T Transmission coefficient at a blade row

η^R Reflection coefficient at a blade row

η^I Reflection coefficient at the intake highlight

Transmission and Reflection (Chapter 4)

θ_u Mean flow angle (upstream)

θ_d Mean flow angle (downstream)

R Density (mean)

U Axial flow velocity (mean)

V Transverse flow velocity (mean)

W Flow velocity (mean)

p_s Static pressure (mean)

ρ Density (perturbation)

u Axial flow velocity (perturbation)

v Transverse flow velocity (perturbation)

w Flow velocity (perturbation)

p Static pressure (perturbation)

N_s No. of blade sections

Φ Velocity potential

Abbreviations

EO Engine order

1F 1^{st} flapwise bending mode

1T 1^{st} torsion mode

ND Nodal diameter

NC Nodal circle

IBPA Inter-blade phase angle

CFD Computational Fluid Dynamics

RANS Reynolds-averaged Navier-Stokes

URANS Unsteady Reynolds-averaged Navier-Stokes

PTBC Physical boundary conditions

RIBC Riemann invariants boundary conditions
IGV Inlet guide vanes
OGV Outlet guide vanes
ESS Engine section stators
VSV Variable stator vanes
HP High pressure
BTT Blade tip timing
WL Working line
HWL High working line
LE Leading edge
TE Trailing edge
R1 Rotor 1
S1 Stator 1
R2 Rotor 2
S2 Stator 2
R3 Rotor 3

Subscripts

P Plunge motion
T Twist motion
G Acoustic gust

Superscripts

- Upstream propagating acoustic waves (direction)
+ Downstream propagating acoustic waves (direction)
l Rotor leading edge (location)
t Rotor trailing edge (location)
i Intake highlight (location)
us Trailing edge of the upstream stator (location)
ds Leading edge of the downstream stator (location)
p Unsteady plane sources (location)
b 'Acoustic bump' (location)
u Upstream field of the rotor
d Downstream field of the rotor
T Transmission/transmitted wave
R Reflection/reflected wave

Contents

1 Introduction **26**

1.1 Overview 26

1.2 Instabilities in Turbomachinery 27

1.3 Objectives 32

1.4 Outline of the Thesis 33

2 Background and Literature Review **36**

2.1 Vibration of Blade-Disk Assembly 36

2.2 Aeroelastic Instabilities of Rotor Blades 40

2.2.1 Synchronous vibration 40

2.2.2 Non-synchronous vibration 41

2.3 Aeroacoustics of Axial-flow Compressors 49

2.3.1 Sound generation due to vibration 50

2.3.2 Propagation of acoustic waves 50

2.3.3 Transmission and reflection of acoustic waves 51

2.4 Prediction Methods for Flutter 53

3 Computational Methods **56**

3.1 Aerodynamic Model 56

3.2 Aeroelastic Model 57

3.3 Treatment of Boundary Conditions 58

3.4 Strategies for Flutter Computation 61

3.5 Method for Wave-splitting 64

4 Formulation of Reduced Order Model **66**

4.1 Overview and Strategy 66

4.2 Generation of Acoustic Waves 67

4.3 Propagation of Acoustic Waves in Cylindrical Duct 68

4.4 Transmission and Reflection at a Blade Row 74

4.5 Acoustic Reflection from the Intake 85

4.6 Resultant Near Blade Unsteady Pressure Field 89

5 Vibration of A Thin Annulus Blade Row 92
5.1 Overview and Problem Description 92
5.2 Computation Model and Grid 93
5.3 Vibration in the Isolated Setup 96
5.3.1 Generation and propagation of acoustic waves 97
5.3.2 Effect of modeshape on aerodynamic damping 108
5.4 Effects of Incoming Acoustic Gust 118
5.5 Low-fidelity Flutter Analysis Method 131

6 Acoustic Driven Fan Flutter Bite 144
6.1 Overview and Problem Description 144
6.2 Test Case and Computation Model 147
6.3 Steady State Validation 149
6.4 Flutter Bite Computations 152
6.4.1 Effect of mass flow rate 154
6.4.2 Computations With 'Acoustic Bump' 156
6.4.3 Computations With Annular Cylindrical Intake 164
6.4.4 Computations With Real Intake 175
6.5 Simple Prediction Method for Flutter Bite 183
6.5.1 Unstable operating conditions for an intake design . . 187
6.5.2 Relationship between intake length and aero-damping 191
6.5.3 Flutter bite speed range 191
6.6 Comparison With Test Results For A Real Intake 193
6.7 Effects of Intake Lip Geometry 195

7 Acoustic Driven Flutter of Embedded Rotors 200
7.1 Overview and Problem Description 200
7.2 Test Case and Computation Model 203
7.3 Steady State Validations 205
7.4 Effect of Mean Flow on the Isolated Rotor 208
7.5 Acoustic Reflection from Flow Boundaries 215
7.6 Computations With Adjacent Blade Rows 223
7.6.1 Effect of flow condition 225
7.6.2 Effect of blade row count 227
7.6.3 Effect of vibration frequency 233

7.6.4 Effect of rotor-stator axial gap 235

8 An Alternative Strategy For Embedded Blade Row Flutter Analysis 239

8.1 Development of the Method 239
8.2 Generated Acoustic Waves Near the Rotor 243
8.3 Acoustic Reflection from a Blade Row 252
8.3.1 Thin annulus blade row 253
8.3.2 Three-dimensional stator vanes 268
8.4 Flutter Computations Using the Simplified Approach 275

9 Conclusion and Further Work 282

9.1 Concluding Remarks 282
9.2 Recommendations for Future Work 287

Bibliography 289

Appendix I: Eigenmode Decomposition in Inviscid Flow 301

Appendix II: Solution of Acoustic Transmission and Reflection at a Blade Row 305

Appendix III: Extract Letter 310

List of Tables

6.1 Comparison of measured and predicted 1F/2ND flutter bite speed for the fan blade using the $L = 0.69D$ intake. 195

List of Figures

1.1 Instabilities in a compressor. 28
1.2 Pure plunge vibration for un-stalled and stalled aerofoils. . . 29
1.3 'Flutter bite' for a fan blade. 31

2.1 Nodal diameter and nodal circle. Contour: direction of motion normal to the plane. 37
2.2 1F/2ND mode for a fan. 38
2.3 Typical aeroelastic vibration events for a compressor. 41
2.4 Typical flutter regimes of a compressor. 43
2.5 Traces of acoustic waves generated by the vibration of rotor blades.(Note: the wiggles of arrow are for illustration purposes only.) 46
2.6 Aerodynamic damping of a rotor blade in a stage setup as a function of rotor-stator axial gap. 48

3.1 Variable area nozzle for exit flow. 60
3.2 Time history of blade displacement for an unstable mode (red) and a stable mode (blue). 62

4.1 Reflection process of acoustic waves generated by the vibration of rotor blades. 67
4.2 Acoustic waves generated by blade vibration at the leading edge and trailing edge of a rotor. 69
4.3 Unsteady pressure contour of an upstream propagating 2ND acoustic wave. 73
4.4 Propagation of acoustic waves in the duct between a rotor and its upstream stator. 74
4.5 Transmission and reflection of acoustic waves at a blade row. 75

4.6 Illustration of (a) a flat plate, (b) a cambered blade and (c) an approximation of a cambered blade using multiple flat plate sections. 76
4.7 Transmission and reflection of an upstream propagating acoustic wave at a flat plate cascade. 76
4.8 Transmission and reflection of an upstream propagating acoustic wave at a cambered blade cascade. 77
4.9 Transmission and reflection of an upstream propagating acoustic wave at a cascade consisting of blades in two flat plate sections. 78
4.10 Transmission and reflection of an upstream propagating acoustic wave at a cascade consisting of blades in two flat plate sections with non-zero mean flow incidence. 84
4.11 Reflection and radiation of acoustic waves at the intake opening. 86
4.12 Flow field and the scatter of acoustic waves at the duct opening. 87
4.13 Traces of acoustic waves generated by the vibration of embedded rotor blades. 89
4.14 Traces of acoustic waves generated by the vibration of fan blades. 90
4.15 Transmission of the reflected waves at the embedded rotor. . 91

5.1 The single passage computation domain. 93
5.2 Tip layer mesh for (a) a flat plate and (b) a cambered blade. 94
5.3 Modeshape for the (a) plunge mode and (b) twist mode. . . . 94
5.4 Vibration of blades in the isolated setup. 96
5.5 Illustration of the leading and trailing edge computation planes for wave-splitting. 97
5.6 Axial variation of the amplitude and phase of acoustic waves, $\theta_s = 45°$, $f_r = 0.84$, plunge mode. 98
5.7 Eigenfunctions (radial) of acoustic modes at the leading edge and the trailing edge, $\theta_s = 45°$, $f_r = 0.84$, plunge mode. . . . 100
5.8 Comparison of axial wavenumber for the first three radial orders in the complex plane, $\theta_s = 45°$, $f_r = 0.84$. 101
5.9 Acoustic pressure generated at the leading edge and the trailing edge for different blade stagger angle θ_s, plunge motion. . 102

5.10 Unsteady pressure contour at four instances of time (in terms of phase relative to blade velocity), $\theta_s = 0°$, plunge mode. Red contour: positive value; Blue contour: negative value. . . 103
5.11 Instantaneous unsteady pressure contour at 90° phase with blade velocity for (a) $\theta_s = 0°$ and (b) $\theta_s = 45°$. Red contour: positive value; Blue contour: negative value. 103
5.12 Acoustic pressure generated at the leading edge and the trailing edge for different blade stagger angle θ_s, twist motion. . . 104
5.13 Unsteady pressure contour at four instances of time (in terms of phase relative to blade velocity), $\theta_s = 0°$, twist mode. Red contour: positive value; Blue contour: negative value. 104
5.14 Mean flow field and the modeshape for the plunge mode for blade row consisting of (a) flat plates and (b) cambered blades. 106
5.15 Acoustic pressure generated at the leading edge and the trailing edge by the vibration of the flat plate and the cambered blade, plunge motion. 107
5.16 Amplitude and phase of modal force for different blade stagger angle θ_s and vibration motion. 108
5.17 Aerodynamic damping for different stagger angle θ_s and vibration motion. 110
5.18 Decomposition of a (two-dimensional) flap mode into a linear combination of a plunge mode and a twist mode. 112
5.19 Aerodynamic damping contributions due to plunge and twist motions, $\theta_s = 45°$, $\gamma = 0.5$. 115
5.20 Aerodynamic damping contributions for different modeshape parameter γ, $\theta_s = 45°$. 117
5.21 Imposing an upstream propagating acoustic gust in the downstream field of the vibrating blade row. 118
5.22 Axial variation of the amplitude and phase of acoustic waves for *Case VG*, phase of incoming gust $\phi^{dp-} = 0°$, $\theta_s = 45°$, $f_r = 0.84$, plunge mode. 120
5.23 Amplitude and phase of outgoing and incoming acoustic waves at the leading edge and the trailing edge, $\theta_s = 45°$, $f_r = 0.84$. 121
5.24 Imposing an upstream propagating acoustic gust in the downstream field of the non-vibrating blade row. 123

5.25 Axial variation of the amplitude and phase of acoustic waves for *Case G*, phase of incoming gust $\phi^{dp-} = 0°$, $\theta_s = 45°$, $f_r = 0.84$, plunge mode. 124
5.26 Modal force as a function of the phase of incoming gust, $\theta_s = 45°$, $f_r = 0.84$, plunge mode. 125
5.27 Aerodynamic damping as a function of the phase of incoming gust, $f_r = 0.84$. 127
5.28 Instantaneous unsteady pressure contour for $\theta_s = 0°$, $f_r = 0.84$. 128
5.29 Modal force as a function of the phase of incoming gust for *Case G*, $f_r = 0.84$, plunge motion. 130
5.30 Aerodynamic damping of the blade vibrating in the flap mode for different modeshape parameter γ, $\theta_s = 45°$, $f_r = 0.84$. . . 130
5.31 Unsteady pressure field near a vibrating blade row with incident acoustic gusts from upstream and downstream. 135
5.32 Modal force as a function of the phase of incoming gust, $\theta_s = 45°$, $f_r = 0.84$, plunge mode. 137
5.33 Comparison of predicted aerodynamic damping due to incoming acoustic gust from downstream, $f_r = 0.84$, plunge mode. 139
5.34 ζ_{GP} as a function of the phase of unsteady lift. 140
5.35 Effect of the constant C on ζ_{GP}. 141

6.1 Illustration of acoustic reflections from the intake. 145
6.2 Domain used for steady state computation. 147
6.3 Modeshape for the 1F mode. 148
6.4 Performance of the fan. 150
6.5 Radial profile of total pressure ratio. 151
6.6 Isentropic relative Mach number contour and streamline. . . . 151
6.7 Domain used for unsteady computation. 152
6.8 Comparison between predicted flutter bite and measured flutter bite. 153
6.9 (a) Characteristic of the fan blade (isolated setup) at $\bar{\Omega} = 0.89$; (b) aero-damping as a function of mass flow rate. 155
6.10 Spanwise distribution of blade aero-damping. 156
6.11 Domain used for flutter computation with 'bump' feature. . . 157
6.12 Aerodynamic damping as a function of bump location. 158

6.13 Instantaneous unsteady pressure contour on the casing surface: (a) unsteady pressure (complete signal); (b) upstream propagating acoustic pressure; (c) downstream propagating acoustic pressure. 159
6.14 Axial variation of amplitude and phase of acoustic waves, $m_{ref} = 0.93$ (bump locations $\frac{L}{\lambda^-} = 0.4$ and $\frac{L}{\lambda^-} = 0.7$ are illustrated by dashed black lines). 160
6.15 Phase difference between the outgoing and reflected acoustic waves as a function of bump location. 162
6.16 Additional aero-damping as a function of phase difference between the outgoing and reflected acoustic waves. 163
6.17 Domain used for flutter computation with annular cylindrical intake. 164
6.18 Illustration of fan operating conditions used for flutter computation. WL: working line; HWL: high working line. 165
6.19 Relative Mach number contour at 98% span of the fan blade. 166
6.20 Aero-damping of the fan as a function of vibration frequency, $L = 1.37D$. 167
6.21 Isentropic Mach number at 90% blade span. 168
6.22 Aero-damping of the fan as a function of intake length, $\sigma = 1.3$. 169
6.23 (a) Normalised amplitude and (b) phase of 2ND acoustic waves in the intake $L = 1.37D, \sigma = 1.3$. 170
6.24 Axial phase change through the intake duct as a function of vibration frequency, $L = 1.37D$. Upstream: $\delta\phi^-$; Downstream: $\delta\phi^+$ 172
6.25 Axial phase change through the intake duct as a function of intake length, $\sigma = 1.3$. Upstream: $\delta\phi^-$; Downstream: $\delta\phi^+$ . . 172
6.26 Amplitude ratio and phase change of acoustic reflection from the intake highlight as a function of vibration frequency, $L = 1.37D$. 173
6.27 Additional aero-damping due to acoustic reflections as a function of phase difference between the outgoing wave and the reflected wave at fan leading edge. 174
6.28 Mach number profiles at different fan speeds (curves with symbol) and an illustration of intake geometry used in this study (black curve). 176

6.29 Aero-damping of the fan as a function of speed on the *HWL* operating line. 177
6.30 Cut-on frequency for different fan speeds. 178
6.31 Amplitude ratio and phase difference between the reflected and the outgoing acoustic waves at the fan face. 178
6.32 Additional aero-damping as a function of the phase difference between the outgoing and the reflected acoustic waves at the fan face, 3ND. 180
6.33 Profiles of intakes used in this study. 181
6.34 Amplitude ratio (top) and phase difference (middle) between the outgoing and the reflected acoustic waves at the fan face; blade aero-damping (bottom) for different intake length. . . . 182
6.35 Additional aero-damping due to acoustic reflections and 'flutter index' as a function of vibration frequency, $L = 1.37D$. . . 184
6.36 Additional aero-damping due to acoustic reflections and 'flutter index' as a function of intake length, $\sigma = 1.3$. 185
6.37 Flutter index τ contour for the intake $L = 1.37D$ as a function of M_x and $\bar{\omega}_m$. 188
6.38 Flutter index contour on the high working line (HWL) as a function of intake length L/D and shaft speed Ω. 190
6.39 Aero-damping of the fan on the operating line, $L = 1.37D$. . 192
6.40 Additional aero-damping due to intake reflections on the operating line, $L = 1.37D$. 193
6.41 Flutter index τ contour for the 1F/2ND mode of rig fan blades with a real intake $L = 0.69D$ as a function of M_x and shaft speed Ω. 194
6.42 Profiles of intake geometry used in this study. 196
6.43 Radial profile of axial Mach number at the outlet. 197
6.44 Amplitude ratio of reflection coefficient for different intake lip geometries. 198

7.1 9-stage E3E high pressure compressor. 201
7.2 The measured flutter event. 201
7.3 Domain for steady state computation. 203
7.4 Mesh of Stator 1, Rotor 2 and Stator 2 at 90% height. 204
7.5 Contour of 1F modeshape for R2. 205

7.6 Spanwise distribution of R2 leading edge displacement for the 1F mode (values are normalised by the maximum resultant displacement). 206
7.7 Compressor operating map between 92.5% and 95% speeds. . 206
7.8 Radial profile comparison of total pressure with measured data. 207
7.9 Operating conditions of R2 used for flutter computation. WL: working line; E: peak efficiency; S: near stall; C: near choke. . 208
7.10 Isentropic relative Mach number and streamline on the suction surface of R2. 209
7.11 Isentropic relative Mach number on the surfaces of R2, C1-E-S1. 210
7.12 Isentropic relative Mach number on the surfaces of R2, C2-E-S2. 210
7.13 Aero-damping of R2 at the peak efficiency operating point *E*. 211
7.14 Aero-damping of R2 on the C1-E-S1 characteristic. 212
7.15 Aero-damping of R2 on the C2-E-S2 characteristic. 213
7.16 Cut-on frequency (in relative frame of reference) for low nodal diameters. 214
7.17 Acoustic reflection from the outflow boundary. 216
7.18 Aero-damping as a function of boundary location. 217
7.19 Amplitude and phase of acoustic waves at the leading edge and trailing edge, (*PTBC/PTBC*, $\frac{L}{\lambda^-} = 0.34$). 219
7.20 Phase difference between the reflected and the outgoing waves at the trailing edge as a function of boundary location (*RIBC/PTBC*). 221
7.21 Additional aerodynamic damping as a function of phase difference between the reflected and outgoing waves at the trailing edge. 222
7.22 Computation domains for flutter analyses: *Case R*, *Case SRS* and *Case RSRSR*. 223
7.23 Computation domains for flutter analyses: *Case SR* and *Case RS*. 224
7.24 Isentropic relative Mach number on the surfaces of R2 at the peak efficiency operating point *E*. 225
7.25 Aero-damping of R2 on the C1-E-S1 characteristic. 226
7.26 Aero-damping of R2 using the *Case R*, *Case SRS* and *Case RSRSR* setups. 227

7.27 Additional aero-damping for *Case R* and *Case SRS* as a function of nodal diameter. 228
7.28 Aero-damping of R2 using the *Case R*, *Case SR* and *Case RS* setups. 229
7.29 Additional aero-damping for *Case SR* and *Case RS* as a function of nodal diameter. 230
7.30 Comparison of additional aero-damping for *Case SRS* and the sum of additional aero-damping for *Case SR* and *Case RS*. 231
7.31 Transmission and reflection of acoustic waves through the embedded rotor. 232
7.32 Aero-damping of R2 as a function of nodal diameter for different blade vibration frequency, *Case R*. 232
7.33 Aero-damping of R2 as a function of nodal diameter for different blade vibration frequency, *Case SRS*. 233
7.34 Additional aero-damping of R2 as a function of nodal diameter for different blade vibration frequency, *Case SRS*. 234
7.35 Illustration of extended the duct between R2 and S2. 235
7.36 Aero-damping of R2 with increased R2-S2 axial gap. 236
7.37 Phase variation of acoustic waves propagating in the duct between R2 and S2. 236

8.1 Imposing acoustic waves in the rotor domain using unsteady plane sources. 240
8.2 Cut-on frequency range (in absolute frame of reference) at (a) the leading edge and (b) the trailing edge of R2. 244
8.3 Cut-on frequency range (in absolute frame of reference) in the situation of low flow to shaft speed ratio. 246
8.4 Axial wavenumber for upstream and downstream propagating acoustic waves at the leading and trailing edges of R2. . . 247
8.5 Mode angle for upstream and downstream propagating acoustic waves at the leading and the trailing edges of R2. 249
8.6 Amplitude and phase of the acoustic waves generated at the leading edge and the trailing edge of R2. 251
8.7 Unsteady pressure contour for an imposed $(2, 0)$ acoustic wave plotted in the cross-section view of a duct. 252

8.8 (a) *Case G+*: imposing a downstream propagating acoustic wave incident on the blade row; (b) *Case G-*: imposing an upstream propagating acoustic wave incident on the blade row. 254
8.9 Illustration of blade row geometry and incident acoustic waves in this study. 255
8.10 Effect of solidity on transmission and reflection coefficients, $\theta_s = 0°$, $M = 0.1$, *Case G-*. 256
8.11 Effect of solidity on transmission and reflection coefficients, $\theta_s = 0°$, $M = 0.1$, *Case G+*. 257
8.12 Effect of solidity on transmission and reflection coefficients, $\theta_s = 45°$, $M = 0.3$, *Case G-*. 259
8.13 Effect of solidity on transmission and reflection coefficients, $\theta_s = 45°$, $M = 0.3$, *Case G+*. 260
8.14 'Covered passage' parameter c_t for upstream propagating acoustic waves (*Case G-*). 262
8.15 Effect of covered passage parameter c_t on transmission and reflection coefficients, $\theta_s = 45°$, $M = 0.3$, *Case G-*. 263
8.16 Effect of chord length on transmission and reflection coefficients, $\theta_s = 0°$, $M = 0.1$, $c/s = 2.0$, *Case G-*. 264
8.17 Effect of camber on transmission and reflection coefficients, $c/s = 2.0$, $c_t = 0.82$, *Case G-*. 266
8.18 Real and imaginary components of axial wavenumber for upstream propagating (−) and downstream propagating (+) acoustic waves at the leading edge (l) and the trailing edge (t) of (a) S1 (left plots) and (b) S2 (right plots). 270
8.19 Transmission and reflection coefficients of upstream propagating acoustic waves generated by R2 vibration at S1, $c_t = 0.72$. 271
8.20 Transmission and reflection coefficients of downstream propagating acoustic waves generated by R2 vibration at S2. . . . 273
8.21 Imposing acoustic waves in the rotor domain using unsteady plane sources. 276
8.22 Aero-damping of R2 in the partially embedded S1/R2 and R2/S2 environments. 277
8.23 Aero-damping of R2 in the embedded S1/R2/S2 environment. 277
8.24 Aero-damping coefficient at 90% span of R2 (0ND). 278

8.25 Aero-damping coefficient at 90% span of R2 (0ND). 279
8.26 Aero-damping coefficient at a function of R2 span (0ND). . . 279

1 Introduction

1.1 Overview

Aeroelastic flutter is a self-feeding vibration of a body in an airstream. The vibration is excited by aerodynamic forces on the object which are in phase with its motion, resulting in a net energy transfer from the surrounding airstream into the vibrating system. Hence the vibration motion is self-sustained and its amplitude grows with time.

Real life examples of flutter failure can be found in cases such as aircraft wings [1], rotors of wind turbines [2] as well as blades in aero-engines [3]. Flutter in a multi-stage compressor, a fan and turbine blades in an aero-engine could result in engine failure or shut down accompanied by damaged blades, and is thus to be avoided at all costs.

The aim of this research is to study the flutter of the embedded blade rows in aero-engines. The term 'embedded' refers to the fact that the blade row of interest is surrounded by other blade rows, for instance rotors in a core compressor or a multi-stage turbine. Moreover, blade rows surrounded by structures such as the intake and nozzle are also broadly considered as 'embedded'. It will be shown in this thesis that aero-acoustic interactions between the blade rows have a significant impact on the flutter stability of such 'embedded' blades.

The need for this research is driven by the fact that modern gas turbine design continues to move towards improved performance, reduced weight and reduced cost [4]. As turbomachinery blade aerofoils are thinned to improve performance and reduce weight, the aeroelastic challenges such as flutter and forced response become more predimonant. Methods for analysing forced response are relatively well established but flutter of an embedded blade row is still poorly understood. Moreover, the use of titanium blade-integrated-disks (blisks) is becoming more common in modern aeroengine designs [3]. Such structures have a very low mechanical damping in con-

trast to traditional bladed-disk assemblies [5]. For such structures, the main source of damping to the blade comes from the air flow, which highlights the importance of accurate prediction of blade damping contribution due to aerodynamic forces.

The traditional CFD approach for aerodynamic damping prediction of such a blade row involves unsteady simulations that treats the embedded blade row of interest in isolation [6–8], which neglects the potential interactions between it and its adjacent blade rows (or structures). The effects of these interactions can be captured by using high fidelity whole annulus multi blade row CFD models, however this approach poses high demands on computational power and time, and cannot be used routinely in the design of an engine. Therefore, this work will focus on the flutter of fans and the embedded rotors in the core compressors of modern axial flow aero-engines under the influence of acoustic reflections from adjacent blade rows (or the intake), with the aim of developing a low-fidelity model that can be used at early design stages of an engine. The proposed model works in a similar fashion to the Campbell diagram, which allows one to identify the region where acoustic reflection driven flutter is likely to occur at early design stages of an engine. It should be emphasised that the interactions studied in this thesis (i.e. between flutter and acoustic reflection) are driven by the reflection of perturbations generated by blade vibration which occurs at the frequency of vibration. These interactions are to be differentiated from the rotor-stator interactions (potential or wake induced) which occurs at the blade passing frequency.

1.2 Instabilities in Turbomachinery

Figure 1.1 shows a schematic operating map of an axial flow compressor as a function of (inlet) corrected mass flow and overall pressure ratio. In this plot the stability boundaries and the working line of the compressor are also displayed. In certain operating range of a compressor, aerodynamic as well as aeroelastic instabilities can occur which could lead to the loss of engine performance or even the break down of blades. Several of the most common instabilities of a compressor (and fan) are briefly introduced below.

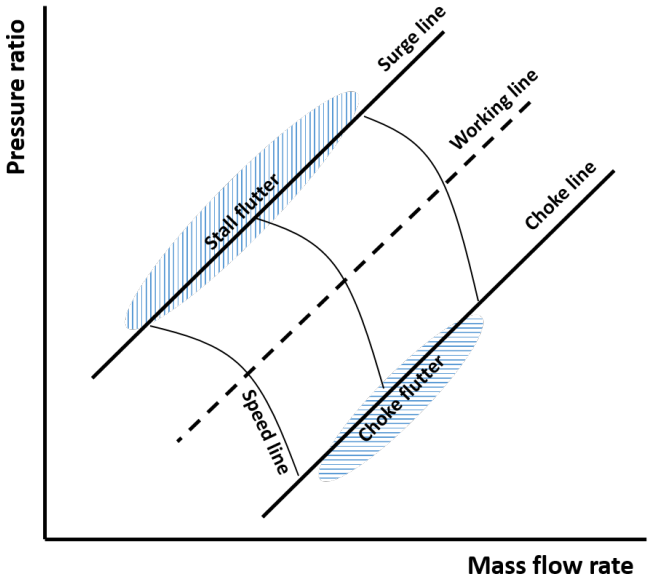


Figure 1.1: Instabilities in a compressor.

Stall and surge

In an ideal situation where blades are infinitely stiff (i.e. structural vibrations are restricted) the compressor becomes unstable to operate once surge is triggered. Compressor surge is driven by the stalling of the blades, accompanied by a complete reversal of the flow and loss of engine power (the ability to produce pressure rise), which is represented as the region above the surge line in the compressor map in Figure 1.1. The surge line of a compressor can be determined by connecting the stall points for all compressor shaft speeds.

Stall flutter and choke flutter

Besides aerodynamic disruptions, instability could be triggered by aeroelastic excitations prior to compressor surge (or rotating stall), where the blade vibration is amplified due to an energy influx from the surrounding air flow into the mechanical structures. Such an instability is self-excited and self-sustained, and does not require the presence of any external forcing (for instance the passing of the wake of an upstream blade row). Figure 1.1 illustrates two typical types of flutter instabilities for a compressor. Stall

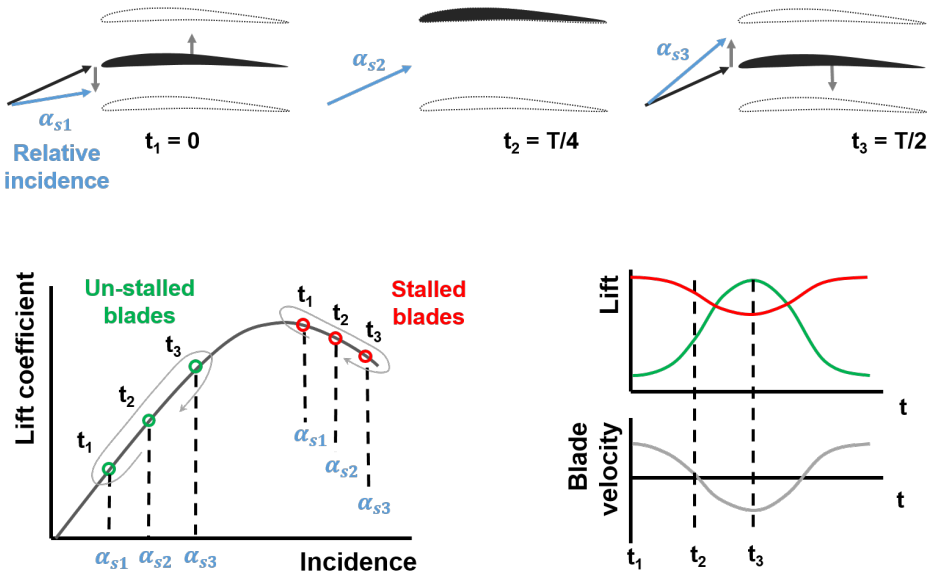


Figure 1.2: Pure plunge vibration for un-stalled and stalled aerofoils.

flutter refers to flutter events that occur near the stall line which are usually accompanied by flow separation on the surface of the blades.

Figure 1.2 shows a simplified demonstration of stall flutter for a two-dimensional aerofoil section vibrating in a pure plunging mode using a quasi-steady analysis. The plots at the top of the figure show the instantaneous vibration motion (grey arrows) and the resulting relative incidence to the aerofoil (blue arrows). The bottom left plot shows the section lift coefficient (idealised with positive slope prior to stall and negative slope post-stall) for this aerofoil as a function of incidence, and the bottom right plots show the time histories for the velocity of the vibration motion and the induced lift on the surfaces of the aerofoil. In these figures the symbol t denotes time, T denotes the period of vibration, α_s denotes the incidence. The velocity of motion and the direction of lift are defined as the upward direction. As can be seen from the plots at the top of the figure, the advance of vibration motion from t_1 (the maximum positive velocity) to t_3 (the maximum negative velocity) results in a continuous increase in the relative incidence. For an un-stalled aerofoil, the increase of incidence leads to an increase in the lift (as shown by the green circles in the lift coefficient plot in Figure 1.2). On the other hand, for a stalled aerofoil operating on the negative slope of the lift coefficient curve, the increase of incidence results in a decrease

of lift on the surfaces of the blade (as shown by the red circles in the lift coefficient plot in Figure 1.2). This trend is reversed as the vibration motion advances from $t_3 = T/2$ through $t_4 = 3T/4$ (not shown as it has the same incidence as t_2) to t_5 (the same as t_1). In this process the relative incidence is decreased with time, and consequently the lift for the un-stalled aerofoil is decreased and the lift for the stalled aerofoil is increased. By comparing the obtained time histories of lift with the velocity of the vibration motion (bottom right plots in Figure 1.2), it is clearly seen that the variation of lift for the un-stalled aerofoil is out of phase with the velocity, which results in positive damping from the flow (as the aerodynamic forces induced by the flow always act against the vibration motion). On the contrary, the variation of lift for the stalled aerofoil is in phase with the velocity of the vibration motion, which results in negative aerodynamic damping, and consequently flutter (as the aerodynamic forces act in the same direction with the blade motion to amplify the vibration level). Figure 1.2 clearly shows how the interaction between the blade motion and the stalled flow (corresponding to the negative slope of the lift coefficient curve) can cause (stall) flutter for a two-dimensional aerofoil section.

For three-dimensional turbomachinery rotor blades operating near the stall line, shock wave movement, boundary layer separation and radial flow migration on the suction surface, driven by adverse pressure gradient, generates unsteady oscillatory forces which have been shown to be the key parameters leading to compressor (or fan) stall flutter [9].

Choke flutter occurs for a transonic passage flow characterised by the interaction between the blade vibration and the oscillatory shock wave movement. The presence of flutter could significantly reduce the stability margin of a compressor, which is defined as the margin between the stability boundary and the working line, thus limiting its safe operating range prior to aerodynamic instabilities.

'Flutter bite'

For specific narrow speed range at part-speed operating conditions near the stall boundary, flutter of a fan blade can occur in the absence of flow separation when the slope of the characteristic is still negative. This situation is illustrated by an example shown in Figure 1.3 (the illustration is based

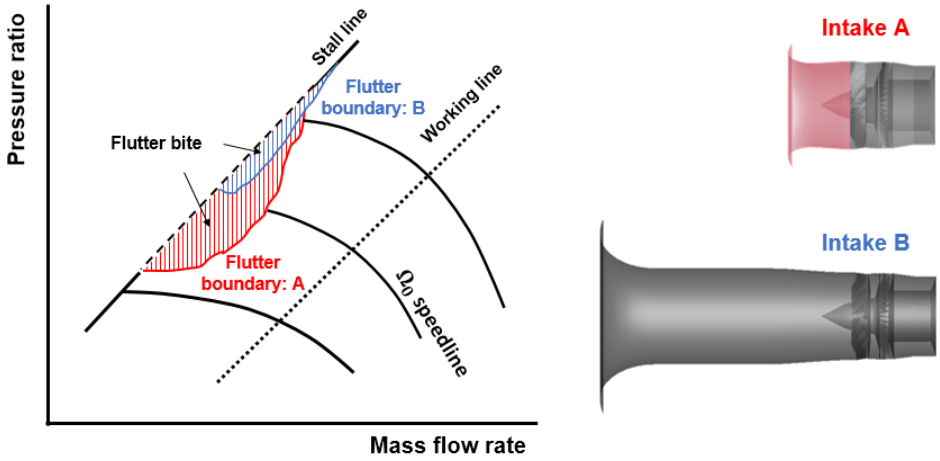


Figure 1.3: 'Flutter bite' for a fan blade.

on test measurements). In this figure the measured stability boundaries for the fan blade using two different intakes (right) are displayed on the fan performance map (left). When the fan operates at the speed of Ω_0 with the 'Intake A', the stall line is preceded by the flutter boundary, and the blade experiences flutter before stall. It is seen that flutter removes a 'bite' from the stability margin of the fan blade, and is thus referred to as 'flutter bite'. On the other hand, flutter stability of the fan blade operating with the 'Intake B' shows a significant change from that using the 'Intake A'. Flutter bite (blue area) occurs at a different speed with a different 'depth of bite' (i.e. loss of flutter margin). This change of flutter stability margin clearly indicates that intake has a significant influence on the flutter stability of fan blades, and should be taken into account in the design stage. It has been shown that, this type of flutter is driven by acoustic reflections from the intake, and typically occurs in low nodal diameter (2ND to 4ND) forward traveling modes for the 1st flapwise bending (1F) mode [10].

One of the important design challenges for compressor (and fan) stability is to minimise the regions of flutter event on the performance map, such as the region of flutter bite shown in Figure 1.3, so as to maximise the regions of stable operating condition. The primary focus of this work is on the flutter of fan blades and embedded rotors in a core compressor in the absence of flow separation. It will be shown that this type of flutter is caused by acoustic reflections from adjacent structures, which can be a

blade row, an intake or a change in duct area, and thus requires accurate modelling of propagating acoustic waves.

1.3 Objectives

The hypothesis of this thesis is that flutter in an embedded environment can occur due to acoustic reflections from adjacent structures. The hypothesis does not assume other unsteady flow features, such as stall, to be irrelevant or unimportant for flutter of such blades. It neither suggests that acoustic reflections always lead to flutter. The core of this thesis is the study of the physics behind the flutter of embedded blade rows, and to establish a relationship between acoustic reflection and flutter. With this in mind, the main objectives of this work are divided into the following:

1. Propose and devise a method to model the generation, propagation and reflection of acoustic waves due to blade vibration.

2. Study the influence of acoustic reflection from adjacent blade rows on flutter stability of the rotor blades in core compressors.

3. Study the effects of acoustic reflection from the intake on flutter stability of the fan blades.

4. Based on the understanding gained, develop a new low-fidelity method which is capable of predicting the possibility of flutter of compressor blades (or fan) due to acoustic reflections.

This work is intended to enhance the physical understanding of embedded blade row flutter driven by acoustic reflections, which can lead to further development of simple design rules for modern aero-engines. It will be shown that the parameters affecting acoustic reflections vary with the mean flow field, duct and blade geometries, spacing between blade rows and the mode of vibration. Therefore efficient methods for dealing with these aspects will need to be developed. In order to devise such a method for the analysis of acoustic reflection driven flutter, the generation, propagation and reflection of acoustic waves need to be considered. The process of the analysis is divided into four stages:

1. Model the generation of acoustic waves due to the blade vibration using unsteady CFD computations.

2. Trace the propagation of acoustic waves in the compressor duct (and intake) using an analytical model.

3. Calculate the reflection (and transmission) of acoustic waves at blade rows (and intake opening) using an analytical approach.

4. Use the information (phase and amplitude) regarding the reflected acoustic waves to determine the flutter stability of the studied rotor, either by simplifying the conventional high-fidelity full annulus multi-row CFD model or using a low-fidelity analytical prediction method.

These aspects, as will be shown in the following chapters, are crucial for the understanding of the embedded blade row flutter.

1.4 Outline of the Thesis

In order to achieve the objectives presented in the previous section, this thesis is structured as follows:

- Due to limited publications regarding the interactions between the vibration of blades, the resulting reflected acoustic waves and flutter, Chapter 2 presents the essential background and established theories for the understanding of this subject. A brief literature review of the current flutter prediction methods based on CFD computations is also outlined.

- Chapter 3 presents the computational methodologies used throughout this thesis. Aerodynamic and aeroelastic solvers for the CFD code used in this work are introduced in this chapter. In order to establish the relationship between the reflected acoustic waves and the blade vibration, in-depth post-processing is required to split the unsteady disturbances in the unsteady CFD solutions into propagating waves. Therefore, the method for such a wave-splitting procedure is also presented.

- Based on the establish theories and previous work reviewed in Chapter 2 and the computational methods introduced in Chapter 3, the formulation of the reduced order model is presented in Chapter 4. The strategy for numerical modelling of the generation of acoustic waves due to the blade vibration is outlined. Analytical methods concerning the propagation of acoustic waves in cylindrical ducts and their reflections at the intake are also presented. Moreover, an analytical method is devised to calculate the transmission and reflection of acoustic waves at a blade row consisting of cambered blades. Armed with the methods presented in this chapter, in-depth analyses can be performed in the following chapters to investigate the relationship between the reflected acoustic waves and flutter.

- Chapter 5 presents the flutter analysis of an isolated thin annulus blade row. The analysis is intended to gain understanding of the fundamental physics of the interactions between the blade vibration, the duct acoustic waves (generated by vibration and incoming due to external sources) and flutter. The blade aerodynamic damping contributions for the plunge motion and the twist motion. The effect of incoming acoustic gusts on the flutter stability of the blade is studied by means of artificially imposed unsteady plane sources. Based on the understanding gained, a low-fidelity flutter analysis method is formulated, which aims to evaluate the effect of incoming acoustic waves on the blade aero-damping using an analytical approach.

- In order to further verify the observations and conclusions made in Chapter 5, the flutter bite of fan blades driven by acoustic reflections from the intake is studied in Chapter 6. For the fan and intake system in this study, the interactions between the blade vibration and the reflected acoustic waves is restricted in the upstream field of the blade (as flutter requires the downstream field to be cut-off [11]). This allows one to study the effect of acoustic reflections from the upstream side of the blade (i.e. intake) without the consideration of downstream effects. Flutter computations are carried out using different intake geometries and by varying key parameters that are important for the propagation and reflection of acoustic waves, with the aim of establishing a relationship between the phase and amplitude of the re-

flected acoustic waves and flutter stability of the blade. Based on the understanding gained, a novel analytical method is presented aiming to evaluate the speed range for which the flutter bite of a fan blade is likely to occur. The results obtained using the proposed method are validated against results obtained from unsteady CFD computations and experimental test.

- In Chapter 7, flutter of embedded rotor blades driven by acoustic reflections from adjacent blade rows is studied. The flutter of such embedded blades is shown to occur at a condition that the acoustic waves are cut-on at both upstream and downstream sides of the blade. This fact adds another layer of complexity to the problem compared with the cases studied in Chapter 6, since acoustic reflections can occur at either side of the rotor, and hence will modify the unsteady flow field at both the leading and trailing edges of the blade. The effect of acoustic reflections from both the upstream and downstream sides of the rotor is studied by means of artificial reflecting structures (reflection due to boundary conditions) and full annulus multi-row computations with the adjacent blade rows.

- Based on the understanding gained in Chapter 5 to Chapter 7, an alternative strategy, which differs from the conventional full annulus multi-row computations, for the flutter analysis of embedded rotor blades is proposed. In this approach, the propagation of acoustic waves in the compressor duct and the reflection at the adjacent blade rows are calculated using an analytical approach. The calculated reflected acoustic waves are then imposed inside the domain of the rotor blade of interest by means of unsteady plane sources. By doing so, flutter computations can be performed in a cost-efficient way using a reduced assembly in the absence of the adjacent blade rows. The development and validation for such a method is presented in Chapter 8. The results obtained by using the proposed method are compared with those obtained from full annulus multi-row unsteady CFD computations.

- Finally, Chapter 9 summaries the main findings in this thesis and concludes with recommendations for future work.

2 Background and Literature Review

There are only a limited number of publications regarding the interactions between the blade vibration, the resulting reflected acoustic waves and flutter. Therefore, this chapter presents the essential background for the understanding of this subject. In the first instance, the vibration of a blade-disk assembly is discussed and is followed by a brief introduction to compressor aeroelastic instabilities, so that the reader can distinguish between different mechanisms of aeroelastic vibration in turbomachines. Established theories and previous work concerning the generation, propagation, transmission and reflection of acoustic waves in turbomachines are summarised. Finally, a brief review of the current flutter prediction methods based on CFD computations is outlined.

2.1 Vibration of Blade-Disk Assembly

Blades in axial flow compressors are commonly attached to the central rotating disk (and the shaft) through either a removable locking mechanism ('bladed-disk') or integral cast into the disk ('blisk') [3]. Hence the vibration of a blade is mechanically coupled with that of the disk and determines the modeshape of the blade vibration. The vibration of a blade-disk assembly can be idealised as the vibration of a two-dimensional annular disk, which is fixed at the center (with respect to shaft) and free along the outer edge (at the tip of rotors) [3].

Figure 2.1 shows some typical examples for the modeshape of a vibrating disk which is free along the outer and inner edges. The + sign (red area) in the figure denotes the out of plane motion and the − sign (blue area) denotes the motion into the plane. For the example shown in Figure 2.1a, the motion of the disk is positive in one half of the annulus and negative

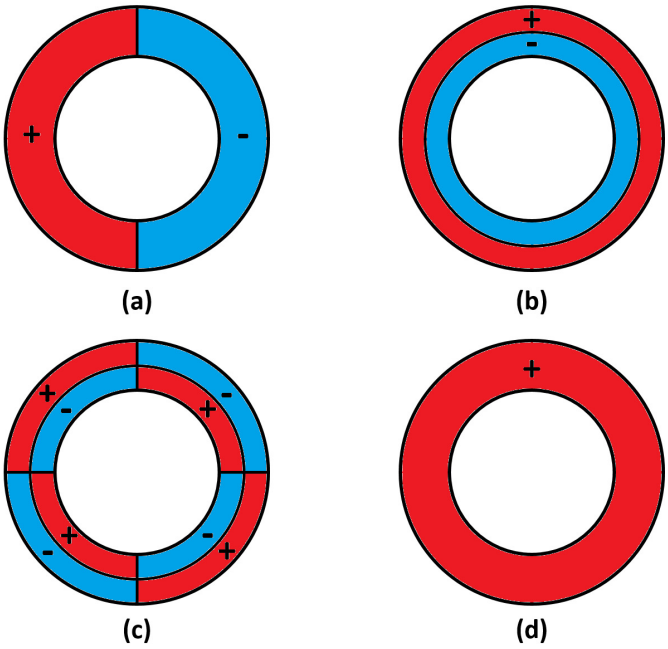


Figure 2.1: Nodal diameter and nodal circle. Contour: direction of motion normal to the plane.

in the other half. The displacement at one location of the disk is equal but negative to that at the location on the opposite end. The zero displacement line separating the two halves of the annulus is denoted as the nodal line, and the number of nodal lines present in the mode is referred to as the nodal diameter (ND). Thus the mode shown in Figure 2.1a is referred to as the 1 nodal diameter (1ND) mode, or sometimes called the first circumferential mode. The motion of the disk rim can thus be represented as a cos (or sin) pattern. Similarly, for the case shown in Figure 2.1b, where the outer and inner halves of the annulus vibrate out of phase, the motionless boundary is formed as a nodal circle (NC) between the two regions. This particular mode is referred to as the 1NC mode, or sometimes called the first radial mode. Moreover, nodal diameters and nodal circles can be present at the same time. The mode shown in Figure 2.1c consists of two nodal diameters and one nodal circle, and is thus referred to as the (2,1) mode, or the first radial harmonic of the 2ND mode. The special case where the whole annulus moves in phase in time is the fundamental 'plane-wave' $(0, 0)$ mode, or simply called the 0ND mode. This is illustrated in Figure 2.1d.

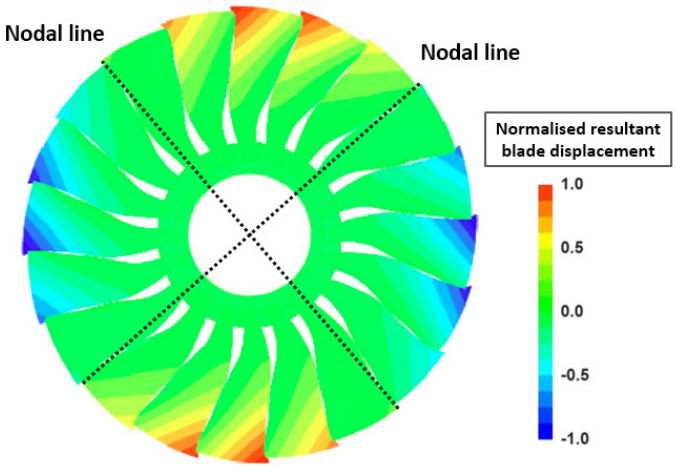


Figure 2.2: 1F/2ND mode for a fan. [12]

The vibration of a blade-disk assembly is analogous to the vibration of the annular disk described above, with the difference being the constraint at the blade root. The blade-disk assembly as a whole vibrates in a pattern analogous to the natural modes of a vibrating disk, where each part of the disk contributes to the motion with a constant phase lag. Figure 2.2 shows an example modeshape for a fan blade, where the blade-disk assembly vibrates in a 2ND pattern in the first flapwise bending (1F) blade mode. The 2ND pattern can be identified since the instantaneous displacement for the blades repeats itself in 180°of the circumference, which results in two motionless nodal lines as illustrated in the figure. Nodal circles are not present for the mode shown in Figure 2.2 as the motion at all radial heights are in phase for each blade.

The frequency of vibration for a blade ω (and hence the frequency of the generated unsteady perturbations) is commonly expressed in the dimensionless form of reduced frequency f_r as

$$f_r = \frac{\omega c}{W} \tag{2.1}$$

where ω is the angular vibration frequency, c is the blade chord and W is the free stream flow velocity. The reduced frequency characterises the ratio between the period of vibration and the time it takes for flow to travel from the leading edge to trailing edge, and is a key parameter in the analysis of flutter instability [3].

For a given blade and disk geometry, the natural frequency and mode-shape are unique for each blade-disk assembly mode, which are determined by the modal content (nodal diameters and nodal circles) of the vibration motion. It is thus sensible to refer to the blade-disk assembly modes by their mode orders, such as the circumferential harmonic m and, less commonly, the radial harmonic n. Moreover, nodal diameters of the blade-disk assembly modes rotate about the engine axis for a rotor, producing the so-called 'travelling waves'. In the work presented here the direction of rotation for the rotor (and the fan) is defined in the positive θ direction. Also, the forward travelling wave is defined for a positive rotation of nodal diameter, where a positive convention of circumferential order $m = +\text{ND}$ is used. Conversely, backward travelling waves correspond to negative nodal diameter rotation, and thus negative convention of circumferential order $m = -\text{ND}$. For a blade row consisting of N_b uniform distributed blades, the highest nodal diameter can be found as $\frac{N_b}{2}$ for even blade counts and $\frac{N_b-1}{2}$ for odd blade counts.

The inter-blade phase angle (IBPA) is defined as the circumferential phase lag between two consecutive blades

$$\text{IBPA} = \frac{2\pi m}{N_b} \tag{2.2}$$

which is constant for a nodal diameter mode in the range between $-180°$ and $180°$. Positive inter-blade phase angle represents forward travelling modes, and negative inter-blade phase angle corresponds to backward travelling modes. The inter-blade phase angle is an important parameter influencing the flutter stability of a blade row [13, 14]. For compressor rotors and fans, flapwise bending modes usually suffer from flutter instability in forward travelling modes with low inter-blade phase angle, whereas the torsion modes tend to have the lowest aero-damping in forward travelling modes close to $90°$ inter-blade phase angle [3].

It is common in the literature to refer to nodal diameter as circumferential order (or circumferential harmonic) and nodal circle as radial order (or radial harmonic). For clarity, the notation of nodal diameter (ND) and nodal circle (NC) is used when discussing the vibration of blade-disk assembly modes, and the (m, n) harmonic notation is used when discussing duct acoustic modes.

2.2 Aeroelastic Instabilities of Rotor Blades

The aeroelastic vibration of blades in turbomachines can be broadly categorised in two types: synchronous vibration and non-synchronous vibration. The term 'synchronous' refers to vibration frequencies that are in sync with (or harmonics of) the shaft speed of the rotor. Synchronous blade vibrations are driven by the periodic forcing induced by the passing of rotor and stator, which only occur at harmonic frequencies of the rotor shaft speed (hence the name 'synchronous'). On the other hand, non-synchronous vibrations (for instance flutter) occur at frequencies different from the shaft speed harmonics. This section briefly describes these two types of blade vibration and the interaction between vibration and duct acoustics.

2.2.1 Synchronous vibration

When the vibration is driven by the periodic forcing due to blades rotating past a distorted pressure field (potential or wake), resonance can occur if the frequency of excitation matches that of the natural frequency of the blade vibration mode. In this situation, the blades vibrate with frequencies that are harmonics of the shaft speed, and the vibration event is referred to as 'synchronous vibration'. This type of aeroelastic instability is excited and sustained by an external forcing, and is thus also known as 'forced response' [15].

Synchronous vibration can usually be identified based on the Campbell diagram [16]. Figure 2.3 shows a typical Campbell diagram. In this plot, the x axis is the rotor shaft speed and the y axis is the frequency. Synchronous vibration occurs at the crossings between lines of constant shaft speed harmonics (Engine Orders (EO)) and the lines of natural frequency of blade modes, as shown by the red circle symbols in this figure. In such situations, the vibration levels of the blade depend on

1. The magnitude of distortion, such as the wake.
2. Correlation between the unsteady pressure and the vibration mode.
3. The aerodynamic and mechanical damping present.

Although determining these parameters can be quite difficult at early design stages of an engine, the Campbell diagram can be used to identify the regions

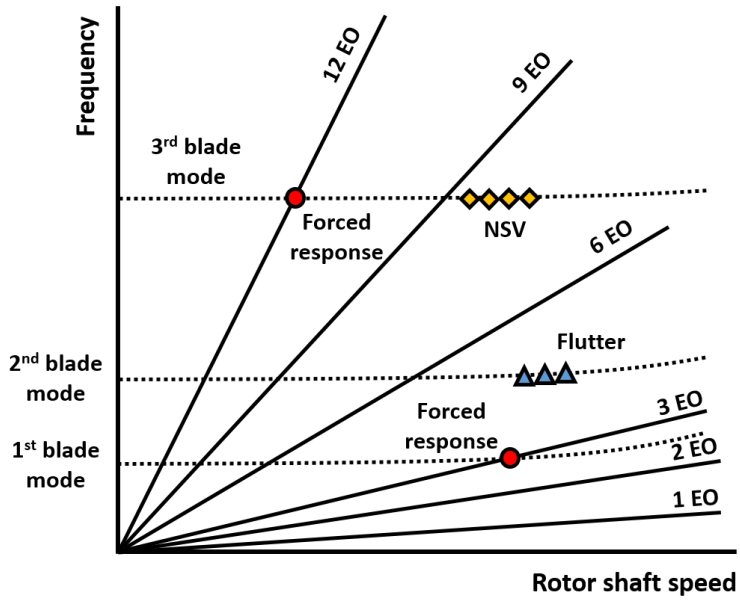


Figure 2.3: Typical aeroelastic vibration events for a compressor.

where synchronous vibration can occur.

2.2.2 Non-synchronous vibration

The term 'non-synchronous vibration' is a general classification of vibration events that occur at frequencies distinct from the engine order harmonics. Depending on the source of excitation, non-synchronous vibration can be broadly classified into three general types:

1. Unsteady flow driven
2. Flutter
3. Acoustic resonance

Unsteady flow driven

The first kind of non-synchronous vibration refers to blade vibrations driven by coherent flow structures such as vortex shedding, buffeting and rotating stall [17–19]. It is worth noting that this type of instability is sometimes referred directly as 'non-synchronous vibration' or 'NSV' in the literatures.

This type of vibration is usually self-excited due to the interaction between the blade and the unsteady flow. It should be noted that, for this type of instability, the unsteadiness in the aerodynamic flow is large scale in respect to the mean flow (thus nonlinear), and the vibration motion is excited and sustained by the unsteadiness of the flow. In such situations, the frequency and inter-blade phase angle of the vibration motion are determined from those of the unsteady aerodynamic excitation source. When the frequency of excitation is close to the natural frequency of a blade mode, the two frequencies can 'lock in' giving rise to high vibration levels, which may result in high cycle fatigue failures (illustrated in Figure 2.3 with diamond symbols). This type of instability presents one of the challenges in aeroelastic analysis of modern turbomachinery designs.

Flutter

Flutter as a self-feeding aeroelastic instability presents one of the biggest challenges in modern aero-engine designs. The mechanism of flutter is explained in Fung [17], and is briefly summarised here. The air flow past a vibrating blade induces a transient variation of aerodynamic loading on the blade surfaces. The induced transient aerodynamic loading (unsteady loading), in return, interacts and modifies the blade motion. This interaction between the unsteady aerodynamic force and the blade motion can lead to the amplification or attenuation of vibration, which determines the aeroelastic stability of the blade. An increase in vibration amplitude is unstable when energy is transferred from the surrounding flow to the mechanical vibration. Conversely, if the blade vibration is suppressed, the flow provides positive damping by removing energy from the vibration motion. This type of instability differs from that of previous section as the unsteadiness is caused by the blade vibration.

Figure 2.4 shows a schematic diagram of typical flutter regimes for a compressor. Stall flutter is one of the most common types of flutter in turbomachines. When a rotor operates near the stall line, shock wave movement, boundary layer separation and radial flow migration on the suction surface, driven by adverse pressure gradients, generate unsteady oscillatory forces which have been shown to be the key parameters leading to compressor (or fan) stall flutter [9]. It should be noted that the unsteady forces here are as

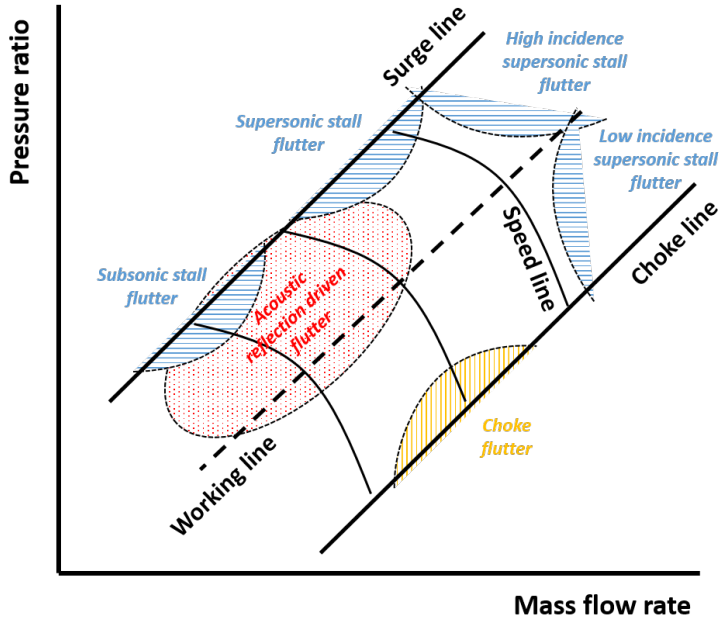


Figure 2.4: Typical flutter regimes of a compressor.

a result of blade vibration. Subsonic stall flutter occurs at part speed near the surge line and is driven by the interaction between the separated flow (or flow migration) and the modeshape of the vibration, whereas supersonic stall flutter is usually driven by shock induced boundary layer separation on the suction surface [20]. Although the exact mechanism of compressor stall flutter near surge is not yet fully understood, it usually occurs far from the working line.

For long aspect ratio blades (other examples include aircraft wings and wind turbine blades), classical flutter poses a threat which usually occurs at low reduced frequencies due to the coupling between the flapwise bending mode and the torsion mode [2]. The initiation of classical flutter does not require the stalling of flow or attached shock wave, and is thus able to occur in the vicinity of the working line. For modern turbomachinery blades, the structural dynamic design usually ensures a relatively high frequency difference between the (low order) flapwise bending modes and torsion modes, therefore mode coupling is unlikely to occur and classical flutter is not a common event in turbomachines.

Flutter of rotor blades occur at frequencies non-synchronous with the

engine order, which is illustrated in Figure 2.3 with the triangle symbols. Unlike forced response, possible regions of flutter cannot be pre-determined from the Campbell diagram without extensive numerical analyses (e.g. unsteady CFD computations). It will be shown in this thesis that, in the absence of mode coupling and stall, acoustic reflections are essential for flutter. Therefore, it is very important to identify this type of flutter, as it can occur very close to the working line of a compressor (as illustrated in Figure 2.4). Therefore, one of the main focuses of this thesis is to develop a new low-fidelity method which can be used in the design stages of an engine to predict the regions that flutter is likely to occur (i.e. the triangle symbols in Figure 2.3).

Acoustic resonance

The compressor operation generates various types of disturbances. Some of these disturbances are deterministic in nature and are characterised by the physical interactions between the blade and the flow. The examples of such disturbances include the harmonics of rotor wakes, acoustic interaction tones between rotor and stator [21], and perturbations generated by the vibration of blades [22, 23]. For instance, the interaction of rotor wakes with its downstream stator produces unsteady aerodynamic loading on the stator blade surfaces, which contributes to one of the main sources of aero-engine noise.

The excitation of blade vibration in a compressor due to acoustic disturbances is commonly referred to as acoustic resonance. Events of acoustic resonance were observed and studied by Parker and his co-researchers [24–26] for cascade vibration excited by vortex shedding from the trailing edge of upstream flat plates. High intensity discrete frequency tones distinct from the harmonics of blade passing were measured in various operating conditions. The relationship between the resonance frequency and the vortex shedding frequency was studied by varying the inlet air speed of the wind tunnel. Events of resonance were measured at air speeds slightly above the critical flow velocity for which the natural vortex shedding frequency (characterised by the Stouhal number) equals the resonance frequency. The recorded resonances were found to be the artifact of two dimensional standing waves in the cascade and in the test wind tunnel, which were later

confirmed analytically by solving the wave equation for the test geometry.

Moreover, acoustic resonance can also occur when the generated acoustic perturbations are trapped between bladed structures in a multi-stage system. This type of problem is driven by the fact that, unlike for fully convected waves, acoustic waves propagating in a rigid-annulus cylindrical duct can change from lossless transmission (cut-on) to exponential decay (cut-off) [21]. The critical condition, usually defined as the cut-off frequency, is a function of the duct geometry, flow Mach numbers and the order of mode (a mathematical expression will be derived in the next chapter).

In a multi-stage compressor (or fan) system, the transition of acoustic waves from cut-on to cut-off can occur at axial positions where a significant change of mean flow swirl takes place, for instance across a rotor row. Moreover, an incident acoustic wave can be partly transmitted and partly reflected by a bladed structure [27]. Therefore, in the situation where the propagation of acoustic waves is confined within the compressor duct due to the barriers of cut-on/off transition and high-level reflections at blade rows, acoustic modes can become 'trapped' between certain axial positions and acoustic resonance for blades within this confined region can occur. This type of 'trapped mode' resonance has been studied by many researchers [28–30], and has been found to be responsible for some instances of large amplitude non-synchronous blade vibrations.

Embedded blade row flutter

As introduced in the last section, the vibration of blades generate unsteady perturbations which can propagate in the duct of a compressor. The generation of these disturbances depends on the flow condition, blade geometry and modes of vibration. These disturbances propagate in the compressor duct between blade rows as waves due to their harmonic nature. Upon impinging on the adjacent blade rows, these propagating waves can be reflected back towards the generation source (i.e. the vibrating blade in this case), and interact with the vibration motion by altering the near blade unsteady flow field. The process of acoustic propagation and reflection between blade rows is illustrated in Figure 2.5. It should be noted that reflection can also occur due to sudden change of impedance in the duct, such as the opening of the intake. Hence the presence of a blade row may not be necessary

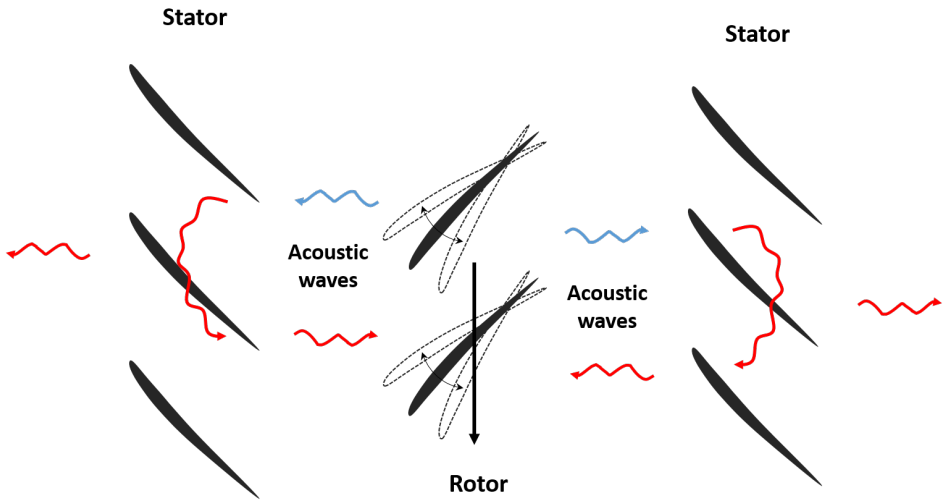


Figure 2.5: Traces of acoustic waves generated by the vibration of rotor blades.(Note: the wiggles of arrow are for illustration purposes only.)

for reflection to occur. The acoustic reflections result in a change of blade unsteady aerodynamic forces (such as unsteady lift and moment), and consequently flutter can occur when the unsteady forcing becomes in phase with the blade motion and the overall system damping becomes negative.

This type of flutter can occur for an embedded rotor in a multi-stage compressor (or fan) in the absence of flow separation or passage shock, and is thus much harder to predict (locate on the compressor map) at the design stage of an engine. The possible region of occurrence for the acoustic reflection driven flutter is illustrated by the red circular region in Figure 2.4. Whereas the flutter stability for an isolated rotor is predominantly determined by the flow on its blade surfaces, the flutter stability for an embedded blade row in a multi-stage system can also be affected by the acoustic reflections from nearby structures (not only the immediately adjacent structures). The typical reflecting structures include the stator vanes surrounding an embedded rotor and the opening of the intake (or exhaust).

Conventional flutter analysis for such an embedded rotor usually involves unsteady CFD computations of the isolated blade row models in an infinitely long duct with the assumption of negligible inter-row interactions. It is becoming increasingly apparent that the effects of adjacent rows are important and need to be accounted for. However, it is only recently that

research has begun to investigate multi-stage effects [31, 32]. Since then, very few publications can be found on this subject. The main findings of these publications are summarised here.

Hall and Silkowski [33] and subsequently Silkowski and Hall [34] developed a coupled mode analysis calculating the aeroelastic response of a two-dimensional blade row embedded in a multi-stage system. The flow field is resolved using a linearised full potential flow model, and the neighbouring blade rows are represented by transmission and reflection coefficients calculated using the linear cascade method developed by Whitehead [35]. The final solution of the problem is achieved by considering prescribed blade vibration and solving the assembled system of equations with transmission and reflection coefficients and inter-row coupling. The analysis showed that, aerodynamic damping of the embedded blade row can be significantly different from that predicted using an isolated blade row model. It was also shown that mode scattering are found of relatively less importance. Hall and Ekici [36] later extended this coupled mode method to accommodate radial eigenmodes based on three-dimensional Euler equations. The developed method was validated against the results of Namba [37] on the unsteady forcing of an oscillating two-row helical rotor blade. Comparison of unsteady aerodynamic force on the blades confirmed that aerodynamic damping of an embedded blade row can be significantly different from that of the isolated setup. In a later work, Ekici and Hall [38] presented a harmonic balance method for aeroelastic calculations of two-dimensional linear and non-linear unsteady flows with the focus on multi-stage effects. By comparing the predicted blade aerodynamic damping with those obtained using a time-domain method and a time-linearised unsteady coupled mode [34, 36], similar conclusions were drawn, signifying the importance of multi-stage effects on the flutter stability of an embedded rotor.

Li and He [39] investigated the influence of rotor-stator axial gap on the predicted aerodynamic damping of a rotor blade in a stage setup. Flutter analysis was performed on a transonic compressor stage consisting of a rotor and a downstream stator, where the rotor blade was excited in the first torsion (1T) mode. Figure 2.6, taken from [39], shows the CFD predicted aerodynamic damping of the rotor blade as a function of rotor-stator axial gap. It is obvious from the plot that the axial gap has a significant influence on the flutter stability of the rotor, where a sinusoidal-like rela-

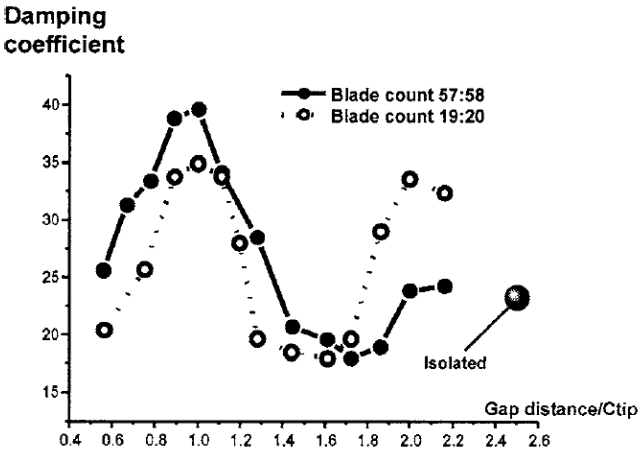


Figure 2.6: Aerodynamic damping of a rotor blade in a stage setup as a function of rotor-stator axial gap, taken from Li and He [39]

tionship can be identified. It was also shown that the change of blade count has a moderate effect on the blade damping variation. Huang et al. [40] conducted a similar analysis for the assembly of a stator and a rotor in a steam turbine stage, where flutter analysis was carried out for a rotor blade vibrating in the first flapwise bending (1F) mode. Predicted aerodynamic damping of the rotor blade showed strong dependency on the axial gap between the upstream stator and the rotor. The findings in these works highlight the importance of multi-stage interactions, on flutter stability of embedded blade rows, however, the paper did not provide any conclusive physical explanations to the mechanism of interactions. Recently, Rahmati et al. [41] conducted a series of flutter analysis of an isolated turbine cascade (the same as that used by Huang et al. [40]), an isolated compressor cascade and a transonic rotor-stator stage based on a frequency-domain method. The calculated aerodynamic damping of the isolated turbine cascade and the isolated compressor cascade showed adequate agreement with the experimental measurements. Flutter analysis of the transonic rotor in the stage setup again confirmed the previous findings that the neighbouring stator has a significant impact on the predicted rotor blade aerodynamic damping.

In a recent EU collaborative project [42] several organisations attempted to predict the flutter of a core compressor test case but there was no general agreement about whether the rotor blades would be stable or not. The

discrepancy in predictions, besides the use of different computational codes, comes from the differences in the treatment of boundary conditions and the number of blade rows included in the simulation, indicating that the flutter prediction of an embedded blade row is not an established technique. Moreover, there are known cases in which the selection of the boundary condition style (i.e. reflecting or non-reflecting) can dramatically change the outcome of the computations (e.g. from stable to unstable) indicating that acoustic reflections from the boundaries have a major impact on the predicted stability.

In summary, the previous work on this subject can be broadly categorised into three intertwined areas: study of the influence of neighbouring blade rows, development of more efficient frequency domain numerical methods and the investigation and revelation of the suitable computation domain (i.e. number of blade rows to model). However, none of them addressed the fundamental question as why and how does this interaction occur. It was evident from these investigations that multi-stage effects are important for the flutter stability of an embedded blade row, yet under what conditions the multi-stage effects are most important are still unknown [36, 39]. Moreover, can these effects be modelled in early design stages of an engine in a cost efficient manner? Therefore, it is the aim of this thesis to address these questions and bridge the knowledge gap to provide a comprehensive picture of the physics behind the embedded blade row flutter.

2.3 Aeroacoustics of Axial-flow Compressors

As described in the last section, the flutter of an embedded blade row can be driven by acoustic reflections from its adjacent structures in the absence of flow separation. Therefore, the understanding of this type of flutter requires the knowledge of acoustic waves originated from the vibration of blade-disk assemblies. This section briefly reviews the established work on the generation, propagation, transmission and reflection of acoustic waves in axial flow compressors.

2.3.1 Sound generation due to vibration

The vibration of blades induces a change of flow incidence and a change of passage area which in return changes its unsteady aerodynamic loading [17]. This change of flow incidence and passage area generate disturbances in density, velocity and pressure around the blade surface, which can propagate away from the blade. In annular cylindrical compressor ducts, these disturbances can propagate along the engine axis (upstream and downstream) away from the source in the form of waves. In the absence of flow separation, turbulent boundary layer and wakes, discrete frequency acoustic waves and shed vorticies (inviscid vortical waves) can be generated due to the vibration motion.

For the past few decades, extensive work has been done on sound generation by rotors, but the main focus has been wake induced rotor-stator interaction tones [21] and broadband noise generation due to turbulence [44]. Very few publications can be found on the sound generation due to blade vibration. Mani [45] obtained an approximate solution to acoustic wave generation by modelling the blades as point forces. Whitehead [22] and Smith [23] individually studied the vibration of a two-dimensional linear cascade consisting of thin flat plates at zero mean incidence, and the generation of perturbations due to bending and torsional vibration. Properties of the generated acoustic and vortical waves, such as the wavenumber, modal amplitude and phase, are found to be dependent on the blade geometry (such as stagger, chord, camber and solidity), flow condition, vibration frequency and inter-blade phase angle. Moreover, the comparison between experimental results and analytical predictions based on Smith shows that neglecting the steady loading of the blade could contribute to under-estimation of the amplitude of acoustic waves generated by blade vibration [23].

2.3.2 Propagation of acoustic waves

The unsteady perturbations generated by blade vibration can propagate in the compressor duct in the form of waves: entropic wave, vortical wave and acoustic wave [46]. The entropic wave, which carries the perturbation of density, and the vortical wave, which carries the disturbances in vorticity, are both convected downstream by the flow. Acoustic waves contain perturbations in density, velocity and pressure, and can propagate in both

the upstream direction and the downstream direction of the flow. Therefore, a vibrating blade row in an annular cylindrical duct can generate an upstream propagating acoustic wave, a downstream propagating acoustic wave and convected entropic and vortical waves. It is worth noting that the entropic and vortical waves are not affected by the 'cut-off' phenomenon since they are fully convected by the flow. The theory of acoustic wave propagation in annular cylindrical ducts is well established, and is covered in detail in [21, 47].

2.3.3 Transmission and reflection of acoustic waves

An acoustic wave impinging on a blade row changes the unsteady aerodynamic loading of the receiving blade row by inducing a change of its surrounding flow field. The blades, driven by the fluctuating unsteady lift, react by emitting unsteady perturbations in its upstream and downstream flow fields [22]. The emitted perturbations, in a similar form to those generated by a vibrating blade, manifest as propagating waves in the duct. Therefore, the incident acoustic wave is observed to be partially transmitted and partially reflected by a blade row. An upstream propagating acoustic wave can be reflected into a downstream propagating acoustic wave and a downstream propagating vortical wave, whereas a downstream propagating acoustic wave induces reflections of only acoustic type (since vortical wave cannot be convected upstream).

The transmission and reflection of acoustic waves by a flat plate cascade was studied by Kaji and Okazaki [27, 48] for a uniform subsonic mean flow. In the first part of Kaji and Okazaki's work [48], a simple semi-actuator disk method was devised with the assumption of infinitesimal blade spacing, finite blade chord and zero camber. Perturbations of the unsteady flow field were assumed to have wave-like solutions. Transmission and reflection coefficients of the incident acoustic wave were calculated by satisfying the continuity of mass flow and conservation of total enthalpy at the leading edge and the trailing edge of the cascade. Transmission and reflection coefficients were found to be a function of duct geometry, mean flow Mach number, speed of sound, blade stagger and mode angle of the incident wave. In the second part of Kaji and Okazaki's work [27], transmission and reflection of acoustic waves by a blade row was studied using an acceleration

potential method where the blades were treated as unsteady distribution of pressure doublets. The effect of finite blade spacing was studied at the 'sub-resonant' (cut-off) and 'super-resonant' (cut-on) conditions. The obtained results showed very similar trends with the results based on the semi-actuator disk method [48] for cut-on conditions. Mani and Horvay [49] studied the problem of arbitrary spacing flat plate cascade using the Wiener-Hopf technique [50] by treating the blades as semi-infinite to solve the 'incidence problem' (reflection) and 'emission problem' (transmission) individually. The solutions were in a good agreement with Kaji and Okazaki [48] at low acoustic wavelength to blade chord ratios, whereas the accuracy deteriorates with the increase of this ratio. Ameit and Sears [51] studied the same problem at the high limit of wavelength to chord ratio using a quasi-steady Prandtl-Glauert analysis to obtain a good agreement with Kaji and Okazaki [48]. Based on the work of Lane and Friedman [52], Whitehead [22] studied the sound generation due to blade vibration and the transmission and reflection of acoustic waves at a flat plate cascade of finite chord and blade spacing. This was achieved by assuming harmonic wave-like solutions which satisfy zero upwash and zero pressure jump at the blade surfaces. A good agreement was obtained with the solutions by [48]. A similar method to [22] was proposed by Smith [23] which treats the blades as a series of continuous singularity distributions. The final solution was obtained through the summation of each singularity solution, and show a good agreement with Kaji and Okazaki [48].

In the absence of bladed structures, reflection of acoustic waves can also occur due to sudden change of duct impedance, for instance at the opening of an intake. Rienstra [53] derived an analytical solution for the radiation, reflection and scattering of acoustic modes at the opening of an exhaust nozzle using a Wiener-Hopf technique [50], based on which the reflection coefficient and power loss for an incident acoustic wave can be obtained. Moreover, due to the axial geometry and flow variation in a compressor duct, a cut-on acoustic mode can become cut-off as it propagates along (or against) the axial direction. Resonance can occur at the interface between cut-on and cut-off, resulting in a complete reflection of an incident wave [54].

2.4 Prediction Methods for Flutter

With the development of computing power, the use of numerical methods for aeroelastic predictions of turbomachinery components is becoming widespread [55]. Based on the interaction treatment between the fluid and the structure, these methods can be broadly categorised into two major branches [55]: classical methods and integrated methods. The coupling effect between the fluid and the structure is modelled in the integrated methods, whereas it is neglected in the classical methods. This section briefly reviews the established methods for flutter computations of turbomachines.

Classical methods deal with aeroelastic vibration in an uncoupled fashion, where the effect of flow on structural vibration is ignored. The solution of the problem is typically formulated as follows: the free vibration of blades is first considered so that the modeshape can be obtained, which is followed by the calculation of unsteady aerodynamic loading due to the imposed modeshape (with arbitrary amplitude), and thus the blade flutter stability. By doing so, the non-linear coupled fluid-structural system can be divided into two linear uncoupled systems, which can be analysed separately (and sequentially) with greatly reduced complexity. Whitehead [14] conducted some early studies on the bending and torsion flutter of a two-dimensional unstalled cascade based on the work of Lane [13] and Lane and Friedmann [52]. It was found that flutter can occur at reduced frequencies below a critical value with a phase difference between the motion of neighbouring blades (later known as the 'inter-blade phase angle'). Methods later developed include the (semi-) actuator disk theories based on linearised cascade solutions for small inter-blade phase angle [56–60], and the eigensolution methods for the aeroelastic equations of motion based on linearised harmonic unsteady aerodynamic coefficients expressed in the frequency domain [61–66].

Computations using the integrated methods are performed, usually based on unsteady CFD computations, by coupling the blade motion with the flow. This is achieved by means of either a fully integrated approach or a partially integrated approach [55]. The fully integrated approach solves the fluid and structural equations simultaneously at the same time step and in a fully coupled fashion. However, this type of method requires careful treatment of the grid discretisation and numerical algorithms [67], and is normally not used in turbomachinery applications. The solution of the

partially integrated method is obtained through separate computations of the fluid and structural equations, where information is exchanged at every (or fixed intervals of) time step on the interface boundary through boundary conditions. In order to minimise the effect of time lag between the fluid and structural computations, computations using the partially integrated method require careful choice of time-stepping. One of the popular approaches of the partially integrated method is the modal representation form of the aeroelastic equations. In this approach, the structural model is represented by the modeshapes of the vibration modes obtained from the undamped eigensolutions using structural finite-element analysis, based on which the global aeroelastic equations can be transformed into a form of modal variables. The obtained modeshapes for the vibration modes of concern are interpolated onto the aerodynamic mesh at the beginning of the computation, and the exchange of information is carried out regularly on blade surfaces at time step intervals. This type of method has been applied to transonic wing flutter, which was the drive for its development, and turbomachinery applications with a good degree of success [6, 68–72]. Moreover, a variation of the partially integrated method has been developed [73–75] where the fluid domain and the structural domain are both modelled in a time-accurate fashion. The motion of the structure is calculated (using the structural model) from the aerodynamic loading (obtained from the fluid dynamics model) of the previous time step, and the solution is advanced in time by calculating the updated aerodynamic forces due to the new structural positions. Since the solutions of the fluid model and the structural model are obtained separately in a staggered order, coupled fluid-structure aeroelastic computations can be carried out using different solvers provided an efficient algorithm for the interface is devised.

Conventional analysis of such a coupled fluid-structure system usually consists of finite-element methods for the structural model, and unsteady three-dimensional Navier-Stokes aerodynamic flow solvers based on time domain methods or frequency domain methods [6, 76–80]. For time domain methods, the unsteady flow solutions are marched in time with appropriate temporal resolution for the frequency of concern. Linear as well as nonlinear aeroelastic interactions (such as limit cycle vibration) can be modelled using the time domain based methods provided appropriate spacial and temporal resolutions are specified. To capture the interaction between

blade rows in a multi-stage system (such as the case for embedded blade row flutter), the time domain methods usually require unsteady computations of full annulus multi-row models with relatively small time steps (since the solution contains harmonics of blade-passing frequencies), which poses very high demands on computing power and time cost. In order to lower the computational cost for unsteady multi-row analysis, methods for aerodynamic flow solutions based on the frequency domain are sought. These methods operate by transforming the aerodynamic flow equations into the frequency domain, based on which solutions for selected frequencies can be obtained. Classical frequency domain methods [36, 81–87] are those based on the assumption that the unsteady flow field can be split into a time-independent component (mean flow field) and a harmonic time-varying component (small amplitude perturbation). The aerodynamic flow equations, either the inviscid Euler equations or the viscous Navier-Stokes equations, can then be linearised and transformed into the frequency domain, which are solved for the frequency of concern. Over the past few years, non-linear methods, such as the non-linear harmonic balance methods, have been developed [88–91] where the aerodynamic flow equations are transformed into the frequency domain and solved for selected frequencies in a non-linear fashion, where coupling between the frequencies are allowed (through the coupling terms in the governing equations). The transformed aerodynamic flow equations for multiple frequencies are non-linear in nature and are solved in an iterative approach. Accuracy of the final solutions are found to be highly dependent on the number of harmonics included in the computation. Due to the formulation of methods in the frequency domain, the computation model can usually be reduced to single-passage by using periodic (phase-lagged) boundary conditions. Moreover, certain treatments of boundary conditions for turbomachinery applications, such as non-reflecting boundary conditions [46, 92, 93], can be implemented in a straightforward fashion as opposed to the time-domain methods.

The unsteady CFD flutter computations performed in this work are based on a partially integrated approach using the modal representation form of the aeroelastic equations. Computations are performed by assuming a high blade-air mass ratio and neglecting the effect due to multi-mode coupling. The methods used in this thesis are introduced in the next chapter.

3 Computational Methods

This chapter briefly introduces the methodology of the computational models that is used throughout this work. Aerodynamic and aeroelastic models employed by the CFD solver are presented along with strategies for unsteady flutter computations. Additionally, a post-processing wave-splitting method to decompose unsteady flow perturbations into propagating waves is presented, which is essential for understanding the physics behind embedded blade row flutter.

3.1 Aerodynamic Model

The aerodynamic solutions are obtained using a 3D, time-accurate, viscous, finite-volume, Reynolds-averaged Navier-Stokes (RANS) compressible flow solver [94].

The solver is based on the one-equation Spalart-Allmaras turbulence model [95]. The parameters in Spalart-Allmaras have been adjusted on previous fans and compressors to get a good agreement near the stability limit; the parameters are held constant throughout the work. The flow variables are represented on the nodes of a generic unstructured grid and numerical fluxes are computed along the edges of the grid. The numerical fluxes are evaluated using Roe's flux vector difference splitting to provide matrix artificial dissipation in a Jameson-Schmidt-Turkel (JST) scheme [96]. The overall solution method is implicit, with second-order accuracy in space and time.

For steady-state flow computations, the solution is advanced in pseudo-time using local time stepping and solution acceleration techniques such as residual smoothing, while dual time stepping is used for time-accurate unsteady computations. The unsteady flow cases are computed as unsteady Reynolds-averaged Navier-Stokes (URANS), with the basic assumption that the frequencies of interest are sufficiently far away from the frequencies of

turbulent flow structures. The resulting CFD solver has been used over the past 20 years for flows at design as well as off design conditions with a good degree of success [12, 97, 98].

3.2 Aeroelastic Model

The aeroelastic computation is performed in a fluid-structure coupled fashion based on the modal representation form. A brief summary of the aeroelastic methods used in this work [6] is given below.

Structural dynamic finite-element analysis of the blade-disk assembly at the shaft speed of interest is carried out (in the absence of air) to obtain the natural frequencies ω and modeshapes Ψ from an undamped eigensolution. As different meshes are commonly used for structural finite-element analysis and CFD analysis, the obtained structural modeshapes are interpolated onto the blade aerodynamic mesh in the form of principle coordinates. The coupling of the structural motion and the aerodynamic solution is achieved by the global aeroelasticity equations as

$$\boldsymbol{M}\ddot{\boldsymbol{x}} + \boldsymbol{C}\dot{\boldsymbol{x}} + \boldsymbol{K}\boldsymbol{x} = \boldsymbol{f} \tag{3.1}$$

where $\boldsymbol{M}$, $\boldsymbol{C}$ and $\boldsymbol{K}$ represent the mass, damping and stiffness matrices of the system, $\boldsymbol{x}$ is the blade displacement vector and $\boldsymbol{f}$ is the aerodynamic force vector on the blade surface. The right hand side of the equation represents the normal aerodynamic loading on the blade $\boldsymbol{f} = p\delta S\boldsymbol{n}$, where p is the static pressure, δS is the local area under loading and $\boldsymbol{n}$ is the unit normal vector on the blade surface. The aerodynamic force consists only of normal unsteady pressure forces as the unsteady viscous shear stresses are typically orders of magnitude smaller. The left hand side of Equation 3.1, representing the blade structural response, is modeled using the obtained mass-normalised modeshape matrix $\boldsymbol{\Phi}$

$$\boldsymbol{x} = \boldsymbol{\Phi}\boldsymbol{q} \tag{3.2}$$

where $\boldsymbol{\Phi} = \frac{1}{\sqrt{m}}\boldsymbol{\Psi}$, m denotes the mass and $\boldsymbol{q}$ is the modal displacement vector. The aeroelastic equations of motion can thus be transformed into

modal variables as

$$\boldsymbol{\Phi}^T \boldsymbol{M} \boldsymbol{\Phi} \ddot{\boldsymbol{q}} + \boldsymbol{\Phi}^T \boldsymbol{C} \boldsymbol{\Phi} \dot{\boldsymbol{q}} + \boldsymbol{\Phi}^T \boldsymbol{K} \boldsymbol{\Phi} \boldsymbol{q} = \boldsymbol{\Phi}^T \boldsymbol{f} \tag{3.3}$$

where $\boldsymbol{\Phi}^T \boldsymbol{f}$ represents the modal force vector. By applying the orthogonality properties of modes one obtains

$$\boldsymbol{\Phi}^T \boldsymbol{M} \boldsymbol{\Phi} = \frac{1}{m} \boldsymbol{\Psi}^T \boldsymbol{M} \boldsymbol{\Psi} = \boldsymbol{I} \tag{3.4}$$

$$\boldsymbol{\Phi}^T \boldsymbol{C} \boldsymbol{\Phi} = \frac{1}{m} \boldsymbol{\Psi}^T \boldsymbol{C} \boldsymbol{\Psi} = \begin{bmatrix} \ddots & & \\ & 2\zeta\omega & \\ & & \ddots \end{bmatrix} \tag{3.5}$$

$$\boldsymbol{\Phi}^T \boldsymbol{K} \boldsymbol{\Phi} = \frac{1}{m} \boldsymbol{\Psi}^T \boldsymbol{K} \boldsymbol{\Psi} = \begin{bmatrix} \ddots & & \\ & \omega^2 & \\ & & \ddots \end{bmatrix} \tag{3.6}$$

The final modal response equation for the blade mode j can thus be written as

$$\ddot{\boldsymbol{q}} + \begin{bmatrix} \ddots & & \\ & 2\zeta_j\omega_j & \\ & & \ddots \end{bmatrix} \dot{\boldsymbol{q}} + \begin{bmatrix} \ddots & & \\ & \omega_j^2 & \\ & & \ddots \end{bmatrix} \boldsymbol{q} = \boldsymbol{\Phi}^T \boldsymbol{f} \tag{3.7}$$

The aeroelasticity equations of motion (Equation 3.7) are advanced in time using the Newmark-β method [99]. Energy transfer between the structural domain (internal of the blade) and the aerodynamic domain (external to the blade) is carried out each time step through boundary conditions, and the aerodynamic mesh is deformed accordingly using a spring analogy [100] to follow the structural deflection.

3.3 Treatment of Boundary Conditions

Unlike CFD analysis of flow over aircraft wings or wind turbines, the inflow and outflow boundaries for turbomachines are usually within one chord away from the blade row of interest. The close proximity of flow boundaries drives the development of non-reflecting boundary conditions so as to minimise the numerical reflections of steady shocks and unsteady perturbations [46, 94]. In this work, two types of far-field flow boundary conditions are studied [101]:

1. Physical boundary conditions: total pressure, total temperature and flow angle at the inflow boundary, and static pressure at the outflow boundary.

2. Non-reflecting boundary conditions, by using characteristics variables of Euler equations.

The first type of boundary conditions represents the minimum of physical knowledge required for the resolution of a flow field. This type of boundary conditions is most commonly used in turbomachinery applications however is known to be numerically reflective for three-dimensional unsteady computations. The numerical nature of this type of boundary conditions can generate non-physical reflections due to outward propagating unsteady disturbances. It has been demonstrated [46, 94] that the treatment of flow boundary conditions can significantly affect the shock position due to its close proximity to the blades. Experiences of past studies show that the induced reflection depends on the complexity of the steady flow field (radial/circumferential flow profile, swirl, shock wave etc.) and the characteristics of the outward propagating waves such as the nodal diameter and axial wavenumber. The numerical reflections of these boundary conditions provide little physical significance, however, they are used in this work to study the impact of acoustic reflections from flow boundaries on the blade aero-damping.

The second type of boundary conditions is based on the characteristics of Euler equations [46], which are also known as the 'Riemann invariants' [101, 102]. The characteristics can be obtained from a general eigenvalue solution of the linearised Euler/Navier-Stokes equations, and are constant for the flow field in analysis, hence the name 'invariants'. For a simple one-dimensional axial flow, there exists three characteristics (or eigenvalues): $U + a$, $U - a$ and U, where U denotes the axial flow velocity and a is the speed of sound. The three characteristics in this case respectively correspond to a downstream propagating acoustic wave, an upstream propagating acoustic wave and a downstream convected wave (in this case an entropic wave), where the value of the characteristic variables represents their speed of propagation. It can be easily identified that acoustic waves propagate with the Doppler shifted sound speed $U + a$ and $U - a$ (due to the convection by the flow), and the speed of the convected wave U de-

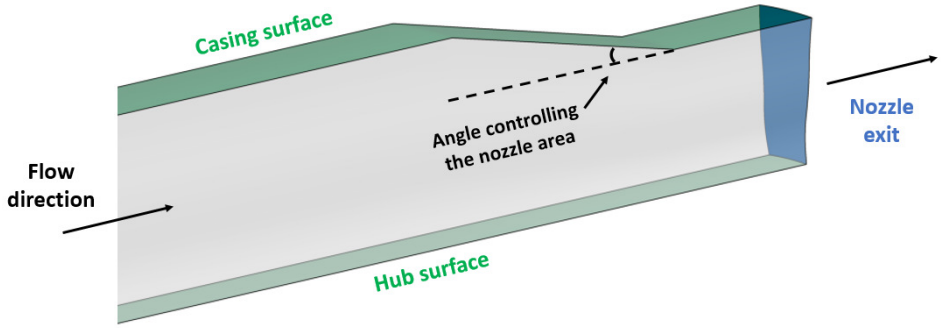


Figure 3.1: Variable area nozzle for exit flow.

pends fully on the flow. For two-dimensional and three-dimensional flow, additional characteristics (convected vortical waves) are introduced corresponding to the additional momentum equations. Applications of this type of non-reflecting boundary conditions on turbomachines can be found in [46]. It is worth noting that efficient exact three-dimensional non-reflecting boundary conditions for time domain Navier-Stokes applications are yet to be developed. Most of the existing non-reflecting boundary conditions employed by current CFD solvers, including the one used in this work, are approximate treatments for unsteady analysis. Therefore, numerical reflections by the Riemann invariants boundary conditions can still occur in the computations, however the amplitude of reflection is much smaller than that due to the physical type of boundary conditions

For the steady state computations computed in this work, physical boundary conditions (will be denoted as 'PTBC' onwards) are applied at the far-field flow boundaries. These include the far-field flow boundaries outside the intake for fan analysis, and the inflow boundary upstream of the inlet guide vane (IGV) (or the ESS) of a whole compressor assembly. The exit flow downstream of a fan stage or the outlet guide vane (OGV) of a whole compressor assembly is controlled by a choked inviscid variable area nozzle. An example of the exit flow nozzle is shown in Figure 3.1. The flow through the nozzle is controlled by changing the angle of the nozzle (i.e. changing the area ratio). It has been shown in [103] that the use of a choked exit flow nozzle is advantageous when the radial distribution of the exit boundary conditions is unknown. In steady state computations, the boundaries at the interface between the stationary and rotating blade rows are modelled as

mixing planes [104], and periodic boundary conditions are applied at the interfaces between blades in the circumferential direction.

For unsteady time-accurate computations, the interfaces between stationary and rotating blade rows are modelled as sliding planes. For inlet and outlet boundaries, non-reflecting boundary conditions based on Riemann invariants (will be denoted as 'RIBC' onwards) are applied for most cases (unless otherwise specified) to minimise numerical contaminations to the solution. The effectiveness of the applied non-reflecting boundary conditions is studied in detail in Section 7.5.

3.4 Strategies for Flutter Computation

The starting point for all flutter computations is the converged steady state solution at the flow condition of interest. By treating the interfaces between blade rows as mixing planes, steady state solutions are obtained for the complete compressor (or fan) assembly (i.e. single passage assembly of all the blade rows) using a single passage approach. The steady state solutions for blade row(s) of interest are subsequently extracted from the complete compressor (or fan) assembly solutions, and are expanded to full annulus when required. From this point on, three types of flutter strategies are used:

1. Full annulus computation with blade displacement tracking.

2. Full annulus computation with prescribed blade motion.

3. Single passage computation with prescribed blade motion.

In the first approach, flutter computations are started by imposing a small initial velocity on the blades for the modes of interest, and the time history of the blade motion is tracked. Figure 3.2 shows two typical examples for blade displacement time history. The vibration mode is unstable when the amplitude of displacement grows with time (red) and stable for decreasing vibration amplitude (blue). The aerodynamic damping of the blade can be obtained from the logarithmic decrement δ_d (log-dec) of the displacement amplitude as

$$\zeta = \frac{\delta_d}{2\pi} \tag{3.8}$$

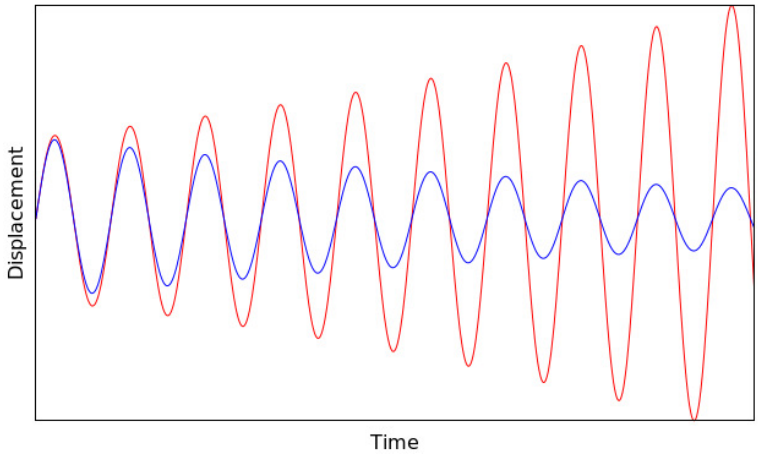


Figure 3.2: Time history of blade displacement for an unstable mode (red) and a stable mode (blue).

where ζ denotes aerodynamic damping. Positive aerodynamic damping corresponds to a stable blade and negative aerodynamic damping indicates flutter. This type of approach allows flutter computations to be performed for a range of blade modes (e.g. 1F and 1T) and all the nodal diameter modes (assembly modes) simultaneously in a single simulation, which is very useful when the unstable blade mode(s) and nodal diameter(s) are not known.

The second approach differs from the first approach in that flutter computations are started by imposing a small and fixed amplitude motion of the blades for a certain blade mode and nodal diameter, i.e. the blade vibration motion is prescribed in a modal pattern which is not affected by the aerodynamic loading. The prescribed blade motion is large enough to be well outside the numerical 'noise', but small enough for the unsteady flow to be well represented as linear. The imposed tip displacements are typically of the order of 0.3% of the blade chord at the tip. The instantaneous lift on the blade can be expressed as a contour integral over the surface as

$$l = \oint p\boldsymbol{n} \cdot \boldsymbol{s} dS \tag{3.9}$$

where l is aerodynamic lift, $p\boldsymbol{n}$ is the local aerodynamic force vector as introduced in Equation 3.1, $\boldsymbol{s}$ is the unit vector normal to the mean flow and $\oint dS$ denotes the contour integral over the surface area.

The flutter stability of the blade is calculated using an energy method based on the work sum of aerodynamic loading. The aerodynamic work per vibration cycle w is computed using

$$w = \int_T \oint p\boldsymbol{n} \cdot \boldsymbol{v} dS dt \tag{3.10}$$

where T is the period of vibration and $\boldsymbol{v}$ is the blade velocity vector in the prescribed mode of vibration. In the absence of mechanical damping, positive work done corresponds to a net energy transfer from the surrounding flow to the blade vibration, hence is an indication of flutter instability. On the contrary, negative work done is associated with positive damping by the aerodynamic forces and thus corresponds to a stable blade. Aerodynamic damping can be computed from the work done per cycle as

$$\zeta = -\frac{w}{v_0^2} \tag{3.11}$$

where v_0 is the amplitude of blade vibration velocity. When there is no aerodynamic coupling between assembly modes, the first approach and the second approach yields very similar blade aerodynamic damping (neglecting the effect due to frequency shift).

The third approach and the second approach differ in the expansion of blade passages, where a single passage of a blade row is computed by imposing phase-lagged boundary conditions at the periodic boundaries. Blade-disk assembly modes (nodal diameter) are simulated through the inter-blade phase angle of the flow solutions on the two periodic boundaries. Aerodynamic work done per cycle and aerodynamic damping are calculated in a similar fashion as the second approach. For the second and third approaches, work done on the blade suction surface or pressure surface as well as its spanwise distribution can be determined to identify the region of instability.

For full annulus computations using the first or the second approach, more than one blade row can be included in the unsteady computations by means of sliding planes. Throughout this work, the first approach is used to determine the unstable blade mode and nodal diameter in a high fidelity multi-row setup which is capable of capturing the influence of adjacent blade rows. Once the unstable mode is determined, the second approach is used

for this particular blade mode and nodal diameter to study the behaviour of acoustic waves (generation, propagation, transmission and reflections) generated by blade vibration. Computations using the third approach is constrained to a single passage single blade row setup. However they are significantly less demanding on computational resources, and provide a cost efficient way to study the influence of acoustic reflections (either from numerical boundary conditions or physical structures) on flutter stability of the rotor of interest. Therefore, most of the early investigative work reported here is carried out using the third approach. It is worth noting that the aim of this work is to predict the onset of flutter, and not the amplitude of limit cycle vibrations, thus the use of the energy method (Strategy 2 and 3) is considered acceptable.

3.5 Method for Wave-splitting

In order to investigate the generation, propagation, transmission and reflection of acoustic waves generated by blade vibration, a wave-splitting procedure based on Moinier and Giles [105] is performed in the compressor duct (and intake) to obtain the properties of acoustic waves. A brief introduction of the method is summarised here, and an outline of the method for eigenmode decomposition for an inviscid flow solution is given in Appendix I.

The decomposition of propagating 3D eigenmodes (into an upstream propagating acoustic mode, a downstream propagating acoustic mode and convected vortical and entropic modes) is performed by solving the Generalised Eigenvalue Problem matrix resulting from the linearised Navier-Stokes equations. The Navier-Stokes equations are linearised with respect to time to form the governing equations (in cylindrical coordinate system) for the unsteady flow disturbances. Harmonic wave-like solutions are assumed in time and axial and circumferential space. The solutions in the radial direction are discretised with appropriate wall boundary conditions applied at the hub and casing surfaces. The final governing equations can be formed as a Generalised Eigenvalue Problem matrix, where the eigenvalues correspond to the axial wavenumber of the wave-like solutions. The splitting of modes can thus be achieved by identifying the direction of mode propagation based on the corresponding axial wavenumber, and by evaluating

the associated amplitude of unsteady pressure and entropic perturbations.

The solution of the Generalised Eigenvalue Problem is carried out numerically based on the temporal and circumferential Fourier transformed unsteady CFD solutions. Axial wavenumbers of propagating modes are computed as the eigenvalues, and the radial distribution of modal amplitude and phase are obtained from the eigenvector solutions. The overall solution of the wave-splitting procedure is of second order accuracy with fourth order artificial dissipation.

The wave-splitting procedure is used repeatedly in this thesis to study the behaviour of propagating acoustic waves. Validation and comparison with analytical solutions are carried out for various cases as will be presented in Chapter 5 to Chapter 8.

4 Formulation of Reduced Order Model

4.1 Overview and Strategy

In order to study the influence of acoustic reflection on flutter stability of an embedded blade row, the generation, propagation and reflection of acoustic waves due to blade vibration need to be modelled. The generation of acoustic waves can be modelled numerically using a single passage single row approach, which is computationally inexpensive and can be performed routinely in the design stage. The propagation of acoustic waves is modelled analytically for an axi-symmetric annular cylindrical duct, and the transmission and reflection of acoustic waves are calculated based on analytical theories for two dimensional cascades. Established analytical methods are extended to model the propagation of acoustic waves in compressor duct and reflection at blade rows. A comparison study is carried out to investigate the accuracy and applicability of the proposed analytical method when applied to three dimensional highly loaded blades.

Figure 4.1 illustrates the entire reflection process of acoustic waves originated from the leading edge and trailing edge of a vibrating embedded rotor. The reflection process can be divided into three stages: (1) outward propagation (from rotor to stator) in the duct between the blade rows, (2) reflection at the stator and (3) backward propagation (from stator to rotor). These three stages are illustrated in Figure 4.1 as three separate components, namely outward, reflection and backward. Modal properties of the generated acoustic waves, such as amplitude and phase, originating from the leading edge and trailing edge of a rotor, are traced analytically throughout the entire reflection process.

The calculated reflected waves can be used in two ways: (1) simplify the CFD model to lower computational cost; (2) devise a low-fidelity analyt-

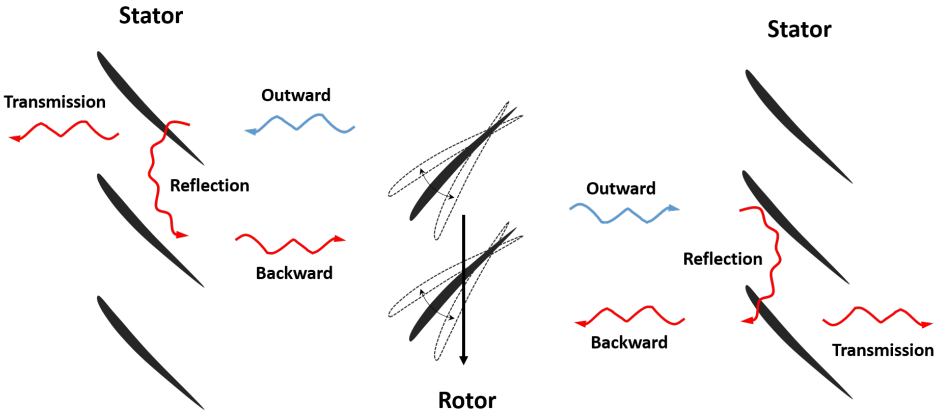


Figure 4.1: Reflection process of acoustic waves generated by the vibration of rotor blades.

ical flutter prediction model. The simplification of the CFD computation model can be achieved by imposing the calculated reflected waves as unsteady plane sources in the domain of the embedded blade row using a single passage single-row approach instead of full annulus multi-row computations. Alternatively, a low-fidelity analytical model can be devised using this information, which is capable of predicting the influence of acoustic reflection on aerodynamic damping of an embedded blade row by examining the amplitude and phase of reflected acoustic waves.

4.2 Generation of Acoustic Waves

The vibration of blades generate unsteady perturbations which can be grouped into three types of waves: entropic wave, vortical wave and acoustic wave [46]. The frequency and nodal diameter of the generated unsteady perturbations (and waves) are directly linked to those of the vibration mode, for instance a 2ND vibration mode will excite all the radial harmonics of the acoustic waves with the same circumferential order (as described in Section 2.1). In the studies considered in this work, the mean flow is assumed to be inviscid and homentropic in the absence of flow separations. Therefore, the generation of entropic perturbation is neglected, and only acoustic and vortical waves are considered.

The generation of waves is modelled numerically using unsteady single

passage single-row CFD computations. Nodal diameter modes are calculated using phase-lagged boundary conditions applied on the periodic boundaries. Inflow and outflow boundary conditions are treated as non-reflecting type (RIBC, Section 3.3) so as to minimise numerical reflections. The blade vibration motion is prescribed with a fixed displacement amplitude using the third flutter computation strategy (Section 3.4), and modal force time history is tracked (right hand side of Equation 3.7). Finally, a wave-splitting procedure (Section 3.5) is carried out, based on the temporal Fourier transformed results of a fully developed vibration cycle, to decompose the unsteady flow disturbances into propagating waves. Modal properties, such as modal eigenfunction, axial wavenumber k_x, modal amplitude A and phase ϕ, of the generated acoustic waves at the leading edge and trailing edge of the rotor can be obtained and used as initial conditions for the propagation analysis. For a given acoustic mode (m, n), the obtained unsteady pressure associated with the outward propagating acoustic waves at the leading edge and trailing edge of the rotor can be expressed as

$$p^{l-}_{m,n} = A^{l-}_{m,n} p^{l-}_{m,n}(r) e^{i(-\omega t + k^{l-}_{x_{m,n}} x + m\theta + \phi^{l-}_{m,n})} \tag{4.1}$$

$$p^{t+}_{m,n} = A^{t+}_{m,n} p^{t+}_{m,n}(r) e^{i(-\omega t + k^{t+}_{x_{m,n}} x + m\theta + \phi^{t+}_{m,n})} \tag{4.2}$$

where p denotes the unsteady pressure, $p(r)$ represents the radial eigenfunction of unsteady pressure and ω is the angular modal frequency. The superscript l denotes waves located at the leading edge of the blade and t denotes waves located at the trailing edge. Modes travelling against the axial direction (i.e. against the direction of flow) are denoted using superscript $-$, and modes propagating in the positive axial direction are denoted using superscipt $+$. The obtained unsteady pressure is assumed with a wave-like solution which is harmonic in time t, axial space x and circumferential space θ.

4.3 Propagation of Acoustic Waves in Cylindrical Duct

For an annular cylindrical duct with hard-walled hub and casing surfaces, the propagation of acoustic waves is characterised by the convected wave

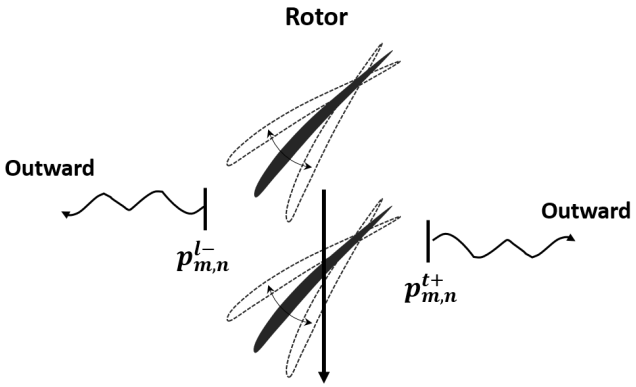


Figure 4.2: Acoustic waves generated by blade vibration at the leading edge and trailing edge of a rotor.

equation

$$\frac{1}{a^2}\frac{D^2p}{Dt^2} - \nabla^2 p = 0 \tag{4.3}$$

where a is speed of sound. For a mean flow field with negligible radial component, the above equation can be expressed in a cylindrical coordinate system (x, r, θ) as

$$\frac{1}{a^2}\frac{\partial^2 p}{\partial t^2} + M_x^2\frac{\partial^2 p}{\partial x^2} + (\frac{M_\theta}{r})^2\frac{\partial^2 p}{\partial \theta^2} + 2\frac{M_x}{a}\frac{\partial^2 p}{\partial x \partial t} + 2\frac{M_\theta}{ar}\frac{\partial^2 p}{\partial \theta \partial t} + 2M_x\frac{M_\theta}{r}\frac{\partial^2 p}{\partial x \partial \theta} = \frac{\partial^2 p}{\partial x^2} - \frac{1}{r^2}\frac{\partial^2 p}{\partial \theta^2} + \frac{1}{r}\frac{\partial p}{\partial r} + \frac{\partial^2 p}{\partial r^2} \tag{4.4}$$

where M_x and M_θ are the Mach numbers for the axial and tangential mean flow (assuming tangential 'wheel' flow, i.e. $M_\theta \propto r$). The sign convention of Mach numbers are chose so that positive values correspond to flow in positive axial and circumferential directions.

Assume the solution is separable, i.e. $p(x, r, \theta, t) = p(x)p(r)p(\theta)p(t)$, with a wave-like form which is harmonic in time, axial space and circumferential space, that is

$$p(x, r, \theta, t) = Ap(r)e^{i(-\omega t + k_x x + m\theta)} \tag{4.5}$$

Substitute Equation 4.5 into Equation 4.4 one obtains

$$(\frac{\omega}{a} - M_x k_x - M_\theta\frac{m}{r})^2 p = k_x^2 p + (\frac{m}{r})^2 p - \frac{1}{r}\frac{\partial p}{\partial r} - \frac{\partial^2 p}{\partial r^2} \tag{4.6}$$

Let

$$\mu^2 = (\frac{\omega}{a} - M_x k_x - M_\theta \frac{m}{r})^2 - k_x^2 \tag{4.7}$$

and Equation 4.6 becomes

$$r^2 \frac{\partial^2 p}{\partial r^2} + r\frac{\partial p}{\partial r} + ((r\mu)^2 - m^2)p = 0 \tag{4.8}$$

Let $\nu = r\mu$ and Equation 4.8 can be transformed into

$$\nu^2 \frac{\partial^2 p}{\partial \nu^2} + \nu\frac{\partial p}{\partial \nu} + (\nu^2 - m^2)p = 0 \tag{4.9}$$

It can be seen that Equation 4.9 is in the form of the Bessel differential equation of integer order m. The general solution of p can thus be expressed using Bessel functions

$$p_m = A_m(J_m(\nu) + \chi_m Y_m(\nu))e^{i(-\omega t + k_x x + m\theta)} \tag{4.10}$$

or

$$p_m = A_m(J_m(\mu r) + \chi_m Y_m(\mu r))e^{i(-\omega t + k_x x + m\theta)} \tag{4.11}$$

where χ_m is a constant which equals zero for cylindrical ducts, and J_m and Y_m are the Bessel functions of the first and the second kind of order m.

By applying the impermeability boundary conditions at the hard-walled hub and casing surfaces

$$\left.\frac{dp}{dr}\right|_{r=r_h} = 0, \quad \left.\frac{dp}{dr}\right|_{r=r_t} = 0 \tag{4.12}$$

one obtains a set of simultaneous equations

$$\begin{cases} J'_m(\mu r_h) + \chi_m Y'_m(\mu r_h) = 0 \\ J'_m(\mu r_t) + \chi_m Y'_m(\mu r_t) = 0 \end{cases} \tag{4.13}$$

which can be combined to give

$$J'_m(\mu r_h)Y'_m(\mu r_t) - Y'_m(\mu r_h)J'_m(\mu r_t) = 0 \tag{4.14}$$

where r_h and r_t are the hub and casing radius of the duct, J'_m and Y'_m are the derivatives of the Bessel functions of the first and the second kind.

For a given hub radius r_h, casing radius r_t and circumferential order m, Equation 4.14 has a set of infinite number of solutions in ascending order of μ with corresponding coefficient $\chi_m = -\frac{J'_m(\mu r_t)}{Y'_m(\mu r_t)}$. The ascending solutions of μ can be found to correspond to increasing radial order n of the propagating acoustic modes. It is observed from Equation 4.7 and Equation 4.14 that the variable μ has the same dimension as a wavenumber, and is dependent on both the circumferential order m and the radial order n. Thus μ is referred to as the radial-circumferential wavenumber $k_{r\theta}$ for the rest of this work.

The radial modal eigenfunction $p(r)$ (Equation 4.1) can thus be found using

$$p_{m,n}(r) = J_m(k_{r\theta m,n} r) + \chi_{m,n} Y_m(k_{r\theta m,n} r) \tag{4.15}$$

The dispersion relation in Equation 4.7 can be written as

$$(k - M_x k_x - M_\theta \frac{m}{r})^2 = k_x^2 + k_{r\theta}^2 \tag{4.16}$$

where $k = \frac{\omega}{a}$ is the free stream wavenumber.

The axial wavenumber k_x of an acoustic mode with circumferential mode order m is obtained as

$$k_{x\,m,n} = \frac{-M_x(k - M_\theta \frac{m}{r}) \pm \sqrt{(k - M_\theta \frac{m}{r})^2 - {k_{r\theta}}^2_{m,n}(1 - M_x^2)}}{1 - M_x^2} \tag{4.17}$$

where a plus sign is chosen for modes propagating in the positive axial direction (i.e. downstream propagating when $M_x > 0$) and a minus sign is chosen for modes propagating in the negative axial direction (i.e. upstream propagating when $M_x > 0$).

It can be seen from Equation 4.17 that the axial wavenumber can have a complex value. Let $k_x = \Re(k_x) + i\Im(k_x)$ and substitute back into Equation 4.11

$$p_{m,n} = A_{m,n}(J_m(k_{r\theta m,n} r) + \chi_{m,n} Y_m(k_{r\theta m,n} r)) e^{-\Im(k_{x\,m,n})x} e^{i(-\omega t + \Re(k_{x\,m,n})x + m\theta)} \tag{4.18}$$

It can be seen from Equation 4.18 that the unsteady pressure for a given acoustic mode of order (m, n) is a temporal and spatial oscillatory function with constant amplitude when $\Im(k_x) = 0$, i.e. the axial wavenumber is real. This type of acoustic wave is referred to as 'cut-on' as it propagates without attenuation in amplitude. On the contrary, the amplitude of the unsteady pressure experiences exponential decay in positive axial direction

when $\Im(k_x) > 0$ and in negative axial direction when $\Im(k_x) < 0$. These correspond to 'cut-off' waves propagating in the downstream direction for $\Im(k_x) > 0$ and upstream direction for $\Im(k_x) < 0$, as their modal amplitude attenuates in the direction of propagation [105].

Therefore the condition for cut-on is given by

$$(k - M_\theta \frac{m}{r})^2 \geq k_{r\theta}^2{}_{m,n}(1 - M_x^2) \tag{4.19}$$

For supersonic mean axial flow ($M_x > 1$), the above condition is always satisfied irrespective of modal properties. For subsonic mean axial flow ($M_x < 1$), two conditions for cut-on can be found

$$\begin{cases} k - M_\theta \frac{m}{r} \geq \sqrt{k_{r\theta}^2{}_{m,n}(1 - M_x^2)} \\ k - M_\theta \frac{m}{r} \leq -\sqrt{k_{r\theta}^2{}_{m,n}(1 - M_x^2)} \end{cases} \tag{4.20}$$

and the corresponding critical frequency, known as 'cut-on frequency' or 'cut-off frequency', can be respectively obtained from

$$\begin{cases} \omega_{m,n}^{c+} = aM_\theta \frac{m}{r} + a\sqrt{k_{r\theta}^2{}_{m,n}(1 - M_x^2)} \\ \omega_{m,n}^{c-} = aM_\theta \frac{m}{r} - a\sqrt{k_{r\theta}^2{}_{m,n}(1 - M_x^2)} \end{cases} \tag{4.21}$$

where acoustic waves are cut-on for modal frequencies above ω^{c+} or below ω^{c-}.

The cut-on ratio σ is defined as

$$\begin{cases} \sigma_{m,n} = \frac{\omega}{\omega_{m,n}^{c+}} & (\omega \geq 0) \\ \sigma_{m,n} = \frac{\omega}{\omega_{m,n}^{c-}} & (\omega < 0) \end{cases} \tag{4.22}$$

which has a value above 1 for cut-on modes and below 1 for cut-off modes.

The propagation of acoustic waves in an annular cylindrical duct can be thought of as following a spiral (or helical) path [47]. Figure 4.3 shows an example of unsteady pressure contour of an upstream propagating 2ND acoustic wave in a blade-to-blade view. For the case shown here, the frequency of excitation is above the cut-on frequency. Acoustic waves propagate in the axial and circumferential direction with a constant amplitude which manifests as a 'spiral' pattern around the annulus. The angle of the

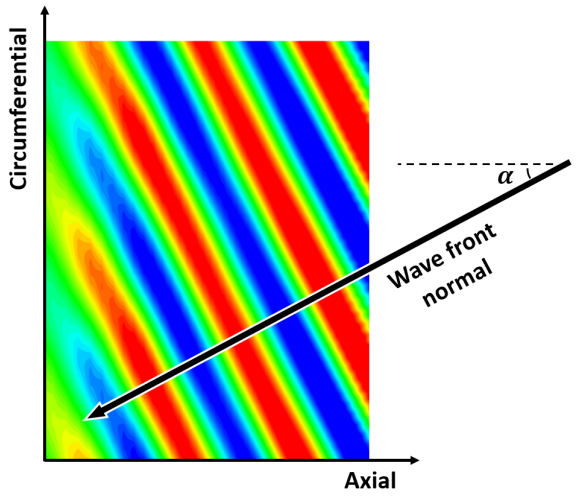


Figure 4.3: Unsteady pressure contour of an upstream propagating 2ND acoustic wave.

wave front with respect to the engine axis α can be determined from the dispersion relation of Equation 4.16 as [106]

$$\alpha_{m,n} = \cos^{-1}\left(\frac{\Re(k_{xm,n})}{k - M_x\Re(k_{xm,n}) - M_\theta\frac{m}{r}}\right) \tag{4.23}$$

Based on the obtained axial wavenumber using Equation 4.17, the axial phase change of the outward and backward propagations in the duct (as for the example illustrated in Figure 4.4) can be calculated as

$$\delta\phi^-_{m,n} = \int^L k^-_{xm,n}dx \tag{4.24}$$

$$\delta\phi^+_{m,n} = \int^L k^+_{xm,n}dx \tag{4.25}$$

where $\delta\phi$ denotes the axial phase change of the propagation and L is the axial distance of propagation. The superscript $-$ denotes upstream propagating acoustic waves and $+$ denotes downstream propagating waves. As the hub and casing wall profile normally varies slowly in the axial direction of compressor ducts, the change in modal amplitude and axial wavenumber during the outward and backward propagation is usually small and can be neglected in the computations. Hence Equation 4.24 and 4.25 can be

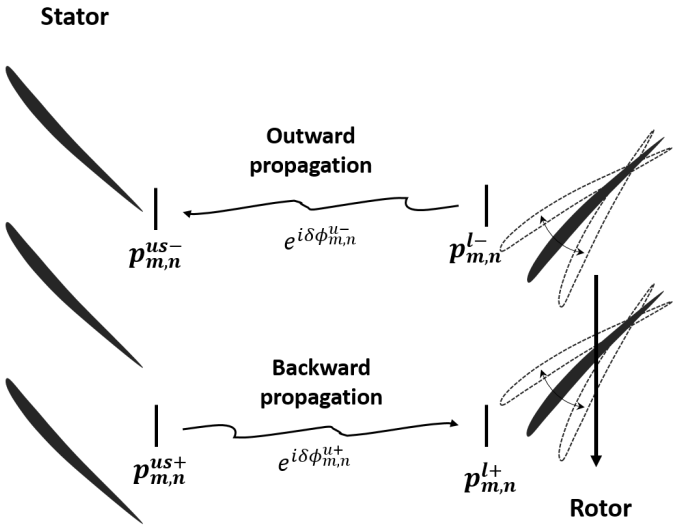


Figure 4.4: Propagation of acoustic waves in the duct between a rotor and its upstream stator.

approximated as

$$\delta\phi^{-}_{m,n} = k_{x}{}^{-}_{m,n} L \tag{4.26}$$

$$\delta\phi^{+}_{m,n} = k_{x}{}^{+}_{m,n} L \tag{4.27}$$

For cases where the axial variation of duct geometry is significant, which results in a non-negligible amplitude variation, the propagation of acoustic waves can be modelled using [107, 108], where sound transmission in a slowly varying duct is described by means of multiple-scales solutions.

The validation and application of the above analytical solution are carried out in the following chapters by comparing results with those obtained using a wave-splitting procedure (Section 3.5).

4.4 Transmission and Reflection at a Blade Row

Based on the method presented in the last section, the propagation of acoustic waves in the duct between blade rows (Figure 4.4) can be modelled analytically. In order to complete the model, i.e. trace the acoustic waves throughout the entire reflection process as illustrated in Figure 4.1, transmission and reflection at a blade row is calculated next, which is illustrated

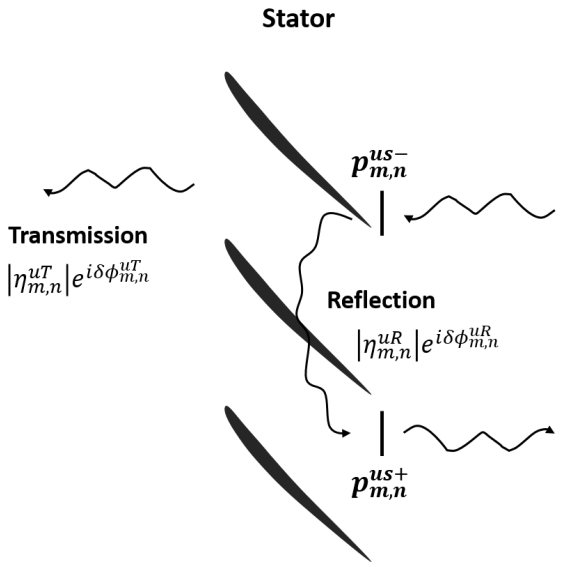


Figure 4.5: Transmission and reflection of acoustic waves at a blade row.

in Figure 4.5.

Established approach

Acoustic waves propagating in the compressor duct can be reflected by bladed structures. When an acoustic wave impinges on a blade row, some of this incident acoustic energy is transmitted, and some of it is reflected. The transmission and reflection of acoustic waves for a two dimensional cascade has been studied by many researchers [22, 23, 27, 48, 51]. A brief review of these established methods has been presented in Section 2.3.

Consider an upstream propagating acoustic wave impinging on a flat plate cascade (Figure 4.6a) in a uniform subsonic mean flow. Part of the incident acoustic wave is reflected and part of it is turned by the cascade to propagate through the passages and transmits into the upstream field. The propagation of acoustic waves in the blade passages is considered one dimensional and parallel to the blades. When the blades have zero loading (zero incidence), the cascade induces zero turning on the flow resulting in a uniform flow field across the cascade. Therefore, the acoustic waves propagating in the upstream field share identical modal properties, such as axial wavenumber and spiral angle, as those propagating in the downstream field. The same principle applies to a downstream propagating acoustic wave imping-

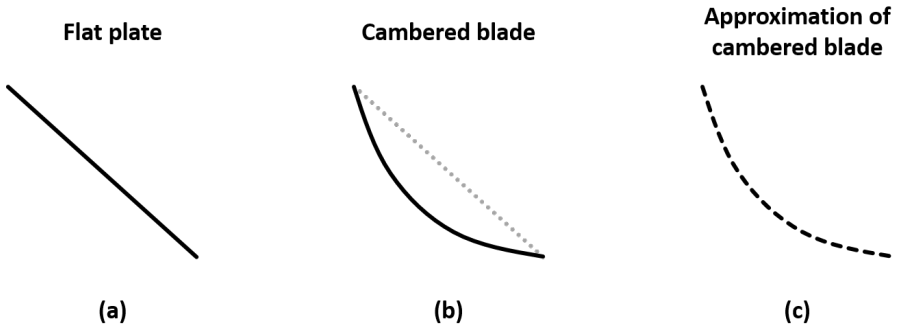


Figure 4.6: Illustration of (a) a flat plate, (b) a cambered blade and (c) an approximation of a cambered blade using multiple flat plate sections.

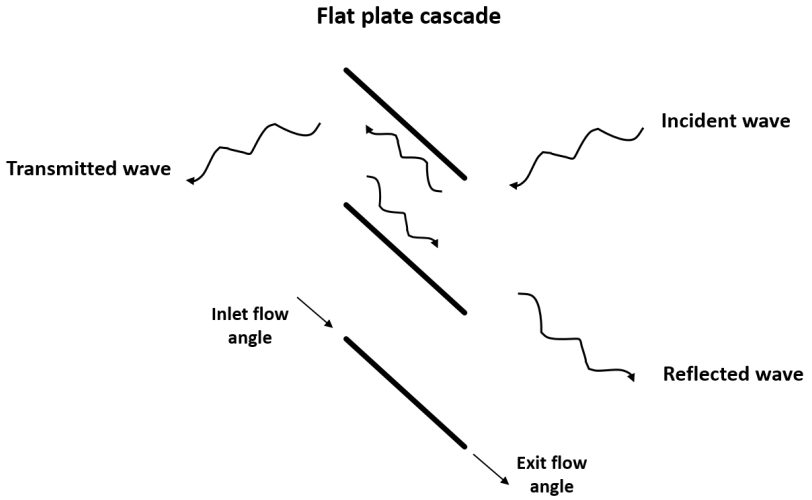


Figure 4.7: Transmission and reflection of an upstream propagating acoustic wave at a flat plate cascade.

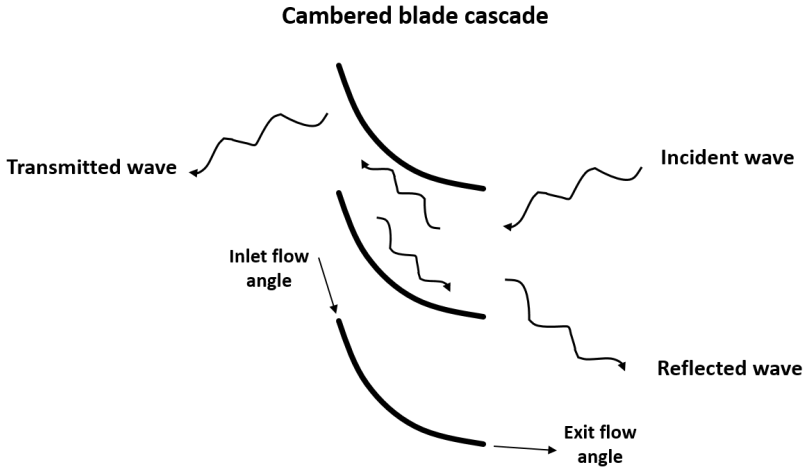


Figure 4.8: Transmission and reflection of an upstream propagating acoustic wave at a cambered blade cascade.

ing on a flat plate cascade. This type of problem, illustrated in Figure 4.7, was studied by Kaji and Okazaki using a semi-actuator disk method [48]. A special condition was obtained where the modal angle of the incident wave coincides with the blade stagger, leading to unity transmission and zero reflection as the incident wave transmits through the cascade unimpeded.

When the blades are cambered (Figure 4.6b), the local stagger angle at the blade leading edge (i.e. inlet metal angle) is different to that at the trailing edge (i.e. exit metal angle) as can be seen in Figure 4.8. The flow induces aerodynamic loading (lift) on the blade since the mean flow angle in the upstream field is different to that in the downstream field. Therefore in this case, acoustic waves propagating in the upstream field no longer share the same modal properties with those in the downstream field (see Equation 4.17 and 4.23). Thus the same mode that is cut-on in the downstream field may be cut-off in the upstream field, and consequently a transition from cut-on to cut-off (or cut-off to cut-on) can occur across a blade row. Moreover, instead of a one dimensional path parallel to the blades, the propagation of acoustic waves in the cascade passages follows the blade curvature. Consequently, the special condition of unity transmission and zero reflection described by Kaji and Okazaki [48] does not exist as work is put in by the blades to turn the incident acoustic wave.

One of the major drawbacks of the semi-actuator disk method, and many

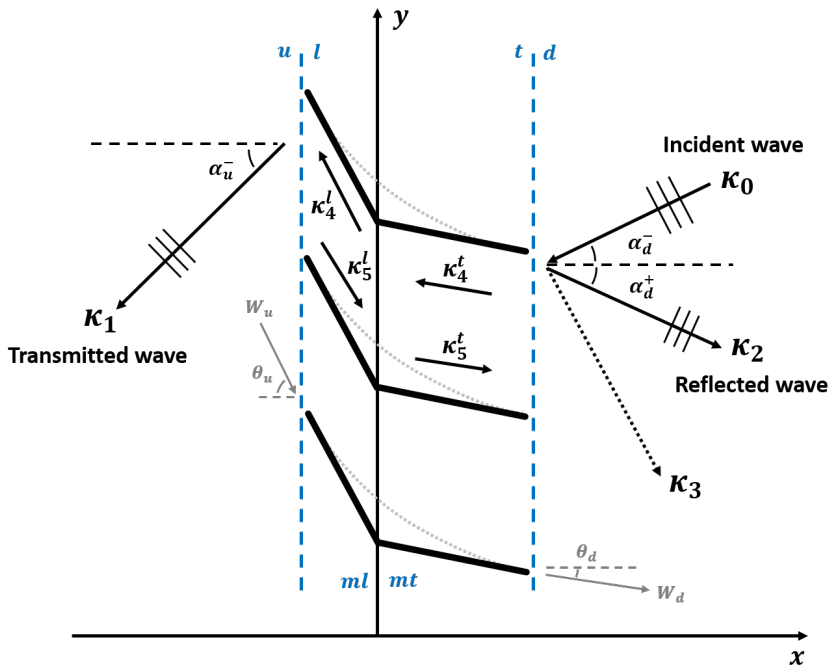


Figure 4.9: Transmission and reflection of an upstream propagating acoustic wave at a cascade consisting of blades in two flat plate sections.

established works, is the lack of camber and flow turning modelling, which requires a varying mean flow field across the cascade. For typical turbomachinery blades the camber of the stators and the change of flow angle across a blade row is significant enough so that it should not be neglected. Therefore, an analytical method is devised here which is capable of modelling blade camber and the change of mean flow angle across the cascade. The formulation of the model follows closely to the semi-actuator disk method by Kaji and Okazaki [48].

Improved method with flow turning

The analytical solution for an acoustic wave impinging on a cascade of cambered blades from downstream is presented here. The solution of an acoustic wave impinging on a cascade of cambered blades from upstream can be obtained in a similar fashion, and is therefore not included here.

A cambered blade can be (ideally) considered as the assembly of an infinite series of connecting flat plate sections with incremental changes of stagger angle (as illustrated in Figure 4.6c). In the absence of vorticity

(potential flow), the turning of flow by this blade is achieved discretely at the joints of connecting sections. Consider the simplest approximation of a cambered blade: two connecting flat plate sections as illustrated in Figure 4.9. The stagger of the front section is aligned with the inlet metal angle of the cambered blade and the stagger of the rear section is aligned with the exit metal angle. In Figure 4.9 the cambered cascade (thick black lines) is shown in the axial-transverse coordinate system. The blue lines and text represent the station name (used as subscript subsequently): u denotes the upstream field just in front of the leading edge; d denotes the downstream field just aft the trailing edge; l denotes the flow field in the blade passage just aft the leading edge; t denotes the flow field in the blade passage just in front of the trailing edge; ml and mt denote the flow field in the blade passage just in front of and aft the section joint.

The mean flow enters the cascade with a velocity W_u and a flow angle θ_u equal to the stagger of the front section (i.e. zero incidence), and exits with a velocity W_d and a flow angle θ_d equal to the stagger of the rear section (Kutta condition). The turning of the mean flow is achieved wholly at the joint between the two blade sections (i.e. at the interface $x = 0$ between ml and mt).

For the case of acoustic wave impinging on the cascade from the downstream side, upstream of the cascade there exists a transmitted acoustic wave κ_1, and downstream of the cascade there exist three waves: an incident acoustic wave κ_0, a reflected acoustic wave κ_2 and a reflected vortical wave κ_3 (neglecting entropic perturbation). In the blade passages, two acoustic waves κ_4^l and κ_5^l propagate in the front section passages, and two acoustic waves κ_4^t and κ_5^t propagate in the rear section passages. Note κ is used only to denote propagating and convected waves, and mode scattering is not considered here.

The vortical wave, which is purely convected by the flow, contains only velocity perturbations and has its direction of travel determined by the mean flow. On the other hand, acoustic waves contain unsteady perturbations in density, velocity and pressure, and can propagate with angles different from the convected waves depending on their frequency and wavenumbers. Mode angles of the incident acoustic wave α_d^-, the transmitted acoustic wave α_u^- and the reflected acoustic wave α_d^+ can be individually obtained from Equation 4.23 based on their respective wavenumbers. The propaga-

tion of acoustic waves inside the cascade passages is considered to be one dimensional and parallel to the blade sections.

For small amplitude perturbations in an inviscid flow, the equations for the unsteady flow field can be described using the linearised Euler equations in a two-dimensional space as

$$\frac{\partial \rho}{\partial t} + U\frac{\partial \rho}{\partial x} + V\frac{\partial \rho}{\partial y} + R\frac{\partial u}{\partial x} + R\frac{\partial v}{\partial y} = 0 \tag{4.28}$$

$$\frac{\partial u}{\partial t} + U\frac{\partial u}{\partial x} + V\frac{\partial u}{\partial y} = -\frac{1}{R}\frac{\partial p}{\partial x} \tag{4.29}$$

$$\frac{\partial v}{\partial t} + U\frac{\partial v}{\partial x} + V\frac{\partial v}{\partial y} = -\frac{1}{R}\frac{\partial p}{\partial y} \tag{4.30}$$

where R, U and V denote the density, axial velocity and transverse velocity of the mean flow field, and ρ, u, v and p denote the density, axial velocity, transverse velocity and pressure for the perturbed field. The variables are arranged so that the upper case symbols denote the variables of the mean flow field, and the lower case symbols denote the variables of the perturbed field. This notation is maintained throughout this section.

The solution for the unsteady perturbation is assumed separable, e.g. $p(x, y, t) = p(x)p(y)p(t)$, with a wave-like form which is harmonic in time, axial space and transverse space, that is

$$\varphi = A_\varphi e^{i(-\omega t + k_x x + k_y y)} \tag{4.31}$$

where φ denotes the variables of unsteady perturbation (which can be ρ, u, v or p), A is the amplitude of perturbation, ω is the perturbation frequency, k_x is the axial wavenumber and k_y is the transverse wavenumber (which is equivalent to the radial-circumferential wavenumber $k_{r\theta}$ in a cylindrical duct).

In order obtain the transmission coefficient and the reflection coefficient, i.e. the relationship between the transmitted wave κ_1 and the incident wave κ_0 and between the reflected wave κ_2 and the incident wave κ_0, a total of 7 boundary conditions are required for 8 unknown waves (7 acoustic waves and 1 vortical wave as illustrated in Figure 4.9).

The boundary conditions for the unsteady perturbations at the leading edge and the trailing edge interfaces of the cascade are defined as follows

(b.c. 1) Continuity of mass flow at the leading edge

(b.c. 2) Conservation of total enthalpy at the leading edge

$$R_u u_u + U_u \rho_u = (R_l w_l + W_l \rho_l) \cos\theta_u \tag{4.32}$$

$$\frac{p_u}{R_u} + U_u u_u + V_u v_u = \frac{p_l}{R_l} + W_l w_l \tag{4.33}$$

(b.c. 3) Continuity of mass flow at the trailing edge

(b.c. 4) Conservation of total enthalpy at the trailing edge

(b.c. 5) Flow at the trailing edge must satisfy the Kutta condition

$$w_t \cos\theta_d = u_d \tag{4.34}$$

$$w_t \sin\theta_d = v_d \tag{4.35}$$

$$p_t = p_d \tag{4.36}$$

To obtain the relationship between the transmitted acoustic wave κ_1, the reflected acoustic wave κ_2 and the incident acoustic wave κ_0, two more boundary conditions are required at the joint between the two blade sections

(b.c. 6) Continuity of mass flow at the section joint

(b.c. 7) Conservation of total enthalpy at the section joint

$$(R_{ml} w_{ml} + W_{ml} \rho_{ml}) \cos\theta_u = (R_{mt} w_{mt} + W_{mt} \rho_{mt}) \cos\theta_d \tag{4.37}$$

$$\frac{p_{ml}}{R_{ml}} + W_{ml} w_{ml} = \frac{p_{mt}}{R_{mt}} + W_{mt} w_{mt} \tag{4.38}$$

The above equations (Equation 4.32 to 4.38) make up for a total of 7 boundary conditions, and can thus be applied to solve for the relationship between any two waves. In order to obtain the relationship of unsteady pressure between the transmitted/reflected wave and the incident wave, characteristic relations of the propagating waves are introduced to eliminate the density and velocity perturbation terms.

The characteristic relations for waves κ_0, κ_1, κ_2 and κ_3 propagating in a two-dimensional cartesian space (in the upstream and downstream fields) can be obtained by substituting the harmonic solutions (Equation 4.31) into

the linearised Euler equations (Equation 4.28 to 4.30), which gives

$$p_0 = -\frac{a_d R_d}{\cos\alpha_d^-} u_d = -\frac{a_d R_d}{\sin\alpha_d^-} v_d \tag{4.39}$$

$$p_1 = -\frac{a_u R_u}{\cos\alpha_u^-} u_u = -\frac{a_u R_u}{\sin\alpha_u^-} v_u \tag{4.40}$$

$$p_2 = \frac{a_d R_d}{\cos\alpha_d^+} u_d = -\frac{a_d R_d}{\sin\alpha_d^+} v_d \tag{4.41}$$

$$(a_d - U_d \cos\alpha_d^-) u_3 = U_d \sin\alpha_d^- v_3 \tag{4.42}$$

where a is the speed of sound. Similarly for the one dimensional propagation of acoustic waves κ_4 and κ_5 in the blade passages the relation is given by

$$p = \pm a R w \tag{4.43}$$

where the $+$ sign is chosen for the downstream travelling wave and the $-$ is chosen for the upstream travelling wave.

Rearranging Equations 4.32 to 4.38 and substitute in the above characteristic relations and the isentropic flow relation for small amplitude perturbations $p = a^2\rho$, one obtains

$$(M_u - \frac{\cos\alpha_u^-}{\cos\theta_u}) p_1 = [(1+M_u)p_5^l - (1-M_u)p_4^l] \tag{4.44}$$

$$[1 - M_u\cos(\theta_u - \alpha_u^-)] p_1 = [(1+M_u)p_5^l + (1-M_u)p_4^l] \tag{4.45}$$

$$-\cos\theta_d p_4^t + \cos\theta_d p_5^t = -\cos\alpha_d^- p_0 + \cos\alpha_d^+ p_2 + a_d R_d u_3 \tag{4.46}$$

$$-\sin\theta_d p_4^t + \sin\theta_d p_5^t = -\sin\alpha_d^- p_0 - \sin\alpha_d^+ p_2 + a_d R_d v_3 \tag{4.47}$$

$$p_4^t + p_5^t = p_0 + p_2 \tag{4.48}$$

$$(1+M_u)p_5^{ml} - (1-M_u)p_4^{ml} = \frac{a_u\cos\theta_d}{a_d\cos\theta_u}[(1+M_d)p_5^{mt} - (1-M_d)p_4^{mt}] \tag{4.49}$$

$$(1+M_u)p_5^{ml} + (1-M_u)p_4^{ml} = \frac{R_u}{R_d}[(1+M_d)p_5^{mt} + (1-M_d)p_4^{mt}] \tag{4.50}$$

where M denotes the flow Mach number.

The complex transmission coefficient η^T and the reflection coefficient η^R can be obtained by rearranging Equations 4.44 to 4.50 and eliminating the unknown unsteady perturbations. For clarity, the complete solution of this problem from this point on is not shown here, and is given in Appendix II

instead.

The complex transmission coefficient η^T and the reflection coefficient η^R are obtained as

$$\eta^T = \frac{p_1}{p_0} \tag{4.51}$$

$$\eta^R = \frac{p_2}{p_0} \tag{4.52}$$

where the amplitude ratio of the transmission coefficient and reflection coefficient are obtained as $|\eta^T|$ and $|\eta^R|$ respectively. The phase change transmitting through and reflecting from the cascade can be obtained from the argument of the complex coefficients

$$\delta\phi^T = \arg \eta^T \tag{4.53}$$

$$\delta\phi^R = \arg \eta^R \tag{4.54}$$

The proposed method can be easily extended by discretising the cambered blade into N_s connecting blade sections ($N_s > 2$) with $2N_s$ acoustic waves propagating in the passages. The introduction of $2(N_s - 1)$ additional unknown waves in the blade passage can be treated with $2(N_s - 1)$ additional boundary conditions at the corresponding interfaces of section joints as demonstrated by Equation 4.37 and 4.38

$$(R_{jl}w_{jl} + W_{jl}\rho_{jl})\cos\theta_j l = (R_{jt}w_{jt} + W_{jt}\rho_{jt})\cos\theta_j t \quad (j = 1, N_s - 1) \tag{4.55}$$

$$\frac{p_{jl}}{R_{jl}} + W_{jl}w_{jl} = \frac{p_{jt}}{R_{jt}} + W_{jt}w_{jt} \quad (j = 1, N_s - 1) \tag{4.56}$$

where j denotes the index of the blade section joint.

The above method is developed based on the assumption that the stagger of the most forward section aligns with the upstream mean flow angle, i.e. zero incidence. In reality, the upstream mean flow angle can be different from the inlet metal angle (i.e. non-zero incidence) for different levels of blade loading as illustrated in Figure 4.10. This can be treated by simply modifying the mean flow triangle in the upstream field in Equation 4.32 and 4.33 as

$$R_u u_u + U_u^* \rho_u = (R_l w_l + W_l \rho_l)\cos\theta_u \tag{4.57}$$

$$\frac{p_u}{R_u} + U_u^* u_u + V_u^* v_u = \frac{p_l}{R_l} + W_l w_l \tag{4.58}$$

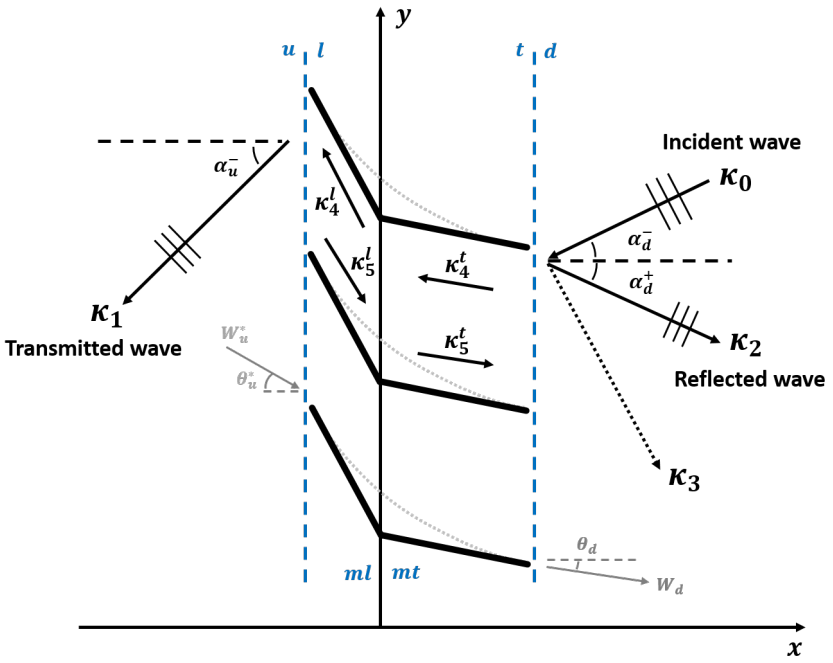


Figure 4.10: Transmission and reflection of an upstream propagating acoustic wave at a cascade consisting of blades in two flat plate sections with non-zero mean flow incidence.

where U_u^* and V_u^* are the velocity components of the upstream flow field, which gives the upstream mean flow angle $\theta_u^* = \tan^{-1} \frac{V_u^*}{U_u^*}$. Similarly, the flow leaving the blade trailing edge can have a different angle from the exit metal angle due to flow separation. This effect is however not modelled in the current work since the main objective is to study the acoustic behaviour and flutter in the absence of flow separation. Moreover, accurate prediction of the change of flow angle at the blade trailing edge requires high-fidelity numerical simulations which defeats the fundamental purpose of this work.

The devised analytical method can be applied to the transmission and reflection of acoustic waves at a cascade consisting of cambered blades for a wide range of flow conditions and wavenumbers. It can be easily shown that when the cascade in study consists of zero-camber flat plates, the devised method converges to the semi-actuator disk method by Kaji and Okazaki [48]. The proposed analytical method is computationally efficient, as it does not require any numerical iterations, which makes it ideal for predictions at the early design stages of an engine. It is worth mentioning that infinitesimal blade spacing is assumed so that the effect of solidity is not represented by the model. Based on the results obtained from unsteady CFD computations, it will be shown that the effect of solidity on the amplitude and phase change of acoustic transmission and reflection at a blade row is negligible for highly cut-on modes. Furthermore, effects of radial mean flow profile is not accounted for in the above method which is developed for a two dimensional flow past a cascade.

The validation and application of the above analytical solution are carried out in the following chapters by comparing results with those obtained using a wave-splitting procedure (Section 3.5). The effectiveness of the improved method concerning mean flow turning is studied and validated in Chapter 8.

4.5 Acoustic Reflection from the Intake

In the absence of bladed structures, acoustic waves can also be reflected at the opening of an intake where a sudden change of duct impendence occurs. Hence acoustic waves generated by the vibration of fan blades can propagate upstream in the intake and be reflected back towards the rotor. This phenomenon is illustrated schematically in Figure 4.11.

The reflection process of acoustic waves originated from the fan leading

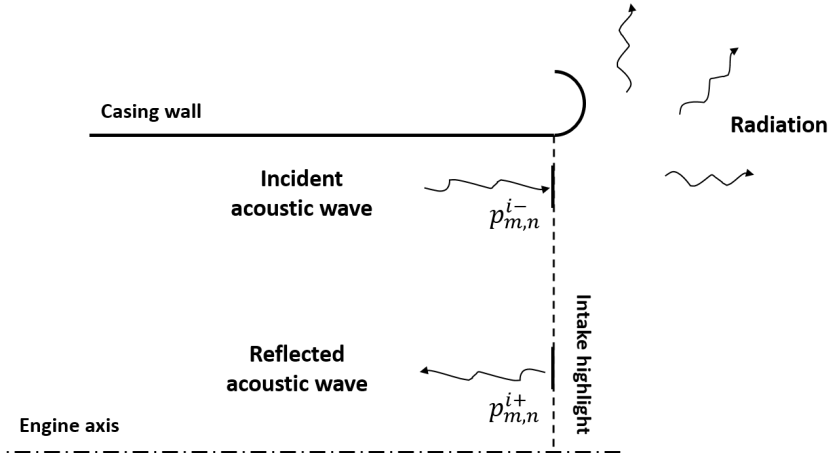


Figure 4.11: Reflection and radiation of acoustic waves at the intake opening.

edge can be divided into three stages: (1) outward propagation in the intake duct, (2) reflection at the intake highlight and (3) backward propagation in the intake duct. The outward and backward propagation in the intake duct can be calculated in the same way as shown in Section 4.3.

Upon reaching the opening of the intake, part of the incident acoustic energy is radiated outwards into the farfield, and part of it is reflected back towards the fan. The scattering of acoustic modes in such a condition was studied by Rienstra [53] where sound radiates from the opening of a cylindrical exhaust duct in a uniform subsonic mean axial flow. The acoustic scattering coefficients were obtained by matching the perturbed acoustic fields along the trailing streams of the casing wall using a Wiener-Hopf technique [50]. This method is adopted in this work for the calculations of acoustic reflection from the intake opening, and an outline of the method is briefly introduced below.

Consider an acoustic wave propagating in a uniform subsonic mean axial flow with density R, axial velocity U and pressure p_s inside an annular cylindrical duct consisting of a semi-infinite casing wall and an infinite hub. Reflection and radiation of sound occur as the incident wave exits the duct opening. This problem is illustrated in the meridian view in Figure 4.12. By considering the unsteady flow field as a superposition of a time-independent mean flow field and a time varying perturbation field (with density $R+\rho R$ and pressure p_s+a^2pR), the governing equations for the linearised flow field

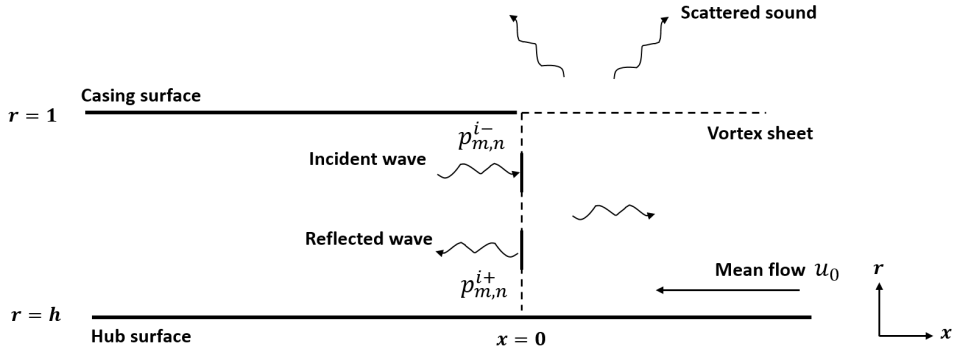


Figure 4.12: Flow field and the scatter of acoustic waves at the duct opening. [53]

can be expressed, using the velocity potential Φ, as follows

$$\frac{\partial \rho}{\partial t} + M\frac{\partial \rho}{\partial x} + \nabla^2 \Phi = 0 \tag{4.59}$$

$$\frac{\partial \Phi}{\partial t} - M\frac{\partial \Phi}{\partial x} = -p \tag{4.60}$$

where $p = \rho$ is the dimensionless unsteady pressure and $M = \frac{U}{a}$ is the flow Mach number.

The pressure perturbation (similarly for the potential) of the incident acoustic wave $p^{i-}_{m,n}$, consisting of the (m, n) duct mode, propagating inside the duct $(x \leqslant 0)$ can be expressed in the harmonic form of

$$p^{i-}_{m,n} = \begin{cases} p_{m,n}(r)e^{i(-\omega t + k_{x^+_{m,n}} x + m\theta)} & (h < r < 1) \\ 0 \qquad (1 < r < \infty) \end{cases} \tag{4.61}$$

where h denotes the hub/tip ratio of the duct. It is assumed that the amplitude of perturbation is small enough to satisfy linearisation. The radial eigenfunction $p_{m,n}(r)$ and axial wavenumber $k_{x^+_{m,n}}$ can be obtained from the end-wall boundary conditions in a similar fashion as shown in Section 4.3.

The governing equations in Equation 4.59 and 4.60 can be combined and expressed in terms of the potential of the scattered field ϕ^s as

$$\left[\frac{\partial^2}{\partial r^2} + \frac{1}{r}\frac{\partial}{\partial r} - \frac{m^2}{r^2} + \frac{\partial^2}{\partial x^2} - (ik + M\frac{\partial}{\partial x})^2\right]\Phi^s = 0 \tag{4.62}$$

where $k = \frac{\omega r_t}{a}$ is the dimensionless wavenumber and the potential of the scattered field Φ^s is calculated by subtracting the potential of the incident wave, i.e. $\Phi^s = \Phi - \Phi^{i-}$. The above equation is in a similar form with the form of the convected wave equation in Equation 4.6, and can be solved using the following boundary conditions

1. Impermeable end-walls: $\frac{\partial \Phi^s}{\partial r} = 0$ for $r = h$, or $r = 1$ and $x < 0$.

2. Unsteady pressure $p^{i-}_{m,n} - (ik + M\frac{\partial}{\partial x})\Phi^s$ is continuous across $r = 1$ for $x > 0$.

3. The potential of the scatter field Φ^s radiating outwards towards infinity.

The discontinuity at the trailing stream behind the casing wall is modelled by a shed vortex parameter, which is not applicable for the intake problem. By performing Fourier transforms of variables in x coordinate and satisfying the aforementioned boundary conditions, the solution of Equation 4.62 can be obtained by means of the Wiener-Hopf technique through mode matching along the trailing stream of the casing wall. For the detailed analytical solutions of this problem the reader is referred to [53].

The complex reflection coefficient η^I for the mode (m, n) can be obtained from the ratio between the pressure perturbation of the reflected wave and the incident wave

$$\eta^I_{m,n} = \frac{p^{i+}_{m,n}}{p^{i-}_{m,n}} \tag{4.63}$$

which is found to be a function of duct geometry, flow Mach number and mode order (m, n) of the incident acoustic wave. The amplitude ratio of reflection coefficient is calculated as $|\eta^I_{m,n}|$ and the phase change at the intake highlight $\delta\phi^I_{m,n}$ is found as the argument of $\eta^I_{m,n}$

$$\delta\phi^I_{m,n} = \arg \eta^I_{m,n} \tag{4.64}$$

The validation and application of the above analytical solution are carried out in Chapter 6 by comparing results with those obtained using a wave-splitting procedure (Section 3.5).

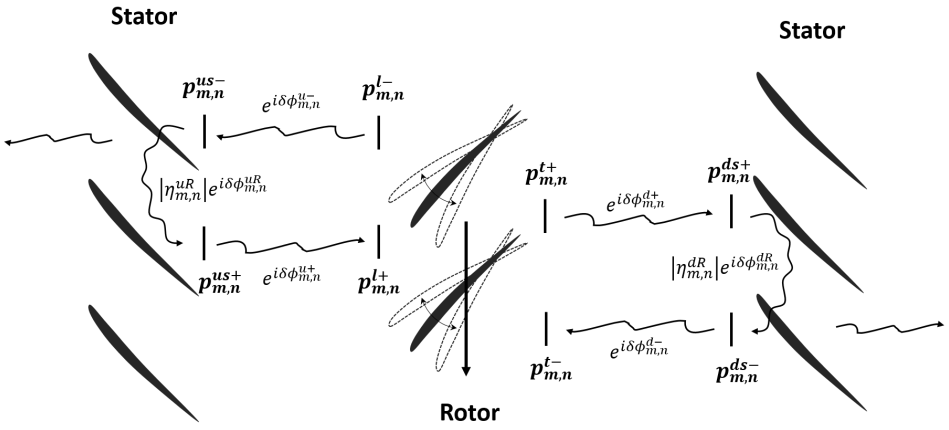


Figure 4.13: Traces of acoustic waves generated by the vibration of embedded rotor blades.

4.6 Resultant Near Blade Unsteady Pressure Field

Having obtained the amplitude variation (Equation 4.52) and phase change (Equations 4.54) of acoustic waves reflecting from a blade row, modal content of the reflected waves at the leading edge and trailing edge of the embedded rotor can be calculated. Figure 4.13 illustrates the complete reflection process for acoustic waves (generated by blade vibration) from the immediately adjacent stators.

The phase of the reflected wave at the leading edge and trailing edge of the embedded rotor can be expressed as

$$\phi^{l+}_{m,n} = \phi^{l-}_{m,n} + \delta\phi^{u-}_{m,n} + \delta\phi^{uR}_{m,n} + \delta\phi^{u+}_{m,n} \tag{4.65}$$

$$\phi^{t-}_{m,n} = \phi^{t+}_{m,n} + \delta\phi^{d+}_{m,n} + \delta\phi^{dR}_{m,n} + \delta\phi^{d-}_{m,n} \tag{4.66}$$

where superscripts $l+$ denotes (reflected) downstream propagating acoustic wave at the leading edge, and $t-$ denotes (reflected) upstream propagating acoustic wave at the trailing edge. Hence the reflected acoustic waves at the leading edge and trailing edge of the rotor can be expressed as

$$p^{l+}_{m,n} = |\eta^{uR}_{m,n}| A^{l+}_{m,n} (J_m(k_{r\theta}{}^{l}_{m,n} r) + \chi^{l}_{m,n} Y_m(k_{r\theta}{}^{l}_{m,n} r)) e^{i(-\omega t + k_x{}^{l+}_{m,n} x + m\theta + \phi^{l+}_{m,n})} \tag{4.67}$$

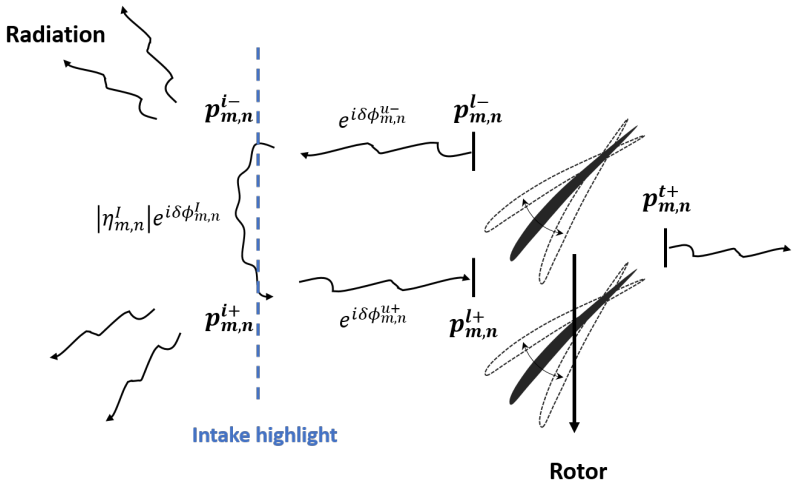


Figure 4.14: Traces of acoustic waves generated by the vibration of fan blades.

$$p^{t-}_{m,n} = |\eta^{dR}_{m,n}|A^{t-}_{m,n}(J_m(k_{r\theta}{}^{t}_{m,n}r) + \chi^{t}_{m,n}Y_m(k_{r\theta}{}^{t}_{m,n}r))e^{i(-\omega t + k_x{}^{t-}_{m,n}x + m\theta + \phi^{t-}_{m,n})} \tag{4.68}$$

Similarly, the reflected acoustic waves from the intake, as illustrated in Figure 4.14, can be expressed as

$$p^{l+}_{m,n} = |\eta^{I}_{m,n}|A^{l+}_{m,n}(J_m(k_{r\theta}{}^{l}_{m,n}r) + \chi^{l}_{m,n}Y_m(k_{r\theta}{}^{l}_{m,n}r))e^{i(-\omega t + k_x{}^{l+}_{m,n}x + m\theta + \phi^{l+}_{m,n})} \tag{4.69}$$

where

$$\phi^{l+}_{m,n} = \phi^{l-}_{m,n} + \delta\phi^{u-}_{m,n} + \delta\phi^{I}_{m,n} + \delta\phi^{u+}_{m,n} \tag{4.70}$$

Furthermore, in situations where the upstream and the downstream fields of the embedded rotor are both cut-on, acoustic waves reflected from the upstream and downstream structures can transmit through the embedded rotor. This situation is illustrated in Figure 4.15 where the unsteady pressure field near the rotor is shown. The transmission of acoustic waves through the rotor blades can be analysed in a similar fashion as that described in Section 4.4 (apart from a change of the frame of reference). In theory, the transmitted waves, $p^{tT+}_{m,n}$ and $p^{lT-}_{m,n}$, can travel to the upstream and downstream structures resulting in a second reflection, and consequently a third and so on. Similarly, for the vibration of an embedded rotor inside a multi-stage compressor, the outgoing acoustic waves can transmit through

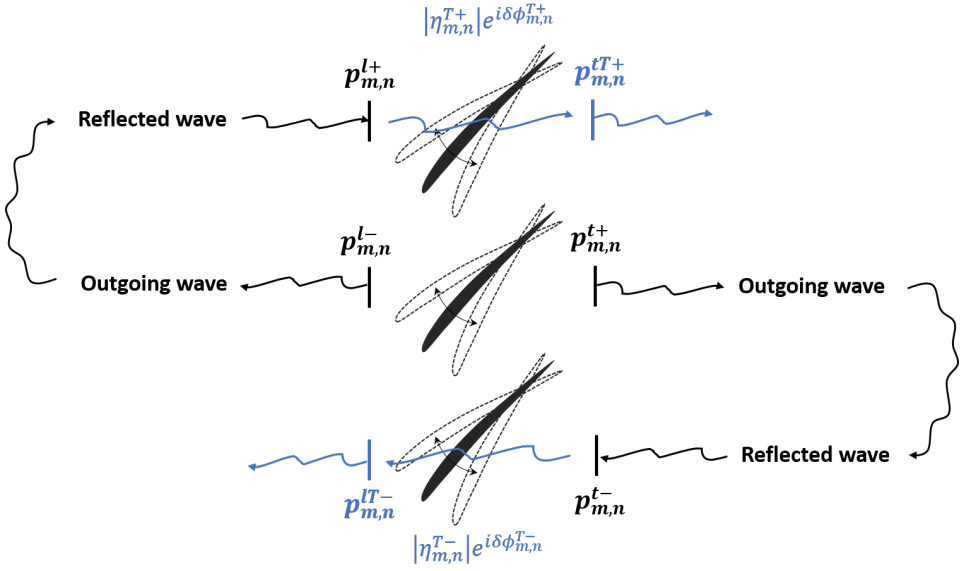


Figure 4.15: Transmission of the reflected waves at the embedded rotor.

the immediately adjacent stators and reflect from blade rows farther away. However, the amplitude of these reflected acoustic waves (through multiple transmissions and reflections as opposed to direct reflection from the immediately adjacent stators) is usually very small, and is thus neglected in the analysis.

In conclusion, it has been shown in this chapter that the complete propagation and reflection process of the acoustic waves generated by blade vibration can be modelled analytically. Armed with the devised analytical model, in-depth understandings can be gained regarding the fundamental mechanisms driving the flutter of embedded rotors by analysing the solutions of unsteady CFD flutter computations. Based on the knowledge gained in the process, reduced order models are proposed which are capable of analysing and predicting the acoustic reflection driven flutter. These aspects will be addressed in the following chapters.

5 Vibration of A Thin Annulus Blade Row

5.1 Overview and Problem Description

Prior to full annulus multi-row flutter analysis of an embedded rotor, vibration of an isolated thin annulus blade row in a long straight duct is studied. In this setup the flow is constrained to two dimensions (axial and tangential). By doing so, the fundamental behaviour of blade vibration and its interaction with duct acoustics can be studied in a straightforward fashion.

In the first part of this work, vibration of a blade row consisting of unloaded thin flat blades in a long straight duct (i.e. without acoustic reflections) is investigated (illustrated by Figure 5.1). Parametric studies are carried out to investigate the effects of reduced frequency, blade stagger and modeshape of vibration on the generated acoustic waves and blade aerodynamic damping. Moreover, the effect of blade loading is studied through computations of a blade row consisting of cambered blades.

In the second part of this work, the effect of an incoming acoustic 'gust' (with the same frequency as blade vibration) on blade flutter stability is investigated. This is achieved by imposing acoustic perturbations inside the domain of the CFD model using unsteady plane sources. It will be shown that the incident acoustic gust affects the aerodynamic damping of the blade by altering the unsteady blade lift. Moreover, it will be shown that the variation of unsteady lift, and consequently the blade aerodynamic damping, due to the incoming acoustic gust can be evaluated analytically and separately from that induced by the blade motion.

The main purpose of this chapter is to gain understandings of the mechanisms behind the interaction between blade vibration and incoming acoustic waves (with the same frequency as blade vibration), which is essential for the understanding of the effects of acoustic reflection on blade flutter sta-

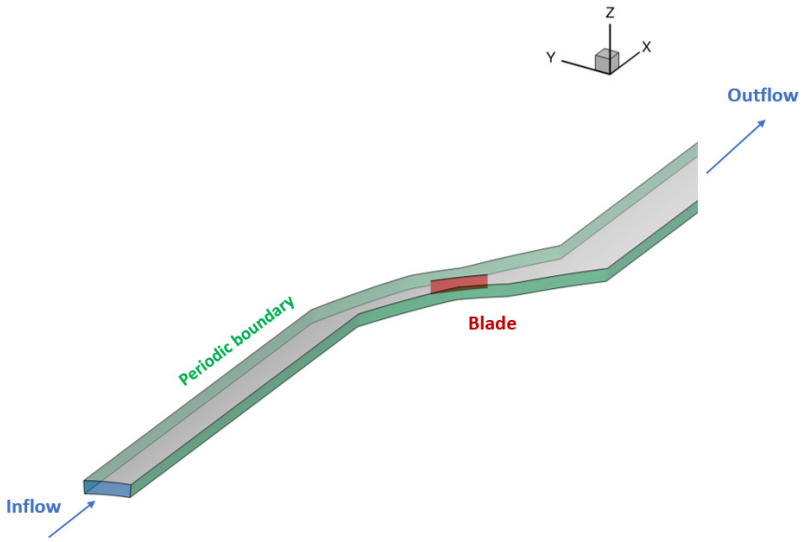


Figure 5.1: The single passage computation domain.

bility and hence the fan 'flutter bite' and embedded blade row flutter which are presented in later chapters.

The other objective of this chapter is to demonstrate the flutter mechanism of a vibrating blade in a very simple setup (in terms of flow and geometry). In other words, the study in this chapter will show that a flat plate in uniform flow can flutter as a result of modeshape (plunge and twisting motions) and acoustic reflections.

5.2 Computation Model and Grid

The computation domain consists of a high hub/tip ratio (0.965) blade row inside a constant radius straight long duct. The blades are designed to have identical aerofoil sections at all radial heights, and are connected to the duct walls at the hub and casing surfaces without tip and hub gaps. The inflow and outflow boundaries of the duct are placed approximately 10 chords away from the blades so as to minimise any numerical interferences.

The grid used for the blading is semi-structured, with hexahedral elements around the aerofoil in the boundary layer region, and prismatic elements in the passage [94]. Figure 5.2 shows some examples of the tip layer mesh in the blade-to-blade plane. The hub and casing surfaces of the duct are

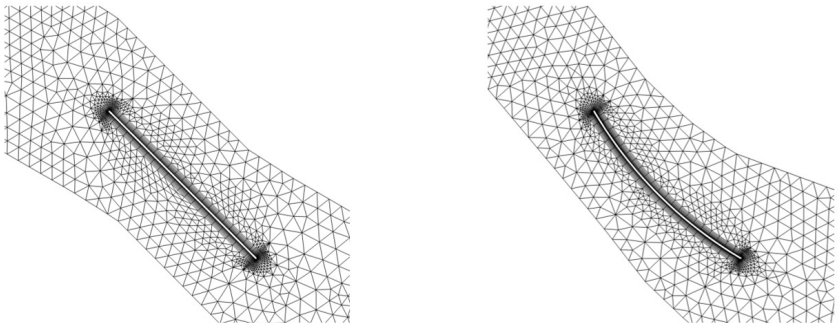


Figure 5.2: Tip layer mesh for (a) a flat plate and (b) a cambered blade.



Figure 5.3: Modeshape for the (a) plunge mode and (b) twist mode.

treated as inviscid to minimise end-wall boundary layer growth (which is not the focus of this work). The passage mesh is resolved using approximately 120,000 grid points with 5 radial mesh layers. In order to accurately resolve the propagation of acoustic waves, approximately 150 mesh points are used per axial wavelength for the shortest wavelength expected.

The steady state flow solutions are obtained by imposing the physical boundary conditions (PTBC, Section 3.3) at the farfield inflow and outflow boundaries with a constant flow Mach number of 0.3. The Mach number is fixed in this case since the variable that matters is the reduced frequency, which is varied through vibration frequency.

Tshe blades are excited in the 0ND pattern for the plunge mode and the twist mode individually, which are illustrated in Figure 5.3. The study concentrates on the 0ND mode for two reasons: (1) it allows the study of the fundamental interaction between blade vibration and the duct acoustics (sound generation and incoming acoustic gust) independent of the effect due to passage volume change (which is not the main focus of this thesis); (2) it allows unsteady CFD computations to be performed in a single passage

fashion (due to zero inter-blade phase angle) so that parametric studies can be performed in an efficient way.

For unsteady time-accurate computations, these boundaries are treated using non-reflecting boundary conditions (RIBC) to minimise numerical reflections. The unsteady computations are performed in a single passage fashion using periodic boundaries. Blade vibration is excited with a prescribed motion using the 3$^{\text{rd}}$ flutter computation strategy (Section 3.4). Aerodynamic damping is calculated from the aerodynamic work based on a fully developed vibration cycle. The physical time step for flutter computations is resolved as 200 time steps for one vibration cycle. This time step was obtained by performing a temporal convergence study.

For all the cases studied, the plunge vibration is started with a constant initial translational velocity of v_{0P} perpendicular to the chord (in the positive circumferential direction). For the twist mode, the center of rotation is the mid-chord of the blade and the motion is started with a constant initial tangential velocity of v_{0T} at the leading edge (in the sense of closing the blade, i.e. increasing stagger). In other words, the plunge motion of the flat plate can be expressed as

$$\dot{h}_P(t) = v_{0P} e^{-i\omega t} \tag{5.1}$$

$$h_P(t) = -\frac{v_{0P}}{i\omega} e^{-i\omega t} \tag{5.2}$$

where $h_P(t)$ is the displacement of the plunge motion perpendicular to the chord and $\dot{h}_P(t)$ is the translational velocity of the blade. Similarly, the twist motion can be expressed as

$$\dot{\theta}_T(t) = \frac{2v_{0T}}{c} e^{-i\omega t} \tag{5.3}$$

$$\theta_T(t) = -\frac{2v_{0T}}{i\omega c} e^{-i\omega t} \tag{5.4}$$

where c is the chord length, $\theta_T(t)$ is the rotation of the blade about mid-chord and $\dot{\theta}_T(t)$ is the angular velocity of the blade. For most of the cases computed in this work (unless otherwise specified), the initial velocity v_0 of the blade is kept constant at a Mach number of 0.0035 for both the plunge and twist motions. Therefore, the maximum displacement decreases with the increase of frequency. For a given frequency, the maximum displacement at the leading edge of blade (and the trailing edge) is roughly the same for

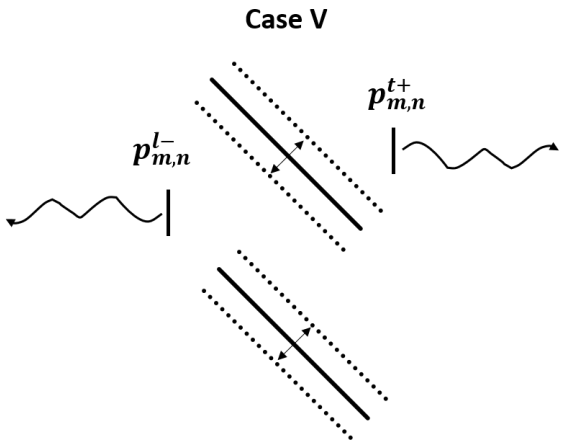


Figure 5.4: Vibration of blades in the isolated setup.

the plunge mode and the twist mode.

5.3 Vibration in the Isolated Setup

In the first part of this work, the vibration of an isolated thin annulus blade row in a long straight duct is studied. The effects of key parameters (such as stagger angle, reduced frequency and modeshape) on the generated acoustic perturbations and blade aerodynamic damping are investigated.

In the work presented here, the stagger of blades θ_s and the flow angle are varied simultaneously so that zero incidence onto the blade can be maintained, while the reduced frequency f_r is varied by varying the blade vibration frequency at a fixed flow condition ($M = 0.3$). By decomposing the generated unsteady disturbances into propagating waves using a wave-splitting procedure (Section 3.5), results obtained from unsteady CFD solutions are compared with the calculations based on the analytical methods (Chapter 4). The accuracy and applicability of the analytical methods are investigated based on these comparisons.

This series of computations is illustrated by the schematic shown in Figure 5.4 where the blades vibrate in isolation in the absence of reflections. This series of cases is referred to as *Case V* in this chapter, where V denotes 'vibration'.

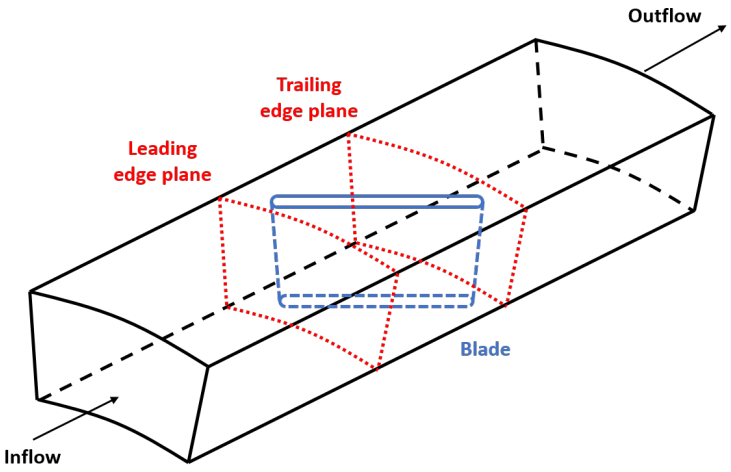


Figure 5.5: Illustration of the leading and trailing edge computation planes for wave-splitting.

5.3.1 Generation and propagation of acoustic waves

In order to study the relationship between the blade vibration and the generated acoustic waves, a wave-splitting procedure is performed in the duct to decompose the unsteady perturbations into propagating waves. The methods for wave-splitting has been described in Section 3.5. The splitting of waves is performed at a number of axial locations upstream and downstream of the blades so as to track the propagation of the generated waves. A plane just in upstream of the blade leading edge and a plane just aft the blade trailing edge (which are illustrated in Figure 5.5), are analysed to obtain the near blade pressure field. Based on the results obtained from wave-splitting of unsteady CFD solutions, properties of acoustic waves (such as axial wavenumber, modal amplitude and phase) at the leading edge and the trailing edge of the blade are obtained and compared with analytical calculations. For all the results to be presented in this section, the amplitude and phase of perturbations on the casing surface are shown. It will be shown by radial eigenfunction plots that acoustic modes behave in a two-dimensional fashion with no radial variation of amplitude. The phase is relative to the blade motion at zero displacement and maximum positive velocity (i.e. with respect to $\dot{h}_P(t)$ and $\dot{\theta}_T(t)$).

A typical example of the wave-splitting results in the near blade field is shown in Figure 5.6, where the amplitude and phase of the acoustic pressure

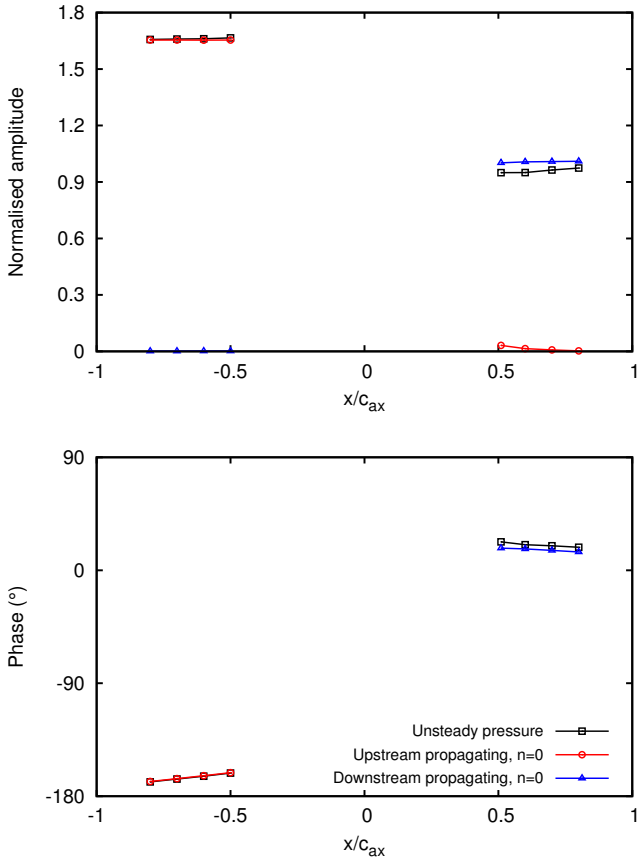


Figure 5.6: Axial variation of the amplitude and phase of acoustic waves, $\theta_s = 45°$, $f_r = 0.84$, plunge mode.

due to the plunge motion are plotted as a function of normalised axial location x/c_{ax}. The axial coordinate x is normalised by the axial chord of the blade c_{ax}, and the amplitude of unsteady pressure is normalised by the amplitude of the the outgoing acoustic wave at the blade trailing edge. In this plot the mod-chord is located at $x/c_{ax} = 0$. It can be seen from this plot that the vibration motion generates unsteady pressure perturbations at the leading edge ($x/c_{ax} = -0.5$) and the trailing edge ($x/c_{ax} = 0.5$), which propagate away from the blade with a constant amplitude for the $(0, 0)$ mode. The wavelength and axial phase velocity of the propagating acoustic waves can be inferred from the slope of the phase against axial coordinate as shown in the phase plot. Based on this relationship, it can be seen from this plot that the waves propagate with a constant axial phase velocity in the duct (constant phase slope). Moreover, the inferred axial phase velocity is different for acoustic waves propagating with and against the flow, which is the result of flow convection effects.

It is seen in Figure 5.6 that the amplitude and phase of acoustic pressure for the $(0, 0)$ mode (red and blue lines) are nearly the same as those of the unsteady pressure (black lines), which indicates that for the case studied the only propagating mode is the $(0, 0)$ mode. This is confirmed by the radial eigenfunction of unsteady pressure, as shown in Figure 5.7, where the amplitude and phase of the $(0, 0)$ mode (red curves) are nearly identical to the unsteady pressure (black curves) in the leading and trailing edge flow fields for all radial heights. The $(0, 1)$ mode (blue curves) is seen to be excited by blade vibration with a very small amplitude since the geometry in this study (hub/tip ratio of 0.965) is not completely two-dimensional.

Figure 5.8 shows the (complex) axial wavenumber for the first three radial orders in the complex plane. The axial wavenumbers computed at the blade leading edge are displayed in this plot (trailing edge yields identical results due to zero flow turning). In this plot the results obtained from wave-splitting of unsteady CFD solutions are compared with the calculations based on the analytical approach (Equation 4.17) for the five reduced frequencies studied. It should be noted that the obtained axial wavenumber is independent of the modeshape of vibration as it is only a function of the mean flow and the vibration frequency. It is seen from the plot that the axial wavenumbers are more or less symmetrical about the imaginary axis. In fact it can be shown (using Equation 4.17) that, for a mean flow of

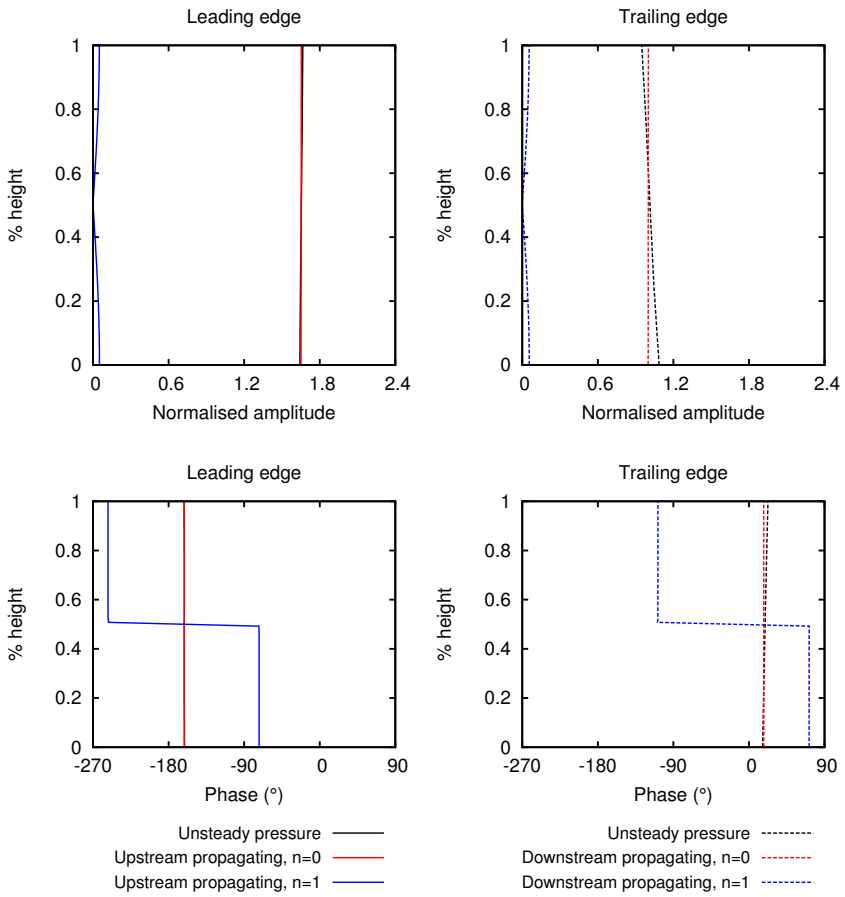


Figure 5.7: Eigenfunctions (radial) of acoustic modes at the leading edge and the trailing edge, $\theta_s = 45°$, $f_r = 0.84$, plunge mode.

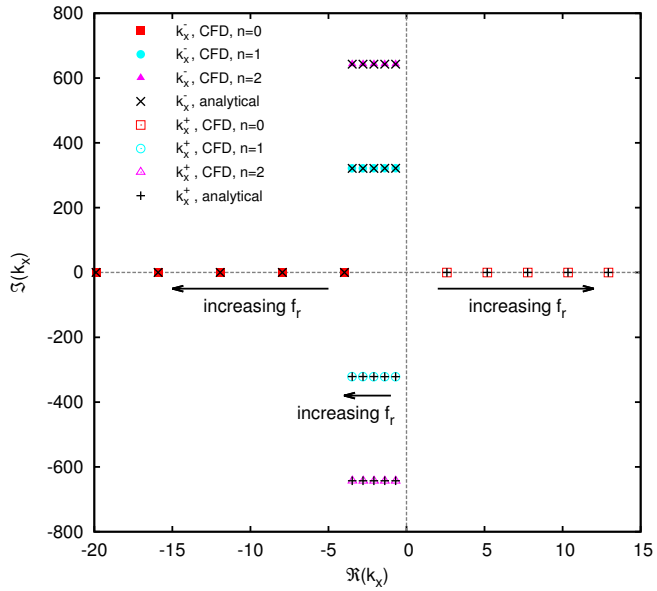


Figure 5.8: Comparison of axial wavenumber for the first three radial orders in the complex plane, $\theta_s = 45°$, $f_r = 0.84$.

$M_x = 0$ the distribution is purely symmetrically about the imaginary axis, whereas the shift of distribution is driven by the increase of the mean flow Mach number and the increase of vibration frequency. By examining the imaginary components of the axial wavenumber in this plot, it is found that modes with radial harmonic $n > 0$ are cut-off (due to $\Im(k_x) \neq 0$) and thus their amplitudes decay exponentially away from the blade. It can be seen from the plot that the results calculated using the analytical method show good agreement with the results obtained from wave-splitting.

Figure 5.9 shows the amplitude and phase of the generated acoustic waves at the leading edge and trailing edge of the blade as a function of reduced frequency for different blade stagger angle θ_s. The amplitude is normalised by the amplitude of unsteady pressure at the trailing edge for the case of $\theta_s = 45°$ at $f_r = 0.84$, and the phase is relative to blade motion of zero displacement and the maximum positive velocity. In this plot results for three blade stagger angle (and consequently the three mean flow angles), $\theta_s = 0°$, $\theta_s = 30°$ and $\theta_s = 45°$ due to the plunge motion are displayed. It is clearly seen from the plot that for a blade stagger of 0°, the vibration motion induces zero unsteady pressure perturbation in the upstream

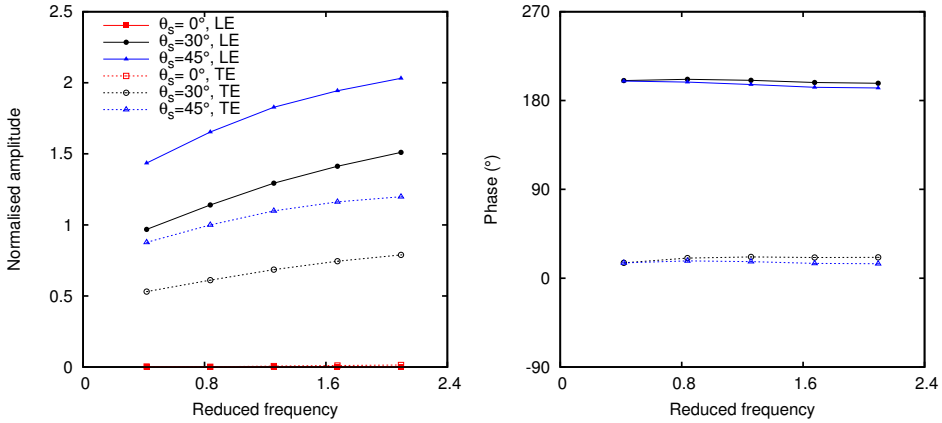


Figure 5.9: Acoustic pressure generated at the leading edge and the trailing edge for different blade stagger angle θ_s, plunge motion.

and downstream fields regardless of the frequency. This can be explained by considering the following: for a blade with zero lift, the instantaneous unsteady pressure induced by the vibration motion is always of equal amplitude and out of phase on the upper and lower surfaces of the blade; these disturbances propagate upstream and downstream in the flow field with the same speed, and consequently add up to zero outside the blade passages. This situation is clearly illustrated by the instantaneous unsteady pressure contour in Figure 5.10 for various phases of blade motion. This phenomenon can also be understood by considering the unsteady loading on the upper and lower surfaces of the blade as dipole sources of equal magnitude directed normal to the chord, which sums up to give a sound field of zero amplitude outside the blade passages (due to the symmetric nature of flow passages about the blade for the stagger of 0°). With the increase of the blade stagger, part of the flow passage becomes 'uncovered' by the blades (as illustrated in Figure 5.11). Therefore, sound generated by the dipole sources, due to the unsteady loading perpendicular to the chord, is (partly) directed outside of the passage at some sections of the blade (as opposed to the case of 0°stagger). This phenomenon is clearly illustrated by the comparison of instantaneous unsteady pressure contour in Figure 5.11 for the blade stagger angles of 0°and 45°. The change of sound directivity pattern due to the change of stagger results in a change in the amplitude of the generated acoustic waves at the leading edge and the trailing edge of the rotor,

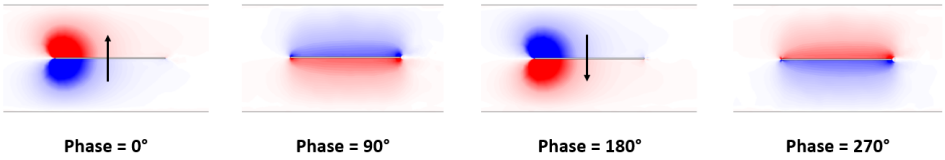


Figure 5.10: Unsteady pressure contour at four instances of time (in terms of phase relative to blade velocity), $\theta_s = 0°$, plunge mode. Red contour: positive value; Blue contour: negative value.

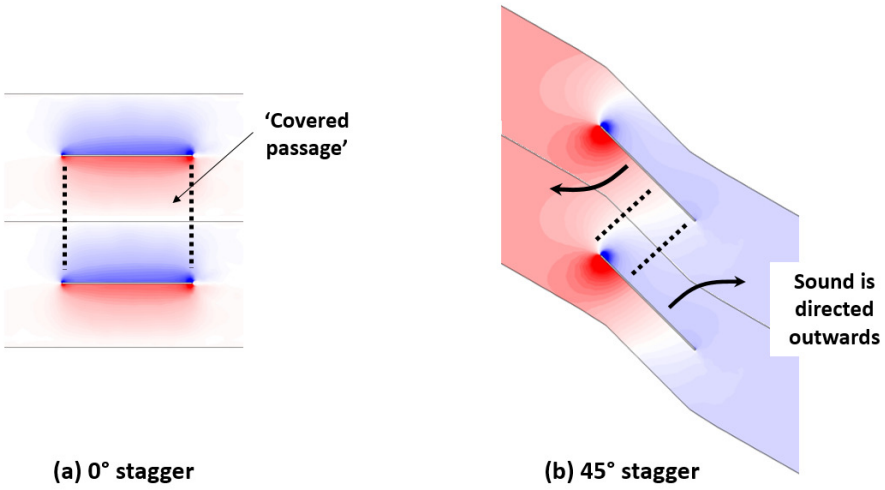


Figure 5.11: Instantaneous unsteady pressure contour at 90° phase with blade velocity for (a) $\theta_s = 0°$ and (b) $\theta_s = 45°$. Red contour: positive value; Blue contour: negative value.

where an increase of unsteady pressure amplitude is seen with the increase of stagger (due to the increase of the 'uncovered passage'). Moreover, it is seen in Figure 5.10 that this type of sound generation due to blade vibration is dominated by the leading edge sources (i.e. higher contour intensity near the leading edge), which explains the higher unsteady pressure amplitude for acoustic waves generated at the leading edge than that at the trailing edge. It is also seen in Figure 5.9 that for the range of frequencies studied, the unsteady pressure amplitude for the generated acoustic waves shows an increase with the increase of reduced frequency.

It can be seen from the phase plot of Figure 5.9 that for the plunge motion, the generated acoustic waves at the blade trailing edge is nearly in phase with blade velocity, whereas a 180°phase difference between the two

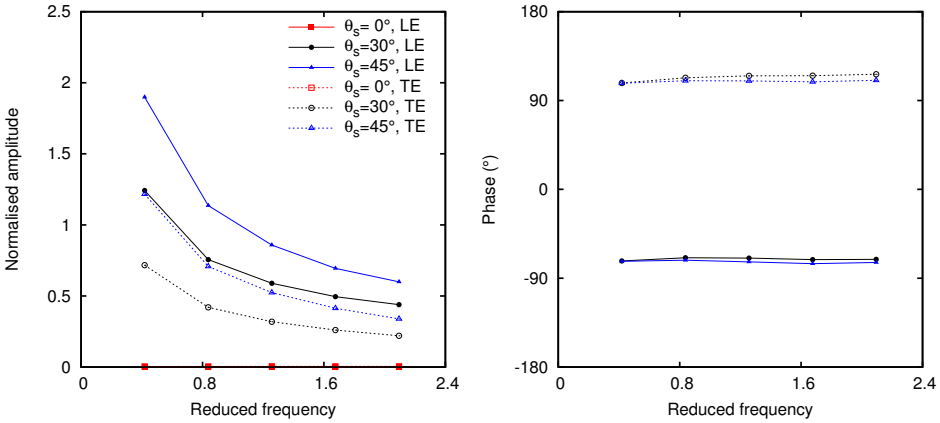


Figure 5.12: Acoustic pressure generated at the leading edge and the trailing edge for different blade stagger angle θ_s, twist motion.

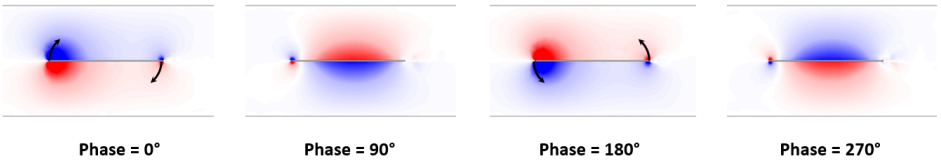


Figure 5.13: Unsteady pressure contour at four instances of time (in terms of phase relative to blade velocity), $\theta_s = 0°$, twist mode. Red contour: positive value; Blue contour: negative value.

quantities is seen at the leading edge. As opposed to the amplitude, the phase of the generated acoustic waves is (nearly) independent of the stagger angle of the blade since it is directly dependent on the phase of unsteady pressure on the surfaces of the blade which does not vary with the change of blade stagger. Moreover, it is seen from the plot that for the frequency range studied, the phase of acoustic waves stays (nearly) constant with the increase of reduced frequency. It should be noted that the phase of acoustic wave for the 0°stagger case is not displayed due to zero amplitude of this wave.

Figure 5.12 shows the amplitude and phase of the generated acoustic waves at the leading edge and trailing edge of the blade due to the twist vibration as a function of reduced frequency. The amplitude is normalised by the amplitude of unsteady pressure at the trailing edge for the case of $\theta_s = 45°$ at $f_r = 0.84$ due to plunge vibration (dotted blue curve in Figure 5.9), and the phase is relative to blade motion of zero displacement and

the maximum positive velocity. In this plot the results for blade stagger angle $\theta_s = 0°$, $\theta_s = 30°$ and $\theta_s = 45°$ are displayed. It can be seen from the plot that the amplitude of unsteady pressure for the generated acoustic waves shows an increase with stagger angle. This is again due to the aforementioned 'uncovered passage' effect which results in the generated sound being directed outside of the blade passages as stagger increases. It is also seen that the phase of the generated acoustic waves at the leading edge is 90°ahead of blade velocity, and that at the trailing edge lags blade velocity by 90°. Moreover, it is seen that the amplitude of acoustic waves increases with the decrease of reduced frequency. This can be explained by considering the quasi-steady analysis of a vibrating two-dimensional aerofoil without the apparent mass terms [17].

For a uniform thickness flat plate vibrating in a pure twist motion about its mid-chord, the unsteady lift on the blade surfaces can be approximated from the linearised equations of motion for force and moment [17] which yield

$$l = \frac{1}{2} c R W^2 C_L'(\alpha_s) \left[\theta_T(t) - \frac{c}{2W} \dot{\theta}_T(t) \right] \tag{5.5}$$

where c is blade chord, R is the mean flow density, W is the mean flow velocity, C_L' is the slope of lift coefficient with respect to the incidence (which is constant for low incidence), α_s is the flow incidence, t is the time, $\theta_T(t)$ is the rotation of the blade about mid-chord and $\dot{\theta}_T(t)$ is the angular velocity of the blade. For the computations performed in this work, the vibration motion for the twist mode is started with a constant initial tangential velocity at the leading edge for all the frequencies studied as shown in Equation 5.3 and Equation 5.4.

By substituting Equation 5.3 and 5.4 into Equation 5.5 one obtains

$$l = \frac{1}{2} c R W^2 C_L'(\alpha_s) v_{0T} \left[-\frac{2}{i\omega c} - \frac{1}{W} \right] e^{i\omega t} \tag{5.6}$$

Based on the above equation, it can be seen that in the low frequency limit, the amplitude of the unsteady lift tends to infinity while the phase approaches 90°with the blade velocity. These findings are in agreement with the observed trends for the amplitude and the phase of generated acoustic pressure (which is a direct result of the unsteady loading variation on the surfaces of the blade) shown in Figure 5.12.

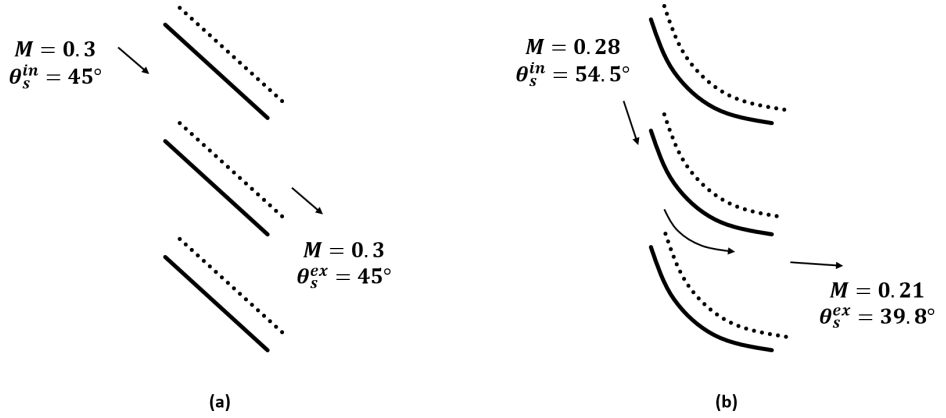


Figure 5.14: Mean flow field and the modeshape for the plunge mode for blade row consisting of (a) flat plates and (b) cambered blades.

In order to study the effects of blade loading on the generated acoustic waves, the 45°stagger flat plate is deformed (by fixing the leading edge and trailing edge points) into a cambered blade which has an inlet metal angle of $\theta_s^{in} = 54.5°$ and an exit metal angle of $\theta_s^{ex} = 39.8°$. The geometry and grid for the cambered blade were shown in Figure 5.2. The mean flow fields (i.e. Mach number and flow angle) at the leading and trailing edges of the blade are also given in Figure 5.14 for the two cases along with the modeshape for the plunge mode used in this study. The mean flow field for the cambered blade has zero incidence at the leading edge, and has the same exit flow angle as the exit metal angle. Flutter computations are carried out for the plunge mode by varying the reduced frequency.

Figure 5.15 shows the comparison of generated acoustic pressure perturbations induced by the vibration of the blade row consisting of flat plates and cambered blades. The amplitudes of unsteady pressure for the two cases are normalised by their respective amplitudes at the blade trailing edge for the reduced frequency of 0.84. This normalisation is made due to the differences in mean flow field for the two cases, so that a comparison of trend with respect to the reduced frequency can be performed. It is clearly seen from the plots that, the unsteady pressure generated by the vibration of cambered blades is different from that due to the flat plates, which indicates that the steady loading on the surfaces of the blade plays a part in the sound generation due to blade vibration. Moreover, for the range of reduced frequencies studied, it can be seen that the amplitude of generated

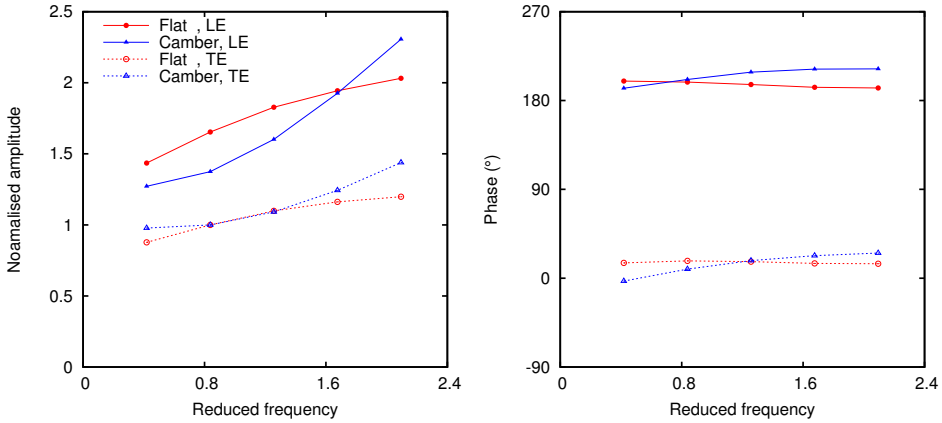


Figure 5.15: Acoustic pressure generated at the leading edge and the trailing edge by the vibration of the flat plate and the cambered blade, plunge motion.

acoustic waves due to the vibration of flat plates shows a different trend to that of the cambered blades. The observations clearly show that the mechanism of sound generation due to blade vibration is dependent on the steady loading, which is in agreement with the findings in [23, 109]. The effect of blade loading on the amplitude of the generated acoustic waves is dependent on the reduced frequency (which is a function of flow, blade geometry and vibration frequency), which shows no definite trend in Figure 5.15. On the other hand, the phase of generated acoustic waves for the two cases shows very small differences, indicating that the influence of steady loading on the phase of unsteady pressure on the surfaces of the blade is small. Moreover, the turning of flow due to blade loading can lead to situations where acoustic waves (for $m > 0$) are cut-on at the leading edge and cut-off at the trailing edge, or vice versa (which will be shown in later chapters for flutter analysis of loaded blade rows). In these situations resonance of the duct acoustic modes may arise which could contribute to further complexity in the radiated sound field.

In conclusion, it has been shown in Figure 5.15 that acoustic perturbations generated by blade vibration are dependent on the steady blade loading. Treatments (e.g. analytical methods) which use blade rows with no mean pressure rise are therefore incapable of reproducing the unsteady pressure field required, and are thus unsuitable for the analysis of acoustic driven flutter studied in this thesis.

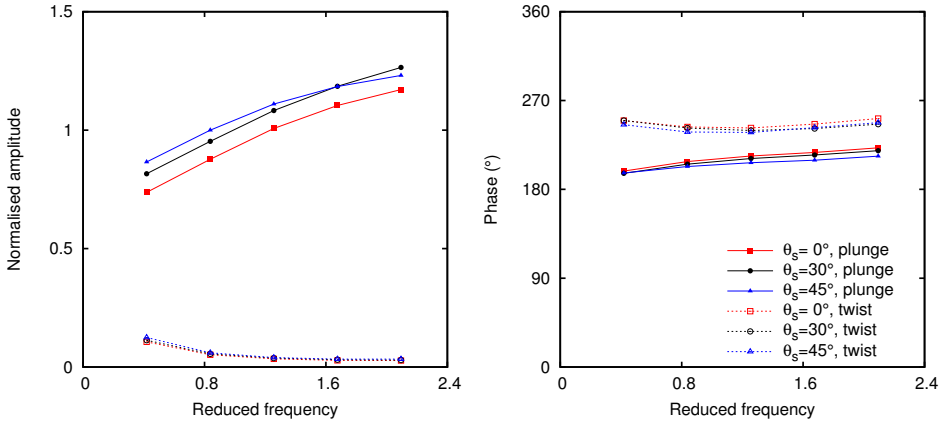


Figure 5.16: Amplitude and phase of modal force for different blade stagger angle θ_s and vibration motion.

The results in this section show that the generation of acoustic waves due to blade vibration is a function of the 'uncovered passage', the reduced frequency, the modeshape and the steady loading. The generated acoustic waves due to the plunge motion is (approximately) out of phase with the blade velocity at the leading edge and in phase at the trailing edge. For the twist motion, the generated acoustic waves are 90°ahead of the blade velocity at the leading edge and 90°behind at the trailing edge. The effect of steady loading is unlikely to be negligible for real turbomachinery bladings, thus the usefulness of analytical methods concerning sound generation due to the vibration of flat plate cascades [22, 23] are limited. Moreover, it is also shown that the axial wavenumber of the acoustic wave, which is an important parameter characterising the propagation of acoustic waves (Equation 4.24 and 4.25), can be modelled analytically with a good degree of accuracy.

5.3.2 Effect of modeshape on aerodynamic damping

In the next step, the effects of stagger angle and modeshape on flutter stability of the flat plate are investigated. Modal force (right hand side of Equation 3.3) and aero-damping of the blade are computed from a complete cycle of the fully developed unsteady CFD solutions.

Figure 5.16 shows the computed amplitude and phase of modal force as a function of the reduced frequency for both plunge and twist motions. In

these plots the amplitude of modal force is normalised by the amplitude due to the plunge motion for the 45°stagger at the reduced frequency of 0.84, and the phase is relative to the blade motion at zero displacement and the maximum positive velocity. In this plot results for three blade staggers, $\theta_s = 0°$, $\theta_s = 30°$ and $\theta_s = 45°$ are displayed. As can be seen in Equation 3.3, the modal force characterises the unsteady loading on the surfaces of the blade due to the interaction between the aerodynamic forces and the blade vibration motion, and thus represents the unsteady lift for a pure plunge motion and the unsteady moment for a pure twist motion. It can be seen from the plots that the calculated modal force is more or less independent of the blade stagger for both the plunge and twist motions. This is because there is no change in the passage volume due to the 0°inter-blade phase angle vibration mode (0ND). In such situations, the vibration of a blade induces nearly no unsteady loading on its adjacent blades (in the same blade row) since there is no aerodynamic forces induced by the compression or expansion of the flow passages. It is also seen from these plots that the amplitude of modal force due to the plunge motion (unsteady lift) increases with the increase of reduced frequency. This shows a similar trend with the amplitude of the generated acoustic waves shown in Figure 5.9 since these two quantities are both driven by the pressure disturbances generated on the surfaces of the blade. The phase of the modal force due to the plunge motion is seen to be out of phase with the blade velocity at low reduced frequencies, and shows a gradual change with the increase of reduced frequency. On the other hand, the amplitude of modal force for the twist motion (unsteady moment) shows a decrease with the increase of reduced frequency, and the phase lags blade velocity by 90°at low reduced frequencies. It is also seen from Figure 5.16 that the modal force due to the twist motion is an order of magnitude smaller than that due to the plunge motion.

These observations can be understood by studying the instantaneous unsteady pressure contour as shown in Figure 5.10 and Figure 5.13 for the plunge and twist motions respectively. The blade vibration induces flow disturbances on the upper and lower blade surfaces, which in turn induce unsteady loading on the blade: unsteady lift and unsteady moment. Depending on the motion of the blade, i.e. plunge or twist, the induced unsteady loading can interact with the vibration motion to either transfer energy into the system or take energy out of it. For the plunge motion (as

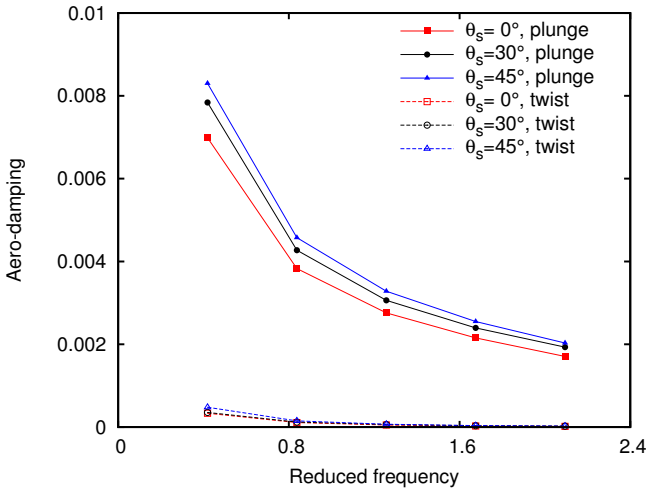


Figure 5.17: Aerodynamic damping for different stagger angle θ_s and vibration motion.

shown in Figure 5.10), the unsteady pressure induces a lift force which acts in the opposite direction of the blade motion (hence the 180°phase difference with the blade velocity) at any instance of time. On the other hand, for the twist motion (as shown in Figure 5.13), the induced unsteady moment at the front half of the blade more or less cancels that induced at the rear half, hence the low amplitude of modal force observed in Figure 5.16.

Figure 5.17 shows the computed blade aerodynamic damping as a function of reduced frequency for both plunge and twist motions. It can be seen from the plot that the aerodynamic damping is positive for all the cases studied. The aero-damping is (nearly) independent of the stagger angle for both the plunge and twist motions. This is again the result of zero passage volume change due to 0°inter-blade phase angle (for the 0ND mode). The global trend of blade aero-damping shows a decrease with the increase of reduced frequency, where the damping tends to zero when the vibration frequency tends to infinity (blade is too stiff to be affected by the flow). Moreover, the aero-damping due to the twist motion is seen to be an order of magnitude smaller than that due to the plunge motion. In order to understand the effect of modeshape on blade aero-damping, an in-depth analysis of the aerodynamic work contribution is considered below.

As described in Section 3.4, the aerodynamic damping of the blade can be obtained by using an energy method by calculating the aerodynamic work

per vibration cycle using Equation 3.10. Consider a blade vibrating in the pure plunge mode, the aerodynamic work can be calculated based on the local unsteady loading vector induced by the plunge motion $p_P \boldsymbol{n}$ and the local blade velocity vector due to plunge motion $\boldsymbol{v}_P$ as

$$w_{PP} = \int_T \oint p_P \boldsymbol{n} \cdot \boldsymbol{v}_P dS dt \tag{5.7}$$

where the variables have the same meaning as in Section 3.4, and the subscript P denotes variables associated with the plunge motion. Equation 5.7 evaluates the aerodynamic work on a blade vibrating in the plunge motion due to unsteady loading induced by the plunge motion, hence the notation w_{PP}. It should be noted that the subscripts are arranged so that the first letter denotes the source of unsteady loading, and the second letter denotes the motion it is applied to. Similarly, the aerodynamic work on a blade vibrating in the twist motion due to unsteady loading induced by the twist motion can be expressed as

$$w_{TT} = \int_T \oint p_T \boldsymbol{n} \cdot \boldsymbol{v}_T dS dt \tag{5.8}$$

where the subscript T denotes variables associated with the twist motion. It is worth noting that both plunge and twist motions induce unsteady lift and moment on the surfaces of the blade. Therefore, the terms p_P and p_T contain unsteady loading of both these two sources induced by the blade vibration. However, by examining Equation 5.7 and Equation 5.8, it is obvious that the unsteady moment contribution of p_P has no effect on the aerodynamic work for the plunge motion $\boldsymbol{v}_P$, and the unsteady lift contribution of p_T has no effect on the aerodynamic work for the twist motion $\boldsymbol{v}_T$ (since the work on the front section of the blade cancels that on the rear section).

The aerodynamic damping for blade vibration in these two situations can be expressed as

$$\zeta_{PP} = -\frac{w_{PP}}{v_{0_P^2}} \tag{5.9}$$

$$\zeta_{TT} = -\frac{w_{TT}}{v_{0_T^2}} \tag{5.10}$$

$$\tag{5.11}$$

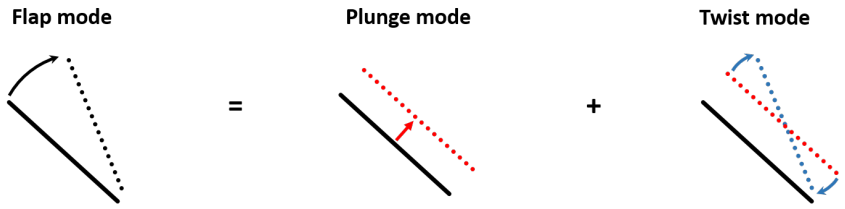


Figure 5.18: Decomposition of a (two-dimensional) flap mode into a linear combination of a plunge mode and a twist mode.

where v_{0P} and v_{0T} are the initial velocities for the plunge motion and the twist motion respectively. The aerodynamic damping shown in Figure 5.17 for the plunge and twist vibrations correspond to ζ_{PP} and ζ_{TT} in the equations above.

The blades (or blade sections) in turbomachines rarely vibrate in the pure plunge mode or the pure twist mode due to complex three dimensional geometries and non-uniform material properties. Instead, the modeshape for such blades usually consists of a combination of plunge and twist motions. It was shown in [11] that the 1st flapwise bending mode (1F) for typical rotor blades, which is usually the most susceptible to flutter, can be decomposed into a linear combination of a plunge component and a twist component (about mid-chord). This decomposition of such a mixed mode (will be referred to as the 'flap' mode in the rest of this chapter) is illustrated in Figure 5.18.

For small amplitude blade vibration in such a mixed mode (Figure 5.18), the instantaneous local velocity vector on the blade surfaces $\boldsymbol{v}$ can be expressed as a linear summation of the components due to a pure plunge motion and a pure twist motion, i.e.

$$\boldsymbol{v}_F = (1-\gamma)\boldsymbol{v}_P + \gamma \boldsymbol{v}_T \tag{5.12}$$

where γ represents the percentage of twist motion in a flap mode, which has a (minimum) value of 0 for pure plunge modes and a (maximum) value of 1 for pure twist modes. The subscript F denotes variables associated with the flap motion. Similarly the unsteady pressure p on blade surfaces can be expressed in terms of contributions induced by the plunge and the twist motions as

$$p_F = (1-\gamma)p_P + \gamma p_T \tag{5.13}$$

It should be noted that the unsteady blade loading is assumed to be proportional to the blade motion for small amplitude vibrations.

Hence the aerodynamic work for a blade vibrating in the flap mode can be obtained from

$$w_{FF} = \int_T \oint ((1-\gamma)p_P + \gamma p_T)\boldsymbol{n} \cdot ((1-\gamma)\boldsymbol{v}_P + \gamma \boldsymbol{v}_T) dS dt \tag{5.14}$$

The above equation can be expanded to give

$$w_{FF} = w_{PP} + w_{PT} + w_{TP} + w_{TT} \tag{5.15}$$

where

$$w_{PP} = (1-\gamma)^2 \int_T \oint p_P \boldsymbol{n} \cdot \boldsymbol{v}_P dS dt \tag{5.16}$$

$$w_{PT} = \gamma(1-\gamma) \int_T \oint p_P \boldsymbol{n} \cdot \boldsymbol{v}_T dS dt \tag{5.17}$$

$$w_{TP} = \gamma(1-\gamma) \int_T \oint p_T \boldsymbol{n} \cdot \boldsymbol{v}_P dS dt \tag{5.18}$$

$$w_{TT} = \gamma^2 \int_T \oint p_T \boldsymbol{n} \cdot \boldsymbol{v}_T dS dt \tag{5.19}$$

The term w_{PT} represents the aerodynamic work for the twist motion due to the unsteady loading induced by the plunge motion, and conversely w_{TP} represents the aerodynamic work for the plunge motion due to unsteady moment induced by the twist motion. These two terms represent the coupling effect between the plunge and the twist components in a flap mode, where energy can be transferred between the two vibration motions through the flow medium. The aerodynamic damping due to these four contributions can thus be expressed as

$$\zeta_{PP} = -\frac{w_{PP}}{(1-\gamma)^2 v_{0_P}^2} \tag{5.20}$$

$$\zeta_{PT} = -\frac{w_{PT}}{\gamma^2 v_{0_T}^2} \tag{5.21}$$

$$\zeta_{TP} = -\frac{w_{TP}}{(1-\gamma)^2 v_{0_P}^2} \tag{5.22}$$

$$\zeta_{TT} = -\frac{w_{TT}}{\gamma^2 v_{0_T}^2} \tag{5.23}$$

which give

$$\zeta_{PP} = -\frac{1}{v_{0_P}^2} \int_T \oint p_P \boldsymbol{n} \cdot \boldsymbol{v}_P dS dt \tag{5.24}$$

$$\zeta_{PT} = -\frac{1-\gamma}{\gamma} \frac{1}{v_{0_T}^2} \int_T \oint p_P \boldsymbol{n} \cdot \boldsymbol{v}_T dS dt \tag{5.25}$$

$$\zeta_{TP} = -\frac{\gamma}{1-\gamma} \frac{1}{v_{0_P}^2} \int_T \oint p_T \boldsymbol{n} \cdot \boldsymbol{v}_P dS dt \tag{5.26}$$

$$\zeta_{TT} = -\frac{1}{v_{0_T}^2} \int_T \oint p_T \boldsymbol{n} \cdot \boldsymbol{v}_T dS dt \tag{5.27}$$

and the aerodynamic damping for the flap mode can thus be written as

$$\zeta_{FF} = \zeta_{PP} + \zeta_{PT} + \zeta_{TP} + \zeta_{TT} \tag{5.28}$$

The physical meanings of these four components are discussed in this paragraph. The aerodynamic work for the plunge motion (i.e. w_{PP} and w_{TP}) is driven by the unsteady lift force on the surfaces of the blade (due to plunge and twist motions respectively), where energy transfer takes place by displacing the blade in the direction normal to the chord. On the other hand, the aerodynamic work for the twist motion (i.e. w_{PT} and w_{TT}) is driven by the unsteady moment on the surfaces of the blade, where energy transfer takes place by rotating the blade about the mid-chord. In other words, the plunge motion and the twist motion each produces unsteady lift force as well as unsteady moment, which in turn interact with the two vibration motions giving rise to the four contributions for aerodynamic work (in a sense analogous to the outer product of two vectors).

It is also important to note that, as can be seen in Equation 5.24 to Equation 5.27, the effect of changing the twist component in a flap mode is to modify the aerodynamic damping for the 'cross product' terms, namely ζ_{PT} and ζ_{TP}. This is obvious since the aero-damping for the pure plunging motion ζ_{PP} and the pure twist motion ζ_{TT} are independent of the amplitude of vibration. With the increase of the twist component (by increasing γ), the aero-damping for the plunge mode driven by the unsteady loading induced by the twist motion ζ_{TP} increases in magnitude, and the aero-damping for the twist mode driven by the unsteady loading induced by the plunge motion ζ_{PT} sees a decrease. This is quite obvious since the increase in the amplitude of twist motion results in a higher induced unsteady loading and

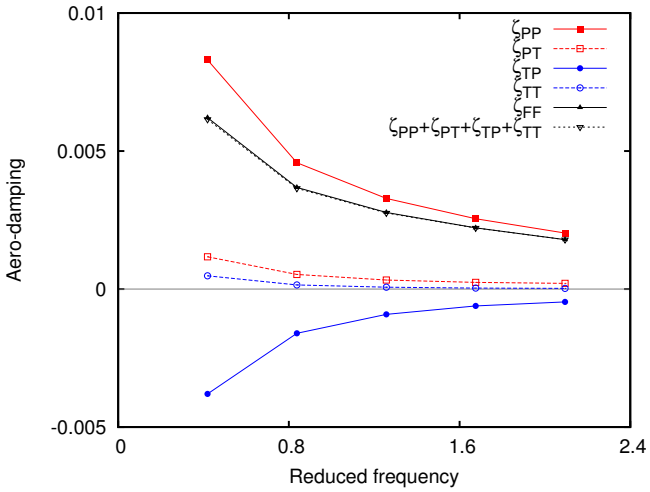


Figure 5.19: Aerodynamic damping contributions due to plunge and twist motions, $\theta_s = 45°$, $\gamma = 0.5$.

thus a higher aerodynamic work.

Based on the above analysis, the aforementioned four blade aero-damping components, namely ζ_{PP}, ζ_{PT}, ζ_{TP} and ζ_{TT}, are calculated from their respective aerodynamic work for the cases studied. The aerodynamic work contributions w_{PP} and w_{TT} are obtained directly from the unsteady CFD solutions for the pure plunge and the pure twist motions (which correspond to the cases presented in Figure 5.17). The aerodynamic work contributions w_{PT} and w_{TP} are obtained without the need of CFD computations using Equation 5.17 and Equation 5.18 through post-processing of unsteady CFD solutions computed using the pure plunge and the pure twist motions. The computed blade aero-damping components for the flap mode with $\gamma = 0.5$ are plotted in Figure 5.19 as a function of reduced frequency for the 45°stagger angle case. It can be seen from Figure 5.19 that the aerodynamic damping ζ_{PT} and ζ_{TT} for the twist motion (unsteady moment driven) are small compared with the aerodynamic damping ζ_{PP} and ζ_{TP} for the plunge motion (unsteady lift driven). This can be understood by looking at the unsteady pressure contour for the pure plunge motion and the pure twist motion shown in Figure 5.10 and Figure 5.13. It can be inferred from these contour plots that the unsteady moment induced by both the plunge and twist vibrations is small compared with the unsteady lift force (normal to the chord), since the unsteady moment generated by the front

half and the rear half of the blade sum up to be nearly zero for any instance of time. Moreover, it can be seen from Figure 5.19 that the aerodynamic damping for the plunge motion due to unsteady lift induced by the plunge vibration (ζ_{PP}) is always positive, and that for the plunge motion due to unsteady lift induced by the twist vibration (ζ_{TP}) is always negative.

In order to further examine the decomposition of aero-damping (Equation 5.28) presented above, unsteady CFD flutter computations are carried out for the same 45°stagger blade row in the flap mode with $\gamma = 0.5$. The modeshape for the flap mode used in this analysis is obtained from the linear summation of the modeshape for the pure plunge and the pure twist modes (as demonstrated in Figure 5.18). The aero-damping for the flap mode ζ_{FF} obtained from unsteady CFD computations is plotted in Figure 5.19 (solid black line) as a function of reduced frequency, which is compared with the sum of the aero-damping contributions ζ_{PP}, ζ_{PT}, ζ_{TP} and ζ_{TT} (dotted black line) obtained from the previous analysis based on the pure plunge and twist modes. It is clearly seen that the the two quantities are identical, which demonstrates the validity of Equation 5.28 for blade vibrations in the flap mode. For the range of reduced frequencies and percentage of twist motion γ studied here, the flap mode is always stable since the aero-damping due to plunge motion induced unsteady lift (ζ_{PP}) is higher than the magnitude of that due to twist motion induced unsteady lift (ζ_{TP}), while the two aero-damping contributions due to unsteady moment (ζ_{TT} and ζ_{PT}) are negligible. The observations are in agreement with those in [11] for a transonic fan blade.

Finally, the effect of modeshape on blade aero-damping is studied. Having demonstrated that the aero-damping of a blade vibrating in a flap mode can be obtained using Equation 5.24 to Equation 5.27 through post-processing of unsteady CFD solutions computed using the pure plunge and the pure twist motions, the blade aero-damping is calculated using these equations by varying the amount of twist component γ without the need of CFD computations. Figure 5.20 shows the comparison of computed blade aero-damping for three different amounts of twist component $\gamma = 0.5$, $\gamma = 0.7$ and $\gamma = 0.8$, which correspond to increasing amount of twist in the flap mode. In this plot the aero-damping for the plunge mode due to plunge-induced unsteady loading (lift) ζ_{PP} is displayed as the dashed curves, the aero-damping for the plunge mode due to twist-induced unsteady loading

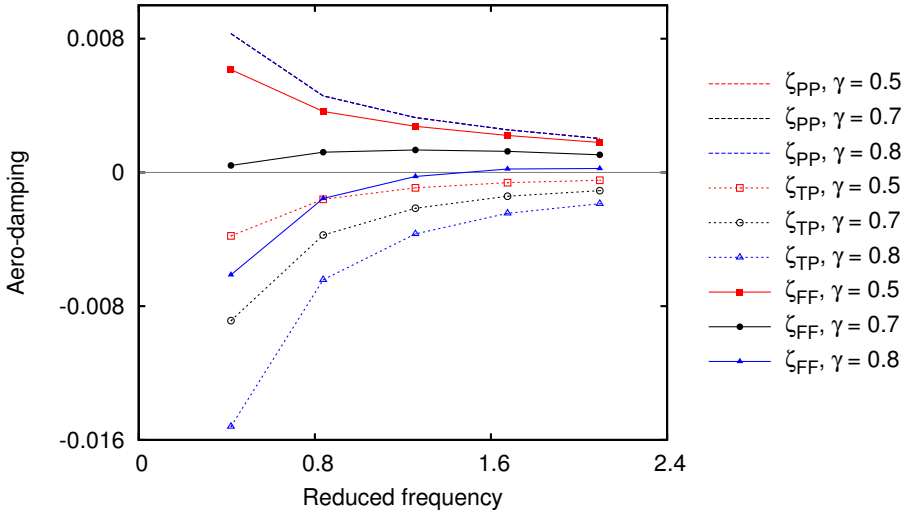


Figure 5.20: Aerodynamic damping contributions for different modeshape parameter γ, $\theta_s = 45°$.

(lift) ζ_{TP} is displayed as the dotted curves, and the aero-damping for the (total) flap mode ζ_{FF} is displayed as the solid curves. It should be noted that the aero-damping contributions for the twist motion ζ_{PT} and ζ_{TT} are negligible and thus not shown in this plot. It can be seen from the plot that the aero-damping ζ_{PP} is (quite obviously) independent of γ, whereas the negative aero-damping ζ_{TP} increases with the increase of γ. The loss of aero-damping ζ_{TP} is more pronounced at low reduced frequencies. This increase of negative aero-damping ζ_{TP} results in a significant loss of blade combined stability for the flap mode ζ_{FF} especially at low reduced frequencies. It is seen that the stability for the flap mode with $\gamma = 0.7$ is reduced to just stable at the reduced frequency of about 0.4, and the flap mode with $\gamma = 0.8$ becomes unstable for reduced frequencies below 1.4.

Figure 5.17 to Figure 5.20 clearly demonstrate the effect of modeshape on flutter stability of a vibrating blade. It is shown that the aero-damping contribution for the unsteady moment driven twist motion is an order of magnitude smaller than that for the unsteady lift driven plunge motion, and can usually be neglected in the flutter analysis of a blade vibrating in the flap mode in low inter-blade phase angle modes. The aero-damping contribution for the twist motion can become higher at large stagger angles and higher inter-blade phase angles where the induced unsteady moment becomes high.

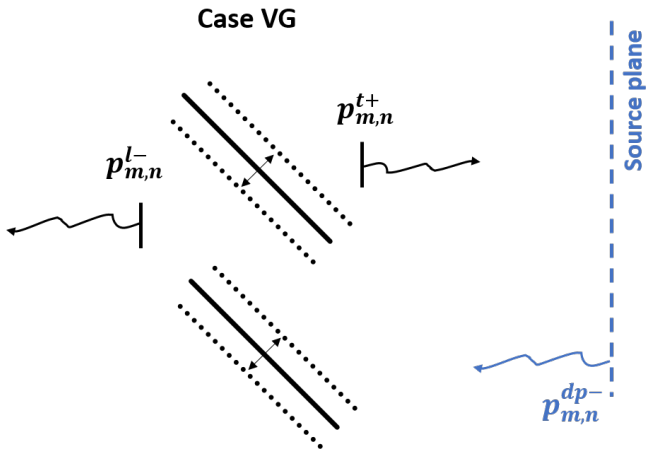


Figure 5.21: Imposing an upstream propagating acoustic gust in the downstream field of the vibrating blade row.

The analysis also demonstrated an important finding that, in the absence of complicated aerodynamics (such as flow separation), it is possible to make a blade flutter by increasing the amount of twist motion in a flap mode. It is worth noting that from experience the amount of twist γ in typical 1F modes of rotor blade is usually less than 0.5. However, the negative aero-damping ζ_{TP} for such cases is normally considerably higher than that for this simple geometry (such as the case shown in [11]). The findings in this analysis also indicate a viable approach of calculating blade aero-damping for a general flap mode by considering the energy transfer between the plunge motion and the unsteady lift generated by both the plunge and twist vibrations (i.e. energy transfer into the twist motion through unsteady moment is neglected). These aspects will be further investigated in a later section (Section 5.5).

5.4 Effects of Incoming Acoustic Gust

In the next step, the vibration of the thin annulus blade row is studied with the presence of an incoming acoustic gust. The purpose of the incoming gust is to mimic a reflected acoustic wave from a blade row (or intake). This is achieved by imposing propagating acoustic waves using unsteady plane sources, which is illustrated schematically in Figure 5.21. The imposed acoustic waves have the same frequency with the blade vibration as they

represent the reflection of the outgoing acoustic waves generated by the vibration motion. By doing so, the interaction between an incoming acoustic wave and the blade vibration can be studied.

For the case studied here, the blade stagger (and the flow angle) is fixed at 45°and the Mach number at $M = 0.3$. The vibration is initiated for the plunge mode and the twist mode with a fixed reduced frequency of 0.84. The amplitude of the gust is kept constant (which will be shown to correspond to a reflected acoustic wave with an amplitude about $|\eta^R| = 0.7$ relative to the outgoing acoustic wave due to the plunge motion at the blade trailing edge). The phase of the gust, which is the only variable in this study, is varied linearly between 0°and 360°. The frequency of the gust is fixed and is the same as the frequency of blade vibration, since it is mimicking the reflection of the acoustic waves generated by blade vibration. For the studies performed here, upstream propagating acoustic waves are imposed from the downstream field of the blades (studies with downstream propagating gusts yield identical conclusions and are thus not presented here). This series of computations are referred to as *Case VG* in this chapter, where *VG* denotes 'vibration and gust'.

Figure 5.22 shows an example of the wave-splitting results in the upstream and downstream fields of the blade. The amplitude and phase of the unsteady pressure are plotted in this figure as a function of non-dimensional axial location. The amplitude is normalised by the amplitude of unsteady pressure for the outgoing acoustic wave at the trailing edge of the blade for *Case V*, and the phase is relative to blade motion at zero displacement and the maximum positive velocity. In this plot the decomposed upstream propagating (red curves) and the downstream propagating (blue curves) acoustic waves for *Case V* and *Case VG* are displayed along with the total unsteady pressure field (black curves) for *Case VG* (the total unsteady pressure field for *Case V* is not shown since it is the same as the upstream and downstream propagating waves generated by blade vibration, see Figure 5.6). In this plot the blade center is located at $x/c_{ax} = 0$ and the acoustic gust is imposed at about $x/c_{ax} = 10$. It can be seen that in the downstream field of the blade ($x/c_{ax} > 0.5$), the imposed acoustic wave (solid red curve) travels upstream towards the blades with a constant axial phase velocity and a constant amplitude (with a ratio of about 0.7 to the outgoing wave). Part of this incoming acoustic wave transmits through the blade passage

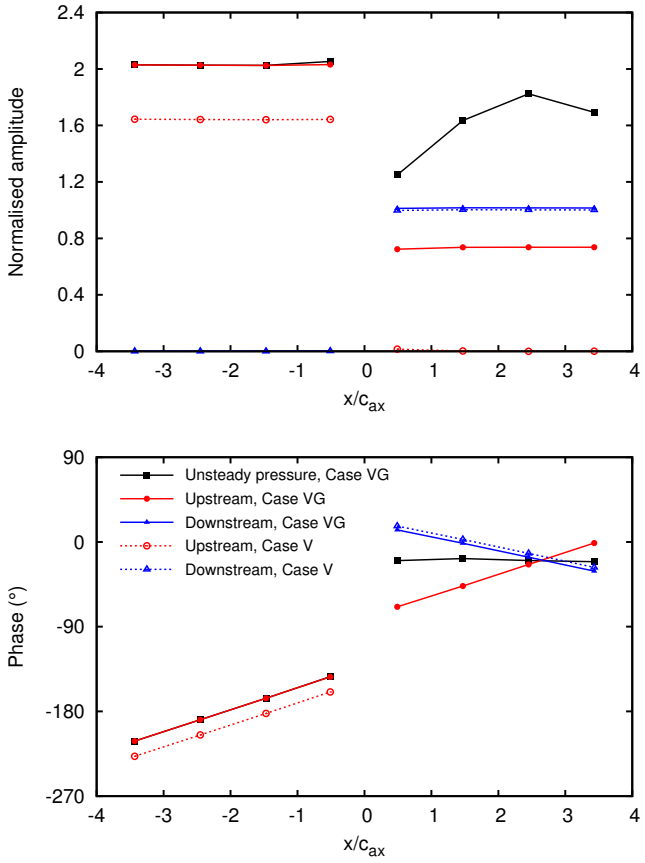


Figure 5.22: Axial variation of the amplitude and phase of acoustic waves for *Case VG*, phase of incoming gust $\phi^{dp-} = 0°$, $\theta_s = 45°$, $f_r = 0.84$, plunge mode.

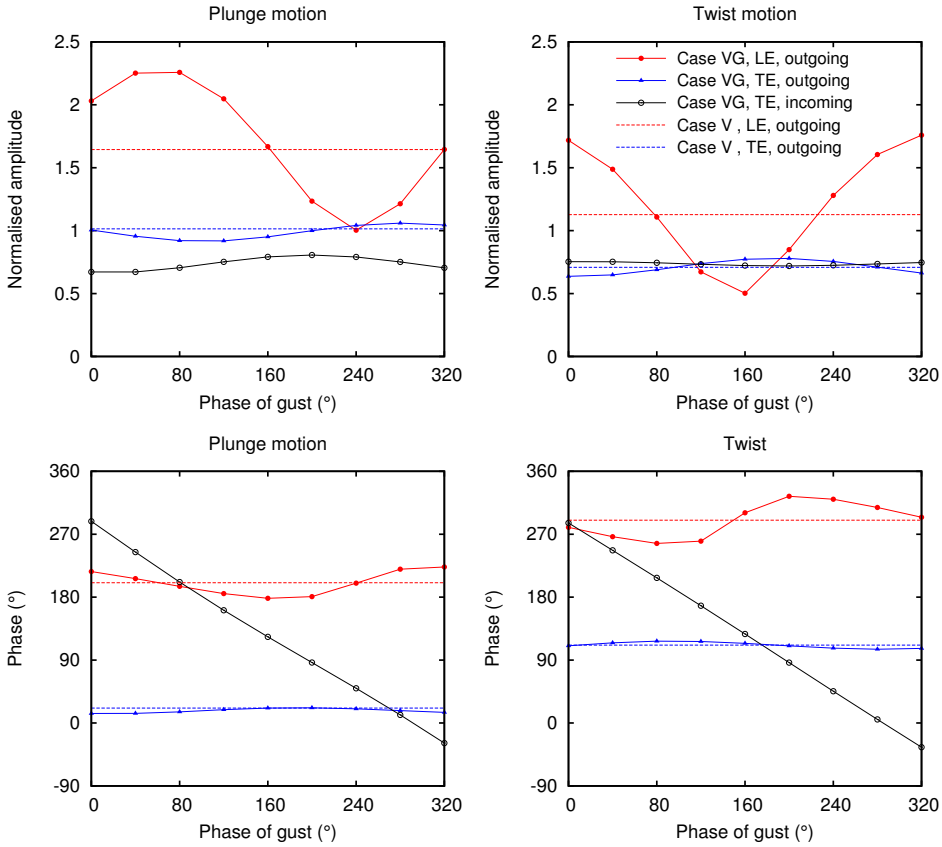


Figure 5.23: Amplitude and phase of outgoing and incoming acoustic waves at the leading edge and the trailing edge, $\theta_s = 45°$, $f_r = 0.84$.

and changes the amplitude and phase of the upstream propagating wave at the leading edge (from dotted red curve to solid red curve, $x/c_{ax} < -0.5$). On the other hand, the downstream propagating wave at the trailing edge (blue curves) does not show significant variation, indicating that for the case studied the amplitude of reflection at the blade is small. Nevertheless, the incoming acoustic wave significantly changes the amplitude and phase of the unsteady pressure field downstream of the blade (from dotted black curve to solid black curve, $x/c_{ax} > 0.5$). It is also seen that the reflection from the inflow boundary is negligible in this case (i.e. the blue curve for $x/c_{ax} < 0$).

Figure 5.23 shows the amplitude and phase of acoustic waves at the leading edge and trailing edge of the blade as a function of the phase of the imposed incoming gust ϕ^{dp-} for *Case V* and *Case VG* setups due to plunge

and twist vibrations. The amplitude is normalised by the amplitude of the outgoing acoustic waves generated by blade vibration at the trailing edge in the absence of incoming gust (i.e. the amplitude of unsteady pressure obtained from *Case V*), and all the phases are relative to blade motion at zero displacement and the maximum positive velocity. It should be noted that the results for *Case V* are obtained in the absence of the incoming gust and are thus obviously independent of the incoming gust phase. Nevertheless the results for *Case V* are shown in this plot as dashed lines for reference. In these plots the outgoing acoustic waves propagating away from the blade are displayed in the red curves (at leading edge) and the blue curve (at trailing edge), and the incoming acoustic waves (at trailing edge) incident on the blade are displayed as the black curves. It should be noted that there are no incoming waves at the leading edge as the acoustic gust is only imposed at a location downstream of the blade. In other words, the incoming acoustic gust is represented by the black curves in the downstream field of the blade; the solid red curves represent the (complex) summed unsteady pressure field at the blade leading edge due to acoustic waves generated by vibration (dashed red curve) and the transmission of the incoming acoustic gust; the solid blue curves represent the (complex) summed unsteady pressure field at the blade trailing edge due to acoustic waves generated by vibration (dashed blue) and the reflection of the incoming acoustic gust.

It can be seen from the plots that the incident acoustic wave at the trailing edge of the blade (black curves) has a nearly constant amplitude and a linearly varying phase (with respect to the phase of incoming gust at the source plane). This is obvious since in this study the imposed perturbation (at the source plane) has a fixed amplitude, and the phase is varied linearly. On the other hand, the amplitude and phase of the outgoing acoustic wave at the leading edge (solid red curve) shows a large oscillation due to the variation of the phase of the incoming gust, whereas a much smaller oscillation is observed for the downstream travelling wave at the trailing edge (solid blue curve). This is due to a higher amplitude of transmission than reflection induced by the incoming gust, which can be clearly demonstrated by the following analysis.

Instead of imposing the unsteady acoustic perturbation in the domain of the vibrating blade row, a similar analysis is carried out where the same acoustic perturbation is imposed while the blade is kept stationary (i.e. no

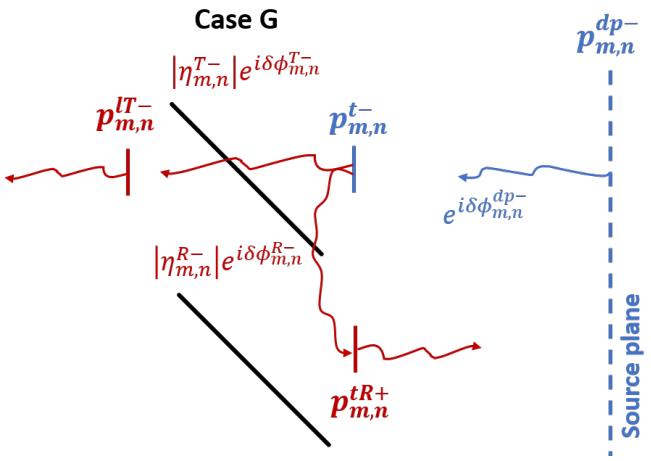


Figure 5.24: Imposing an upstream propagating acoustic gust in the downstream field of the non-vibrating blade row.

vibration). By doing so, the transmission and reflection of the imposed perturbation at the blade row can be investigated, and the contribution to modal force (right hand side of Equation 3.3) due to the incoming gust alone can be evaluated in a straightforward fashion. It is worth noting that in this setup the modal force on the blade is computed in the usual fashion (i.e. 3$^{\text{rd}}$ flutter computation strategy shown in Section 3.4 with prescribed zero blade displacement), however the blade vibration motion is not affected by it (i.e. remains stationary). By doing so, the effect of the incoming acoustic gust on the blade loading and the aero-damping can be studied in the absence of the perturbations generated by the blade vibration (i.e. *Case V*). This series of computations with incoming gust alone are referred to as *Case G* in this chapter, where *G* denotes 'gust'. By comparing the results of *Case V*, *Case G* and *Case VG*, a judgement can be made regarding the linearity of the problem (i.e. whether the effects due to the vibration motion and the incoming acoustic gust are coupled or independent).

Figure 5.25 shows an example of the wave-splitting results in the upstream and downstream fields of the blade, where the amplitude and phase of the unsteady pressure for acoustic waves are plotted as a function of axial location. The amplitude of unsteady pressure is normalised by the amplitude of the outgoing acoustic waves generated by the plunge vibration at the trailing edge, in the absence of incoming gust. It is seen from this plot that when

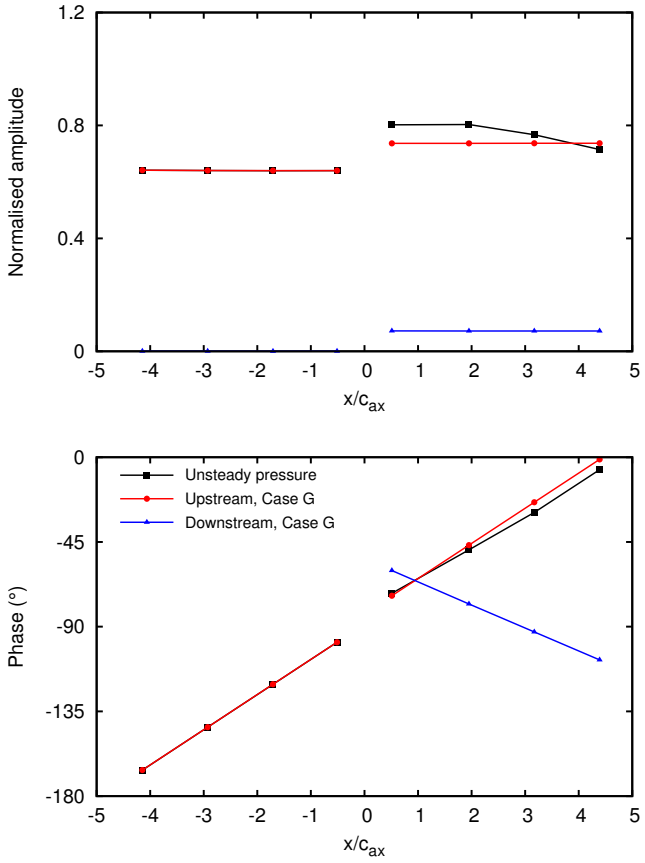


Figure 5.25: Axial variation of the amplitude and phase of acoustic waves for *Case G*, phase of incoming gust $\phi^{dp-} = 0°$, $\theta_s = 45°$, $f_r = 0.84$, plunge mode.

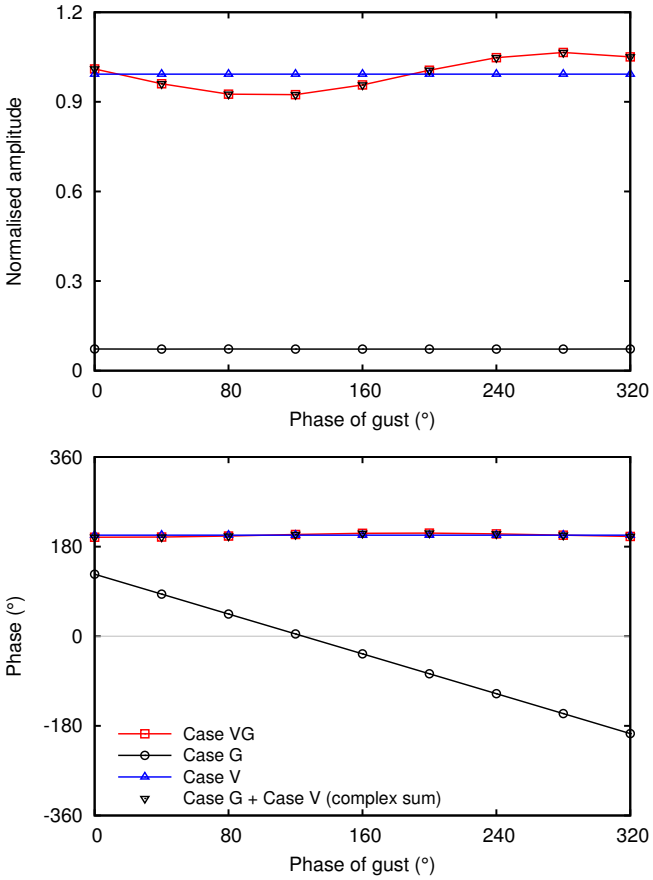


Figure 5.26: Modal force as a function of the phase of incoming gust, $\theta_s = 45°$, $f_r = 0.84$, plunge mode.

the upstream propagating acoustic perturbation (red curve $x/c_{ax} > 0.5$) impinges on the blade row (which is situated at $-0.5 < x/c_{ax} < 0.5$), part of it is transmitted (red curve $x/c_{ax} < -0.5$) and part of it is reflected (blue curve $x/c_{ax} > 0.5$). For the geometry and flow condition studied here, the amplitude of the transmission coefficient (about 0.85) is much higher than that of the reflection coefficient (about 0.1), which clearly explains the larger oscillation of unsteady pressure amplitude at the leading edge of the blade compared with the trailing edge of the blade as shown in Figure 5.23. It is stressed that this observation is not general and is only particular for this test case.

In order to study the influence of the incoming gust on the vibration motion for the stationary blade row (*Case G*), modal forces are calculated

and compared with that for the vibrating blade row with the incoming gust (*Case VG*). The results are plotted in Figure 5.26 as a function of the phase of the incoming gust. Moreover, the modal force due to the vibration of the isolated blade row in the absence of an incoming gust (*Case V*) is also shown in this figure as a reference, which is plotted as a flat line as it is obviously independent of the gust phase. In these plots the amplitude is normalised by the amplitude of modal force for *Case V*, and the phase is relative to the blade motion at zero displacement and maximum positive velocity. It can be seen from the amplitude plot that due to the incoming acoustic gust, the modal force on the vibrating blade (*Case VG*) is seen to oscillate sinusoidally around the values in the absence of gust (*Case V*). The amplitude of this oscillation is dependent on the amplitude of the imposed gust. On the other hand, the modal force on the stationary blade induced by the incoming acoustic gust alone (*Case G*) shows constant amplitude and linearly varying phase with respect to the incident wave, which is obvious since the amplitude of the gust is fixed (and imposed) and the only variable in this case is the phase of the imposed wave. Moreover, by taking the complex summation of the modal force for *Case V* (blue curve) and *Case G* (black curve), it can be seen that the calculated complex sum (black triangles) shows good agreement with the modal force for *Case VG* (red curve). This is a strong indication that for small amplitude vibrations, which are the case in the situation of flutter onset, the unsteady loading on the blade surfaces can be linearly decoupled into a component due to the vibration motion and a component due to the incoming gust. These two components are independent and can be evaluated separately. Therefore the unsteady lift on the surfaces of the blade can be obtained by a complex summation as

$$l = l_{vib} + l_{gust} \tag{5.29}$$

where l denotes the unsteady lift on the blade surfaces, l_{vib} denotes the unsteady lift contribution due to blade vibration in the absence of incoming gust (i.e. without reflection), l_{gust} denotes the unsteady lift contribution due to the incoming gust alone. By performing similar analyses for the twist motion (which is not presented here), the unsteady moment can be

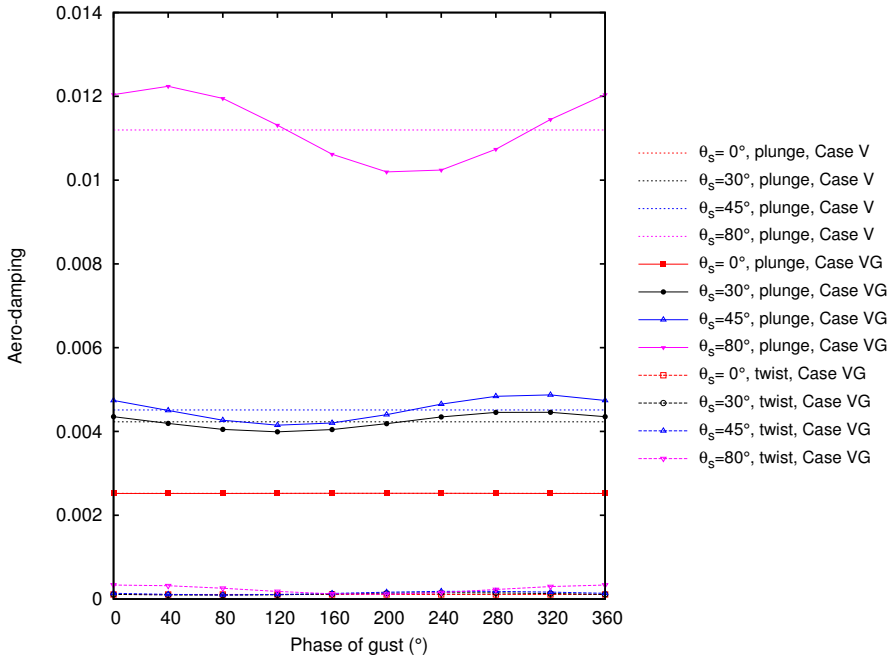


Figure 5.27: Aerodynamic damping as a function of the phase of incoming gust, $f_r = 0.84$.

shown to behave in a similar fashion as

$$m = m_{vib} + m_{gust} \tag{5.30}$$

where m denotes the unsteady moment on the blade surfaces. It will be shown in the next section that this is an important finding which allows one to evaluate the effect of incoming gust (acoustic reflection) on blade aero-damping independently from that due to the blade motion (in the absence of reflections).

In the next step, aerodynamic damping of blades are calculated using the energy method (Equation 3.10) from the unsteady CFD solutions, which are plotted in Figure 5.27 as a function of the phase of the incoming gust. For all the cases in this study the reduced frequency of vibration and the amplitude of the incoming gust are fixed, and the only variable is the phase of the incoming gust. In this plot the aero-damping of the blade with stagger angle of 0°, 30°, 45°and 80°are displayed as the dashed curves for the plunge vibration *Case V*, solid curves for the plunge vibration *Case VG*, and dotted

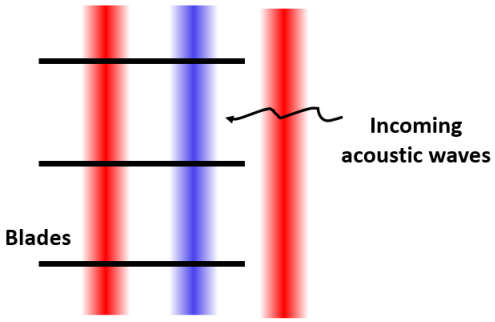


Figure 5.28: Instantaneous unsteady pressure contour for $\theta_s = 0°$, $f_r = 0.84$.

curves for the twist vibration *Case VG*. It is worth noting that, for clarity, the results for the twist vibration *Case V* are not shown in this plot as the blade aero-damping for this mode does not change significantly from *Case V* to *Case VG*.

It can be seen from the plot that, as expected, the incoming acoustic gust affects the blade aero-damping (*Case VG*) in a sinusoidal fashion. The blade aero-damping for the plunge mode with the presence of the incoming gust (*Case VG*) is seen to oscillate about the aero-damping for the isolated blade (*Case V*) with a period of 360°(*Case VG* for the twist vibration shows similar trend with respect to *Case V* and is not shown here). The aero-damping for the 0°stagger blade row is independent of the incoming 0ND gust since the incident acoustic wave induces zero blade loading at all instances of time (as illustrated in Figure 5.28). In other words, the incident acoustic wave travels through the blade row unimpeded, which means, from an energy point of view, the incoming perturbations induce zero loading and thus zero work on the vibrating blade. With the increase of blade stagger, the effect of the incoming gust becomes more pronounced, and the most destabilising condition occurs at different gust phases. This is a result of the increase in amplitude and a shift in phase of the unsteady blade loading.

These trends are shown in Figure 5.29 where the amplitude and phase of the computed modal force for the plunge motion due to the incoming gust alone (*Case G*) are plotted as a function of the gust phase (modal force for the twist motion shows similar trend and is not presented here). In these plots the amplitude is normalised by the amplitude of modal force for the 45°stagger *Case V*, and the phase is relative to the blade motion at

zero displacement and maximum positive velocity. It is clearly seen that the incident acoustic gust induces zero loading on the 0°stagger blade, and the amplitude of unsteady loading increases with the increase of stagger angle (i.e. the increase of 'uncovered passage'). This can be explained as follows: as the blade stagger angle increases, the mode angle of the incident acoustic wave (which is 0°with the engine axis for the 0ND mode) becomes more aligned with the direction of lift force on the surfaces of the blade (perpendicular to the chord); this change results in an increase in the amplitude of unsteady blade loading as stagger is increased. Moreover, the phase of the unsteady loading shows a shift with respect to the phase of the incoming gust, which explains the shift of the most destabilising condition with respect to the gust phase in Figure 5.27. It is seen in Figure 5.27 that the most destabilising condition occurs when the unsteady loading (unsteady lift for the plunge motion studied) is in phase with the blade velocity, i.e. at about $\phi^{dp-} = 120°$ for 30°and 45°stagger angles and about $\phi^{dp-} = 210°$ for 80°stagger angle.

The mechanism behind this observation will be explored in detail in the next section. Furthermore, it is clearly seen that the aero-damping of the blade for the pure twist motion (ζ_{TT}, driven by the unsteady moment) is again an order of magnitude smaller than that for the pure plunge motion (ζ_{PP}, driven by the unsteady lift), indicating that the effect of the incoming acoustic gust is dominated by the interaction between the gust-induced unsteady lift and the plunge motion of blade vibration. This conclusion is likely to hold for low inter-blade phase angle modes where the induced unsteady lift is dominant, and can become invalid for large inter-blade phase angle modes where the effect of unsteady moment becomes more important.

Finally, the effect of incoming acoustic gust on flutter stability of the blade vibrating in the flap mode is studied by performing flutter computations for the 45°stagger angle blade row in the *Case VG* setup. It is important to note that in this study the only variables are the phase of incoming gust, and the amount of twist in the flap mode γ. The obtained aero-damping are plotted in Figure 5.30 as a function of the phase of the incoming gust for three different modes: $\gamma = 0.5$, $\gamma = 0.7$ and $\gamma = 0.8$. In this plot the aero-damping of the blade in the isolated *Case V* setup (as shown in Figure 5.20) is also displayed as a reference. It is again seen that the incoming gust induces positive and negative effects on flutter stability of the blade. Moreover, the

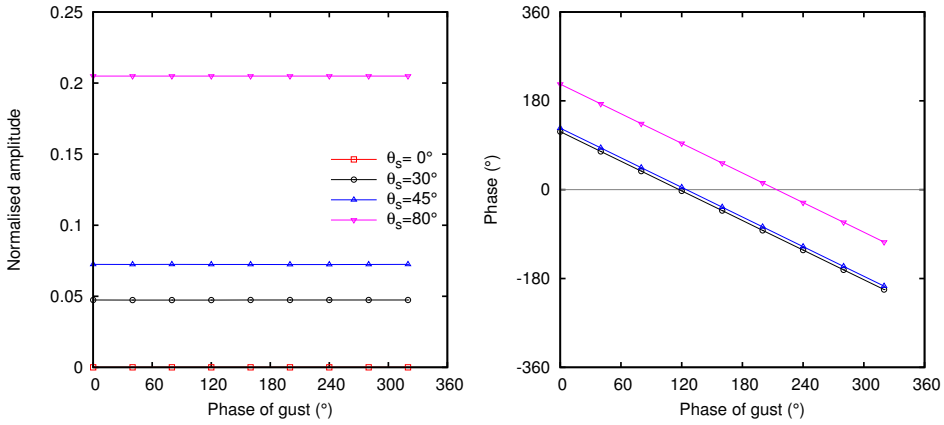


Figure 5.29: Modal force as a function of the phase of incoming gust for *Case G*, $f_r = 0.84$, plunge motion.

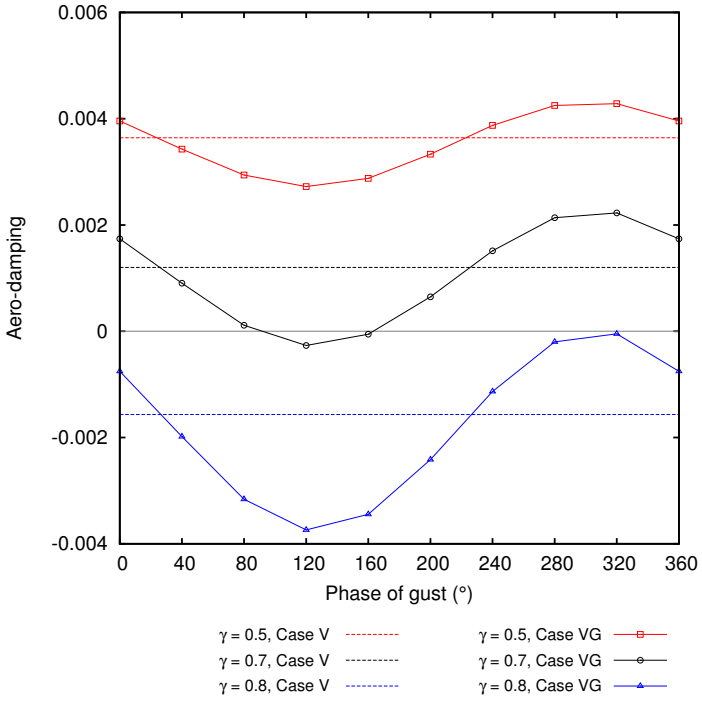


Figure 5.30: Aerodynamic damping of the blade vibrating in the flap mode for different modeshape parameter γ, $\theta_s = 45°$, $f_r = 0.84$.

variation of blade aero-damping due to the change in incoming gust phase shows a very similar trend with the variation of aero-damping for the pure plunge motion (solid blue curve in Figure 5.27), which again indicates that the effect of incoming gust is dominated by the interaction between the gust and the plunge motion. It is also seen that the amplitude of aero-damping variation increases with the increase of twist in the modeshape. This observation will be explained through the aerodynamic work analysis in the next section. Importantly, it is seen that the combine effects of increasing the twist component in the modeshape (from $\gamma = 0.5$ to $\gamma = 0.7$) and the presence of the incoming acoustic gust (with $\phi^{dp-} = 120°$) result in the flutter of an otherwise stable mode ($\gamma = 0.5$, *Case V*). It will be shown in the following chapters that this is an important finding which shows that flutter is most likely to occur when the lowest aerodynamic damping due to blade motion (flow and modeshape driven) and the most detrimental effect due to acoustic reflections coincide.

The effect of incoming acoustic gust on blade aerodynamic damping is clearly shown in this section. Based on the observations and conclusions made so far, a low fidelity method for flutter analysis of a blade vibrating in the 1st flapwise bending (1F) mode with low inter-blade phase angles (which are prone to 1F flutter) is proposed. The model is capable of evaluating the effect of incoming acoustic wave on aerodynamic damping of a blade, and the formulation of the model is described in the next section.

5.5 Low-fidelity Flutter Analysis Method

The effect of incoming acoustic gust on the aerodynamic damping of a vibrating blade has been clearly shown in the previous sections. The incident acoustic wave induces unsteady loading on the blade surfaces which in turn changes the aerodynamic work and damping. Moreover, the unsteady loading due to the blade motion and the incoming gust seem to be independent and can be analysed separately. This finding indicates that the aerodynamic damping contribution (which is dependent on the blade loading) due to the blade motion and the incoming acoustic wave are also likely to be independent and can be analysed separately. Furthermore, for low inter-blade phase angle modes, the aerodynamic damping for the twist motion (ζ_{PT} and ζ_{TT} driven by the unsteady moment generated by the plunge and

twist vibrations respectively) is an order of magnitude smaller than that for the plunge motion (ζ_{PP} and ζ_{TP} driven by the unsteady lift generated by the plunge and twist vibrations respectively), which can thus be neglected in the flutter analysis. It is worth mentioning again that for a modeshape consisting of a combination of plunge and twist motions, for instance the 1st flapwise bending (1F) mode for typical turbomachinery blades (Figure 5.18), the unsteady lift induced by the twist motion can interact with the plunge motion to produce damping (positive or negative) for the blade (i.e. ζ_{TP}).

Based on the knowledge gained, a low-fidelity analytical method for flutter analysis of a blade vibrating in the 1st flapwise bending (1F) mode with low inter-blade phase angles (which are prone to 1F flutter) is devised in this section. The method is capable of evaluating the influence of incoming gust (e.g. acoustic reflections from a blade row) on the blade aerodynamic damping. The main purpose of the method is to determine the most destabilising condition due to incoming acoustic gusts where flutter is likely to occur. In other words, the aim is to find the condition for the most blade aero-damping loss due to the presence of a known incoming acoustic gust (i.e. the phase of gust relative to blade motion which corresponds to the trough of aero-damping curve in Figure 5.27). This is achieved by calculating the unsteady lift contribution, and consequently the corresponding aerodynamic work, induced by the incoming acoustic gust. The formulation of the method is described below.

As shown in the previous sections, the aero-damping of the blade vibration in such mode (1F, low IBPA) is dominated by the unsteady lift driven aerodynamic work on the plunge motion (i.e. w_{PP} and w_{TP}), while the contributions for the twist motion due to unsteady moment (i.e. w_{PT} and w_{TT}) are negligible. In the same sense, the blade aero-damping contribution due to incoming acoustic gusts is dominated by the aerodynamic work due to unsteady lift induced by the gust and the plunge motion of the blade. Therefore, for a blade vibrating in a flap mode characterised by Equation 5.12, the aerodynamic work component for the plunge motion due to the incoming acoustic gust alone w_{GP} can be evaluated as

$$w_{GP} = \int_T \oint p_G \boldsymbol{n} \cdot (1-\gamma) \boldsymbol{v}_P dS dt \tag{5.31}$$

where $p_G \boldsymbol{n}$ represent the local unsteady loading vector induced by the in-

coming gust alone, $(1-\gamma)\boldsymbol{v}_P$ is the blade velocity vector due to the plunge motion, and the subscript GP denotes the gust (G) as the source of loading and plunge (P) as the vibration motion. The corresponding aerodynamic damping can be calculated as

$$\zeta_{GP} = -\frac{1}{1-\gamma}\frac{1}{v_{0_P}^2}\int_T \oint p_G \boldsymbol{n} \cdot \boldsymbol{v}_P dS dt \tag{5.32}$$

The above equation clearly shows that the aero-damping contribution due to the incoming gust increases with the increase of γ, which explains the observation made in Figure 5.30 that the effect of the incoming gust becomes more pronounced for modes with higher twist component.

For a plunge motion, the local blade velocity vector $\boldsymbol{v}_P$ is the same at all the locations on the surfaces of the blade. Thus the aerodynamic work contributions for the plunge motion due to the unsteady lift induced by the plunge vibration (Equation 5.16), the twist vibration (Equation 5.18) and the acoustic gust (Equation 5.31) can be respectively written as

$$w_{PP} = (1-\gamma)\int_T l_P v_P dt \tag{5.33}$$

$$w_{TP} = (1-\gamma)\int_T l_T v_P dt \tag{5.34}$$

$$w_{GP} = (1-\gamma)\int_T l_G v_P dt \tag{5.35}$$

where

$$l_P = (1-\gamma)\oint p_P \boldsymbol{n} \cdot \boldsymbol{s} dS \tag{5.36}$$

$$l_T = \gamma \oint p_T \boldsymbol{n} \cdot \boldsymbol{s} dS \tag{5.37}$$

$$l_G = \oint p_G \boldsymbol{n} \cdot \boldsymbol{s} dS \tag{5.38}$$

where $\boldsymbol{s}$ is the unit vector normal to the mean flow, l_P is the unsteady lift induced by the plunge motion, l_T is the unsteady lift induced by the twist motion and l_G is the unsteady lift induced by the incoming gust.

Therefore, the aerodynamic damping of the blade can be evaluated using

$$\zeta_{PP} = -\frac{1}{1-\gamma}\frac{1}{v_{0_P}^2}\int_T l_P v_P dt \tag{5.39}$$

$$\zeta_{TP} = -\frac{1}{1-\gamma}\frac{1}{v_{0_P}^2}\int_T l_T v_P dt \tag{5.40}$$

$$\zeta_{GP} = -\frac{1}{1-\gamma}\frac{1}{v_{0_P}^2}\int_T l_G v_P dt \tag{5.41}$$

where ζ_{GP} is the blade aero-damping for the plunge motion due to gust-induced unsteady lift.

For a blade vibrating in the flap mode with the presence of incoming acoustic gusts (e.g. reflection from a blade row), the overall aero-damping of the blade can be approximated by

$$\zeta = \zeta_{PP} + \zeta_{TP} + \zeta_{GP} \tag{5.42}$$

where the aero-damping contributions due to unsteady moment ζ_{PT}, ζ_{TT} and ζ_{GT} are neglected.

The devised equations for blade aero-damping contribution due to the vibration motion and the incoming acoustic gust are un-coupled, and can be evaluated separately. The de-coupling of the aero-damping contributions shown in the above equations is driven by the fact that the unsteady lift contributions due to these sources are un-coupled as shown in Figure 5.26.

In practice, the evaluation of the unsteady lift on the surfaces of the blade (l_P, l_T and l_G) requires unsteady CFD computations with the corresponding sources (vibration or gust) imposed. In order to achieve the objective of this section, which is to find the condition for the largest loss on blade aero-damping due to the presence of a known incoming acoustic gust, an efficient way is sought to evaluate the aero-damping contribution due to the acoustic gust ζ_{GP}. A low-fidelity approach is presented here, where the unsteady lift induced by the incoming gust is calculated analytically without the need of unsteady CFD computations.

Consider a vibrating blade row with acoustic waves incident from the upstream and the downstream sides, the unsteady pressure field at the leading edge and the trailing edge (illustrated in Figure 5.31) can be evaluated as a complex sum of perturbations generated by blade vibration and the per-

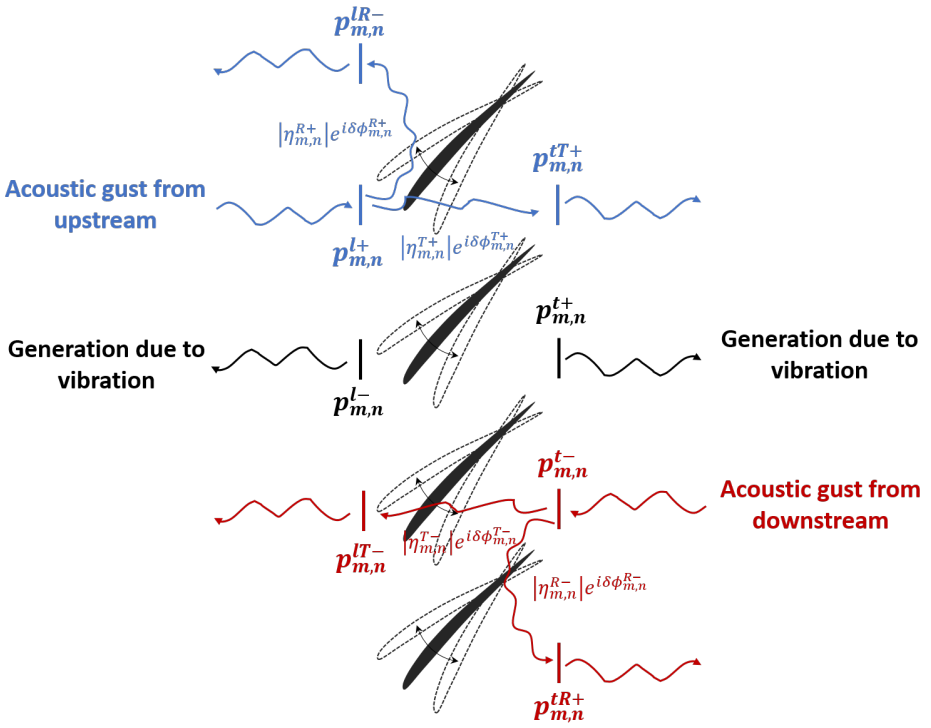


Figure 5.31: Unsteady pressure field near a vibrating blade row with incident acoustic gusts from upstream and downstream.

turbations induced by the incoming gusts:

$$p^l = p^{l-} + p^{l+} + p^{lT-} + p^{lR-} \tag{5.43}$$

$$p^t = p^{t+} + p^{t-} + p^{tT+} + p^{tR+} \tag{5.44}$$

where p^{l-} and p^{t+} represent the generated waves at the blade leading edge and trailing edge due to vibration, p^{l+} and p^{t-} represent the incoming acoustic gust incident at the leading and trailing edges of the blade, and p^{lT-}, p^{lR-}, p^{tT+} and p^{tR+} represent the transmission and reflection of the incoming gusts at the blade row (as illustrated in Figure 5.31). It should be noted that the complex unsteady pressure p in the above equations is a function of x, r, θ and t, which has the form of Equation 4.1.

Assume the blade row behaves like an 'actuator disk', in that the unsteady lift on the surfaces of the blades l, induced by the vibration motion and the incoming acoustic gust, can be approximated from the (complex) unsteady pressure rise across the blade row as

$$l = C(p^l - p^t) \tag{5.45}$$

where C is a real constant (i.e. without phase term). It should be clarified that the above equation represents a very basic approximation for the actual unsteady lift, and is not applicable to a blade row with 0°stagger. In order to examine the application of the above relationship, unsteady lift on the surfaces of the blade calculated using the above equation is compared with the results obtained from unsteady CFD solutions.

Figure 5.32 shows a comparison between the unsteady lift obtained from unsteady CFD solutions and calculated using Equation 5.45. In these plots the results for *Case V*, *Case G* and *Case VG* due to the plunge vibration of the 45°stagger blade at the reduced frequency of 0.84 are displayed. The value of the real constant C is initially adjusted for *Case V* so that the unsteady lift calculated using Equation 5.45 (blue line) is the same as that obtained from the unsteady CFD solutions (blue triangles), which is fixed for all the subsequent calculations for *Case G* and *Case VG*. The unsteady lift contributions due to the vibration motion alone (*Case V*) and the incoming

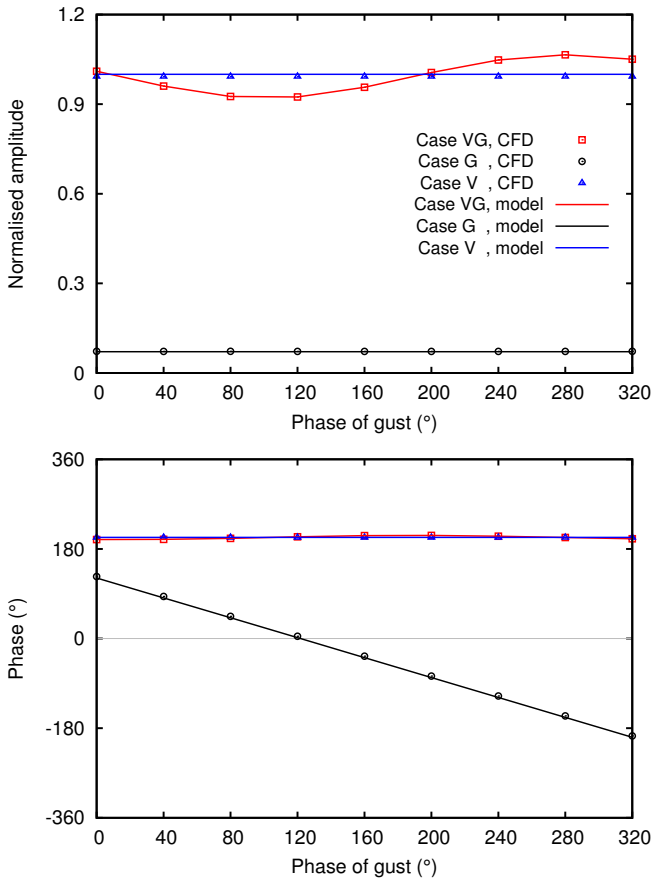


Figure 5.32: Modal force as a function of the phase of incoming gust, $\theta_s = 45°$, $f_r = 0.84$, plunge mode.

acoustic gust alone (*Case G*) are calculated using

$$l_{vib} = C(p^{l-} - p^{t+}) \tag{5.46}$$

$$l_{G-} = C(p^{lT-} - p^{t-} - p^{tR+}) \tag{5.47}$$

$$l_{G+} = C(p^{lR-} + p^{l+} - p^{tT+}) \tag{5.48}$$

where l_{vib} represents the unsteady lift induced by the vibration motion ($l_{vib} = l_P + l_T$), and l_{G-} and l_{G+} represent the contributions due to incident upstream propagating and downstream propagating acoustic gusts, where

$$l_G = l_{G-} + l_{G+} \tag{5.49}$$

For the case studied here $l_{G+} = 0$. Thus the contribution due to the incoming gust alone (*Case G*) is calculated from l_{G-} and the overall unsteady lift (*Case VG*) is calculated from $l = l_{vib} + l_{G-}$ where $l_{vib} = l_P$.

In the plots of Figure 5.32, the amplitude of unsteady lift is normalised by the amplitude of *Case V*, and the phase is relative to blade motion at zero displacement and the maximum positive velocity. The CFD results shown in these plots are identical to those shown in Figure 5.26. It is clearly seen in Figure 5.32 that the variation in amplitude and phase of the unsteady lift calculated using the above equations (solid lines) show good agreement with those obtained from unsteady CFD computations (symbols). It should be stressed again that the same constant C parameter is used for all the calculations shown in this plot (i.e. for all the solid lines). The observation confirms the assumption that the unsteady lift can be approximated by the unsteady pressure rise across the blade. Moreover, by studying Equation 5.45, it can be deducted that the real constant C has an effect only on the amplitude of the unsteady lift, whereas the phase of the unsteady lift is determined wholly by the unsteady pressure field near the blade which is not affected by the constant C. The rest of this section focuses on demonstrating that determining the most destabilising condition due to incoming acoustic gusts requires only the phase of the unsteady lift, which is independent of the value of C.

Figure 5.33 shows a comparison between the aerodynamic damping computed from unsteady CFD solutions and calculated using Equation 5.42. In this plot the blade aerodynamic damping for the plunge mode with (*Case*

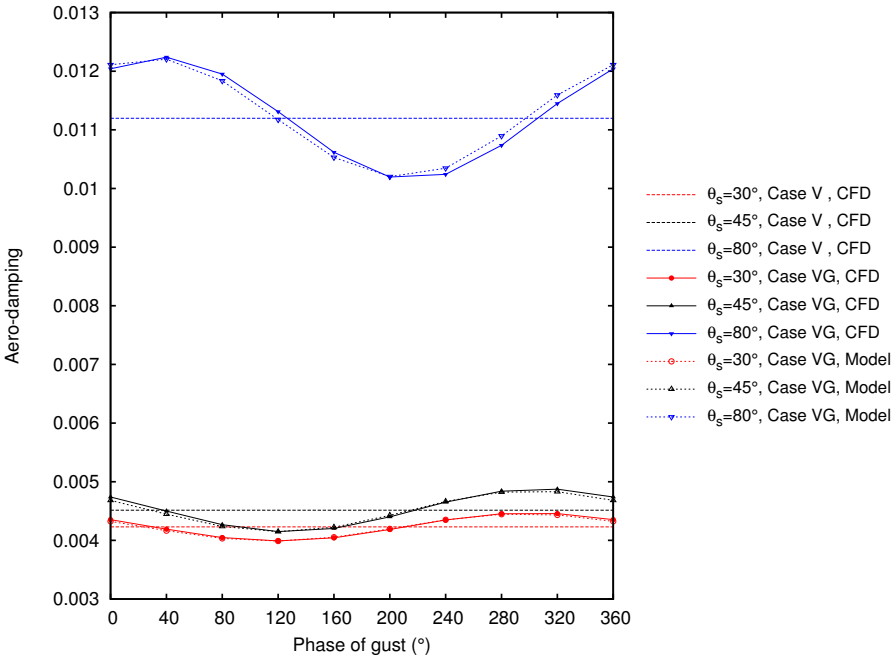


Figure 5.33: Comparison of predicted aerodynamic damping due to incoming acoustic gust from downstream, $f_r = 0.84$, plunge mode.

VG) and without (*Case V*) the presence of the incoming gust for stagger angle of 30°, 45°and 80°is displayed. It should be noted that the blade aero-damping for the isolated *Case V* is obtained from a computation in the absence of the gust which is obviously not a function of the gust phase, however the values are shown in this plot as dashed lines for reference. It can be seen from the plot that when an appropriate constant C (which fits the amplitude relation between the unsteady lift and the unsteady pressure rise for *Case V*) is used, the variation of blade aerodynamic damping for *Case VG* calculated using the devised method show good agreement with that obtained from unsteady CFD computations. The transition of aero-damping trend from *Case V* (constant-value dashed curves) to *Case VG* (sinusoidal varying dotted curves) is determined entirely based on the devised analytical method without the need of unsteady CFD computations for *Case VG*, where the constant C is obtained from *Case V*. Importantly, the most detrimental condition, i.e. phase of the incoming gust corresponding to the most aero-damping loss ('troughs' of curves), is calculated with good degree of accuracy. It will be shown in the following analysis that

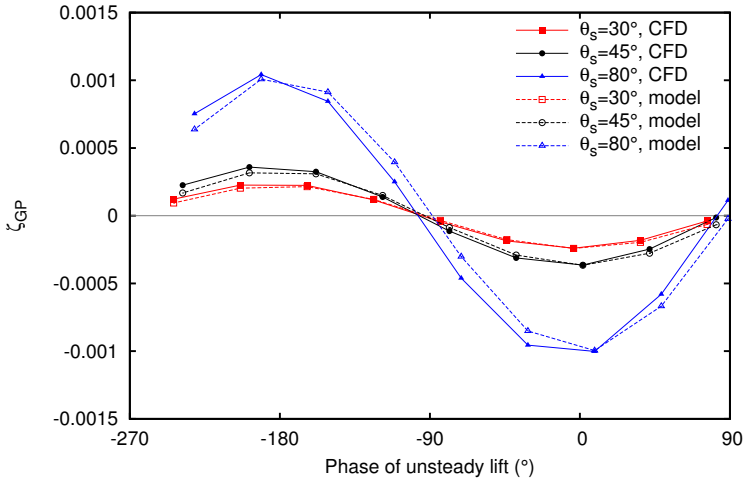


Figure 5.34: ζ_{GP} as a function of the phase of unsteady lift.

the value of C does not play a part in determining the phase of gust corresponding to the most destabilising condition. In order to further examine the effect of the incoming acoustic gust on blade aero-damping, the aero-damping contribution due to the gust alone ζ_{GP} is calculated for the cases shown in Figure 5.33 and is plotted in Figure 5.34.

Figure 5.34 shows the aero-damping contribution due to the incoming gust alone ζ_{GP} as a function of the phase of the unsteady lift induced by the incoming gust (i.e. phase of l_G). The aero-damping ζ_{GP} denoted as 'CFD' in this plot is calculated from the difference between the aero-damping obtained from unsteady CFD solutions for *Case VG* and *Case V* shown in Figure 5.33, and the aero-damping ζ_{GP} denoted as 'model' in this plot is calculated using Equation 5.41 and Equation 5.47. In this plot the phase of the unsteady lift is relative to the blade motion at zero displacement and the maximum positive velocity. It is clearly seen that the influence of the incoming gust changes the blade aero-damping sinusoidally about 0 when plotted against the phase of unsteady lift. The blade aerodynamic damping contribution ζ_{GP} calculated using the devised method shows good agreement with that computed from the aero-damping differences obtained from unsteady CFD computations. The most de-stabilising condition occurs when the unsteady lift contribution due to the incoming gust is in phase with the blade velocity, and the most stabilising condition occurs when the two quantities are out of phase. No effect can be identified for 90°phase dif-

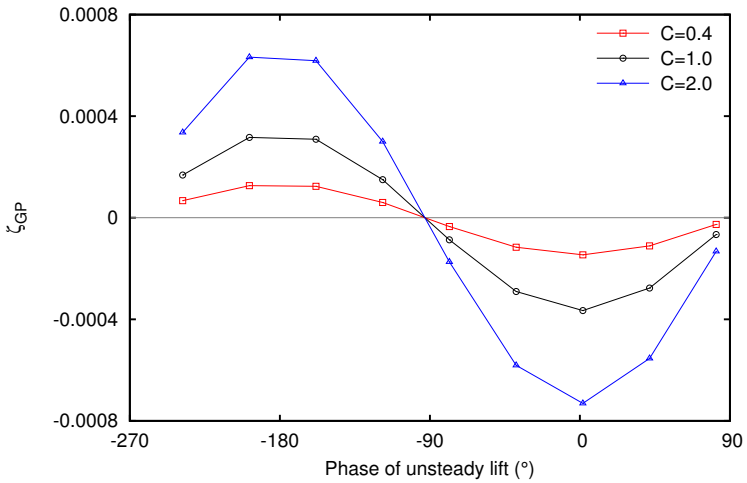


Figure 5.35: Effect of the constant C on ζ_{GP}.

ference. This observation becomes obvious by investigating Equation 5.35, where the aerodynamic work has the largest positive value when l_G and v_P are in phase (which results in the largest negative aero-damping).

In order to investigate the effect of the constant C on the calculated additional aero-damping due to the incoming gust, ζ_{GP} is calculated using Equation 5.41 and Equation 5.47 with different values for C. The obtained ζ_{GP} is plotted in Figure 5.35 as a function of the phase of unsteady lift for the 45°stagger case using three different values of C. The value of C shown in this plot is normalised by the value of C used for the 45°case shown in Figure 5.33, so that the curve for $C = 1.0$ in this plot represent the same curve as the dashed black curve in Figure 5.34. In this plot results for $C = 0.4$, $C = 1.0$ and $C = 2.0$ are displayed. It can be clearly seen from the plot that the value of C changes only the amplitude of ζ_{GP}, whereas the phasing relation between ζ_{GP} and the unsteady lift remains unchanged.

In conclusion, a low-fidelity analytical method for flutter analysis of a blade vibrating in the 1st flap mode with low inter-blade phase angles is presented in this section. Several conclusions can be made based on the findings

1. The aerodynamic damping for the twist motion (ζ_{PT} and ζ_{TT} driven by the unsteady moment generated by the plunge and twist vibrations respectively) is an order of magnitude lower than that for the plunge motion (ζ_{PP} and ζ_{TP} driven by the unsteady lift generated by the

plunge and twist vibrations respectively) for low inter-blade phase angle modes, which can be neglected in the flutter analysis for 1F modes.

2. The aerodynamic damping contribution due to the blade motion and the incoming acoustic gust are shown to be independent and can be analysed separately.

3. The evaluation of the damping contribution due to the incoming gust alone (ζ_{GP}) can be carried out by calculating the aerodynamic work due to the incoming acoustic waves analytically.

4. The effect of incoming acoustic gusts (e.g. reflection from blade rows) on flutter stability of the blade can be captured by the proposed low-fidelity method.

5. The unsteady lift on the surfaces of the blade can be approximated from the unsteady pressure rise from the leading edge to the trailing edge of the blade for low inter-blade phase angle modes. A (real) constant C is used to adjust the amplitude of the calculated unsteady lift, which is shown to have no effect on the condition for which the most aero-damping loss occurs due to the incoming gust.

6. The analysis confirms the relationship between the phase of the unsteady lift induced by the incoming acoustic gust and the phase of blade velocity for the plunge motion, where the most destabilising condition occurs when the two quantities are in phase, and the most stabilising condition occurs when they are out of phase.

This chapter is intended to bridge the gap between the analytical methods presented in the previous chapter, which were devised with the simplifications of two dimensional cascade theories, and the realistic three-dimensional blading with non-uniform flow profile and more complex geometries (which will be presented in the following chapters). Moreover, the analysis provides a good benchmark for the upcoming chapters based on which the effect of three-dimensional flow on the accuracy of the analytical calculations can be investigated. It was also demonstrated in this chapter that, in the absence of complicated aerodynamics, it is possible to make

a blade flutter through the combined effects of modeshape and acoustic reflections.

Based on the knowledge gained in this chapter, the analysis is continued, to look at the effects of incoming acoustic gusts on the flutter stability of a fan blade (due to acoustic reflections from the intake) and an embedded rotor blade (due to acoustic reflections from adjacent blade rows).

6 Acoustic Driven Fan Flutter Bite

The main findings of this chapter have been reported in [10, 110].

6.1 Overview and Problem Description

This chapter describes the work on the aeroelastic instability of fan blades, commonly called stall flutter, which occurs at part speed operating conditions near the stall boundary. Although it is called stall flutter, this type of event does not require the stalling of the fan blade and can occur when the slope of the characteristic is still negative. This phenomenon has been illustrated in Figure 1.3. In such cases the stability boundary of the blade is defined by the minimum of the stall and flutter boundary. For specific narrow speed range, flutter is seen to remove a 'bite' from the lines marking the limit of stable operating condition of the blade on a pressure ratio versus mass flow rate plot, hence the term 'flutter bite'. This type of flutter typically occurs in low nodal diameter (ND) forward traveling modes (2ND-4 ND, which corresponds to an inter-blade phase angle between 30°and 75°) for the first flapwise bending (1F) mode.

It was shown in [12] that the two independent mechanisms cause fan blade flutter:

1. Flow and mode shape driven: caused by the the interactions between the unsteady pressure generated by blade vibration and the mode-shape.

2. Acoustic reflection driven: caused by the reflection of acoustic waves generated by blade vibration.

It was shown in [11] that the key aerodynamic driver for the flow and modeshape driven flutter is the shock induced boundary layer separation

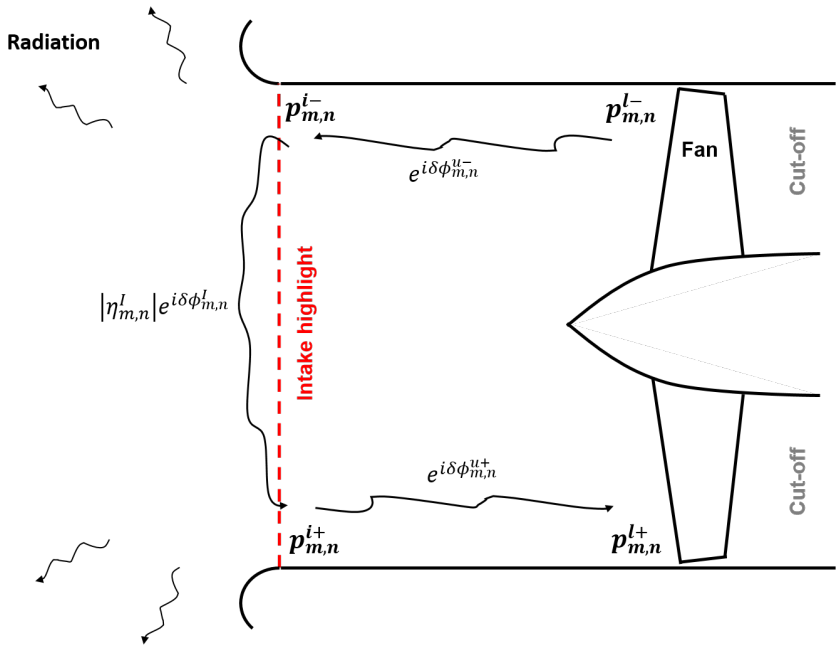


Figure 6.1: Illustration of acoustic reflections from the intake.

(thickening). For the fan studied, flow separation caused a radial migration of the flow toward the tip, which triggered the loss of aerodynamic damping in that region. It was also shown that the amount of twist in the 1F mode is a key mechanical parameter, where an increase in the amount of twist in the mode would result in a loss of flutter stability. The dependence of flutter on the modeshape was also demonstrated in Chapter 5 for the simple test case. Moreover, it was shown that as a pre-condition for flutter, the acoustic disturbances produced by the blade vibration must be cut-on on the upstream side and cut-off on the downstream side, hence the blade can only flutter in a certain frequency range at each fan speed.

The acoustic reflection driven flutter requires the upstream field of the fan to be cut-on, so that acoustic perturbations generated by the vibration of blades can propagate in the intake and be reflected at the duct opening. The mechanism of this type of flutter is illustrated in Figure 6.1. It will be shown that flutter of fan blades due to acoustic reflections can be related to the phase difference between the reflected acoustic wave and the the outgoing acoustic wave (generated by blade vibration). Moreover, it was shown in [11] that the acoustic driven flutter may occur on its own in the

absence of flow separation since the driving mechanism of acoustic reflection is independent of flow on the blade surfaces. However, it is unlikely to be a problem on its own when the aero-damping contribution due to the blade motion (i.e. damping due to flow and modeshape) is high. The worst case, i.e. the sharpest drop in the flutter bite region, occurs when the flow and modeshape driven flutter and acoustic reflection driven flutter coincide at the same fan speed. In such situations it is sufficient to consider only the acoustic reflection from the intake, since the flow and modeshape driven flutter requires the downstream field to be cut-off. The work presented in this chapter concentrates on the flutter of fan blades operating in such conditions.

The first objective of this chapter is to explain how the interaction between the flow, the blade vibration and the reflected acoustic wave results in fan blade flutter. This is achieved by studying the relationship between the amplitude and phase of the reflected wave and its influence on blade aerodynamic damping using unsteady CFD computations. The effects of key parameters, such as vibration frequency and intake length, on the amplitude and phase of the reflected wave (and hence blade flutter stability) are investigated.

In order to achieve this objective, studies on the flutter bite of fan blades are carried out in three steps:

1. Computations with 'acoustic bump'.
2. Computations with annular cylindrical intakes.
3. Computations with real intakes.

These studies will be presented sequentially in the following sections of this chapter. The complexity of problem is gradually increased in this three-step analysis, based on which the relationship between the reflected acoustic wave and the flutter bite of fan blades can be studied in a comprehensive fashion. It will be shown that the computations with an 'acoustic bump' feature upstream of the fan (which reflects acoustic waves) allow the study of the phasing relation between the reflected acoustic wave and the aero-damping of the fan. The computations with annular cylindrical intakes, which are simplified geometries of real intakes, further allow the study of the effect of the amplitude of reflection from intake opening. Finally, the findings

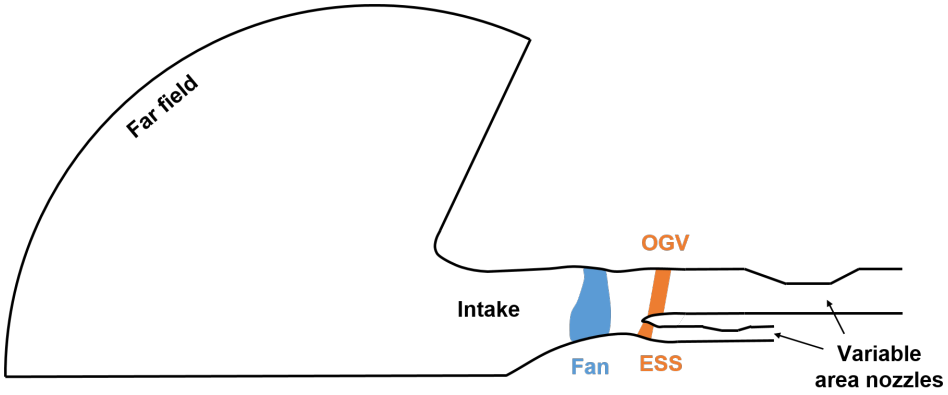


Figure 6.2: Domain used for steady state computation.

obtained from the studies based on simplified geometries are verified in real applications by performing flutter analyses for the fan blade with real intake geometries.

Accurate prediction of flutter stability of such a fan would require whole annulus unsteady computations of the fan and intake at various operating conditions and speeds (to find the region of flutter bite), which poses very high demands on both computational time and power, and cannot be used routinely in the early design stages. Therefore, in the next step, a new low-fidelity model that can predict the effect of acoustic reflections from the intake on flutter of fan blades is presented. The assessment of the intake design requires only the working line of the fan (inlet axial Mach number as a function of shaft speed), the blade vibration frequency and the geometry of the intake, which are available in the early design stages of new engines. Using this method, operating speeds at which the fan is prone to flutter bite can be easily identified. The proposed model will be validated against results obtained from unsteady CFD flutter computations, and applied to test cases with a real intake geometry to predict the flutter bite speed.

6.2 Test Case and Computation Model

A rig wide-chord fan blade, typical of low-speed modern civil designs, is used as the benchmark geometry for this study. The domain used for the steady state computations is shown in Figure 6.2. It includes the complete fan assembly with outlet guide vanes (OGV), engine section stators (ESS)

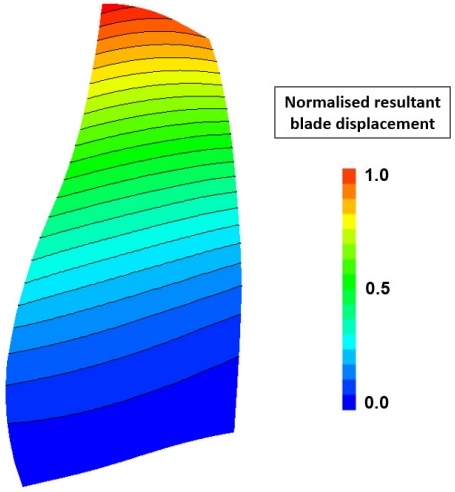


Figure 6.3: Modeshape for the 1F mode.

and a symmetric intake upstream of the fan. The fan used in this study has 20 blades and a hub-tip ratio of about 0.3 at the leading edge.

The grids used for the blading are semi-structured, with hexahedral elements around the aerofoil in the boundary layer region, and prismatic elements in the passage [94]. The end-wall boundary layers are resolved by refining the grid radially towards the hub and casing. A typical passage mesh contains approximately 350,000 grid points with 40 mesh layers on the blade and 5 layers in the tip gap. In order to accurately resolve the propagation of acoustic waves, approximately 120 grid points are axially aligned for the shortest axial wavelength.

In the steady computations, the interface boundaries between the stationary intake domain and the rotating fan domain are modelled as mixing planes, whereas in the unsteady computations they are treated as sliding planes. The boundary conditions for the far field boundaries are set to atmospheric conditions. The flow through the fan is controlled by placing two choked variable-area nozzles downstream of the fan (see Figure 6.2). The nozzle downstream of the ESS controls the bypass/core flow ratio and is fixed at each speed. Constant speed characteristics are obtained by adjusting the area of the exit nozzle downstream of the OGV. The operating conditions considered correspond to sea level static and zero cross wind.

In all the flutter computations presented in this paper, the blades are

excited in the first flapwise bending (1F) mode with a reduced frequency of 0.54. The 1F modeshape is shown in Figure 6.3 in terms of blade displacement amplitude. All the flutter computations in this work are performed using a whole assembly approach, where the 1st flutter computation strategy is used to find the least stable nodal diameter and the 2nd flutter computation strategy is used to study the the intake acoustics for the nodal diameter of interest (Section 3.4). The physical time step for flutter computations is resolved as 200 time steps for one complete cycle of the acoustic mode of concern in the stationary frame of reference. This time step was obtained by performing a temporal convergence study.

For the studies in this chapter, the rotational speed of the fan Ω is made non-dimensional using the blade tip Mach number $\bar{\Omega} = \Omega r_t / a_0$, where Ω is the shaft speed, r_t is the fan tip radius, and a_0 is the speed of sound at the local stagnation condition of the inlet flow. The mass flow through the fan is appropriately expressed in terms of a non-dimensional mass flow $\bar{m} = \dot{m}\frac{\sqrt{c_p T_0}}{A_d p_0}$, where p_0 and T_0 are stagnation pressure and temperature into the fan, and A_d is the duct cross-section area. For the present work what matters is the ratio of $\bar{m}$ to the value on the working line, $\bar{m}_{wl}$. The ratio of non-dimensional mass flows is therefore expressed here by $m_{ref} = \frac{\bar{m}}{\bar{m}_{wl}}$ and varying m_{ref} is equivalent to varying the exit nozzle area. In this work the mass flow is made non-dimensional by the value of $\bar{m}_{wl}$ at $\bar{\Omega} = 0.89$ (which experienced flutter bite in the experimental test).

6.3 Steady State Validation

The constant speed characteristic of the fan blade at the speed which flutter bite was measured ($\bar{\Omega} = 0.89$) is obtained through steady state computations of the single passage (Figure 6.2) by varying the area of the exit nozzle downstream of the OGV. The steady state results shown here are reproduced from [11]. The main aim of this section is

1. To demonstrate the accuracy of the CFD model on predicting flow at off-design conditions.

2. To show the main aerodynamic drive that can cause flutter of fan blades, which is very important for the completeness of this work.

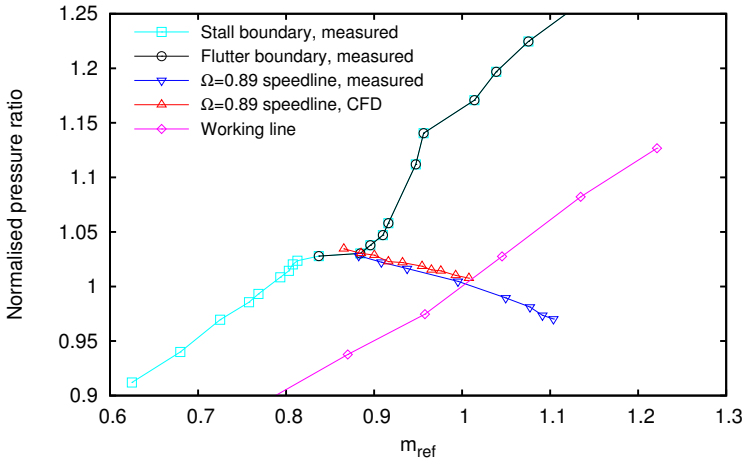


Figure 6.4: Performance of the fan.

Figure 6.4 shows the comparison between the calculated and measured pressure ratio of the fan blade (inlet to fan exit) as a function of m_{ref} over the speed range of $\bar{\Omega} = 0.65$ to $\bar{\Omega} = 1.1$. The pressure ratio is normalised by the pressure ratio at the working line operating condition for the speed of $\bar{\Omega} = 0.65$ computed using CFD. In this plot the measured and computed speedline for the speed of $\bar{\Omega} = 0.89$, the normal operation working line and the measured stability boundaries (stall and flutter) are displayed. For the fan speed in this study ($\bar{\Omega} = 0.89$), the stall boundary is preceded by the flutter boundary, i.e. flutter event was recorded on the fan blade prior to stall during the test. Thus a shorter characteristic can be seen for the measured $\bar{\Omega} = 0.89$ speedline than that computed using steady state CFD analysis. It can be seen from the plot that the fan performance is predicted with reasonable accuracy.

Figure 6.5 shows the radial profile of total pressure ratio (leading edge to trailing edge) for operating points $m_{ref} = 0.93$ (near stall) and $m_{ref} = 0.97$ (working line) on the $\bar{\Omega} = 0.89$ speedline. It can be seen from the plot that the measured and computed total pressure ratio are in good agreement, which confirms the capability of the CFD code used in this work in predicting the mean flow.

Figure 6.6 shows the isentropic relative Mach number contour on the suction surface of the blade for operating points $m_{ref} = 0.93$ and $m_{ref} = 0.97$ on the $\bar{\Omega} = 0.89$ speedline. The blade surface streamlines are also

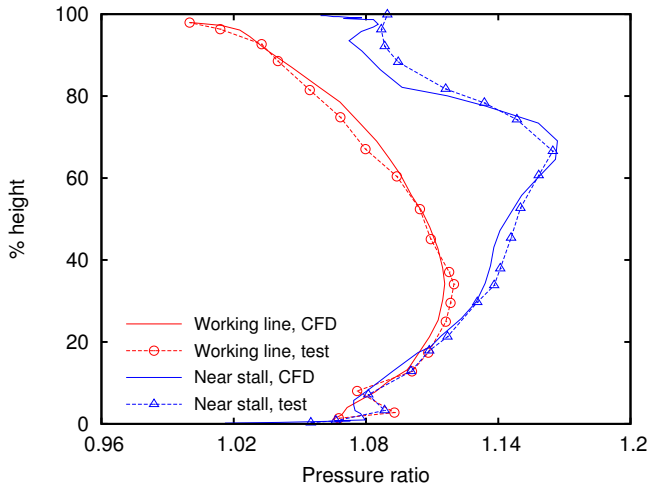


Figure 6.5: Radial profile of total pressure ratio. [11]

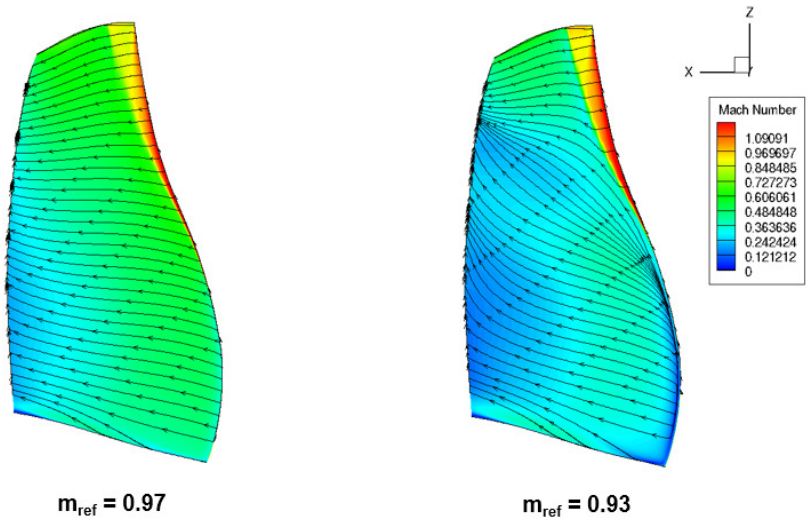


Figure 6.6: Isentropic relative Mach number contour and streamline. [11]

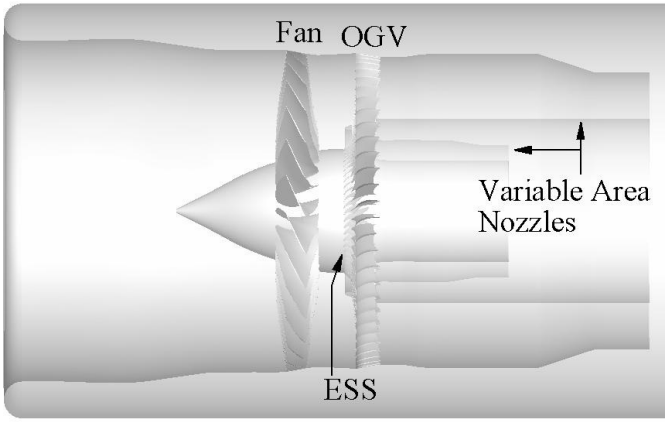


Figure 6.7: Domain used for unsteady computation.

shown in this plot overlayed on the Mach number contour. At this speed, the relative inlet Mach number is sonic at the tip and subsonic at lower spans (apart from the suction peak due to flow acceleration around the leading edge). At the operating point $m_{ref} = 0.97$, the flow on the blade is attached and the streamlines follow blade stream sections. At the condition closer to stall ($m_{ref} = 0.93$), separated flow driven by shock induced separation near the leading edge is seen to migrate radially outwards at about 70% span. This flow feature has been demonstrated as the key factor in the flow-modeshape driven flutter of fan blades [11]. The importance of this phenomenon on flutter will be shown in the following section.

6.4 Flutter Bite Computations

Prior to in-depth analysis of the effect of acoustic reflection on flutter stability of the fan blade, the flutter bite of the fan obtained from unsteady CFD computations is compared with that measured in the test. The flutter computations are performed for the whole domain shown in Figure 6.7 using the 1st flutter computation strategy (Section 3.4).

Figure 6.8 shows the comparison between the calculated and measured stability boundaries for both flutter and stall over the speed range of $\bar{\Omega} = 0.65$ to $\bar{\Omega} = 1.1$. In this plot the measured and CFD stability boundaries are represented by the black and red lines respectively. The CFD boundary is obtained by taking the minimum damping from 2ND, 3ND and 4ND

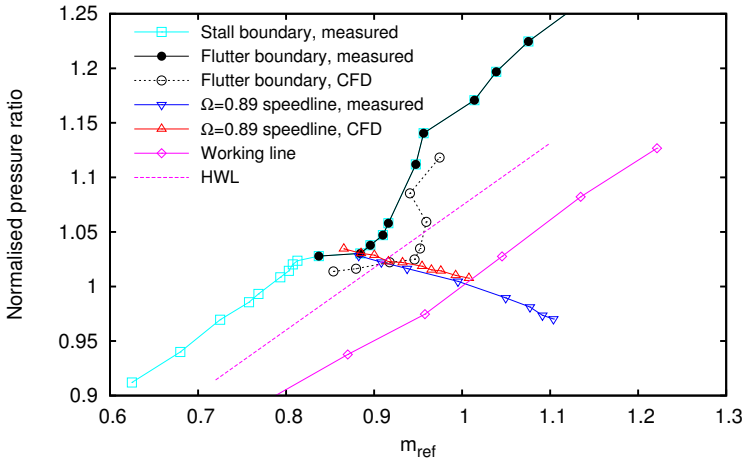


Figure 6.8: Comparison between predicted flutter bite and measured flutter bite.

modes. However, both CFD and measured data indicate a 3ND flutter around the flutter bite (at the speed of $\bar{\Omega} = 0.89$). The calculation, based on the known frequency and mode of vibration [11], shows instability due to flutter at somewhat higher mass flow rate than those measured. The higher computed mass flow for instability is attributed to the presence of some mechanical damping and mistuning in the real fan [3] which is wholly omitted in the present calculations. The trend is well predicted, notably the flutter bite around the sonic speedline of $\bar{\Omega} = 0.89$. The phenomenon of flutter bite is clearly shown in this plot where a substantial drop of stability margin for the fan blade is identified. The dotted purple line (denoted by *HWL*) in Figure 6.8 represents a high working line which cuts through the flutter bite, and is used for understanding the effects of fan speed on flutter in the following analyses.

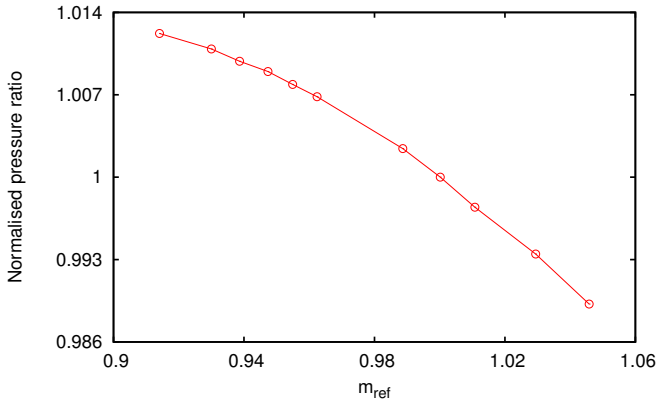
It is clearly show in Figure 6.8 that the CFD code used in this study is capable of predicting the flutter bite with reasonable degree of accuracy. In order to study the physics behind the flutter bite observed in Figure 6.8, flutter computations are carried out for the fan blade with simple intake geometries. To achieve this, the fan blade is separated from the whole assembly (i.e. by removing the intake, ESS and OGV shown in Figure 6.7). At the exit, boundary conditions obtained from the steady state computations are prescribed.

6.4.1 Effect of mass flow rate

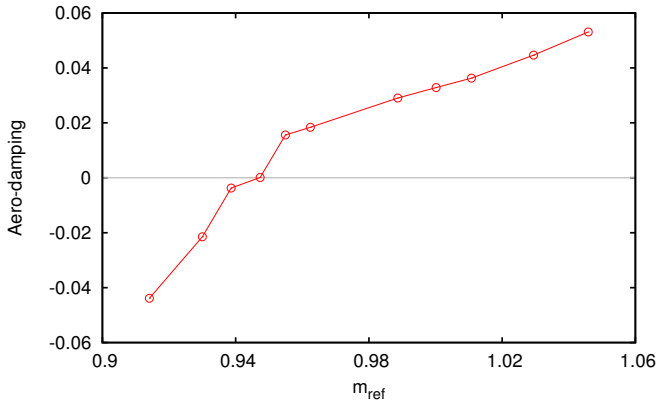
Prior to flutter computations with various intake geometries, the effect of mass flow rate is studied. The results of this section are reproduced from [11] and is shown to demonstrate the effect of aerodynamics on fan flutter, which is essential for the understanding and completeness of this chapter. In this setup, steady state computations are performed by attaching a long straight duct upstream of the fan, which is throttled on its own based on the obtained steady state solutions. Based on the domain and the steady state solutions obtained, flutter computations are performed for the 1F/2ND mode at a reduced frequency of 0.54 for all the operating points on the constant speed characteristic $\bar{\Omega} = 0.89$. The computations are performed for the isolated blade setup in the long straight duct using the single passage (3^{rd} flutter computation strategy).

Figure 6.9 shows the calculated pressure ratio and aero-damping of the fan (in a long straight duct without the intake, ESS and OGV) as a function of m_{ref} at the non-dimensional speed of $\bar{\Omega} = 0.89$. The pressure ratio in this plot is normalised by the pressure ratio at $m_{ref} = 1.0$. It can be seen from the plot that the blade aero-damping decreases as mass flow rate is reduced. The blade aero-damping becomes negligible at about $m_{ref} = 0.95$, which was shown in [11] to be the result of the migration of flow radially outwards on the suction surfaces of the blade (also see Figure 6.6).

Figure 6.10 shows the calculated aero-damping of the blade as a function of span. It is seen that for high mass flow rates $m_{ref} > 0.98$ the fan blade is positively damped at all span sections. As the mass flow rate is reduced, negative aero-damping is seen at blade sections above 80% span. The magnitude of the negative aero-damping patch increases with further reduction in mass flow rate, which results in a zero blade damping at $m_{ref} = 0.95$ and negative damping at $m_{ref} < 0.95$. This phenomenon was studied in detail by Vahdati and Cumpsty [11] and it was found that the observed negative aero-damping in the tip region of the blade is driven by the separated flow migrating radially outboard as shown in Figure 6.6. This flow feature was concluded as a key aerodynamic factor for the flow-modeshape driven flutter of the fan blades, which is responsible for flutter of fan operating near the stall boundary. However, this phenomenon is not the focus of this thesis as the aim is to understand and predict flutter of fan blades due to acoustic



(a)



(b)

Figure 6.9: (a) Characteristic of the fan blade (isolated setup) at $\bar{\Omega} = 0.89$; (b) aero-damping as a function of mass flow rate.

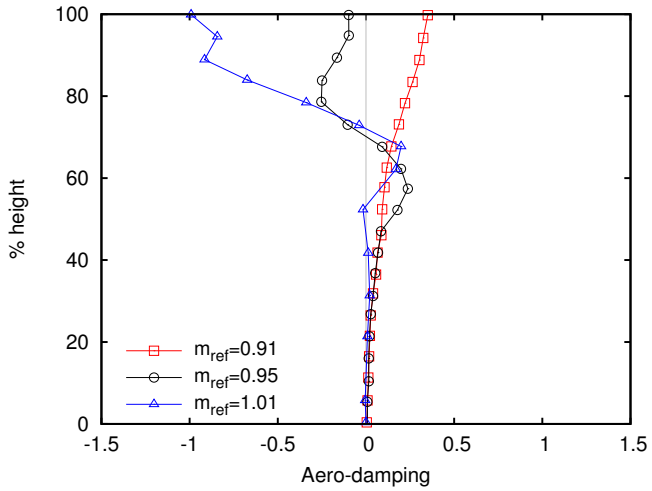


Figure 6.10: Spanwise distribution of blade aero-damping. [11]

reflections. In other words, is it possible to make an aerodynamically stable blade (such as $m_{ref} = 0.98$) unstable by means of acoustic reflections (from the intake), i.e. can aeroacoustics overpower aerodynamics in terms of the effect on blade flutter stability? This is achieved by performing flutter computations with an 'acoustic bump' feature first.

6.4.2 Computations With 'Acoustic Bump'

In the first part of this work, the phase relation between the reflected acoustic wave and the acoustic reflection driven flutter is investigated by means of an 'acoustic bump' feature upstream of the fan as illustrated in Figure 6.11. It was shown in [12] that by modelling an intake as a uniform cylinder plus a 'bump', it is possible to change the aerodynamic damping of the blade by changing the location of the bump. The change of blade aerodynamic damping is caused by the change of the phase of the reflected wave. However, the work did not establish any relationship between blade aerodynamic damping and the phase of the reflected acoustic wave. In order to devise a simple prediction model and establish some design rules, it is essential to determine the phase relation between the blade aero-damping and the reflected acoustic wave. To achieve this goal, flutter computations are performed by varying the location of the bump relative to the fan.

Flutter analyses are conducted for the 1F/2ND mode at a reduced fre-

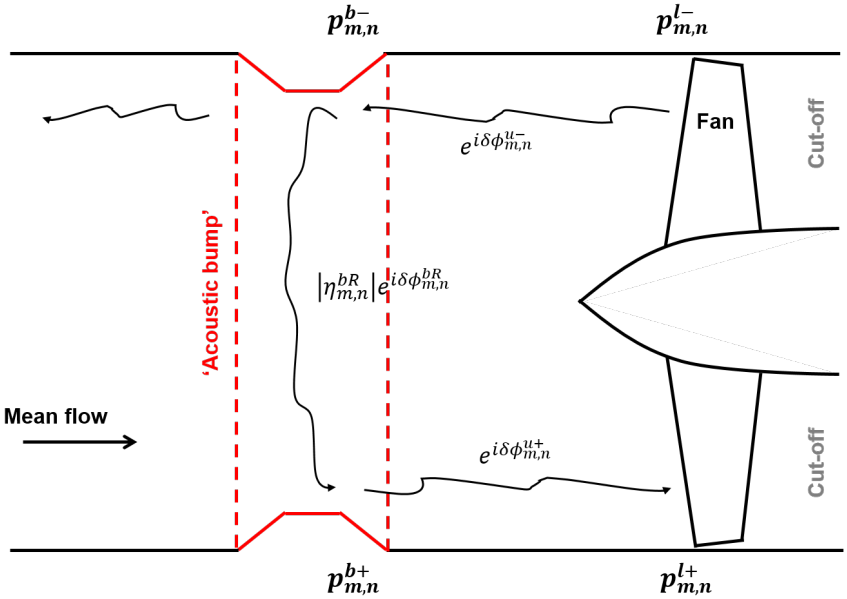


Figure 6.11: Domain used for flutter computation with 'bump' feature.

quency of 0.54 for the three operating points $m_{ref} = 0.93$, $m_{ref} = 0.95$ and $m_{ref} = 0.99$ on the constant speed characteristic $\bar{\Omega} = 0.89$ (see Figure 6.8). For the cases studied here, the inlet axial Mach number in the intake is around 0.4. In each computation series the fan operates at a fixed operating point while the location of the bump is varied with respect to the fan.

Figure 6.12 shows the computed aerodynamic damping of the fan as a function of non-dimensional distance from the fan face for the three operating points considered. The non-dimensional distance $\frac{L}{\lambda^-}$ denotes the ratio between the distance from the bump to fan leading edge and the wavelength of the upstream propagating acoustic wave. The calculated blade aerodynamic damping in a long straight duct in the absence of bump (shown in the previous section) is shown in Figure 6.12 as straight dashed line (since it is obviously independent of the bump location). It can be seen from this plot that the aerodynamic damping of the fan with bump feature is a function of bump location, and varies in a sinusoidal fashion around the aero-damping due to blade motion. The aerodynamic damping is seen to repeat itself with a period of approximately one wavelength of the upstream propagating acoustic wave, indicating that acoustic wave in the duct between the bump

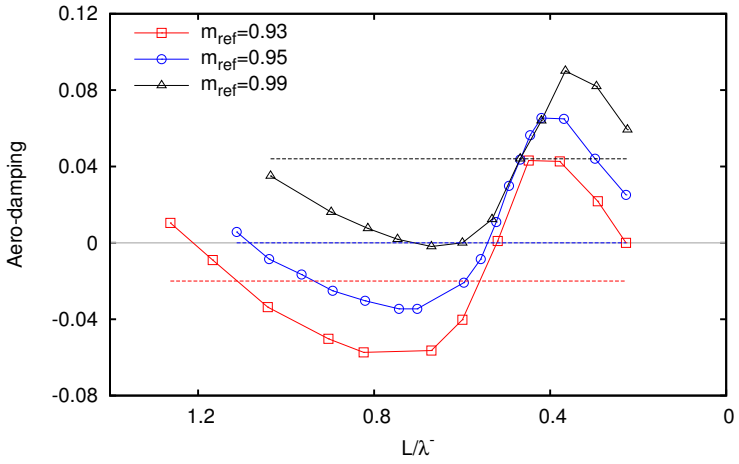


Figure 6.12: Aerodynamic damping as a function of bump location.

and fan is a key parameter for the flutter stability of the fan-bump system. It is seen from the plot that a stable operating point (e.g. $m_{ref} = 0.95$) can become unstable due to inappropriate bump placement (e.g. $\frac{L}{\lambda^-} = 0.7$), which clearly illustrates how flutter bite can occur for a fan-intake system. Conversely, beneficial effects can be seen for certain bump locations where the presence of the bump provides additional positive damping to the blade. An example can be seen where the unstable operating point $m_{ref} = 0.93$ becomes stable when the bump is placed at $\frac{L}{\lambda^-} = 0.4$. It will be shown in a later section that for a real intake such situations can occur and the intake can provide additional aerodynamic damping at some speeds. Moreover, for operating points where the aero-damping due to blade motion is high (e.g. $m_{ref} = 0.99$), the change of blade aerodynamic damping due to the presence of bump does not result in negative aerodynamic damping. This confirms the statement (in the introduction of this chapter) that the acoustic driven flutter is unlikely to be a problem on its own when the aero-damping contribution due to the blade motion is high.

In order to investigate the relationship between bump location and the propagating acoustic waves, a wave-splitting procedure is performed to split the unsteady perturbations in the duct into propagating waves, based on which a relationship between the (reflected) acoustic waves and fan flutter stability can be established. Figure 6.13 shows the instantaneous unsteady pressure contour on the casing surface upstream of the fan. In this plot the

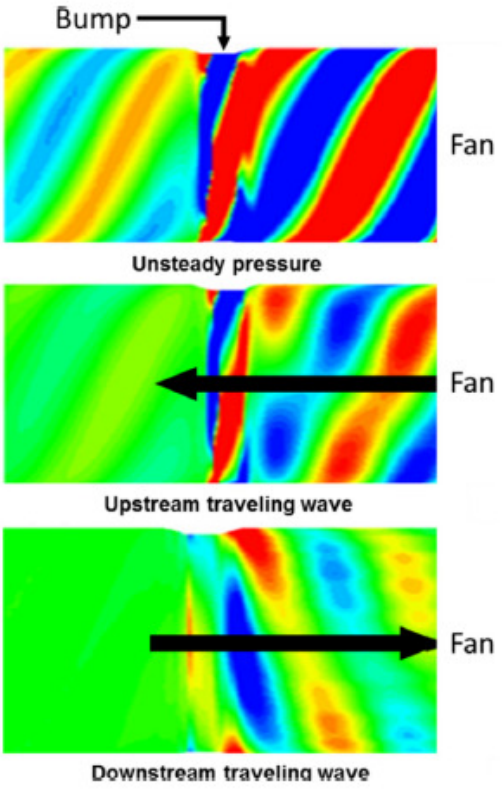


Figure 6.13: Instantaneous unsteady pressure contour on the casing surface: (a) unsteady pressure (complete signal); (b) upstream propagating acoustic pressure; (c) downstream propagating acoustic pressure.

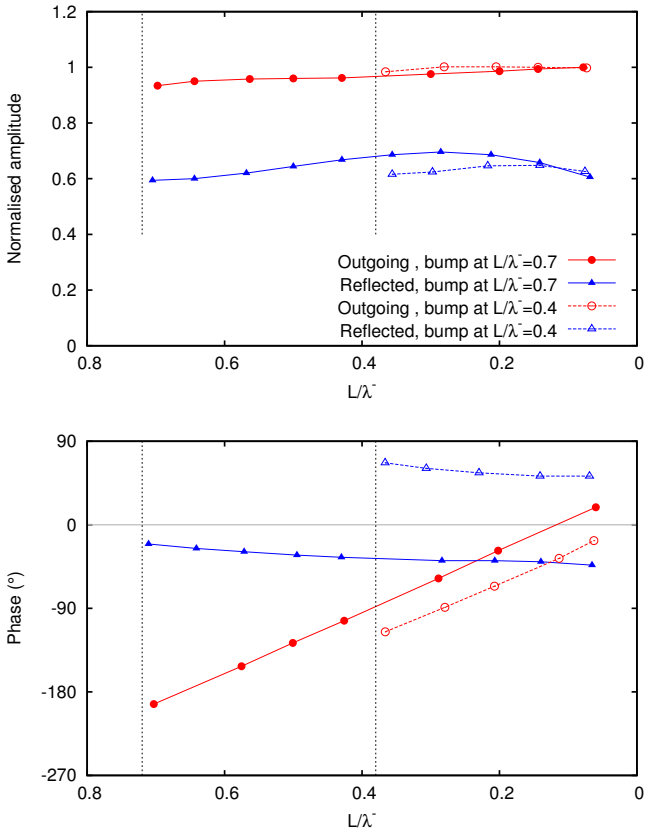


Figure 6.14: Axial variation of amplitude and phase of acoustic waves, $m_{ref} = 0.93$ (bump locations $\frac{L}{\lambda^-} = 0.4$ and $\frac{L}{\lambda^-} = 0.7$ are illustrated by dashed black lines).

upstream propagating and the downstream propagating components, which are obtained through post-processing of the unsteady pressure, are also displayed. It is clearly seen that as the outgoing acoustic wave impinges on the bump, part of it is transmitted and part of it is reflected. Figure 6.14 shows the amplitude and phase of unsteady pressure of the propagating acoustic waves as a function of axial location for the operating point $m_{ref} = 0.93$. The amplitude of unsteady pressure is normalised by the amplitude of upstream propagating acoustic wave at the fan leading edge, and the phase is relative to the phase of unsteady pressure at the fan face. In this plot a stable bump placement $\frac{L}{\lambda^-} = 0.4$ and an unstable bump placement $\frac{L}{\lambda^-} = 0.7$ are displayed. The leading edge of the fan is situated at about $\frac{L}{\lambda^-} = 0.05$. It can be seen from these plots that the vibration of blades generates acoustic waves which propagate with a constant phase speed and a nearly constant amplitude between the fan and the bump. Acoustic waves are reflected by the bump, due to sudden change of duct area, with a significant amplitude ratio and approximately 180°phase change. For the flow condition and bump geometry studied here the amplitude of reflection coefficient is about 0.65. The wavelength and phase velocity of the outgoing and reflected waves can be inferred from the slope of phase against axial distance in the phase plot. It is seen from the phase plot that the waves propagate with a (nearly) constant axial phase velocity towards (and reflected back from) the intake highlight. The effective axial phase speed (corresponding to the axial wavenumber) of the downstream propagating wave (blue curves) is much higher (with a Mach number of ˜3.8), due to a much smaller axial wavenumber, than that in the upstream direction (red curves) (Mach number of ˜0.37). Hence a lower gradient can be seen for the phase curve of the downstream travelling wave.

Figure 6.15 shows the phase difference between the outward propagating and backward propagating acoustic waves at the leading edge of the fan as a function of non-dimensional bump location. The results for operating points $m_{ref} = 0.93$ and $m_{ref} = 0.99$ are shown here. It is seen from this plot that the relationship between the phase difference and the bump location shows a linear trend. Moreover, it is seen that by non-dimensionalising the distance by the wavelength of the upstream propagating acoustic wave, the phase difference for the two flows becomes the same. This is quite obvious since the axial phase change of acoustic waves is proportional to the wavenumber

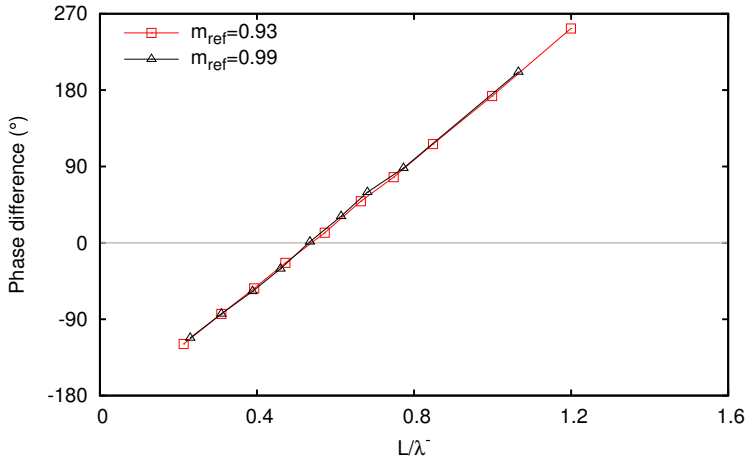


Figure 6.15: Phase difference between the outgoing and reflected acoustic waves as a function of bump location.

as shown in Equation 4.24 and 4.25.

Based on the the phase difference relation shown in Figure 6.15, the aerodynamic damping of the blade, which has been shown in Figure 6.12, can be plotted against the phase difference between the outgoing acoustic wave and the reflected acoustic wave at the blade leading edge. Figure 6.16 shows the addition aerodynamic damping due to acoustic reflection from the bump as a function of this phase difference for two operating conditions of $m_{ref} = 0.93$ and $m_{ref} = 0.99$. The 'additional aerodynamic damping' is defined as the difference in blade aero-damping with and without the presence of the acoustic reflection, and represents the additional [1] effect of acoustic reflection on flutter stability of the blade. In other words, the additional aero-damping is calculated as the change from blade aero-damping in a long straight duct (dashed lines in Figure 6.12) to blade aero-damping with the presence of the bump (solid lines in Figure 6.12). The term 'additional aero-damping' will be used repeatedly throughout this work, and thus will be referred to without the quotation marks for clarity. It is seen from the plot that, despite the difference in flow between the two operating conditions, the additional aero-damping due to acoustic reflection from the bump is very similar when plotted against the phase difference between the reflected and outgoing acoustic waves. Hence it can be concluded that the

[1]The expression 'additional' can mean increase or decrease in the context of this thesis.

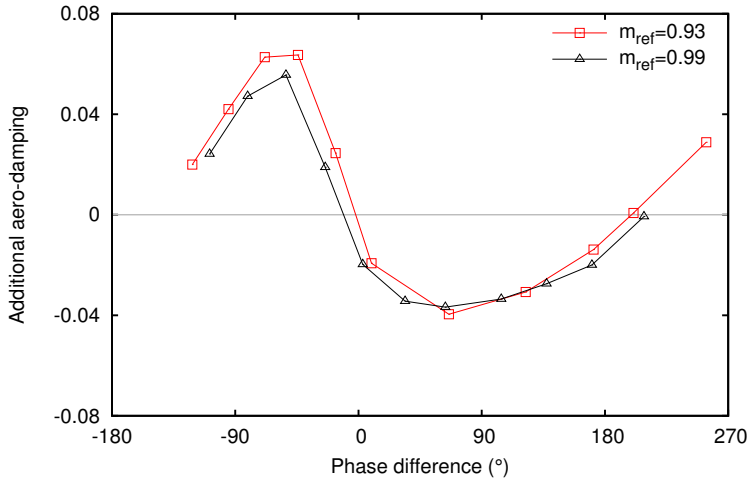


Figure 6.16: Additional aero-damping as a function of phase difference between the outgoing and reflected acoustic waves.

additional aero-damping due to acoustic reflection from the bump (acoustic reflection driven) can be evaluated independently from the aero-damping due to blade motion (flow and modeshape driven). This finding is in agreement with the observations and conclusions for the analysis conducted in Chapter 5, where the aero-damping contribution due to the unsteady loading induced by the blade motion and the unsteady loading induced by the incoming acoustic waves can be evaluated separately (which is also demonstrated by the derivation of Equation 5.42). Another very important observation can be made in Figure 6.15. The bump location which has the most beneficial effects to fan flutter stability corresponds to approximately $-90°$, and the location with most detrimental effects corresponds to approximately $90°$. For a phase difference of $0°$ the effects of the bump on blade aero-damping is almost zero.

The above analysis with the 'acoustic bump' clearly demonstrates how flutter bite can occur for a fan blade with the intake. Three main conclusions can be made from this analysis:

1. The contribution to aerodynamic damping due to the blade motion (flow and modeshape driven) and acoustic reflection from the intake (acoustic reflection driven) are independent and can be analysed separately.

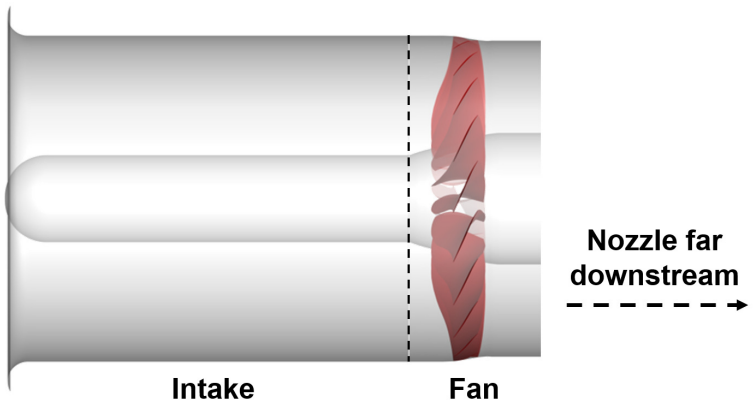


Figure 6.17: Domain used for flutter computation with annular cylindrical intake.

2. Intake length and Mach number are the key parameters which determines the phase of the reflected acoustic wave for the acoustic reflection driven flutter.

3. The analysis reveals a relationship between the phase difference (between the outgoing and reflected acoustic waves) and the aero-damping contribution due to acoustic reflection from the intake. The most destabilising condition occurs at approximately 90° phase difference.

In the next step, the effect of other parameters (such as vibration frequency) on the phase and amplitude of the reflected acoustic wave on fan flutter stability is investigated. Moreover, the reflection of acoustic waves at the opening of the intake is studied. This is achieved through computations with artificially created annular cylindrical intakes.

6.4.3 Computations With Annular Cylindrical Intake

In the second part of this study, effect on flutter stability of fan blades due to acoustic reflection from an axi-symmetric annular cylindrical intake is studied. The phasing relation between the intake length and Mach number and the blade aero-damping was demonstrated in the previous section. The main objectives of this part of the work are to establish the relationship between the amplitude of the reflected acoustic wave with blade aero-damping, and to study the effects of key parameters (such as blade vibration frequency) on the reflected acoustic wave. Moreover, comparisons are made between the

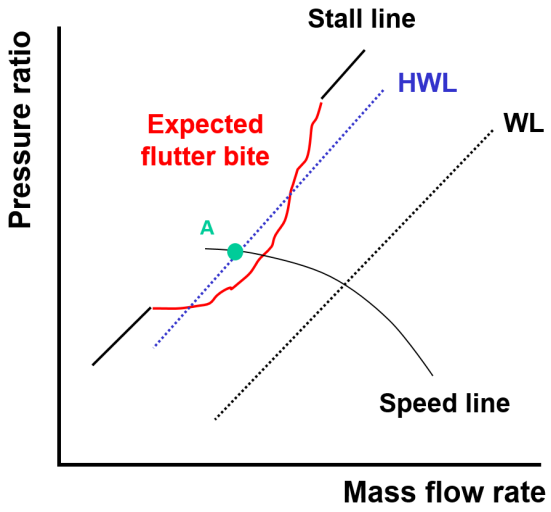


Figure 6.18: Illustration of fan operating conditions used for flutter computation. WL: working line; HWL: high working line.

results obtained from unsteady CFD solutions and the calculations based on the analytical theories (as presented in Chapter 4), which provide the foundation for the development of a simple model.

The geometry of the intake used in this study is shown in Figure 6.17. The axi-symmetric intake studied in this work has a hub/tip ratio of $h = 0.27$, which terminates at the inlet of fan domain as illustrated by the dashed black line in Figure 6.17. It is worth noting that the intake geometry used in this study is not a representation of a common design. However, this simplified geometry allows one to explore fan-intake interactions in more detail. Moreover, the intake walls are treated as inviscid so as to avoid end-wall boundary layer losses. By doing so the mean flow on the fan blade remains unchanged independent of the intake length, and hence allows one to vary the length of the intake to study its effects on fan flutter stability.

Figure 6.18 illustrates the operating map (at part speed) for the fan with the annular cylindrical intake studied in this work. Most of the computations in this work are performed at the non-dimensional fan speed of $\bar{\Omega} = 0.89$ (which showed the deepest flutter bite in Figure 6.4). It should be noted that the steady state flow in this study is slightly different from that shown in the previous section due to a different intake geometry. The high working line (HWL) close to the stall boundary (see Figure 6.4), which

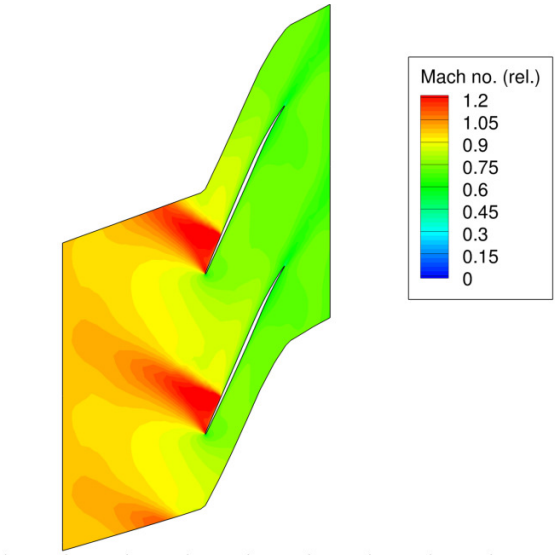


Figure 6.19: Relative Mach number contour at 98% span of the fan blade.

cuts through the flutter bite, is also illustrated in Figure 6.18. Most of the flutter computations in this work are performed at a fixed flow condition on the high working line (denoted as 'A' in Figure 6.18). At this condition, the inlet relative Mach number at the blade tip is around 0.95. At the operating points studied, the shock is expelled from the passage as illustrated by the contour of relative Mach number shown in Figure 6.19). The Mach number in the intake is about 0.5.

Full annulus unsteady CFD flutter computations are performed, using the 2^{nd} strategy, for the 1F/2ND and 1F/3ND modes with and without the annular cylindrical intake. Flutter computations are performed at the fixed flow condition 'A' by varying the fan vibration frequency ω (and consequently the cut-on ratio σ (Equation 4.22)) and the intake length L independently. Moreover, flutter computations are carried out by varying the fan speed (on the high working line) for a fixed intake length and blade vibration frequency, so that the speed range of flutter bite can be investigated. By varying these key parameters, the relationship between the amplitude and phase of the reflected acoustic wave and the aerodynamic damping of fan blades can be established, based on which a simple flutter bite prediction model is proposed.

Figure 6.20 shows the aero-damping variation of the fan blade as a func-

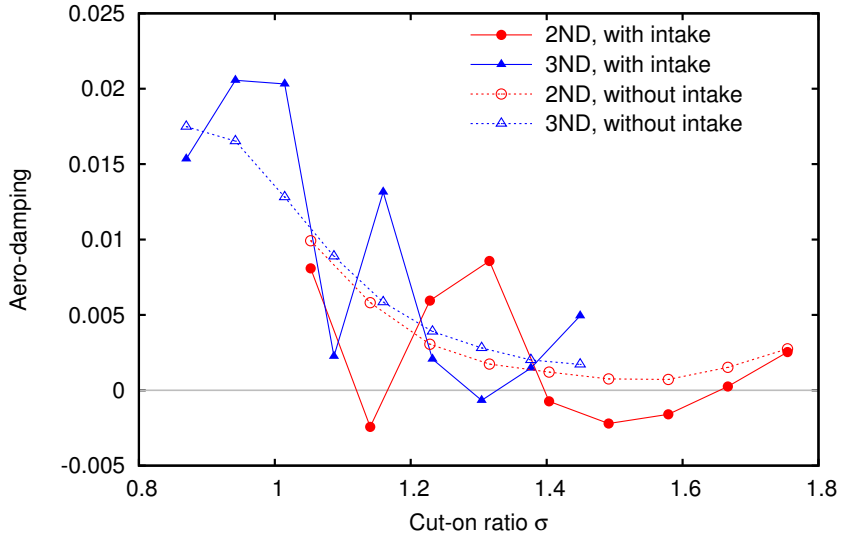


Figure 6.20: Aero-damping of the fan as a function of vibration frequency, $L = 1.37D$.

tion of cut-on ratio σ with an intake length of $L = 1.37D$. The dashed lines in Figure 6.20 show the blade aero-damping computed for the isolated rotor in a long straight duct, which represent the aerodynamic damping due to blade motion in the absence of acoustic reflection. As can be seen from the plot, the isolated fan without intake shows positive aero-damping for all vibration frequencies studied, suggesting that at the operating condition studied, the rotor is stable in the absence of acoustic reflections. With the introduction of the intake, the aero-damping of the fan changes significantly from that of the isolated setup. It should be emphasised that, this is not due to the change of flow on the fan, as the numerical setup ensures that the steady base flow on the fan is approximately the same for computations with and without the intake, which is confirmed by the comparison of isentropic Mach number for the isolated rotor and the rotor in the fan-intake assembly shown in Figure 6.21. Positive as well as negative effects on aero-damping can be observed in Figure 6.20, and a cyclic variation of aero-damping can be seen when $\sigma > 1$ (i.e. when the acoustic modes are cut-on in the intake), and the amplitude of damping variation is seen to decrease with the increase of σ. Moreover, the least damped condition shifts from about $\sigma = 1.6$ for the isolated fan computations with non-reflecting boundary conditions. It can be seen from the plot that flutter occurs with the intake at two separate

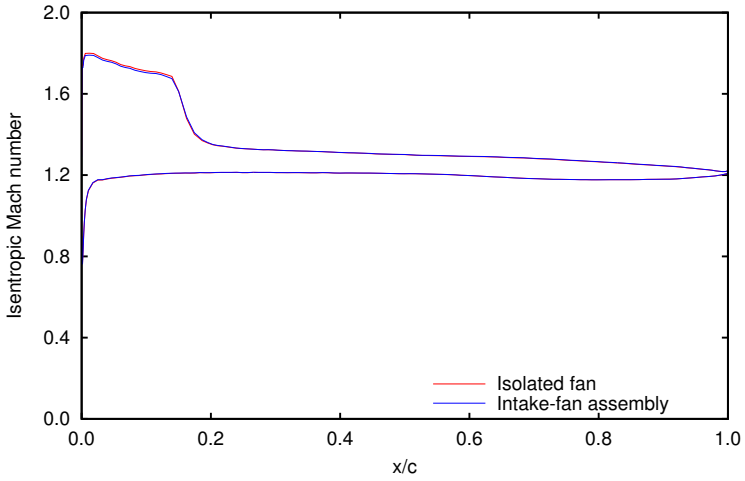


Figure 6.21: Isentropic Mach number at 90% blade span.

frequency bands: around $\sigma = 1.13$ and $1.4 < \sigma < 1.65$ for the 2ND mode and around $\sigma = 1.3$ for the 3ND mode.

A similar analysis was performed with a constant cut-on ratio of $\sigma = 1.3$ for the 2ND and 3ND modes with varying intake length L at the same fixed steady flow condition. It should be emphasised that the steady flow condition does not vary with the increase of intake length as the intake wall is treated as inviscid, i.e. there is no boundary layer growth along the casing walls. In Figure 6.22, the calculated aero-damping of the fan blade is plotted against the non-dimensional intake length L/λ_m^-. The length of the intake L is normalised by the wavelength of the upstream propagating acoustic wave λ_m^-. It is seen from this plot that the damping curves are a function of intake length and repeat themselves with a period of approximately one wavelength of the upstream propagating acoustic wave. Positive and negative effects on aero-damping are again clearly shown in this plot, where the largest decrease on aero-damping is seen at the intake length of $L/\lambda_m^- = 1.8$ for the flow condition and vibration frequency studied. The findings show a similar behaviour with the studies using the 'bump' feature. The length of intake is confirmed as a key parameter for the aero-damping of the fan and intake system, which clearly defines when the 'flutter bite' occurs depending on the vibration frequency of the blade and Mach number in the intake.

In order to study the propagation and reflection of acoustic waves from the intake and their relationship with the blade aero-damping, a wave-splitting

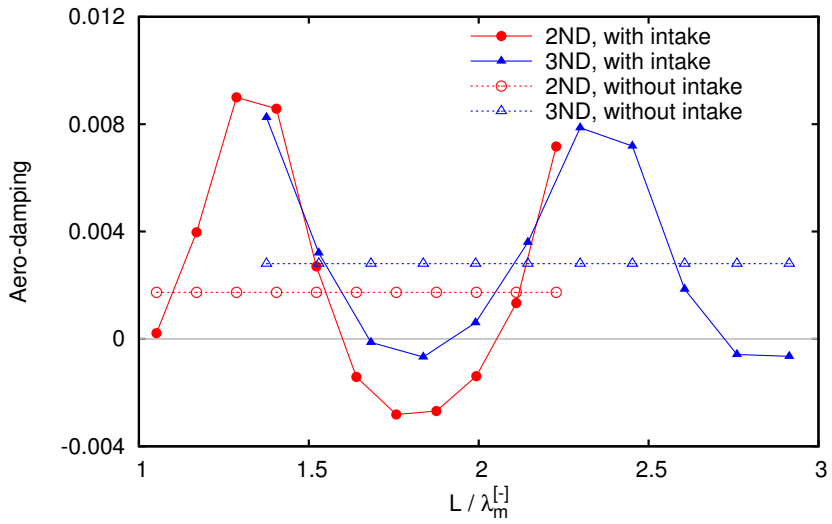
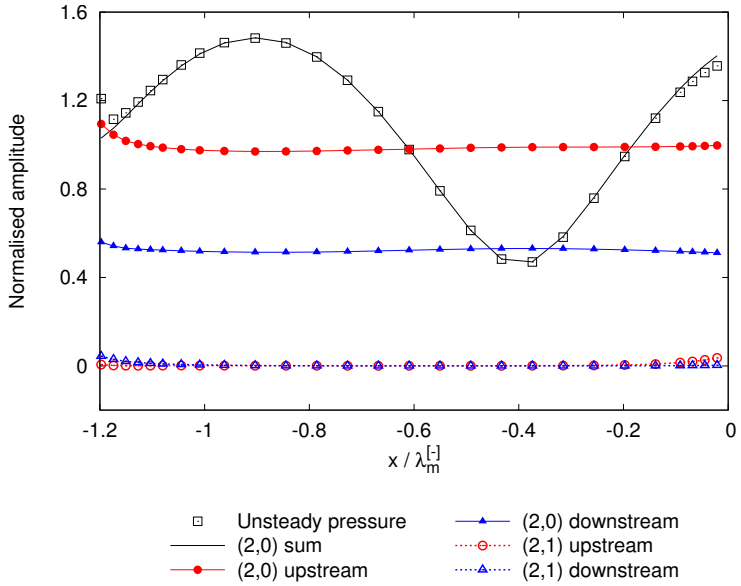
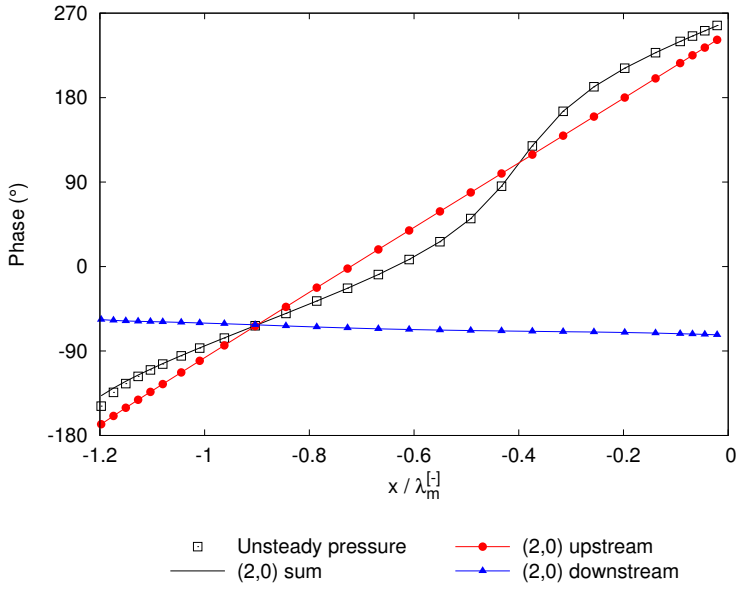


Figure 6.22: Aero-damping of the fan as a function of intake length, $\sigma = 1.3$.

procedure is performed in the intake duct to obtain the amplitude and phase of the outgoing pressure wave and its reflection from the intake highlight. The amplitude and phase of the upstream and downstream propagating waves in the intake duct for the 2ND mode with $\sigma = 1.3$ and $L = 1.37D$ are plotted against the non-dimensional axial coordinate x/λ_m^- in Figure 6.23. In this plot the leading edge of the fan is situated at $x/\lambda_m^- = 0$ and the intake highlight is located at $x/\lambda_m^- = -1.2$. It can be seen from the plot that the fundamental radial order of the 2ND mode, i.e. the $(2,0)$ mode, is cut-on upstream of the fan, and propagates in the direction against the flow with approximately constant amplitude (solid red curve). Upon reaching the intake highlight, it is reflected back as a cut-on $(2,0)$ mode towards the fan (solid blue curve) with a significant portion of the incident amplitude (approximately 0.5 in this case). Moreover, the vibration of the fan with the 1F/2ND mode also excites its higher radial harmonics ($n = 1, 2, ...$). The upstream propagating $(2,1)$ mode is plotted in Figure 6.23a (dashed red curve) and can be seen to have a non-zero amplitude close to the leading edge of the fan ($x/\lambda_m^- = 0$). However, modes with radial order higher than $n = 0$ are found to be cut-off for the low vibration frequencies of the first flap mode, so that their amplitudes are rapidly attenuated. It is also noticed that at the intake highlight ($x/\lambda_m^- = -1.3$) the incident $(2,0)$



(a)



(b)

Figure 6.23: (a) Normalised amplitude and (b) phase of 2ND acoustic waves in the intake $L = 1.37D, \sigma = 1.3$.

mode is scattered into its radial harmonics, and a finite amplitude can be seen for the downstream propagating $(2,1)$ mode at the intake highlight (dashed blue curve). However as the reflected higher order modes are cut-off, they will have negligible impact on the unsteady pressure field near the fan. This is confirmed by the fact that the amplitude of the $(2,0)$ mode (solid black curve in Figure 6.23a), calculated as the complex sum of upstream and downstream propagating components of the $(2,0)$ mode, lies more or less on top of the unsteady pressure obtained from the temporal Fourier transformed unsteady flow solutions (black square symbols). In other words, the unsteady pressure content in the intake duct is dominated by the fundamental radial order mode (i.e. the $(2,0)$ mode). Hence in the rest of this paper only the fundamental radial order is considered.

The wavelength and phase velocity of the outgoing and reflected waves can be inferred from the slope of phase against axial distance in Figure 6.23b. It is seen from this plot that the waves propagate with a (nearly) constant axial phase velocity towards (and reflected back from) the intake highlight. The effective axial phase speed of the downstream propagating wave (blue curve) is much higher (Mach number of ˜35.2) than that in the upstream direction (red curve) (Mach number of ˜1.0) (which can be calculated from Equation 4.17), hence a lower gradient can be seen for the phase curve of the downstream travelling wave.

Based on the results obtained from wave-splitting, the phase change of acoustic waves propagating through the intake duct can be obtained as the difference between the phase at the fan leading edge and the phase at the intake highlight, namely $\delta\phi^{u-}$ and $\delta\phi^{u+}$ in Figure 6.1. These results are plotted as the solid curves in Figure 6.24 as a function of vibration frequency and in Figure 6.25 as a function of intake length. The results obtained from wave-splitting are compared with values calculated using the analytical method (Equation 4.24 and 4.25) in this plot. It can be seen from Figure 6.24 that the phase difference increases with the increase of vibration frequency. This is justified by the fact that, as the mode becomes more cut-on, its (real) axial wavenumber increases and axial wavelength decreases, resulting in an increase in the overall phase change proportional to $\Re(k_x)$ (see Equation 4.24 and 4.25). It is also seen that the values calculated from the linear theory show a good agreement with the values obtained from the wave-splitting of the unsteady CFD solutions. Moreover, as expected, the

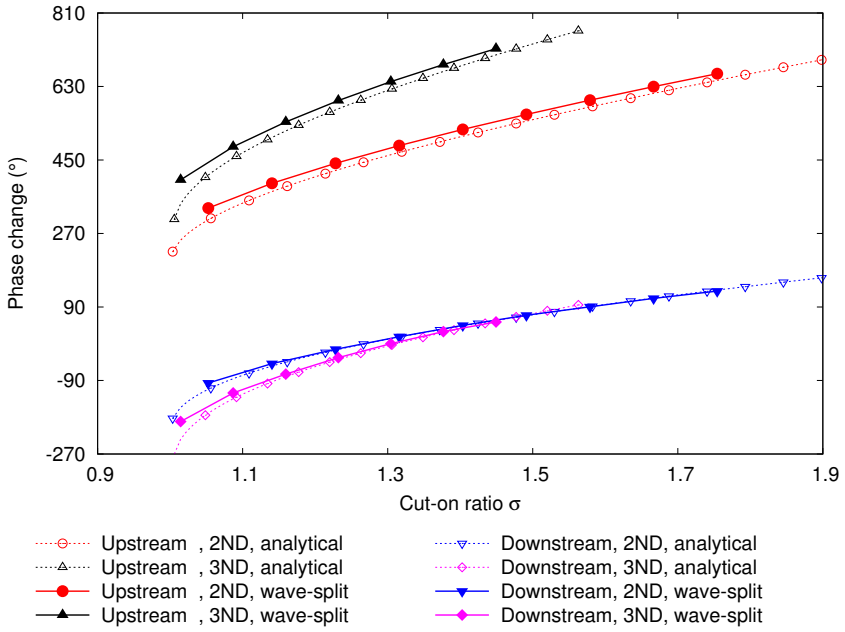


Figure 6.24: Axial phase change through the intake duct as a function of vibration frequency, $L = 1.37D$. Upstream: $\delta\phi^-$; Downstream: $\delta\phi^+$

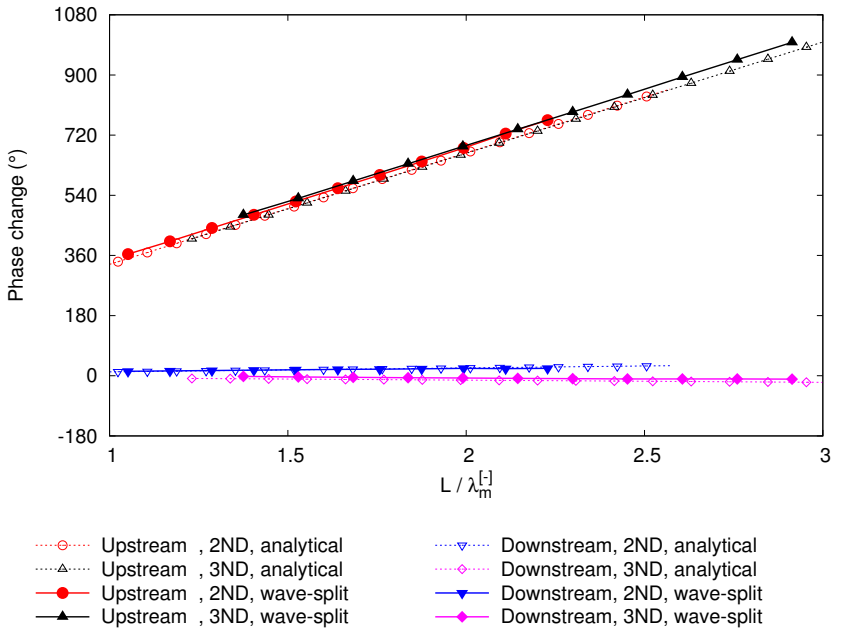


Figure 6.25: Axial phase change through the intake duct as a function of intake length, $\sigma = 1.3$. Upstream: $\delta\phi^-$; Downstream: $\delta\phi^+$

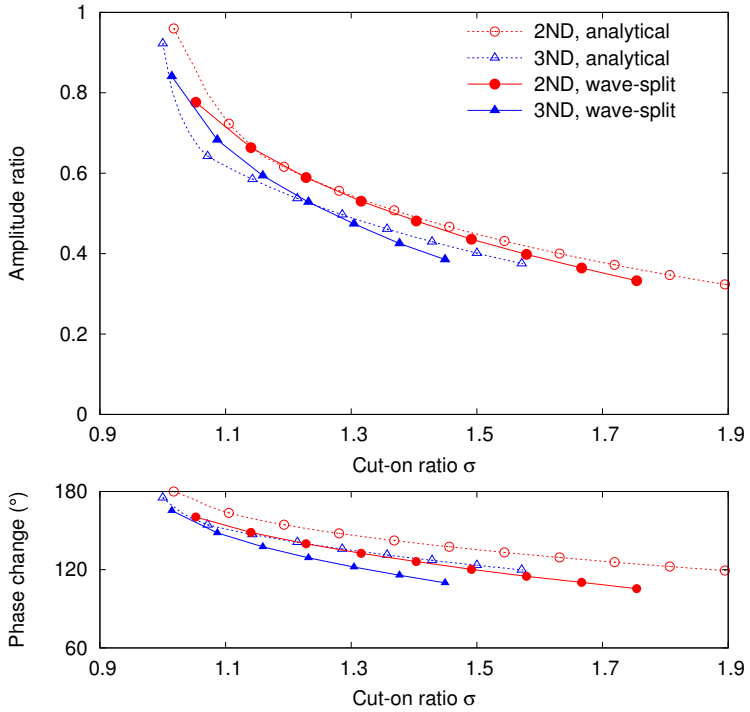


Figure 6.26: Amplitude ratio and phase change of acoustic reflection from the intake highlight as a function of vibration frequency, $L = 1.37D$.

phase change shows a linear relationship with intake length as can be seen in Figure 6.25. Relatively small discrepancies can be seen between the values based on the analytical method and the values obtained from the wave-splitting of the unsteady CFD results, and the trend of the phase change is very well represented.

When the acoustic wave reaches the intake highlight, part of the incident outgoing acoustic wave transmits through the intake opening and radiates outwards to the farfield (illustrated in Figure 6.1). Part of this outgoing wave is reflected back towards the fan with an attenuation in modal amplitude and a change of phase. These parameters are calculated (at the intake highlight) for the cases studied based on the results obtained from wave-splitting of unsteady CFD solutions. In Figure 6.26, the amplitude ratio ($|\eta^I|$) and phase change ($\delta\phi^I$) of acoustic reflections at the intake highlight obtained from unsteady CFD solutions are compared with values calculated analytically (Section 4.5).

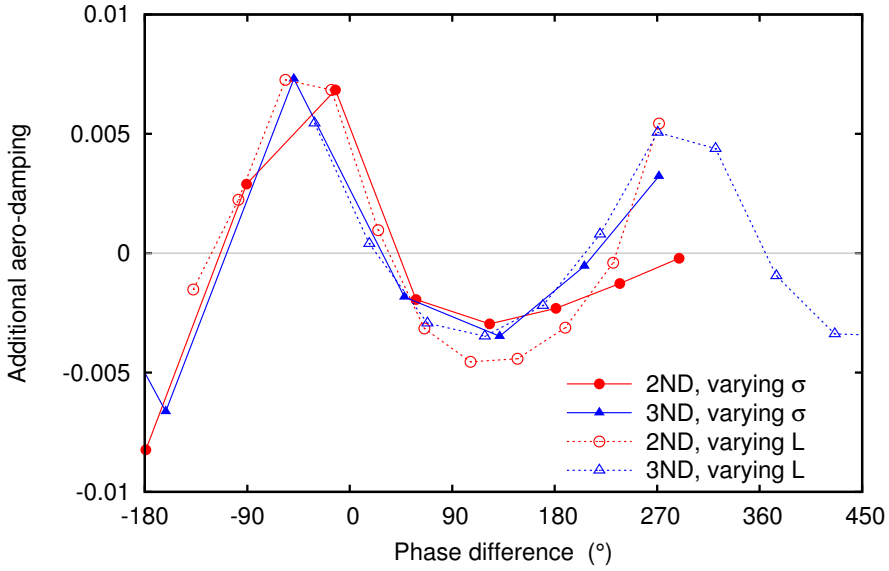


Figure 6.27: Additional aero-damping due to acoustic reflections as a function of phase difference between the outgoing wave and the reflected wave at fan leading edge.

It can be seen from the plots that when the mode is just cut-on, (nearly) total reflection occurs at the opening of the intake with an amplitude ratio close to 1 and a phase change of 180°. As the mode becomes more cut-on, the acoustic reflection from the intake opening is reduced in amplitude as well as showing a change in phase. Moreover, it is seen that these trends are adequately predicted by the analytical model. The discrepancies between them are likely to come from the radial profile of flow in the intake (which is assumed to be uniform by the analytical model) and the analytical simplifications in the geometry of duct opening, which could result in a slightly different radiation mechanism. Nevertheless, an adequate agreement can be seen between the values obtained from wave-splitting of 3D unsteady CFD solutions and the analytical model.

Based on the the phase of acoustic wave obtained from wave-splitting, the relationship between the additional aerodynamic damping due to acoustic reflection from the intake (i.e. difference between the solid and dashed lines in Figure 6.20 and Figure 6.22) the phase difference between the reflected acoustic wave and the outgoing acoustic wave at the blade leading edge can be established. Figure 6.27 shows the calculated additional aero-damping due to acoustic reflection from the intake for the aforementioned cases with

varying vibration frequency and intake length, plotted as a function of this phase difference. It can be seen from the plot that the cases with varying vibration frequency and varying intake length can be unified to show a common trend: minimum damping contribution at approximately 90°phase difference and maximum damping contribution at approximately -90°phase difference. The obtained relationship is in a good agreement with the findings using the 'bump' feature. Moreover, for the case when blade vibration frequency is varied (i.e. varying σ), the influence of acoustic reflection from the intake shows a gradual decrease with the increase of frequency (which manifests as an increase in phase difference). This phenomenon can be explained by the decrease in the amplitude of reflected acoustic wave with increasing frequency as shown in Figure 6.26.

The above analysis with the annular cylindrical intake clearly demonstrates the mechanism of acoustic reflection from the intake and its interaction with the blade aerodynamic damping. Three further conclusions can be made (besides those in agreement with the previous section) from this analysis:

1. Vibration frequency and thus fan speed (which modifies the frequency of acoustic modes in the stationary frame) are also key parameters for the acoustic reflection driven flutter. The variation of frequency, besides the effects on flow and modeshape driven flutter, influences both the amplitude and phase of the reflected acoustic wave.

2. For a fixed phase of the reflected wave, the influence of acoustic reflection on blade aero-damping seems to be proportional to the amplitude of reflected acoustic wave.

3. The complete acoustic reflection process in the intake can be calculated with a good degree of accuracy by analytical methods without the need of CFD computations.

6.4.4 Computations With Real Intake

It was shown in the previous studies that by modeling an intake as an infinite length cylinder with a 'bump' and an artificially created annular cylindrical intake, the flutter bite can be captured and its relationship with the reflected acoustic wave was obtained. In this section the effects of a

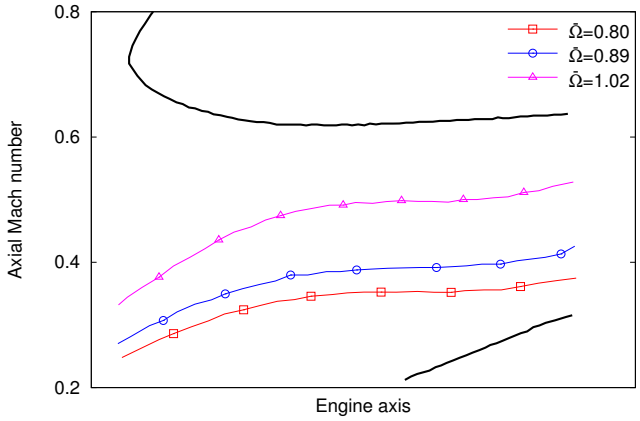


Figure 6.28: Mach number profiles at different fan speeds (curves with symbol) and an illustration of intake geometry used in this study (black curve).

real intake on flutter is studied and the findings of the previous section are examined for this geometry.

The domain used in this study contains a real intake geometry, fan and a long cylinder downstream of the fan (as shown in Figure 6.7 with OGV and ESS removed). In the previous section, the phase difference between the outgoing acoustic wave and the reflected acoustic wave at the fan face was changed by changing the location of the bump. However, the length of a real intake is set by other operability requirements. Therefore, in the first part of this study the phasing between the outgoing wave and the reflected wave at the fan face is changed by changing the fan speed which is also representative of the real engineering problem. A change in fan speed will alter the axial Mach number in the intake, which (as will be shown) changes the amplitude and phase of the reflected waves from the intake lip. Furthermore, as the fan speed reduces and the intake Mach number decreases, the outgoing acoustic wave will eventually cut-off which decays axially. The intake profile used in this study is illustrated (not to scale) in Figure 6.28. Computations were performed for the 2ND and 3ND modes at the reduced frequency of 0.54, along a constant working line shown by *HWL* in Figure 6.8.

Figure 6.29 shows the computed aero damping for 2ND and 3ND modes plotted against blade tip Mach number $\bar{\Omega}$. Also shown in this plot is the aero damping for the case without intake (this case was achieved by attaching a

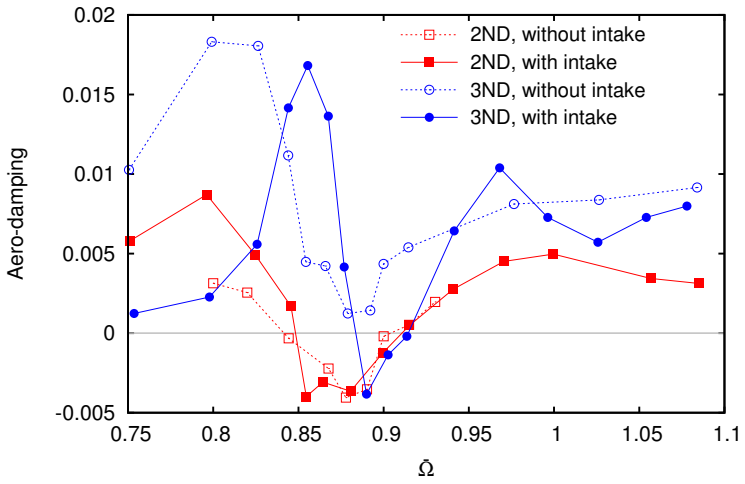


Figure 6.29: Aero-damping of the fan as a function of speed on the *HWL* operating line.

long straight duct upstream of the fan, Section 6.4.1). The behavior of the case without intake (dashed curves) is only dependent on the flow on the blade and mechanical properties of the blade, which was described in detail in [11]. It can be seen from this plot that the reflections from intake can play an important part in flutter and can change the flutter stability of the blade significantly. For this particular intake, reduced frequency and the fan blade used in this study, the intake effects are more pronounced for the 3ND mode than the 2ND mode, which is in agreement with measured data shown in Figure 6.8. Moreover, it is seen from this plot that for the case without intake both 2ND and 3ND modes show a minimum damping at $\bar{\Omega} = 0.87$; the addition of intake moves the minimum damping for 2ND and 3ND mode to $\bar{\Omega} = 0.85$ and $\bar{\Omega} = 0.89$ respectively. It is also seen from the plot that, the 3ND mode has a further drop in aero damping at $\bar{\Omega} = 1.02$. It will be shown in the next section that this drop is attributed to a second (high speed) flutter bite.

In order to establish a relationship between acoustic reflection and flutter and understand the above observations, a wave-splitting procedure is performed (similar to the previous sections) to split the unsteady perturbations in the intake into propagating waves. Figure 6.30 shows the cut-on frequencies plotted against $\bar{\Omega}$ for 2ND and 3ND acoustic waves at the fan face. The dashed black line in Figure 6.31 is the blade vibration frequency

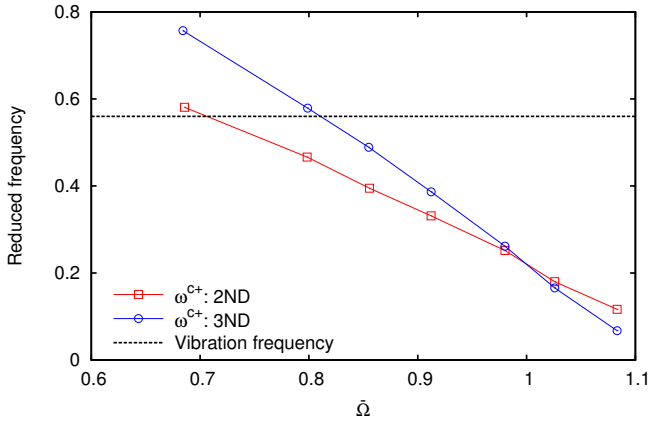


Figure 6.30: Cut-on frequency for different fan speeds.

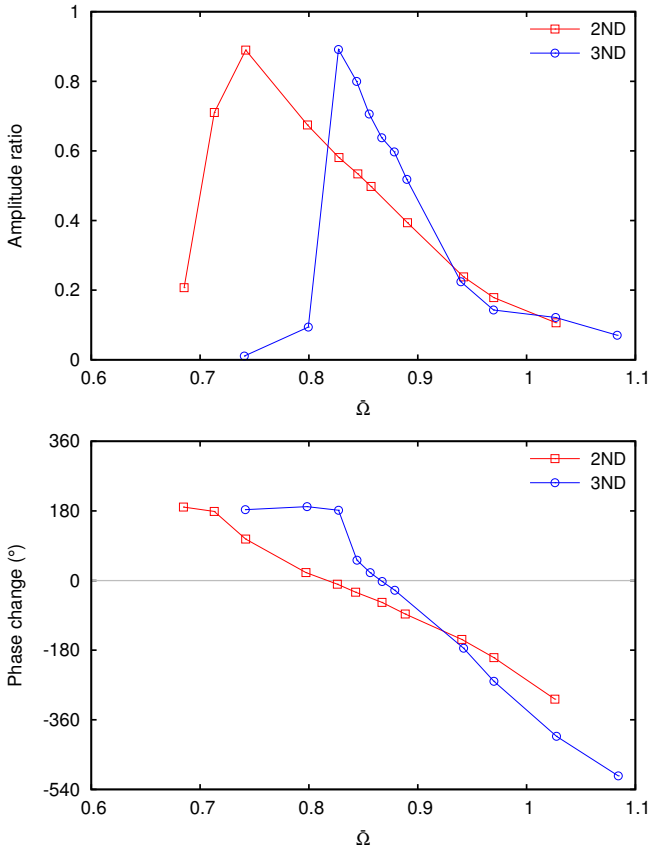


Figure 6.31: Amplitude ratio and phase difference between the reflected and the outgoing acoustic waves at the fan face.

used in this set of computations, and the crossing of this line with the red or blue line shows the fan speed at which the corresponding acoustic mode becomes cut-on at this frequency. From this plot it can be seen that the 2ND mode becomes cut-on at $\bar{\Omega} = 0.74$ and the 3ND mode becomes cut-on at $\bar{\Omega} = 0.83$.

Figure 6.31 shows the obtained amplitude ratio and phase change between the reflected acoustic wave and the outgoing acoustic wave at the fan face. The following observations can be made from Figure 6.31:

1. For a cut-on wave the phase difference between the reflected acoustic wave and the outgoing acoustic wave is dependent on the fan speed. The change in fan speed changes the Mach number in the intake and the properties of the generated acoustic waves (such as axial wavenumber), which consequently changes the phase of the reflected wave. A similar trend was observed in Figure 6.24 when the vibration frequency of the blade is varied.

2. The amplitude of the reflected wave experiences a resonance when the mode is just cut-on. This resonance occurs when the wave is cut-on at the fan face but (due to decreasing Mach number shown in Figure 6.28) becomes cut-off in the intake. However, the minimum damping of the intake does not occur at this point since the outgoing wave and the reflected wave show 180°phase difference at the fan face, which (as was shown in previous sections) does not correspond to the phasing criterion for flutter bite (90°for most destabilising and 180°for no effect).

3. For a cut-off wave the amplitude of reflected wave is nearly zero. This is due to the fact that the amplitude of the outgoing acoustic wave is attenuated exponentially in the intake in such cases, and so there would be minimum reflection from the highlight. This was also observed for the cut-off $(2, 1)$ mode shown in Figure 6.23.

4. The amplitude of the reflected wave decreases as fan speed increases. The rate of decrease is much higher for the 3ND mode than the 2ND mode. This is caused by the change in the properties of the outgoing acoustic waves (such as axial wavenumber and mode angle). A similar

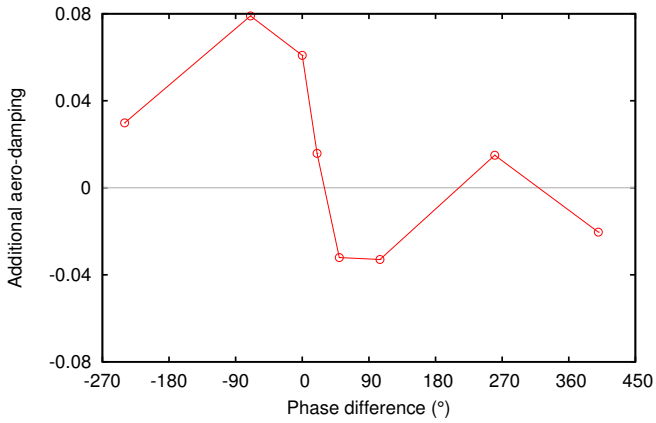


Figure 6.32: Additional aero-damping as a function of the phase difference between the outgoing and the reflected acoustic waves at the fan face, 3ND.

trend was observed in Figure 6.26 when the vibration frequency of the blade was varied.

5. The decrease in 3ND damping at high speed $\bar{\Omega} = 1.02$ is due to the fact that at this speed the phase difference between upstream travelling wave and the reflected wave becomes almost 90°again. However, the amplitude of the reflected wave is quite small at this speed and hence the drop in damping is not as severe as that at $\bar{\Omega} = 0.89$. Moreover, as can be seen from Figure 6.29, the aero-damping for the isolated blade (without reflection) is quite high at this speed and hence the resultant aero-damping remains positive.

Figure 6.32 shows the additional aero-damping due to acoustic reflection from the intake obtained from the difference between the solid and dashed curves in Figure 6.29 for the 3ND mode plotted against the phase difference between the outgoing acoustic wave and the reflected acoustic wave. On comparing this plot with that of Figure 6.16 and Figure 6.27, it is seen that the plots show very similar trends indicating that the conclusions made in the previous sections can be applied to a real intake.

In the next step, the effect of intake length on flutter is studied. The profile of the three intakes used in this study is shown in Figure 6.33 with the black profile being the datum intake.

By conducting similar analyses as shown earlier, the amplitude ratio and

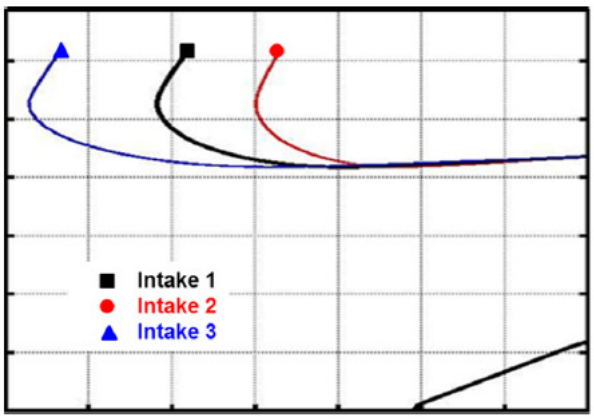


Figure 6.33: Profiles of intakes used in this study.

phase difference between the reflected acoustic wave and the outgoing acoustic wave are obtained at the fan face. The results are plotted in Figure 6.34 together with the blade aero-damping for these profiles as a function of $\bar{\Omega}$. It is seen from these plots that, the amplitude ratio of the reflection coefficient does not change significantly with intake length, which is obvious as it is mainly dependent on the flow Mach number (as shown in Figure 6.31) and the properties of acoustic wave (such as the vibration frequency as shown in Figure 6.26) for a fixed intake lip geometry. However, as the intake length increases, the time for the wave to travel from the fan face to the highlight and back increases, which results in an increase in the phase difference between the outgoing wave and reflected wave. Consequently, the fan speed at which the intake induces the most destabilising effect (90°phase difference) moves to a lower speed. This can be clearly seen in Figure 6.34 where the longer intake (*Intake 3*) reaches 90°at a lower speed than the shorter intakes. Also shown in Figure 6.34 with shaded red area is the region where intake effects are destabilising (labeled 'danger zone'). It can be seen that, as the intake length decreases, which results in a reduction of the slope of the phase plot, the speed range which lies in the danger zone increases. The computed blade aero-damping for the three intakes used is also shown in Figure 6.34. It is seen that the increase in intake length moves the flutter bite to a lower speed.

The above analysis with real intakes clearly demonstrates that the observations and conclusions made in the previous sections using simplified

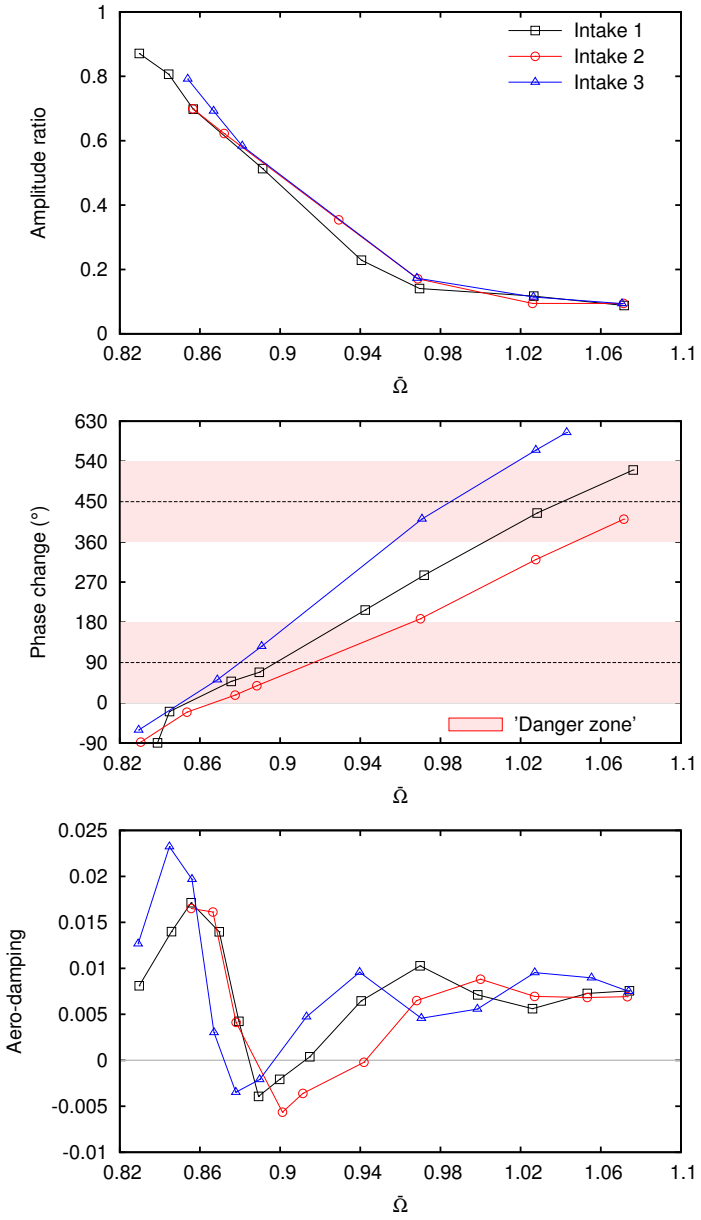


Figure 6.34: Amplitude ratio (top) and phase difference (middle) between the outgoing and the reflected acoustic waves at the fan face; blade aero-damping (bottom) for different intake length.

geometries are valid for real intake geometries. Based on the observations and conclusions obtained, a simple analytical model is proposed to predict the acoustic reflection driven flutter for fan blades.

6.5 Simple Prediction Method for Flutter Bite

The analysis in this section is for the simple annular intake presented in Section 6.4.3. By studying the the effects of key parameters, such as intake length and vibration frequency, it was established (in the previous section) that for the acoustic reflection driven flutter the most stabilising condition corresponds to the phase of the reflected wave 90°ahead of the outgoing wave, and the worst flutter condition is when the reflected wave lags by 90°. Moreover, the influence of acoustic reflection on the blade aero-damping seems to be proportional to the amplitude of the reflected acoustic wave. Therefore it is plausible to introduce a parameter, namely the 'flutter index' τ, which characterises the susceptibility of fan flutter stability to acoustic reflections from the intake

$$\tau_{m,n} = |\eta^I_{m,n}| sin(\phi^{l+}_{m,n} - \phi^{l-}_{m,n}) \tag{6.1}$$

where ϕ^{l-} is the phase of the outgoing (upstream propagating) acoustic wave (generated by blade vibration) at the blade leading edge, ϕ^{l+} is the phase of the reflected (downstream propagating) acoustic wave at the blade leading edge, and (m, n) is the mode index of acoustic waves generated by the blade-disk assembly mode vibration of nodal diameter m. As shown before in Section 6.4.3, for fan blade designs in typical modern aero-engines, the blade vibration frequency for which the flutter bite occurs is usually quite low that the acoustic modes with radial order $n > 0$ are highly cut-off in the intake (i.e. cut-off ratio $\sigma << 1$). Therefore for the acoustic reflection driven flutter studied in this work only modes with radial order of $n = 0$ are considered.

The proposed index has a form of a sine function and a range of values from -1 to 1. The form of a sine function is chosen since the influence shows a cyclic repeating trend with the variation of the phase of the reflected acoustic wave (as shown in Figure 6.16, Figure 6.27 and Figure 6.32). The introduced flutter index has a value of 1 when the reflected wave leads the

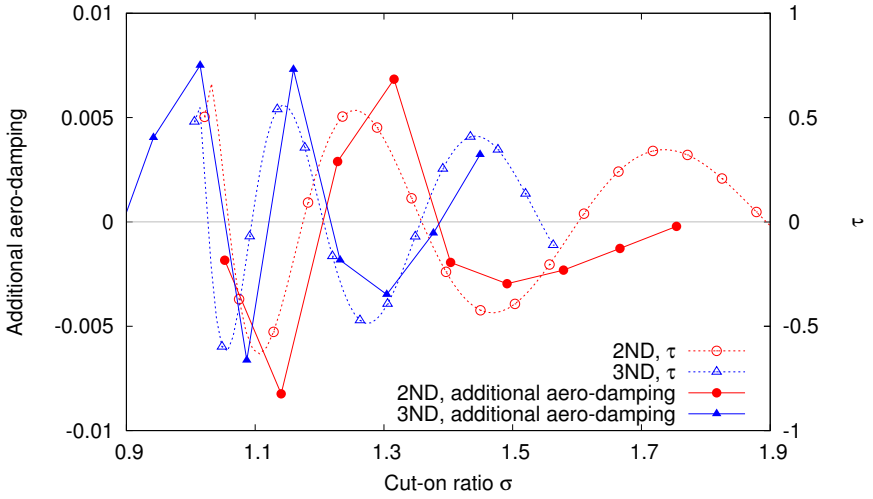


Figure 6.35: Additional aero-damping due to acoustic reflections and 'flutter index' as a function of vibration frequency, $L = 1.37D$.

outgoing wave by 90°(i.e. most stabilising effect due to reflection), and a value of -1 when the reflected wave lags the outgoing wave by 90°(i.e. most de-stabilising effect due to reflection). The phase of the outgoing acoustic wave ϕ^{l-} (generated by blade vibration), and consequently the phase of the reflected wave ϕ^{l+}, are functions of the flow and fan vibration characteristics. However, the proposed 'flutter index' τ requires only the difference between them (i.e. $\phi^{l+} - \phi^{l-}$) and can be computed from Equation 4.24, Equation 4.25 and Equation 4.64 without any knowledge of the fan vibration characteristics and flow on the blade.

In order to investigate the effectiveness of the proposed method, the calculated flutter index is compared with the additional aerodynamic damping due to acoustic reflection for the annular cylindrical intake case (calculated from the results shown in Figure 6.20 and Figure 6.22). The calculated additional aero-damping are compared with the calculated flutter index in Figure 6.35 as a function of cut-on ratio and Figure 6.36 as a function of intake length.

It can be seen from Figure 6.35 that a sinusoidal-like cyclic variation of the calculated additional aero-damping due to acoustic reflections from the intake (solid curves) is present when the mode is cut-on. The amplitude of variation is seen to decrease with the increase of vibration frequency, which is a result of decreasing reflection amplitude as the mode becomes more

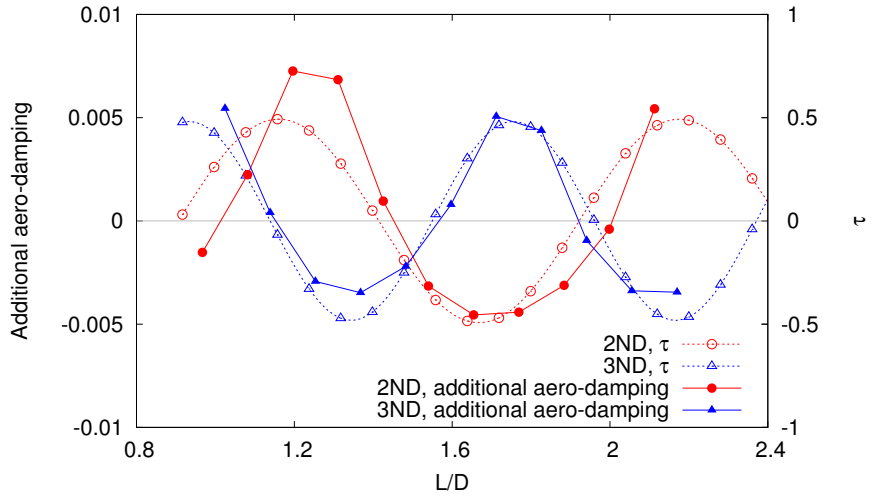


Figure 6.36: Additional aero-damping due to acoustic reflections and 'flutter index' as a function of intake length, $\sigma = 1.3$.

cut-on (shown in Figure 6.26). Moreover, it is also seen that the period of variation increases with the increase of frequency, which can be explained by the decrease of the slope of phase change in Figure 6.24. The calculated flutter index $\tau_{m,n}$, plotted as the dashed curves, shows good agreement with the variation of the additional aero-damping. The amplitude variation of the additional aero-damping, as well as the trend of variation, are both well represented by the flutter index. Therefore, the frequency range in which flutter bite is likely to occur, i.e. regions with negative additional aero-damping, can be easily identified with the help of the proposed flutter index.

Figure 6.36 shows the calculated additional aero-damping due to acoustic reflections from the intake as a function of intake length (normalised by the intake diameter D). As expected, the additional aero-damping shows a sinusoidal cyclic variation about the zero axis since the only varying parameter in this case is the intake length (which in turn changes the phase of reflected waves). The period of variation is approximately one wavelength of the upstream propagating wave (the downstream propagating wave shows negligible phase change as shown in Figure 6.23b). As opposed to the trend of damping variation shown in Figure 6.35, the amplitude of variation stays constant due to a constant reflection coefficient from the intake opening. Moreover, it can be seen that flutter bite occurs at different conditions for

the 2ND mode ($L/D = 1.3$) and the 3ND mode ($L/D = 1.8$) for the case studied. It is also noticed that due to the difference in axial wavelength, some intake lengths are shown to provide positive damping on both the 2ND and 3ND modes (e.g. $L/D = 1.1$) at this flow condition and vibration frequency. It is worth noting that the length of the intake is varied over a wide range of values so as to gain understanding of its effects on acoustic wave propagation in the intake and the flutter stability of the fan blades. In real applications an intake geometry of $L/D > 1$ is not very common.

It is seen in Figure 6.35 and Figure 6.36 that the proposed flutter index shows good correlation with the additional aerodynamic damping due to acoustic reflection from the intake. However, as opposed to the aerodynamic damping, the evaluation of the flutter index can be achieved analytically without the need of unsteady CFD computations. Therefore, the proposed flutter index provides an efficient way of evaluating the susceptibility of fan blades to flutter due to acoustic reflections from the intake. The power of the proposed methodology will be demonstrated in the rest of this section by analysing the effects of parameters which are found to be important to acoustic reflection driven flutter.

As shown in Section 4, the behaviour of acoustic waves propagating in the intake are determined by the intake geometry (length, hub and casing radii), axial flow Mach number M_x (flow in the intake has zero swirl) and vibration frequency in stationary frame of reference. The natural vibration frequency of the fan can be obtained from a FE structural dynamics analysis and is a function of the shaft speed. The frequency $\bar{\omega}_m$ in stationary frame of reference (which is normalised by the blade vibration frequency at the working line mass flow $\bar{m}_{wl}$ at the speed of $\bar{\Omega} = 0.89$ in the work presented here) can be expressed as

$$\bar{\omega}_m = \frac{\omega + m\Omega}{\omega_{ref}} \tag{6.2}$$

The frequency $\bar{\omega}_m$ in the above equation combines the fan shaft speed Ω and the blade vibration frequency ω. The influence of these three parameters, namely the intake geometry L/D, flow Mach number M_x and frequency $\bar{\omega}_m$, on blade aero-damping variation can be characterised by the proposed flutter index τ.

In general, the proposed flutter index can be used in three ways:

(1) Determine the unstable operating conditions for a particular intake de-

sign, i.e. regions with negative contribution to the blade aero-damping due to acoustic reflections from the intake. To achieve this goal, 'flutter index' matrix can be computed for a fixed intake length L/D by varying the axial flow Mach number M_x and the modal frequency $\bar{\omega}_m$ independently.

(2) Determine the relationship between the intake length and the additional aero-damping due to intake acoustics for a fixed fan operating line. To achieve this goal, the 'flutter index' matrix can be computed by varying the intake length L/D and the modal frequency $\bar{\omega}_m$ independently. For a fixed fan operating line, the axial flow Mach number M_x is determined by the fan shaft speed Ω (or in other words $\bar{\omega}_m$ as shown in Equation 6.2).

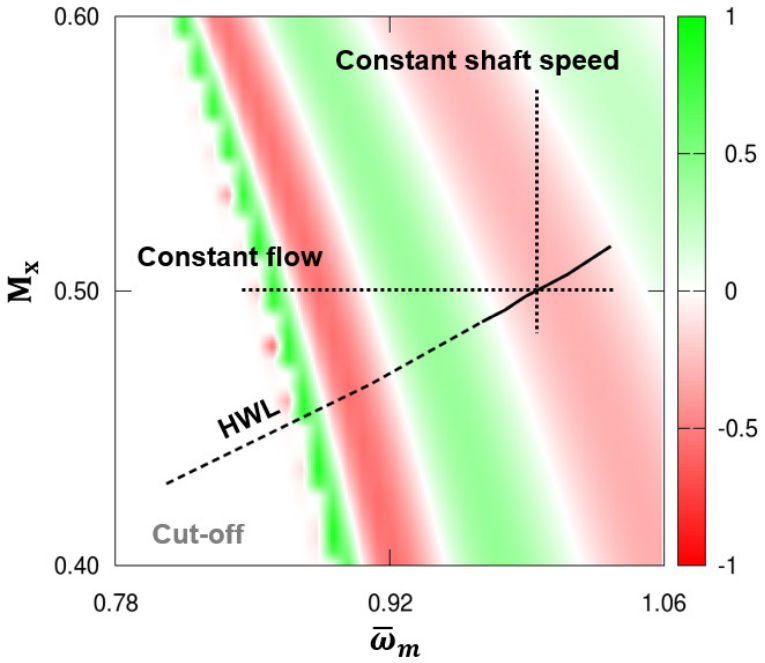
(3) Determine the flutter bite speed range for a fixed fan operating line. To achieve this goal, the 'flutter index' can be calculated for a fixed intake length L/D and a fixed fan working line (i.e. M_x is dependent on $\bar{\omega}_m$).

These applications are discussed in detail in the following sections.

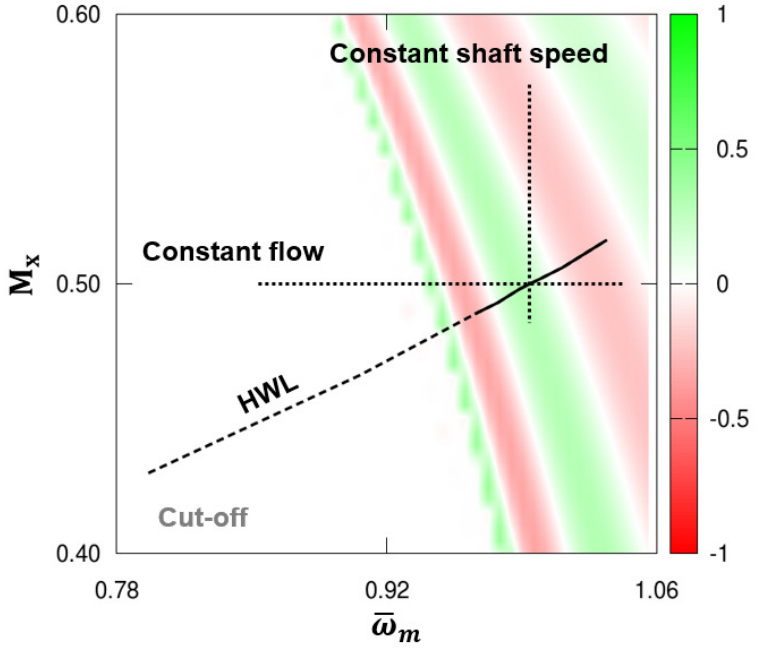
6.5.1 Unstable operating conditions for an intake design

For a particular intake design (fixed L/D), it is possible to calculate the amplitude and phase of the acoustic reflections and the corresponding flutter index matrix as a function of axial flow Mach number M_x and the modal frequency $\bar{\omega}_m$.

Figure 6.37 shows the contour plot of the calculated flutter index matrix as a function of axial flow Mach number M_x and modal frequency $\bar{\omega}_m$ for an intake length of $L = 1.37D$. The contour of the flutter index is defined as green for beneficial effects (i.e. positive values of additional aero-damping due to acoustic reflections from the intake), and red for detrimental effects (i.e. negative values of additional aero-damping) and white for no effect. In the cut-off region, which can be seen at the lower left corner of the plot with low M_x and $\bar{\omega}_m$, the intake has negligible effects on the damping of the fan. It is worth mentioning that for modes that are slightly cut-off (close to the border of the cut-off region), acoustic waves generated by the vibration



(a) 2ND



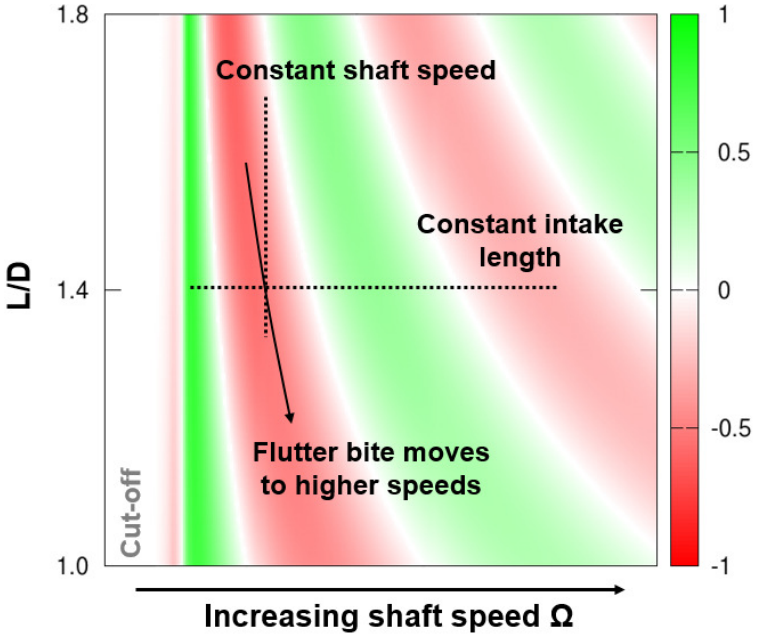
(b) 3ND

Figure 6.37: Flutter index τ contour for the intake $L = 1.37D$ as a function of M_x and $\bar{\omega}_m$.

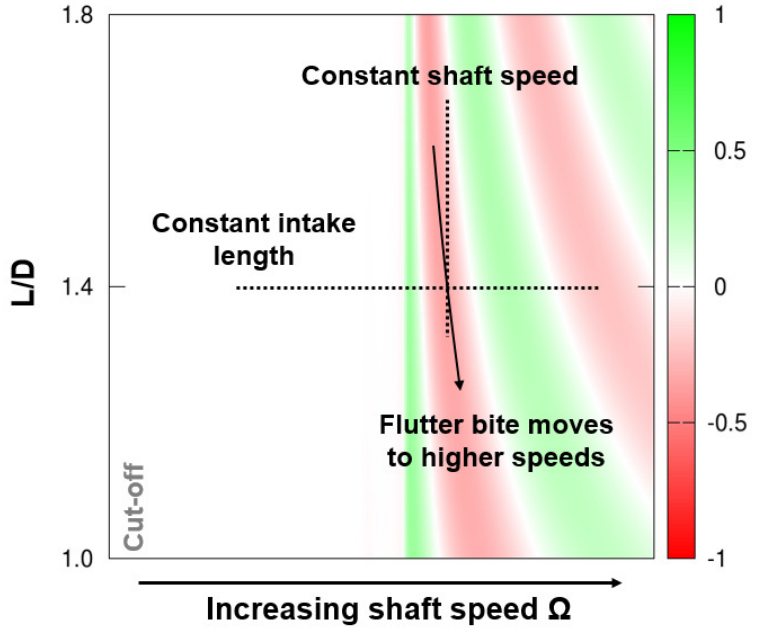
of the fan can still propagate to and be reflected from the intake opening, though their amplitude and effect are weakened by the exponential decay.

It can be seen from Figure 6.37 that the 2ND mode becomes cut-on at a lower axial Mach number and frequency (in stationary frame) than the 3ND mode, indicating that the intake has a wider region of influence on the 2ND mode. As M_x or $\bar{\omega}_m$ increase, in other words when the mode becomes more cut-on, the relative amplitude of acoustic reflections from the intake decreases (as shown in Figure 6.26), which manifests as a gradual decay of contour colour intensity in Figure 6.37. Moreover, it is also seen from Figure 6.26 that the period of variation increases with the increase of frequency, which can be identified as the widening of the contour bands towards higher frequencies in Figure 6.37.

The usefulness of this type of contour plot can be explained as follows: for a particular intake design, i.e. intake length and diameter, one can construct the contour plot of flutter index matrix independent of the design of the fan. Having obtained the contour plot(s) for the mode(s) of concern, one can map the working line (M_x in the intake as a function of fan speed or similarly as a function of frequency $\bar{\omega}_m$) for various fan designs on the contour to calculate potential flutter bite speed range. This is illustrated in Figure 6.37 which shows a constant exhaust nozzle area high working line (HWL) for the case studied (black curve). The effects of acoustic reflections from the intake can thus be investigated based on the crossings of the operating line with the flutter index contour, and the fan speed range where the blades are prone to flutter bite can be easily identified as the crossing with the red bands. The operating speed range corresponding to the potential flutter bite (characterised by the phase difference between the outgoing and the reflected acoustic waves) can be predicted by the proposed analytical model without the need for unsteady CFD computations. This method can be very useful during experimental testing stages of an engine, where possible flutter bite regions need to be identified prior to engine running. Furthermore, the predicted speed range for flutter bite can be used to narrow down the range within which unsteady CFD investigations may be required, which could lead to a significant reduction of computational time and resources.



(a) 2ND



(b) 3ND

Figure 6.38: Flutter index contour on the high working line (HWL) as a function of intake length L/D and shaft speed Ω.

6.5.2 Relationship between intake length and aero-damping

For a particular fan blade design, there is a known relationship between M_x and the fan speed Ω giving $\bar{\omega}_m$ as shown in Equation 6.2. It is possible then to study the effects of the intake geometry (L/D) on fan flutter stability. Figure 6.38 shows the contour of the calculated flutter index matrix as a function of frequency $\bar{\omega}_m$ and the intake length L/D based on the fan working line (the solid black curve shown in Figure 6.37). A decrease of band intensity can be identified with the increase of shaft speed. Moreover, as a result of smaller phase change through the intake duct, it is seen from the plot that shorter intakes show slower variation of the flutter index than those of longer intakes. It is also noticed that the intensity of the contour is higher at frequencies just above cut-on and decreases with the increase of frequency (as shown in Figure 6.26). Therefore longer intakes induce more cycles of positive and negative effects on blade aero-damping than shorter intakes, whereas shorter intakes have a wider span of individual beneficial effect band (green) and detrimental effect band (red). It is also seen from the plot that longer intakes have a tendency of moving the flutter bite to a lower speed, which is in agreement with the findings in the studies with the real intake (in the previous section). The observations are in agreement with the CFD computations shown in Figure 6.34.

The usefulness of this type of contour plot can be shown as follows: for a particular fan design the known relationship between M_x and $\bar{\omega}_m$ can be used to construct the contour plot of 'flutter index' as a function of intake geometry L/D and frequency $\bar{\omega}_m$. This can become useful in the early design stages of an engine where an intake is to be designed or chosen to avoid potential flutter bites.

6.5.3 Flutter bite speed range

In order to explore the applicability of the proposed flutter index contour plots, flutter computations of the 2ND and 3ND modes were carried out by varying the fan speed along the high working line (illustrated as the solid black curve in Figure 6.37). Experimentally measured vibration frequencies of the fan at each speed for the 1F mode were used in the computations. The calculated aero-damping of the fan in the fan-intake assembly system ($L = 1.37D$) along the high working line is plotted in Figure 6.39 and is

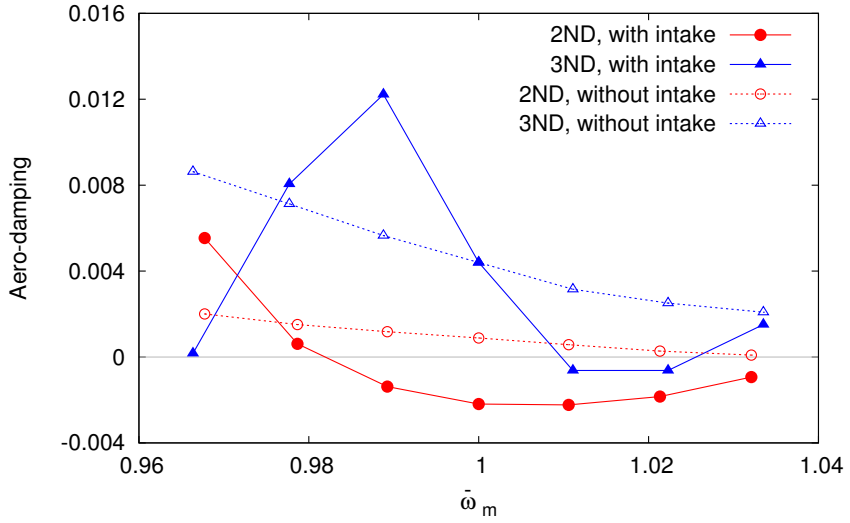


Figure 6.39: Aero-damping of the fan on the operating line, $L = 1.37D$.

compared with the aero-damping of the isolated rotor as a function of $\bar{\omega}_m$ (corresponding to increasing shaft speed Ω). It can be seen from the plot that in the absence of acoustic reflections, the fan is predicted to be stable for both 2ND and 3ND modes over the speed range studied. With the introduction of acoustic reflections from the intake, an unstable region (i.e. flutter bite) is seen to occur at $0.99 < \bar{\omega}_m < 1.03$ for the 2ND mode and $1.01 < \bar{\omega}_m < 1.02$ for the 3ND mode.

Figure 6.40 shows the calculated additional aero-damping due to acoustic reflections from the intake (as the difference between the solid and dashed lines in Figure 6.39) compared with the calculated flutter index, where a good agreement can be seen between them. The flutter bite speed range is correctly calculated for the 3ND mode, and is under-predicted by approximately 1% (in terms of $\bar{\omega}_m$) for the 2ND mode.

The power of the proposed methodology is clearly demonstrated in this section. Contour plots of the calculated flutter index matrix can be constructed for a particular intake design, on which the operating lines of different fan designs can be mapped and the potential flutter bite speed range can be determined. The proposed flutter index plots for fan flutter bite are in a sense similar to the Campbell diagram for rotor-stator interactions, where possible instabilities can be identified in the design stage without the need for experimental testing or unsteady CFD computations. Moreover,

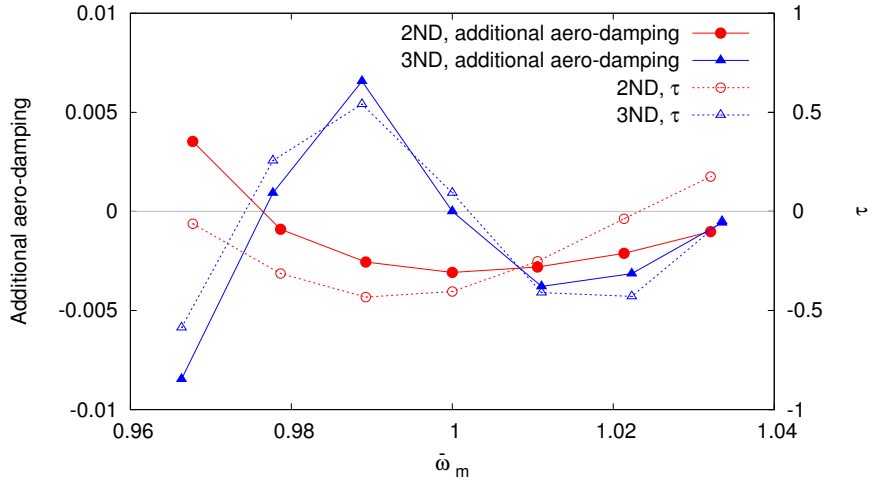


Figure 6.40: Additional aero-damping due to intake reflections on the operating line, $L = 1.37D$.

for a given fan blade and intake design, the predicted speed range for flutter bite can be used to narrow down the range of CFD flutter computations, leading to a significant reduction of computational time and resources that are valuable in the design stages of an engine.

6.6 Comparison With Test Results For A Real Intake

Based on the proposed methodology, the flutter index is used in this section to predict the speed range of flutter bite due to acoustic reflection from a real intake geometry.

The intakes used on most of the modern aero-engines differ from the intakes investigated in the previous sections due to the geometry of spinner and a more complex streamline profile of the casing walls, which result in a non-uniform flow field and a more complex behaviour of propagating acoustic modes. The amplitude and phase of the acoustic waves propagating in such an intake cannot be accurately represented with the assumption of a constant radius and axial Mach number. This type of problem has been investigated by Rienstra [107] and Cooper and Peake [108] where sound propagation was studied in a slowly varying cylindrical duct. Analytical results regarding the variation of mode amplitude and phase change in the

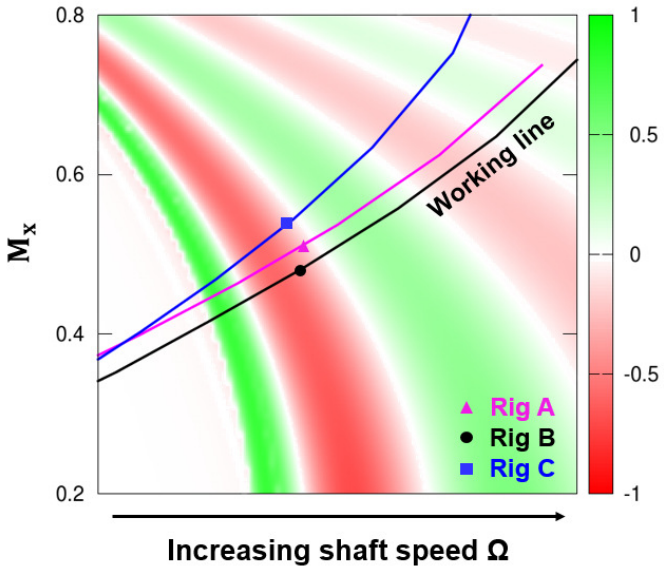


Figure 6.41: Flutter index τ contour for the 1F/2ND mode of rig fan blades with a real intake $L = 0.69D$ as a function of M_x and shaft speed Ω.

axial direction were obtained with some degree of success.

On the other hand, the criterion for the maximum decrease in aero-damping at a phase difference of 90°(i.e. flutter index of -1) is independent of the intake geometry (as demonstrated by the computations with the 'acoustic bump', the annular cylindrical intake and the real intake). Therefore the current model is able to be extended for the application to real intakes. This is achieved by discretising the intake duct axially and solving the wave equation locally based on the local duct geometry and the local axial Mach number using Equation 4.26 and Equation 4.27. The phase variation of the propagating waves can be obtained as a sum of phase changes through the discretised sections.

The proposed method is applied on three rig fan blades to predict the speed of flutter bite due to acoustic reflection from a real intake geometry ($L = 0.69D$) [10]. Using the same intake, experimental tests were performed at various speeds for the three fan blades, during which the operating lines and stability boundaries were measured.

Figure 6.41 shows the calculated flutter index along with the measured operating lines of the three rig fan blades. The location of the deepest

Speed	Rig A	Rig B	Rig C
Measured	75%	71%	80%
Model	73%	70%	78%

Table 6.1: Comparison of measured and predicted 1F/2ND flutter bite speed for the fan blade using the $L = 0.69D$ intake.

flutter bite for the three blades measured in the test (corresponding to the minimum flutter margin) are also show in this plot as solid dots. Moreover, Table 6.1 shows the comparison between the measured and calculated fan speeds corresponding to the deepest part-speed flutter bite. It can be seen from Figure 6.41 and Table 6.1 that the predicted flutter bite speeds show good agreement with the measured results. The under-prediction of the flutter bite speed is believed to come from the radial profile of flow in the intake (which is assumed to be uniform by the analytical model) and the differences in the geometry of duct opening. Nevertheless, the behaviour of the part-speed flutter bite of fan blades driven by acoustic reflection from the intake is well represented by the proposed methodology. Moreover, it is seen from Figure 6.41 that a second flutter bite occurs at high speed, which has a slightly wider speed range but a much lower 'depth' (i.e. lower contour intensity). This observation is in agreement with the findings in Section 6.4.4, e.g. the two 'danger zones' highlighted in Figure 6.34 accompanied by the loss of blade aero-damping.

6.7 Effects of Intake Lip Geometry

The analytical prediction method for flutter bite presented in Section 6.5 is devised based on the assumption of infinitesimally thin intake wall, where the geometry of the lip is ignored. This is rarely the case in real applications, where the geometry of the lip is carefully design for other operability considerations. Therefore, the effect of intake lip geometry, namely the lip radius, on the reflected acoustic waves is investigated in this section.

Figure 6.42 shows the profiles for the four intakes used in this study. The intakes considered in this study are of axi-symmetric design with a straight casing wall profile and a constant radius lip geometry. Four different lip radii are studied here, namely $r_{lip}/D = 0.05$, $r_{lip}/D = 0.12$, $r_{lip}/D = 0.24$

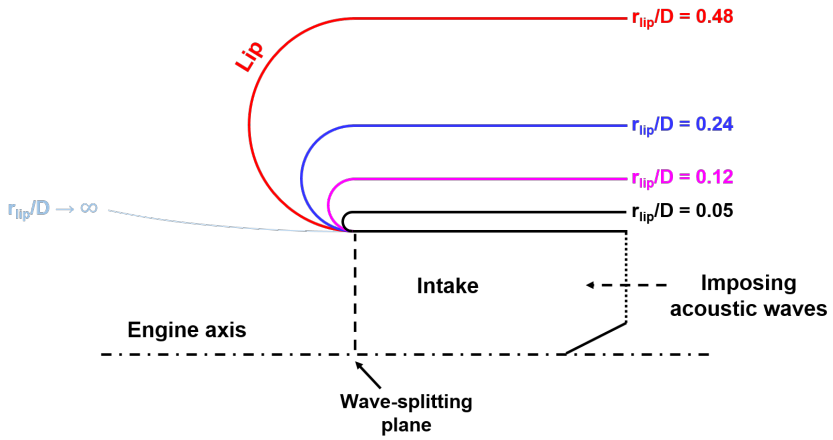


Figure 6.42: Profiles of intake geometry used in this study.

and $r_{lip}/D = 0.48$. It is worth noting that the intake geometries studied here may not be representative of typical industrial design, however they allow one to investigate the effect of lip radius in a straightforward fashion.

In this study, computations are performed for the intake in an isolated setup (i.e. without the fan). The mean flow in the intake is computed through steady state CFD computations with sea-level static atmospheric boundary conditions at far-field inlet boundaries and static pressure boundary conditions at the outlet boundary ($PTBC$ introduced in Section 3.3). The boundary conditions are fixed for all the computations for different intake geometries. The average mean flow Mach number in the intake in this study (roughly) corresponds to the operating point $m_{ref} = 0.95$ of the fan at the non-dimensional speed of $\bar{\Omega} = 0.89$ (Figure 6.4). Figure 6.43 shows the radial profile of calculated flow Mach number at the outlet boundary (dotted line in Figure 6.42) for the four intake geometries. The calculated Mach number profiles are similar for the four intakes studied, with the exception of a small discrepancy at the top 15% radial height for the case of $r_{lip} = 0.04$. This difference is the result of increased turning and acceleration of flow at the intake lip as the lip radius is reduced.

Based on the mean flow solution obtained, unsteady computations are performed in a full annulus approach by imposing acoustic perturbations near the outlet boundary using plane sources (which is mimicking the outgoing acoustic waves generated by the vibration of the fan blades). The imposing of acoustic perturbations is achieved in the same manner as shown

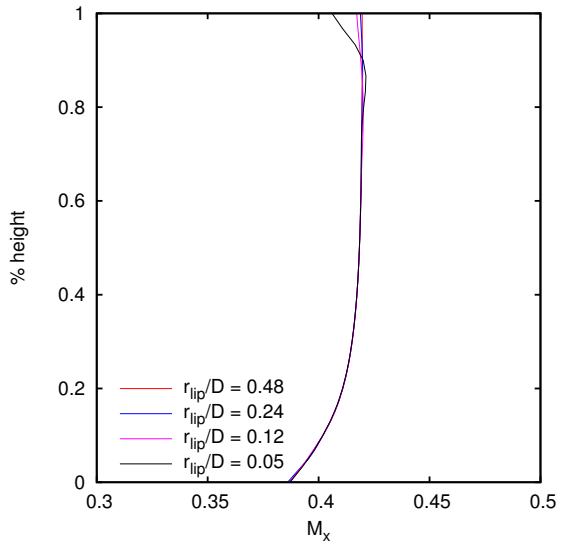


Figure 6.43: Radial profile of axial Mach number at the outlet.

in Section 5.4. In this study acoustic waves with a 2ND pattern and varying perturbation frequency are imposed. The imposed acoustic waves will propagate to the intake highlight and reflect from the opening, which allows investigations of the lip geometry effect on the reflected acoustic wave. The physical time step for the unsteady computations is resolved as 200 time steps for one complete cycle of the acoustic mode of concern in the stationary frame of reference. This time step was obtained by performing a temporal convergence study. A wave-splitting procedure is performed to split the unsteady perturbations into propagating waves, based on which the amplitude ratio of the reflection coefficient at the intake highlight can be obtained.

Figure 6.44 shows the amplitude ratio of reflection coefficient obtained from wave-splitting of unsteady CFD solutions as a function of cut-on ratio (or blade vibration frequency). The reflection coefficient is calculated at the axial location corresponding to the highlight of the $r_{lip}/D = 0.05$ intake for all the cases (as illustrated by the dashed line in Figure 6.42). Also shown in this plot is the reflection coefficient calculated using the analytical method described in Section 4.5. It can be seen from the plot that a resonance is experienced at the cut-on ratio of 1 when the acoustic mode is just cut-on. The amplitude of reflection decreases as the mode becomes more cut-

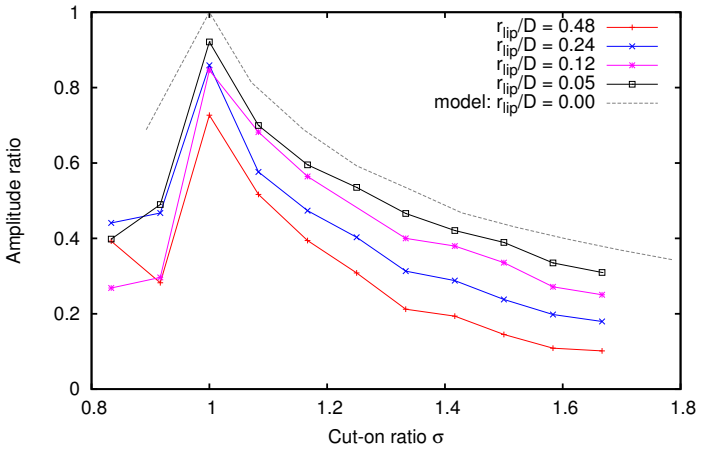


Figure 6.44: Amplitude ratio of reflection coefficient for different intake lip geometries.

on. These observations are in agreement with the findings in the previous sections. More importantly, the amplitude of reflection coefficient for the four intake geometries is lower than the analytically calculated values, which shows an decrease with the increase of the lip radius. This can be understood by considering the two extreme situations: $r_{lip}/D = 0$ and $r_{lip}/D = \infty$. Due to the assumptions made, the analytical calculations represent the thin duct wall limit with $r_{lip}/D = 0$. On the other hand, as r_{lip}/D tends to infinity, the intake opening vanishes as it transforms into a long straight cylindrical duct (as shown in Figure 6.42), which results in zero amplitude of reflection as there is no duct area change (i.e. no impedance change). Therefore, the amplitude of reflection for any real intake lies between the region bounded by the two aforementioned limits. With the increase of lip radius, the amplitude of reflection coefficient changes from a value close to the analytical predictions ($r_{lip}/D = 0$) to a value of zero (r_{lip}/D approaches ∞). It should be mentioned that the phase change of acoustic waves reflecting from the intake opening is not presented here since the (axial) reflection location is different for each geometry due to different intake length (from the most forward point of lip to the outlet).

The effect of intake lip geometry is clearly shown in this study, where the amplitude of reflection shows dependency on the radius of the lip. These effects are not captured by the analytical method which assumes zero lip radius. Accurate prediction of the effect due to acoustic reflection from a

real intake would require the consideration of the effect due to lip geometry, which requires further improvements of the analytical model. Moreover, with the increase of lip radius, the reflection mechanism of acoustic waves from the intake opening, which is assumed to occur wholly at the intake highlight plane in the analytical method, becomes more complex due to the continuous change of duct geometry and flow field in the lip region. An in-depth aero-acoustical study of the reflection mechanism at such an intake opening may shed more light on these findings. In general, the decrease of intake lip radius leads to a higher reflection amplitude, and is thus more likely to cause flutter.

7 Acoustic Driven Flutter of Embedded Rotors

The main findings of this chapter have been reported in [111, 112].

7.1 Overview and Problem Description

This chapter describes the work on the flutter of an embedded rotor in a multi-stage compressor due to acoustic reflections from other blade rows in the compressor. This type of flutter does not require the stalling of the blade and can occur when the slope of the characteristic for the rotor is still negative. The need for this research is driven by the outcome of recent rig tests for an embedded rotor within a multi-stage compressor, where such a flutter event was recorded in the absence of flow separation and at a relatively high reduced frequency on the surfaces of the rotor blade. Moreover, Titanium blade-integrated-disks ('blisks') are becoming widely used over traditional bladed-disk assemblies leading to a significant reduction of blade mechanical damping [5]. For such structures, the main source of damping to the blade comes from the air flow. Thus accurate prediction of blade damping contribution due to aerodynamic forces becomes vital.

During a sea-level working line acceleration vibration survey of the E3E axial flow core engine (Figure 7.1 [4, 113]), non-synchronous vibration was measured on the blades of Rotor 2 blisk within the 9-stage high pressure (HP) compressor. Figure 7.2 shows the time history of the rotor speed and the measured blade response using 'Blade Tip Timing' (BTT) and casing mounted pressure transducer signals ('Kulites') during the vibration event. Analysis of the measured data confirmed the cause of instability to be flutter in the 1st flapwise bending (1F) mode with a zero nodal diameter (0ND) pattern, and at a reduced frequency of 0.67.

This phenomenon was very unusual as it occurred in a very narrow speed

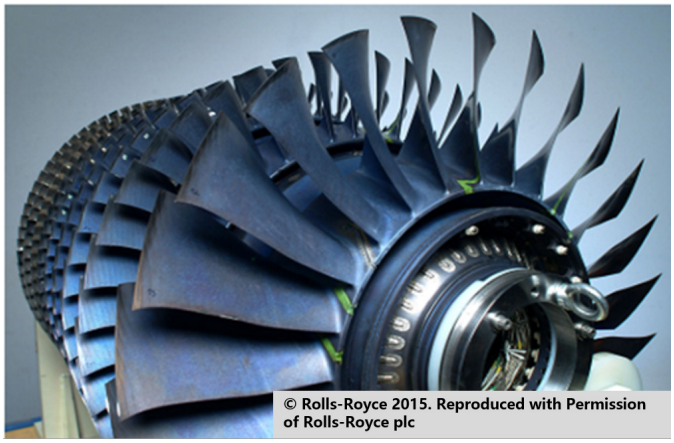


Figure 7.1: 9-stage E3E high pressure compressor.

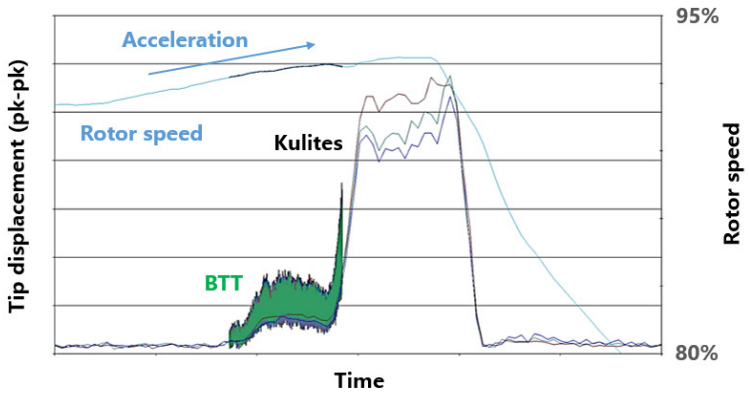


Figure 7.2: The measured flutter event.

range (around 93.1% speed) at a flow condition well away from stall. Moreover, the vibration occurred at a reduced frequency significantly higher than the typical critical flutter frequencies of about 0.4 for 1F mode [3]. For the flow condition at which the flutter event was recorded, the acoustic fields upstream and downstream of the rotor were found to be cut-on for low inter-blade phase angle modes (obviously the $(0, 0)$ mode is always cut-on), which indicates that the main cause of flutter is not related to the flow and modeshape driven flutter described in [11].

In order to determine the cause of the instability and to avoid future damage to the engine, flutter analyses for the embedded rotor were carried out using unsteady CFD computations at the speed and flow condition of the measured flutter event. However, computation of the isolated rotor using non-reflecting boundary conditions showed no indication of flutter, which confirmed that the cause of the flutter event was not due to the flow-modeshape interactions. Moreover, predicted stability of the rotor was found to be highly dependent on the boundary condition style used (reflecting or non-reflecting) in the unsteady flutter computations. Therefore, acoustic reflection from adjacent blade rows was considered to be the likely cause of the flutter event.

The first objective of this chapter is to investigate the influence of acoustic reflection on the flutter stability of the embedded rotor (i.e. the rotor which experienced flutter instability in the aforementioned test). This is achieved by studying the influence of numerical acoustic reflection from flow boundaries on the predicted blade aerodynamic damping using unsteady computations for the isolated rotor. It will be shown that acoustic reflection due to reflecting boundary conditions may lead to significant over- or under-predictions of the flutter stability of the isolated rotor. Moreover, by splitting the unsteady disturbances into propagating acoustic waves, the relationship between the reflected acoustic wave (from flow boundaries) and its influence on blade aero-damping is studied in this approach.

In the next step, flutter computations are performed in a full annulus multi-row approach to determine the cause of flutter instability for the embedded rotor. It will be shown that, this type of flutter is driven by the acoustic reflection from the blade rows adjacent to the embedded rotor. Moreover, physical insights are obtained regarding the effects of key parameters that are important to acoustic reflection driven flutter, such as

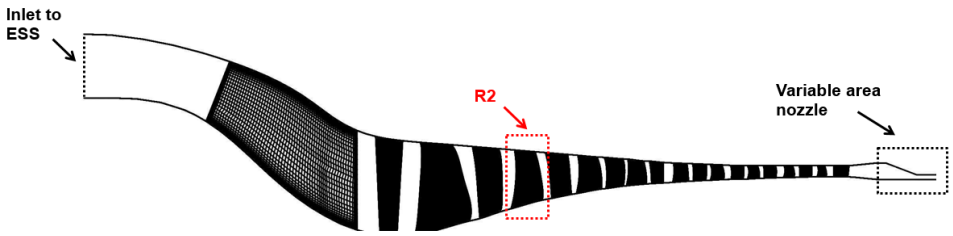


Figure 7.3: Domain for steady state computation.

the vibration frequency and the axial gap between blade rows. The understanding gained could be used to draw out some guidelines for future compressor designs and to devise an alternate strategy for the flutter analysis of embedded rotors.

7.2 Test Case and Computation Model

The test case used for the computations in this chapter, namely the E3E axial flow core engine, was designed and tested by Rolls-Royce Deutschland [4, 113]. The test high-pressure compressor featured 9 highly loaded stages on a single spool contributing to an overall pressure ratio of 22:1, where Titanium blisks were installed on the front stages for weight saving. The inlet guide vanes (IGV) and the first three stages of stator vanes have adjustable blade stagger angle (i.e. variable stator vanes (VSV)) which operate with different settings for varying rotor speed. The domain for steady state computation is shown in Figure 7.3, which includes the engine sector stators (ESS), the whole HP domain and a variable area exit nozzle (as demonstrated in Figure 3.1). The Rotor 2 (R2) of the HP compressor, which experienced flutter instability during the experimental test, is highlighted in the figure. The test rotor has 45 blades and a hub/tip ratio around 0.7. The two adjacent stators, Stator 1 (S1) and Stator 2 (S2), have 38 and 54 blades respectively. It should be noted that for all the studies performed in this chapter, the shroud flow and the penny gaps at the ends of the IGV and VSVs are not modelled. These aspects can be influential in resolving the secondary flows and predicting compressor performance, however, they are of very little importance for the studies of acoustic reflection driven flutter (which is dominated by the inviscid effects).

The grids used for the blading are semi-structured, with hexahedral el-

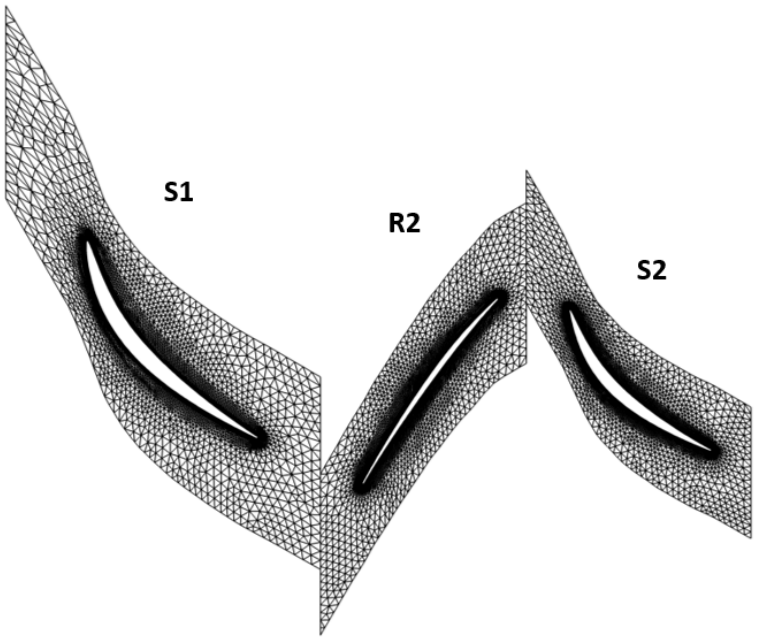


Figure 7.4: Mesh of Stator 1, Rotor 2 and Stator 2 at 90% height.

ements around the aerofoil in the boundary layer region, and prismatic elements in the passage [94]. The end-wall boundary layers are resolved by refining the grid radially towards the hub and casing. Typical passage mesh contains about 300,000 grid points with 39 mesh layers on the blade and 6 layers in the tip gap. In order to accurately resolve the propagation of acoustic waves, approximately 120 mesh points are aligned axially for the shortest wavelength expected.

In the steady computations, the interface boundaries between the stationary intake domain and the rotating fan domain are modelled as mixing planes, whereas in the unsteady computations they are treated as sliding planes. Periodic boundary conditions are prescribed at the passage boundaries so that steady state computations can be carried out in a single passage fashion. The steady state flow solutions for the whole compressor assembly are obtained by imposing boundary conditions of total pressure, total temperature and flow angle (*PTBC*, Section 3.3) at the ESS inlet boundary, while the exit flow is controlled by a choked nozzle (i.e. no boundary conditions needed at the outlet boundary). Constant speed characteristics are obtained by varying the outlet mass flow rate through the adjustment

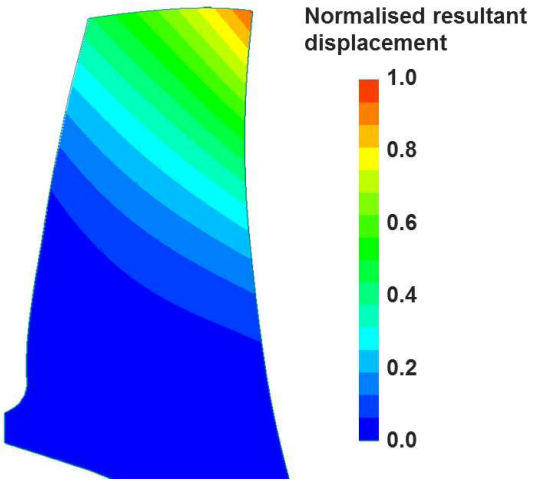


Figure 7.5: Contour of 1F modeshape for R2.

of the exit nozzle area.

Based on the obtained steady state solutions for the whole compressor assembly, flutter computations are carried out for the embedded rotor (R2) at the speed which flutter instability was recorded in the experimental test. In all the flutter computations performed in this work, the blades of Rotor 2 are excited in the first flapwise bending (1F) mode. The modeshape for the 1F mode is shown in Figure 7.5 where the contour represents the blade displacement magnitude. Figure 7.6 shows the spanwise distribution of the blade displacement magnitude at the leading edge for the 1F mode, which clearly illustrates a tip dominated motion. For most of the cases studied in this chapter, the blades vibrate at a reduced frequency of 0.67 (unless otherwise specified).

7.3 Steady State Validations

The overall performance of the whole compressor at the speed which flutter was observed (93.1% aerospeed) is computed by varying the exit nozzle area. A comparison of computed results with experimental measured data is shown in Figure 7.7, which shows the predicted overall pressure ratio plotted against normalised inlet mass flow rate. The computed results at 93.1% aerospeed are compared against measured data at 92.5% speed and 95% speed (due to obvious lack of experimental data at 93.1% speed). It

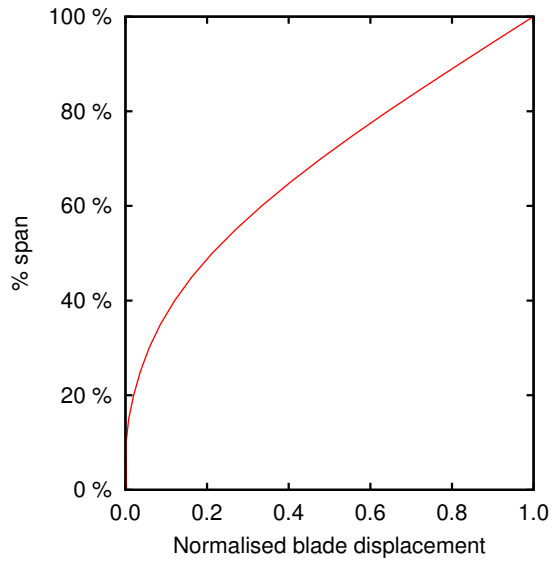


Figure 7.6: Spanwise distribution of R2 leading edge displacement for the 1F mode (values are normalised by the maximum resultant displacement).

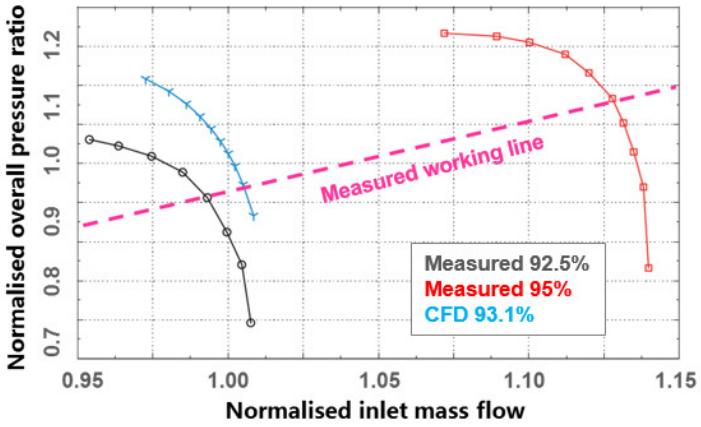


Figure 7.7: Compressor operating map between 92.5% and 95% speeds.

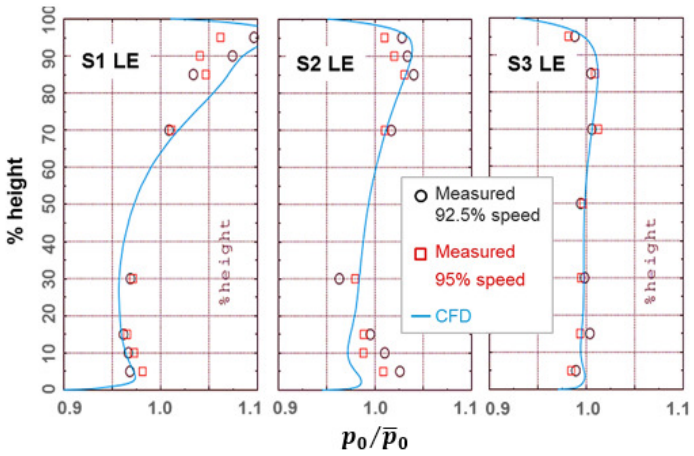


Figure 7.8: Radial profile comparison of total pressure with measured data.

can be seen from the plot that the overall performance is predicted with reasonable accuracy. It should be mentioned that, the last point on the measured 92.5% speed characteristic does not represent the surge boundary at this speed.

Figure 7.8 shows the comparison of computed and measured total pressure profiles at the leading edge of front stage stators, namely S1, S2 and S3. In this plot the solutions at the peak efficiency operating condition (CFD solution at 93.1% speed and measured data at 92.5% and 95% speeds) are displayed. The experimental profiles were measured with leading edge total pressure tappings at various radial heights. The values of total pressure p_0 in this plot are normalised by the respective radial average $\bar{p}_0$. A good agreement between the CFD results and measured data can be seen at the leading edge of Stator 1 and Stator 3. The slight mismatch between CFD and measured total pressure at the root of S2 is believed to be the result of flow separation at the hub of S1 (which then migrates radially outwards), which was not captured in the CFD computations. It should however be emphasised that the results obtained from CFD computations shown in the plot are at 93.1% speed, which are compared with the measured data at 92.5% speed and 95% speed. As can be seen from the measured data in this plot, a small increase of shaft speed (from 92.5% speed to 95% speed) reduces the intensity of this separation by a significant amount and brings the measured data more in line with CFD results. Nevertheless, the general

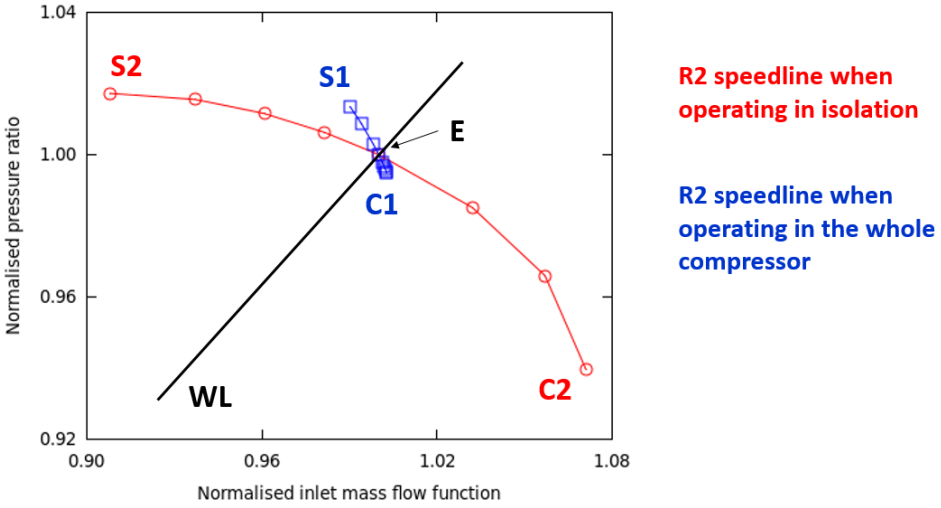


Figure 7.9: Operating conditions of R2 used for flutter computation. WL: working line; E: peak efficiency; S: near stall; C: near choke.

trend is reasonably well calculated especially at higher span locations where the maximum blade displacement occurs and aerodynamic damping induced by the flow is dominant (Figure 7.6).

The steady state flow field at the condition of flutter instability is shown to be in reasonable agreement with the measured data. It will become clear in the following section (by studying the change of R2 aero-damping for various operating conditions) that the discrepancy in the predicted flow field around Rotor 2 does not contribute to the cause of the measured flutter instability.

7.4 Effect of Mean Flow on the Isolated Rotor

Prior to studying the effect of acoustic reflection on flutter stability of the rotor, flutter analyses are performed to investigate the effect of mean flow condition on the blade aero-damping.

Figure 7.9 shows the obtained constant speed characteristics of R2 (at 93.1% speed) plotted as total pressure ratio versus normalised inlet mass flow function. The values in this plot are normalised by the values at the peak efficiency operating point (E). In this plot two characteristics of R2 for the same shaft speed are displayed. The characteristic of R2 when operating in the whole compressor (blue line) is obtained from the steady state com-

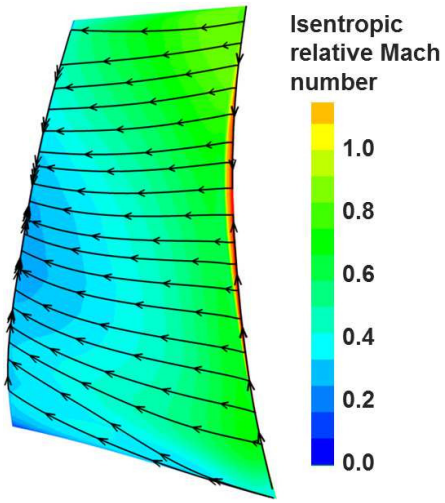


Figure 7.10: Isentropic relative Mach number and streamline on the suction surface of R2.

putations of the whole compressor assembly (i.e. the complete HP shaft) which has been presented in Section 7.3. The working line (WL) and the peak efficiency operating point (E) for this setup are also displayed on this plot. The domain and steady state solution of R2 at the peak efficiency operating point are extracted from the whole compressor computation, based on which the rotor is throttled on its own by scaling the back pressure. The obtained characteristic of R2 using such an approach is displayed in Figure 7.9 as the red line. It can be seen from the plot that by throttling R2 on its own, a much longer characteristic can be obtained. This is because for computations of the whole compressor assembly at this speed, the flow is choked at the stage downstream of R2 (i.e. in the block of R3 and S3). In such situations the throttling of the whole compressor (by means of changing the exit nozzle area) is mainly attributed to the increase of loading in the back stages.

Most of the flutter computations performed in this chapter (unless otherwise specified), the rotor operates at the peak efficiency point, which is illustrated as point E in Figure 7.9. At this condition, the inlet relative flow Mach number at the blade tip is around 0.8 and the flow remains subsonic (apart from the suction peak) over the blade surfaces. Moreover, it is stressed again that at this condition, the flow on the rotor blade surface remains attached and the streamlines at the edge of boundary layer follow the

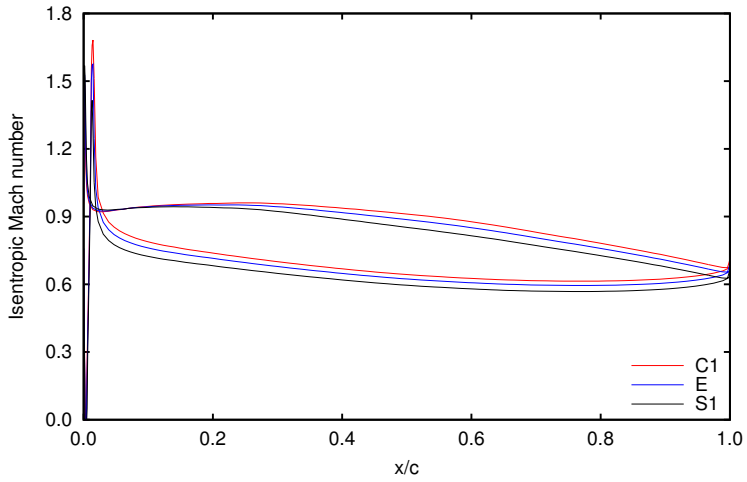


Figure 7.11: Isentropic relative Mach number on the surfaces of R2, C1-E-S1.

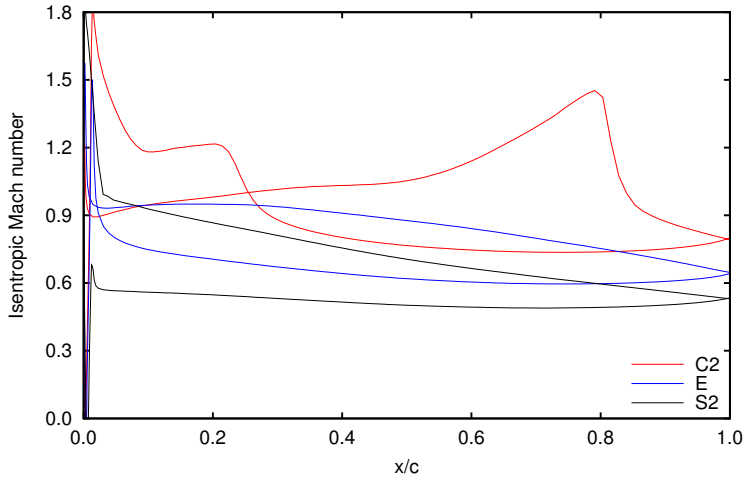


Figure 7.12: Isentropic relative Mach number on the surfaces of R2, C2-E-S2.

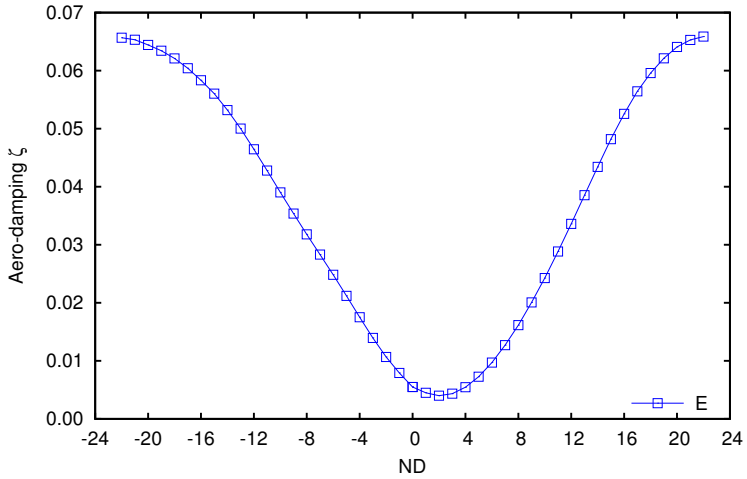


Figure 7.13: Aero-damping of R2 at the peak efficiency operating point *E*.

blade stream sections. This has been illustrated by the isentropic relative Mach number contour and the velocity streamline on the suction surface of R2 in Figure 7.10. In order to study the effect of flow on aerodynamic damping of R2, flutter computations are performed for the isolated rotor (in a long straight duct, i.e. without reflection) at the near choke and near stall operating points on the two characteristics shown in Figure 7.9, namely the *C1-E-S1* and the *C2-E-S2*. Figure 7.11 and Figure 7.12 show the comparison of the isentropic Mach number on R2 surfaces for the aforementioned operating points on the two characteristics. It can be seen that by throttling R2 on its own, the flow on the blade is varied in a wider range, where a shock is clearly seen in the blade passage for the operating point *C2*.

All the flutter computations performed in this section use the full annulus isolated blade row approach (1^{st} flutter computation strategy in Section 3.4). The physical time step used for flutter computation is fixed at 200 time-steps per vibration cycle. This time step is obtained by performing a temporal convergence study.

Figure 7.13 shows the computed aerodynamic damping of R2 at the peak efficiency operating point *E* as a function of nodal diameter. In this plot the aero-damping for the isolated rotor from -22ND to 22ND (corresponding to IBPA from -176°to 176°) is shown. As can be seen from the plot, the isolated rotor shows positive aero-damping for all the nodal diameters, suggesting that the rotor is stable in the absence of interactions from other blade

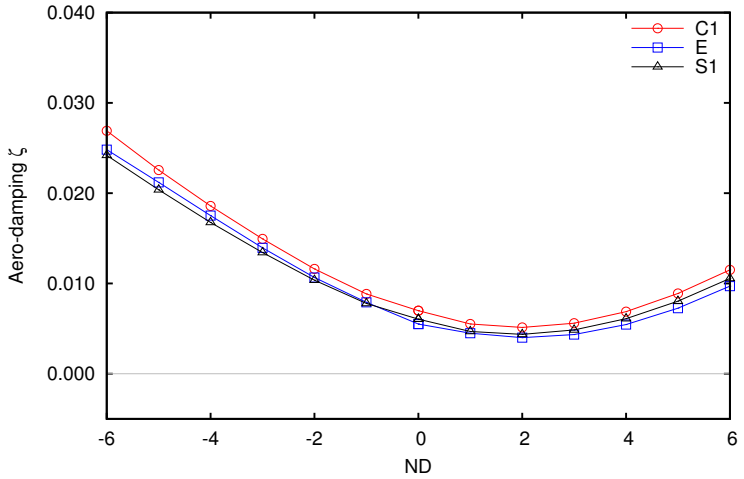


Figure 7.14: Aero-damping of R2 on the C1-E-S1 characteristic.

rows. The least damped mode is seen at 2ND (IBPA=16°). Moreover, the aero-damping of the isolated rotor shows a rapid increase for higher nodal diameters. Considering the statement made and confirmed in the previous chapter that acoustic reflection driven flutter is unlikely to be a problem on its own when the aero-damping contribution due to the blade motion is high (Section 6.1), the higher nodal diameters in this case should not pose a stability concern, and are thus not considered in the following analyses. Therefore, for the case studied here, nodal diameters in the range of -6 to 6 (which corresponds to an inter-blade phase angle between 48°and 48°) are studied.

Figure 7.14 shows the computed aerodynamic damping of R2 as a function of nodal diameter. In this plot the results for the operating points *C1*, *E* and *S1* when operating in the whole compressor are displayed. The aero-damping distribution of higher nodal diameters are not shown. As can be seen from the plot, the isolated rotor shows positive aero-damping for all the nodal diameters. It is clearly seen in Figure 7.14 that the aerodynamic damping of R2 does not vary significantly with the throttling of the whole compressor. This is obvious since the flow on the R2 blade surfaces remains largely the same as the compressor is throttled (as shown in Figure 7.11).

Figure 7.15 shows the computed aerodynamic damping of R2 as a function of nodal diameter. In this plot the results for the operating points *C2*, *E* and *S2* when R2 is operating in isolation with scaled back pressure are

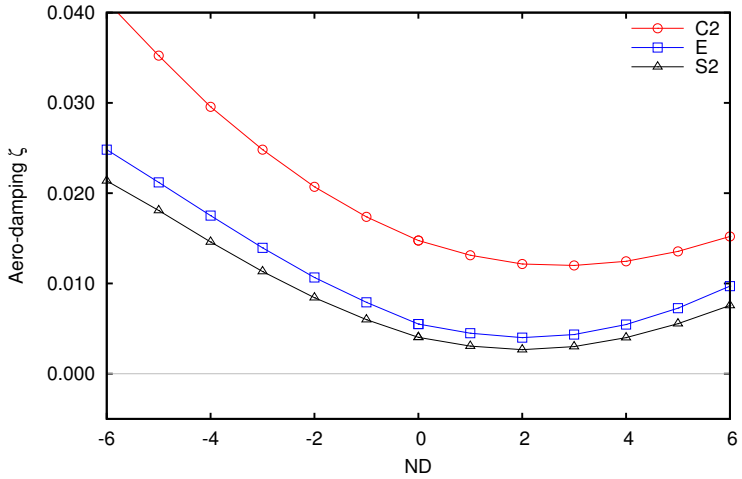


Figure 7.15: Aero-damping of R2 on the C2-E-S2 characteristic.

displayed. It can be seen from the plot that aerodynamic damping of R2 when throttled on its own (*C2-E-S2*) shows a larger variation than that due to the throttling of the whole compressor (*C1-E-S1*), which is the result of larger flow change on the surfaces of the blade (as shown in Figure 7.12). A decreasing trend in R2 aero-damping is observed when the operating point moves closer to stall. However, what's important is that the aerodynamic damping of R2 remains positive for operating conditions ranging from *C2* to *S2*.

The observations based on Figure 7.14 and Figure 7.15 indicate that the flutter of the Rotor 2 does not occur by itself (i.e. without acoustic reflection). Furthermore, due to the high hub/tip ratio blade geometry (especially in high-pressure compressors), the flow and modeshape driven flutter caused by the migration of separated flow on the blade suction surface is unlikely to occur [11]. In such situations, the blade is more likely to encounter stall rather than flutter. Therefore, flutter of such a rotor blade would require the acoustic reflections from adjacent blade rows.

Figure 7.16 shows the cut-on frequencies of acoustic modes at the leading and trailing edge of R2 as a function of nodal diameter for the first two radial orders ($n = 0, 1$). The cut-on frequencies are calculated based on the mean flow solution using Equation 4.21. The results for low nodal diameters are shown as most cut-on acoustic modes are situated in this range. Also shown in this plot is the blade vibration frequency of the R2 at the reduced

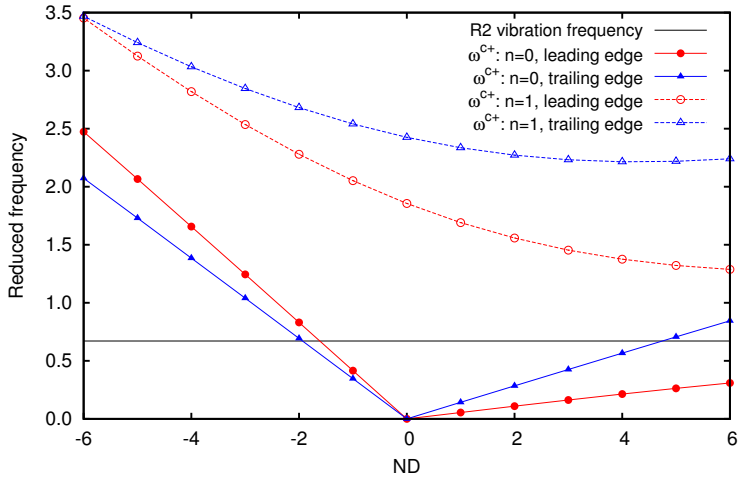


Figure 7.16: Cut-on frequency (in relative frame of reference) for low nodal diameters.

frequency of 0.67 (black line). The frequencies shown in this plot are in the relative (rotor) frame of reference (hence a constant vibration frequency line due to disk stiffness). It is seen from this plot that for the flow and vibration frequency studied, the acoustic field for the radial order $n = 0$ (solid curves) is cut-on between -1ND and 4ND at the trailing edge of R2, and cut-on between -1ND and 6ND (for the range of ND shown here) at the leading edge. The wider cut-on region at the leading edge than the trailing edge is attributed to the flow turning by the rotor (i.e. increase in swirl). On the other hand, the cut-on frequencies for the radial order $n = 1$ (dashed curves) are significantly higher compared with those for $n = 0$ (solid curves), resulting in all the $n = 1$ modes being cut-off for the flow condition and blade vibration frequency in this study. The same conclusion can be made for radial orders $n > 1$, where the cut-on frequencies increase with the increase of radial harmonic. For the least damped modes of R2, in the vicinity of 0ND to 4ND, the acoustic modes of radial order $n = 0$ are cut-on on both upstream and downstream sides of R2. This can lead to two consequences: (1) aero-damping of the isolated rotor does not change significantly with the variation of mass flow [11], which was observed in Figure 7.15; (2) these acoustic waves (generated by blade vibration) can propagate in the compressor duct without attenuation and be reflected from the other blade rows.

The following sections will concentrate on explaining the influence of the acoustic reflection and establishing the relationship between the reflected acoustic wave and its effect on blade aerodynamic damping. All the computations are performed at the peak efficiency operating point (E) (unless otherwise specified).

7.5 Acoustic Reflection from Flow Boundaries

It was shown in the previous chapter (Chapter 6) that acoustic reflections from a 'bump' feature plays an important role in the flutter stability of a fan blade. Moreover, it is possible to change the aerodynamic damping of the blade by changing the location of the bump, i.e. by changing the phase of the reflected wave. Similarly, acoustic reflections caused by the numerical boundary conditions at the inflow and the outflow boundaries could also affect the prediction of flutter stability for an embedded rotor. Therefore, for the studies in this section, the physical boundary conditions ($PTBC$, Section 3.3), which are commonly used in turbomachinery applications and are known to be reflecting, are used to reflect acoustic waves from known locations. The outcome of this study is two-fold: (1) study the influence of acoustic reflection from boundary conditions on the predicted flutter stability of a rotor blade; (2) investigate the relationship between the reflected acoustic wave and the blade aerodynamic damping. Moreover, the study will demonstrate the consequences of inaccurate boundary conditions on the flutter prediction of an isolated rotor.

Flutter analyses of the isolated R2 are conducted for the 1F/1ND mode at a reduced frequency of 0.67 at the peak efficiency operating condition (point E in Figure 7.9). At this condition, the 1ND mode (IBPA=8°) is cut-on on both the upstream and downstream sides of the rotor, and is known to reflect from the flow boundaries using the $PTBC$ boundary conditions. The choice of other low inter-blade phase angle modes would give similar conclusions, and only the results for 1ND mode are presented here. The flutter computations are performed using the single passage approach (3^{rd} flutter computation strategy in Section 3.4). The physical time step used for flutter computation is fixed at 200 time steps for one blade vibration cycle. This time step is obtained by performing a temporal convergence study.

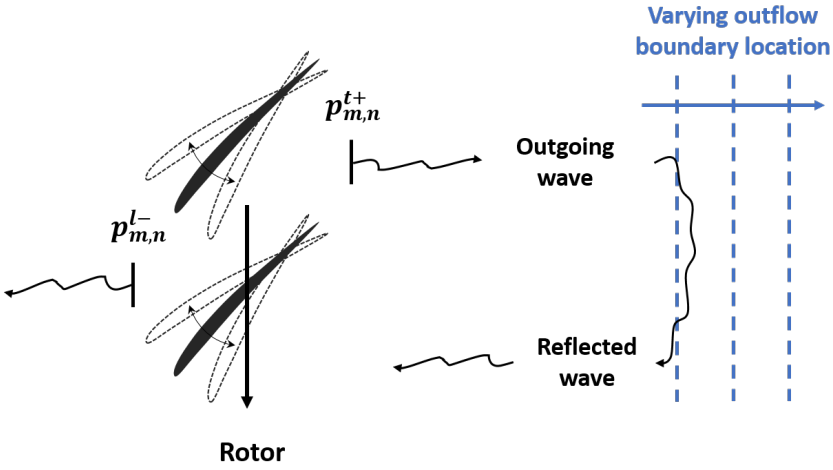


Figure 7.17: Acoustic reflection from the outflow boundary.

In the first step, flutter computations are performed with the outflow boundary placed at different axial locations (the variation of the inflow boundary location yields similar conclusions and is not presented here). Figure 7.17 illustrates schematically the variation of outflow boundary location. The variation of outflow boundary location is achieved by attaching a straight duct downstream of the rotors. In order to maintain (roughly) the same steady state operating condition for computations with different boundary locations, the end-walls of the extension duct are modelled as inviscid so as to minimise boundary layer growth. Different combinations of boundary conditions are applied at the inflow and outflow boundaries to study their effects on the predicted blade aerodynamic damping. The obtained results are categorised into four series:

- *PTBC/PTBC*: reflecting *PTBC* at both inflow and outflow.
- *PTBC/RIBC*: reflecting *PTBC* at inflow and non-reflecting *RIBC* at outflow.
- *RIBC/PTBC*: non-reflecting *RIBC* at inflow and reflecting *PTBC* at outflow.
- *RIBC/RIBC*: non-reflecting *RIBC* at both inflow and outflow.

where *PTBC* corresponds to the boundary conditions of total pressure, total temperature and flow angle for the inflow and static pressure for the outflow,

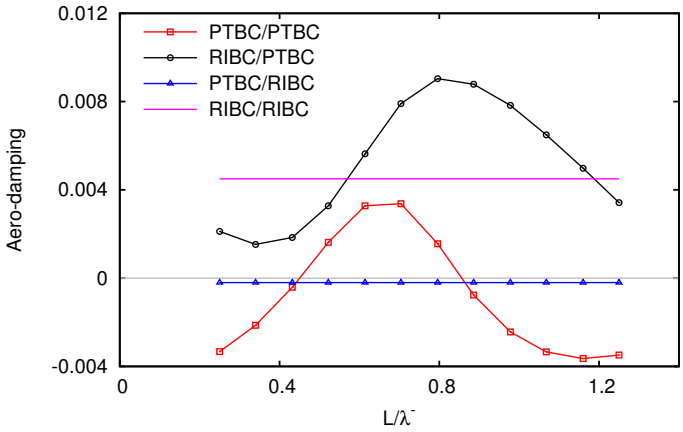


Figure 7.18: Aero-damping as a function of boundary location.

and *RIBC* denotes non-reflecting boundary conditions based on Riemann invariants (Section 3.3). It should be emphasised that the base steady flow remains nearly the same regardless of the boundary conation styles used. Moreover, the results in Figure 7.14 and Figure 7.15 show that the steady flow does not influence the aero-damping significantly.

Figure 7.18 shows the blade aerodynamic damping computed using unsteady CFD computations as a function of non-dimensional distance. The non-dimensional distance $\frac{L}{\lambda^-}$ denotes the ratio between the distance from the outflow boundary to rotor trailing edge L and the wavelength of the upstream propagating acoustic wave λ^- at the trailing edge. The results for the four series of computations are discussed in the following paragraph.

The series with non-reflecting boundary conditions at both inflow and outflow boundaries (*RIBC/RIBC*, pink curve) represent the computations of the isolated rotor in a long straight duct, where acoustic reflection is absent from both upstream and downstream. Hence the obtained blade aero-damping does not vary with the location of the outflow boundary. The series with non-reflecting boundary conditions prescribed at the inlet and reflecting boundary conditions at the outlet (*RIBC/PTBC*, black curve) is similar to the computations of the rotor with an 'acoustic bump' (Section 6.4) in the downstream field, where the location of the bump was varied relative to the rotor. Despite the introduction of acoustic reflection from the outlet boundary, the aero-damping of the blade remains positive, where the least stable condition is found at a distance of about 0.34 and the most

stable condition is at about 0.8. Moreover, it is important to note that for the condition studied, the amplitude of aero-damping variation is nearly the same order of magnitude as the blade aero-damping due to the vibration motion alone (i.e. *RIBC/RIBC*, pink curve). The series with reflecting boundary conditions at the inlet and non-reflecting boundary conditions at the outlet (*PTBC/RIBC*) is shown as the blue curve. It is seen that the change of outlet location does not affect the aero-damping of the rotor blade since acoustic reflection occurs only upstream of the rotor at the inlet, which remains unchanged (in terms of amplitude and phase) when the location of the outflow boundary is varied. Moreover, a decrease of blade aero-damping is seen from the series *RIBC/RIBC* to *PTBC/RIBC*, which is attributed to the effect of acoustic reflection from the inflow boundary (which has a destabilising effect for the location of inflow boundary in this study). It is seen that the presence of acoustic reflection from the inlet causes the blade to be just unstable for this particular inlet location. The series with reflecting boundary conditions at both the inlet and outlet (*PTBC/PTBC*) is shown as the red curve. Similar to the trend of the series with reflecting boundary conditions only at the outlet (black curve), the blade aero-damping shows a cyclic variation (more or less about the blue curve) with respect to the boundary distance. It is seen that the blade becomes unstable for a wide range of boundary locations ($0.2 < \frac{L}{\lambda^-} < 0.4$ and $0.9 < \frac{L}{\lambda^-} < 1.2$), and the minimum aero-damping is seen at a different boundary location (compared with the case using *RIBC/PTBC*).

It is clear from the plot that the styles of unsteady boundary conditions have a significant impact on the predicted flutter stability of the isolated rotor, where the change of blade aero-damping due to acoustic reflection can be in the same order of magnitude as the aero-damping due to the blade motion. The findings highlight the importance of the development and implementation of exact unsteady three-dimensional non-reflecting boundary conditions, which remain difficult in practice for time domain CFD solvers [46]. The influence of acoustic reflection on blade flutter stability is clearly shown in Figure 7.18, where the stable blade can become unstable due to acoustic reflections from the upstream and downstream (e.g. at $\frac{L}{\lambda^-} = 0.34$). It is also seen from Figure 7.18 that the variation of blade aero-damping repeats itself with a cycle of approximately one wavelength of the upstream propagating acoustic wave, indicating a relationship between the blade aero-

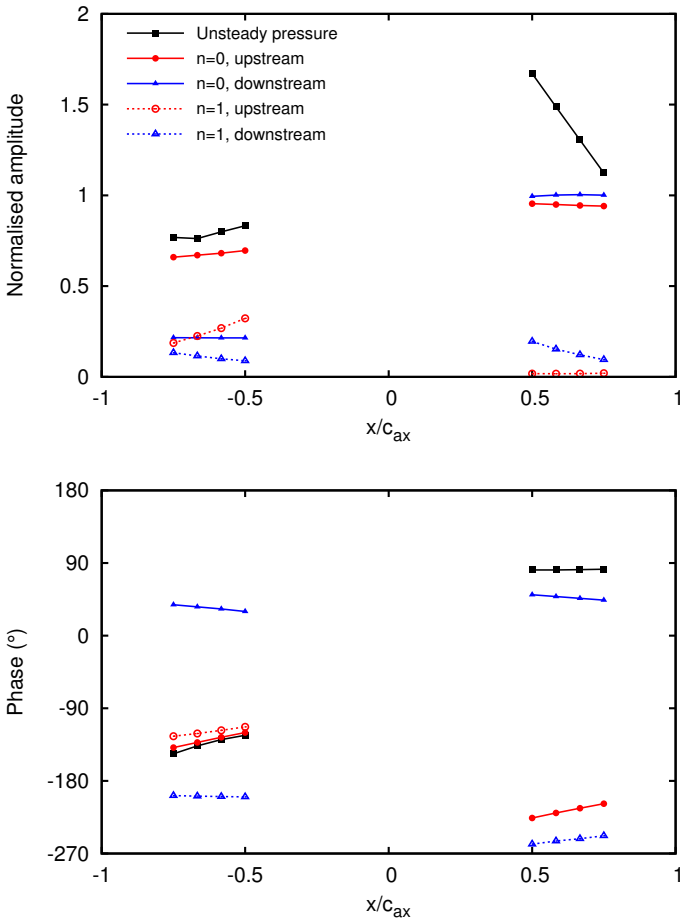


Figure 7.19: Amplitude and phase of acoustic waves at the leading edge and trailing edge, ($PTBC/PTBC$, $\frac{L}{\lambda^{-}} = 0.34$).

damping and the phase of reflected acoustic waves.

In order to investigate the unsteady pressure field around the blade and establish the relationship between the reflected wave and the blade aero-damping, a wave-splitting procedure is performed at the leading and trailing edges of the blade to obtain the amplitude and phase of propagating acoustic waves (i.e. outgoing waves generated by vibration and their reflection from flow boundaries). Figure 7.19 shows the amplitude and phase of unsteady pressure for the upstream (red curves) and downstream (blue curves) propagating acoustic waves as a function of non-dimensional axial location x/c_{ax}. In this plot the results for the first two radial orders ($n = 0, 1$) for the boundary distance of $\frac{L}{\lambda^{-}} = 0.34$ using reflecting bound-

ary conditions at both the inlet and outlet ($PTBC/PTBC$) are displayed. For the plot shown here the leading edge and trailing edge of the blade are located at $x/c_{ax} = -0.5$ and $x/c_{ax} = 0.5$ respectively. It can be seen from these plots that the vibration of blades generates acoustic waves (red curves at $x/c_{ax} < -0.5$ and blue curves at $x/c_{ax} > 0.5$) which propagate away from the blade with a constant phase speed and a nearly constant amplitude. Due to the variation of modeshape along the span (Figure 7.6), the vibration motion excites infinite number of harmonics of the 1ND duct acoustic mode. The amplitude of these excited harmonics decreases with the increase of radial order n, which can be seen in Figure 7.19 for the first two radial orders $n = 0$ and $n = 1$ (the amplitude of higher harmonics are too small and thus not plotted). However, for the flow condition and blade vibration frequency in this study, the acoustic modes with radial order $n > 1$ are cut-off at both the leading and trailing edges of the rotor (see Figure 7.16), resulting in an exponential decay of amplitude as they propagate away from the blade (Equation 4.18). This effect can be clearly seen in Figure 7.19 (dotted curves) where the amplitude of the generated acoustic waves with radial order $n = 1$ diminishes to nearly zero within an axial distance of a quarter of Rotor 2 tip axial chord. Therefore, these higher radial order acoustic modes ($n > 0$) are not considered in the analysis of acoustic reflection from the adjacent blade rows (will be presented in the next chapter). It is also seen in Figure 7.19 that acoustic waves are reflected at the inflow and outflow boundaries with a significant amplitude ratio. For the flow condition and boundary conditions studied here the amplitude of reflection coefficient for the cut-on $n = 0$ mode is about 0.3 at the inflow boundary and about 1.0 at the outflow boundary.

Figure 7.20 shows the phase difference between the outgoing and reflected acoustic waves at the trailing edge of the blade as a function of non-dimensional boundary location. The phase difference is calculated from the difference between the solid red and the solid blue curves at the blade trailing edge ($x/c_{ax} = 0.5$) in Figure 7.19. In this plot the results for the series computed with non-reflecting boundary conditions at the inlet and reflecting boundary conditions at the outlet ($RIBC/PTBC$) are displayed. It is seen from this plot that the relationship between the phase difference and the boundary location shows a linear trend. This is obvious since the only varying parameter in this study is the phase of the reflected wave from

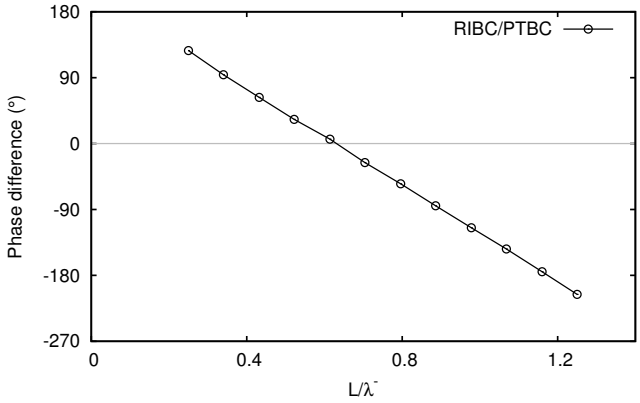


Figure 7.20: Phase difference between the reflected and the outgoing waves at the trailing edge as a function of boundary location (*RIBC/PTBC*).

the outlet boundary (see Equation 4.24 and 4.25).

Based on the the phase relation shown in Figure 7.20, the additional aerodynamic damping of the blade due to acoustic reflection can be calculated and plotted against the phase difference between the reflected acoustic wave and the outgoing acoustic wave at the trailing edge of the blade (similar to the analysis for the fan and intake system conducted in Chapter 6). The additional aero-damping is calculated from the difference between the series computed using *RIBC/PTBC* and the series computed using *RIBC/RIBC*, which represents the additional aerodynamic damping due to acoustic reflection from the outflow boundary. It can be seen from this plot that, for the case studied, the boundary location which has the most beneficial effects to the flutter stability of the rotor blade studied corresponds to approximately $-90°$ and the location with most detrimental effects corresponds to approximately $90°$. For a phase difference of $0°$ and $-180°$ the effects of acoustic reflection on blade aero-damping is almost zero. The observed trend shows similarities with the trend observed in the fan with 'acoustic bump' study (Section 6.4.2), however, the condition for the most destabilising effect obtained in this analysis is unlikely to be universal since the acoustic mode is cut-on on both sides of the blade (as opposed to the fan studied in Section 6.4.2). In such situations when both upstream and downstream sides of the rotor are cut-on, the effect of acoustic reflections has to be analysed with the consideration of the transmission and reflection of the reflected

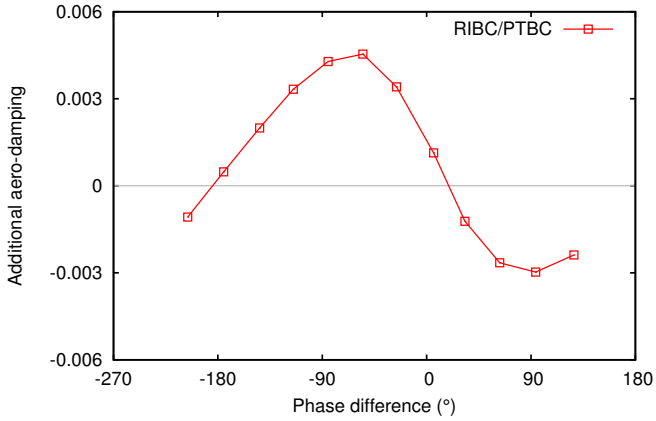


Figure 7.21: Additional aerodynamic damping as a function of phase difference between the reflected and outgoing waves at the trailing edge.

acoustic waves at the rotor. This type of analysis can be conducted in a similar fashion as presented in Section 5.4 and Section 5.5.

In conclusion, it is found in this work that acoustic reflection has significant influence on the flutter stability of a rotor blade. The analysis presented in this section highlights the importance of non-reflecting boundary conditions for unsteady CFD flutter computations, which are shown to have a significant impact on the predicted stability of the isolated rotor. Moreover, the results using reflecting boundary conditions indicate that the effect of acoustic reflection on blade aerodynamic damping may be analysed using an alternate strategy (i.e. without the need of full annulus multi-row computations) by calculating the amplitude and phase of the reflected acoustic waves using analytical methods (Chapter 4). This approach (which will be presented in Chapter 8) would allow a significant reduction of model size and computational time, enhancing the feasibility of conducting flutter analysis of embedded rotors under the influence of acoustic reflections in the early design stages of an engine.

It is worth mentioning that the approach take here is similar to the flutter computations of the fan blade with 'acoustic bump' (Section 6.4). However, as the acoustic mode (the 1ND mode in this study) is cut-on both upstream and downstream of the blade, acoustic reflections can interact with the blade vibration by influencing the unsteady pressure field at both the leading edge and the trailing edge (as opposed to nearly only influencing the leading edge

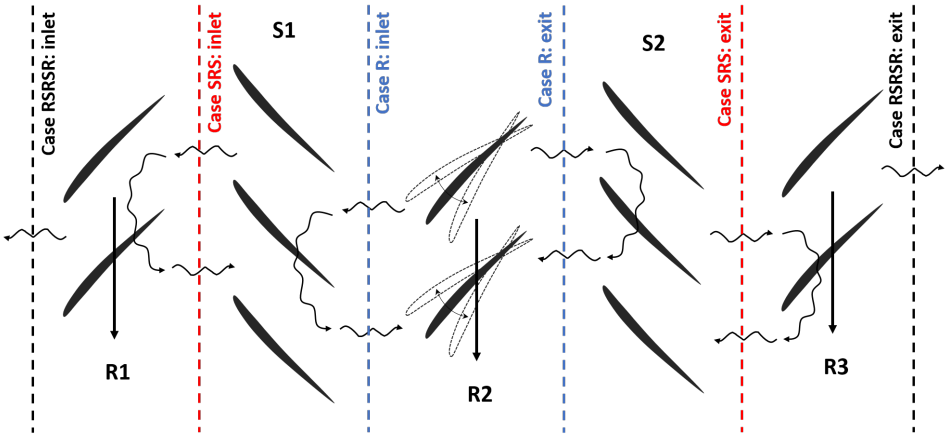


Figure 7.22: Computation domains for flutter analyses: *Case R*, *Case SRS* and *Case RSRSR*.

pressure field for the fan case studied in Chapter 6). This fact adds an extra layer of difficulty in the analysis of acoustic reflection driven flutter, which requires in-depth studies of the change of unsteady pressure field at the leading and trailing edge of the blade due to acoustic reflections.

7.6 Computations With Adjacent Blade Rows

In the next step, the effects of acoustic reflections from blade rows on the flutter stability of the embedded rotor (R2) are studied based on full annulus multi blade row unsteady CFD computations. Aerodynamic damping of the test rotor (R2) is studied with and without the presence of its adjacent blade rows. By using this approach, the cause of R2 flutter instability is determined and the effects of key parameters such as vibration frequency and axial gap are studied.

Figure 7.22 and Figure 7.23 illustrates the computation assemblies studied in this work. In this figure the locations where the inflow and outflow boundaries terminate for each computation assembly are marked with dashed lines. Five computation assemblies are considered in this work:

- *Case R*: Isolated R2.
- *Case SRS*: 3-row assembly of S1, R2 and S2.
- *Case RSRSR*: 5-row ssembly of R1, S1, R2, S2 and R3.

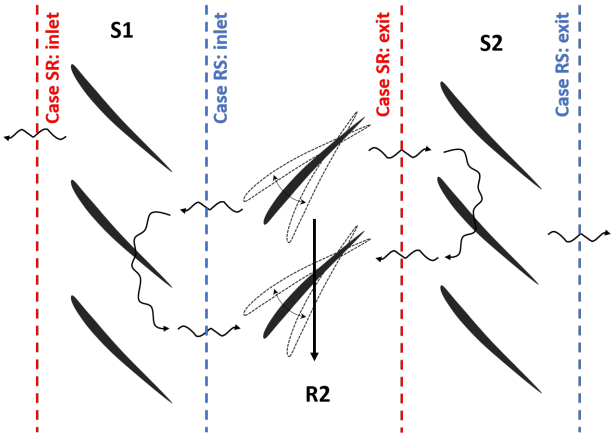


Figure 7.23: Computation domains for flutter analyses: *Case SR* and *Case RS*.

- *Case SR*: 2-row assembly of S1 and R2.
- *Case RS*: 2-row ssembly of R2 and S2.

where the name of each case represent the physical configuration of the assembly, for instance *SR* denotes assembly of stator-rotor and *SRS* denotes the abbreviation of 3-row assembly, and will be used in the rest of this section (and in the next chapter) to represent the corresponding setup.

The required boundary conditions for the above assemblies (at the flow boundaries where the domain is terminated) are extracted from the whole compressor steady state solutions, and prescribed onto the boundaries of the corresponding assembly domains using non-reflecting boundary condition (RIBC). By doing so, the same steady state operating condition is maintained for computations of different assemblies, where the base steady flow on R2 is kept (nearly) the same regardless of the number of blade rows included in the computation. This is demonstrated by the comparison of isentropic relative Mach number in Figure 7.24, where the unsteady time-averaged solution of *Case R* and *Case SRS* are in good agreement with the steady state mean flow solution of *Case R*. By performing flutter analyses using the above assemblies, effects of the adjacent blade rows (i.e. R1, S1, S2 and R3) on flutter stability of the embedded R2 are investigated, based on which the cause of the R2 flutter instability is determined.

All the flutter computations performed in this section use the full annulus multi blade row approach (1^{st} strategy in Section 3.4), and are conducted

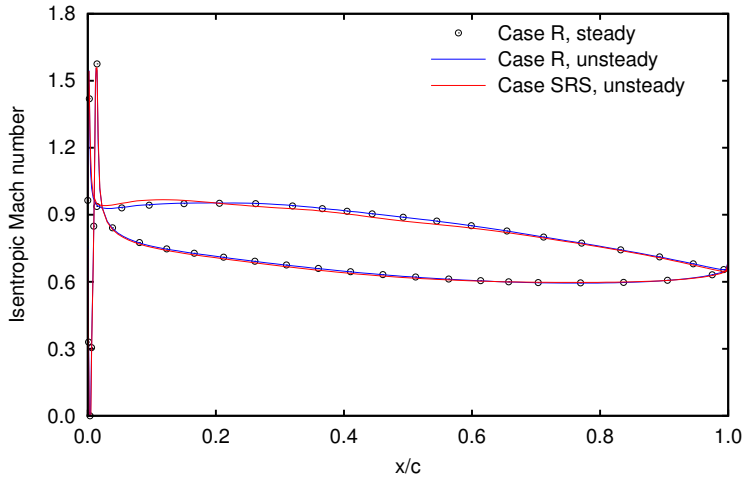


Figure 7.24: Isentropic relative Mach number on the surfaces of R2 at the peak efficiency operating point *E*.

for the 1F mode at a reduced frequency of 0.67 at the peak efficiency operating condition (unless otherwise specified). The physical time step used for flutter computation is fixed at about 40 time-steps per R2/S2 blade passing, which corresponds to approximately 88 time steps for one period of the highest inter-blade phase angle mode in the stationary frame of reference. This time step is obtained by performing a temporal convergence study.

7.6.1 Effect of flow condition

In the first step, the flutter stability of R2 in the embedded *Case SRS* setup is investigated with the throttling of the whole compressor, i.e. from operating points C1 to S1.

Figure 7.25 shows the computed aerodynamic damping of R2 as a function of nodal diameter. In this plot the peak efficiency operating point *E* for the isolated *Case R* (i.e. without reflection) and the operating points *C1*, *E* and *S1* (when operating in the whole compressor) for the embedded *Case SRS* are displayed. The aero-damping for the isolated *Case R* at point *E* is the same as the results shown in Figure 7.14, and the results at *C1* and *S1* for *Case R* are not shown here as they do not differ significantly from that at operating point *E* (Figure 7.14). For clarity of the plot, higher nodal diameters are not shown since the blade aero-damping is very high (see Figure 7.13). As can be seen from the plot, the isolated rotor shows

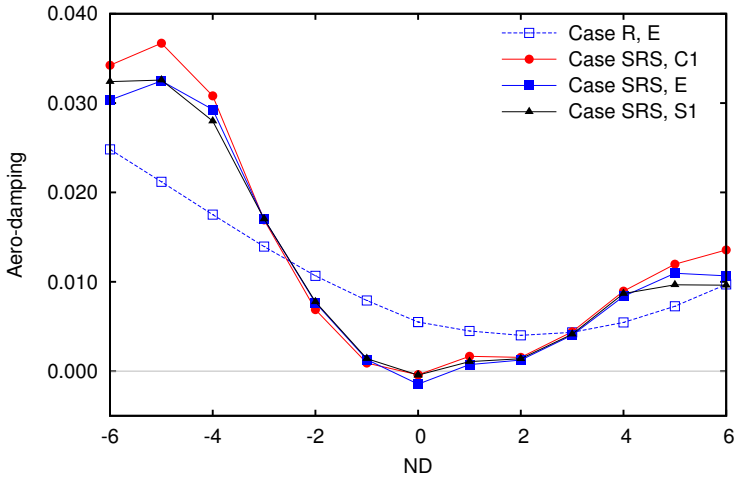


Figure 7.25: Aero-damping of R2 on the C1-E-S1 characteristic.

positive aero-damping for all the nodal diameters. With the introduction of upstream and downstream stators, the aero-damping of the embedded rotor changes significantly from that of the isolated blade row. It is stressed again that, this is not due to the change of flow on R2 as the numerical set up ensures that the base steady flow on R2 is roughly the same in all the computations (see Figure 7.24). Positive, as well as negative effects on aero-damping can be observed from the plot. Moreover, the least damped mode shifts from 2ND (in *Case R*) to 0ND (in *Case SRS*), and flutter is seen at 0ND with a small negative damping which is in accordance with experimental observations. It is important to note that the maximum change of blade aero-damping due to the presence of adjacent blade rows is two orders of magnitude higher than the mechanical damping for blisks (typically of the order $1.0e^{-5}$) [5].

The influence of the adjacent blade rows on flutter stability of the embedded rotor is clearly seen based on this plot, where the stable isolated rotor becomes unstable due to the interaction between the blade rows. This interaction between the blade rows is not attributed to rotor-stator interactions (potential or wake) since the frequency of concern is well below the blade passing frequencies, which are an order of magnitude higher than that of the blade vibration. It will be shown later that the driving mechanism of flutter is of acoustic origins due to the interaction between the blade vibration and the resulting unsteady pressure. Moreover, the variation in

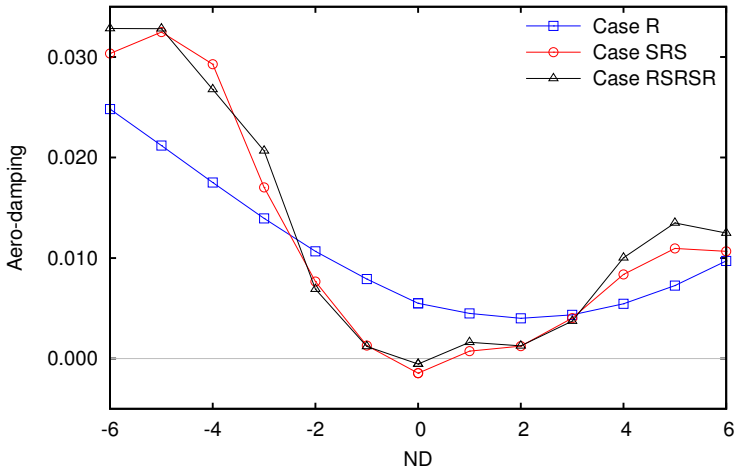


Figure 7.26: Aero-damping of R2 using the *Case R*, *Case SRS* and *Case RSRSR* setups.

R2 aero-damping from the isolated setup (*Case R*) to the embedded setup (*Case SRS*) seems independent of the change of operating condition, which is again due to the nearly unchanged flow field in the three blade rows (i.e. S1 and S2).

7.6.2 Effect of blade row count

It has been shown in Figure 7.25 that the inclusion of S1 and S2 changes the aerodynamic damping of R2 significantly, which highlights the influence of acoustic reflections from these two immediately adjacent stators. In order to study the influence of blade row not immediately adjacent to the embedded R2, computations with the *Case RSRSR* assembly (which additionally includes R1 and R3) are performed at the peak efficiency operating point *E*. Figure 7.26 shows the comparison of computed aerodynamic damping of R2 using the isolated *Case R*, embedded 3-row *Case SRS* and embedded 5-row *Case RSRSR* assemblies. It can be seen from the plot that the inclusion of blade rows not immediately adjacent to R2 (R1 and R3 in this case) does not result in further changes in the predicted aero-damping of R2. The observation indicates that the main influence of acoustic reflection comes from blade rows immediately adjacent to the embedded rotor for the case studied. It is theoretically possible that the main contribution of acoustic reflections come from blade rows not immediately adjacent to the embedded

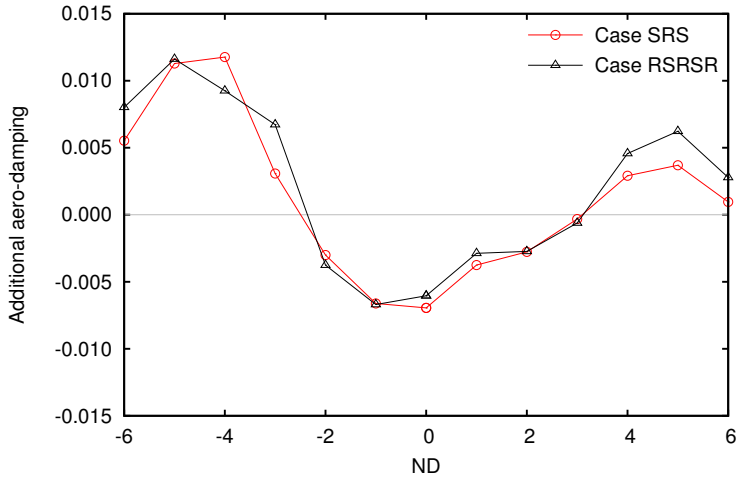


Figure 7.27: Additional aero-damping for *Case R* and *Case SRS* as a function of nodal diameter.

rotor. However, this requires the reflection and multiple transmissions of acoustic waves in the compressor, which can be shown (based on the transmission and reflection coefficients calculated in the next chapter) to result in negligible amplitude for typical flows and geometries for compressor blading.

In order to study the effects of acoustic reflection on different nodal diameter modes, additional aero-damping due to acoustic reflection from blade rows (abbreviated as 'additional aero-damping' in the rest of this section) is calculated for *Case SRS* and *Case RSRSR*, and is plotted in Figure 7.27 as a function of nodal diameter. The additional aero-damping is calculated (in a similar fashion to studies in Chapter 6) as the difference between the aero-damping using the embedded setup and the isolated setup (e.g. the difference between *Case SRS* and *Case R*). This term is used repeatedly in the rest of this section as it provides a good measure of the the influence of acoustic reflection on blade flutter stability. It can be seen from the plot that the additional aero-damping shows an almost cyclic variation about zero when plotted against the nodal diameter. Positive and negative effects due to acoustic reflection are clearly shown in this plot where the largest decrease in aero-damping is seen between -2ND and 2ND and the largest increase in stability is seen in the vicinity of -5ND and 5ND. Moreover, by comparing the calculated additional aero-damping for the 3-row and 5-row cases, it is confirmed that R1 and R3 which are not immediately adjacent

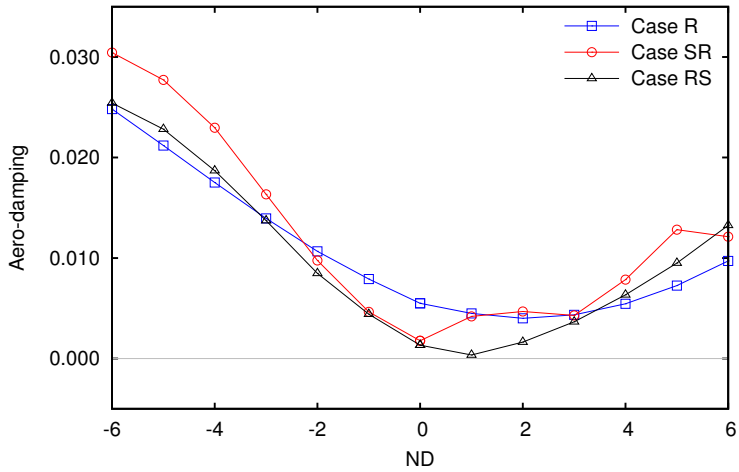


Figure 7.28: Aero-damping of R2 using the *Case R*, *Case SR* and *Case RS* setups.

to the embedded R2 have little influence on its flutter stability. Therefore, it is appropriate to assume that the interactions from not immediately adjacent blade rows are negligible for the case studied, and in order to reduce computational cost those blade rows are not considered in the rest of the analyses.

The observed cyclic variation of additional aero-damping with respect to nodal diameter can be explained as follows: the phase of the reflected wave is a function of axial wavenumber (Equation 4.24 and 4.25), which as can be seen from Equation 4.17 is a function of nodal diameter. Therefore, for each nodal diameter, the reflected wave reaches the rotor blade at different phase of a vibration cycle. Reflected acoustic waves from adjacent blade rows interact with the unsteady pressure field generated by the vibration motion, which can result in beneficial or detrimental effects (depending on the phase of reflected waves) to the overall flutter stability of the embedded rotor. In the case studied here, reflections from the adjacent stators have a negative impact on the 0ND mode of R2, which is responsible for the flutter event predicted by CFD and observed in the experiment.

In the next step, a set of two blade row analyses (*Case SR* and *Case RS*) are performed to determine the contribution to the aero-damping variation of R2 due to acoustic reflection from each stator. Figure 7.28 shows the computed aero-damping of R2 for the isolated *Case R*, the partially-embedded

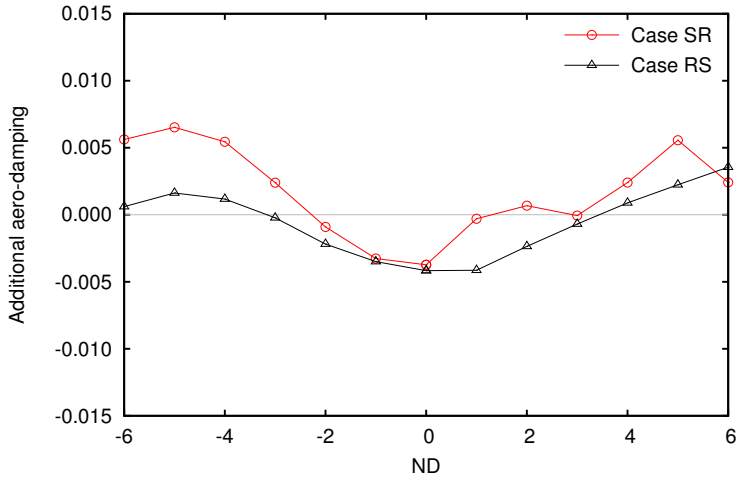


Figure 7.29: Additional aero-damping for *Case SR* and *Case RS* as a function of nodal diameter.

Case SR and the partially-embedded *Case RS* assemblies. It can be seen from the plot that the presence of S1 or S2 changes the aero-damping of R2 differently, for instance the effect due to S1 is seen to be stronger at 5ND and the effect due to S2 is stronger in 1ND. However more importantly, the presence of either stator by itself does not lead to negative aero-damping of R2, indicating that the flutter instability of R2 requires acoustic reflections from both the upstream and the downstream stators. Figure 7.29 shows the calculated additional aero-damping due to acoustic reflection for the aforementioned 2-row analyses. A cyclic trend of additional aero-damping is found when either the upstream or downstream stator is included in the unsteady computation. Acoustic reflections from the upstream stator as well as the downstream stator result in a decrease in blade aero-damping for some nodal diameters such as 0ND and 1ND.

Figure 7.30 shows the calculated additional aero-damping from the two immediately adjacent stators (S1 and S2) as a function of nodal diameter. In this plot the additional aero-damping calculated from the 3-row case is compared with the sum of additional aero-damping calculated from the 2-row cases. In other words, this plot compares the red line in Figure 7.27 with the sum of the red and black lines in Figure 7.29. It is seen from this plot that the two lines show very similar trend for the range of nodal diameter shown here, indicating that (at least for low nodal diameter modes) the

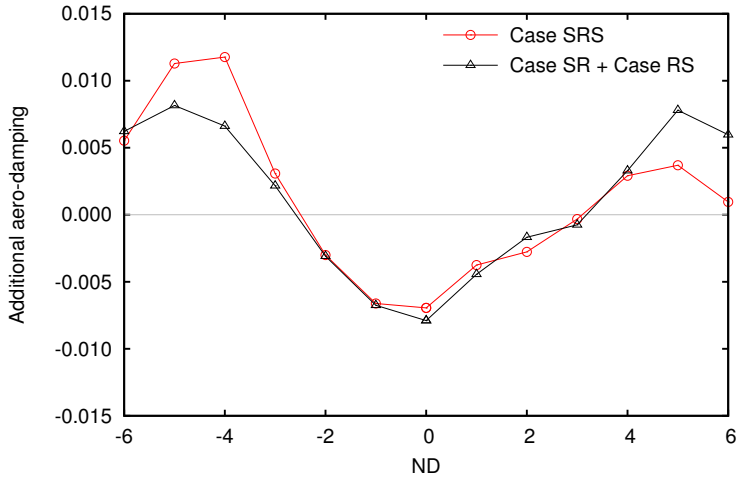


Figure 7.30: Comparison of additional aero-damping for *Case SRS* and the sum of additional aero-damping for *Case SR* and *Case RS*.

acoustic reflection from the stator on one side do not (or only with a very small amplitude) further interact with the stator on the other side which can result in additional changes to the near blade pressure field of R2. The possible interaction process through multiple stages of transmission and reflection is illustrated in Figure 7.31. However, this interaction is unlikely to have a significant influence due to the multiple occurrences of amplitude loss during the transmission and reflection process. The discrepancies in Figure 7.30 at higher nodal diameters are believed to be the artifact of post-processing.

Figure 7.26 to Figure 7.30 clearly demonstrate that the flutter instability of R2 for the 0ND mode is driven by acoustic reflection from both the upstream S1 and the downstream S2. In the absence of either stator, the rotor is predicted to be stable for all the nodal diameters. Based on the knowledge gained in the work conducted in the previous section, the destabilising effect for the 0ND mode by both the stators can be attributed to the phasing between the reflected acoustic wave and the outgoing wave generated by blade vibration. Therefore in the next step, the effects of blade vibration frequency and the axial gap between the rotor and the stator, which are key parameters affecting the propagation of acoustic waves, are investigated.

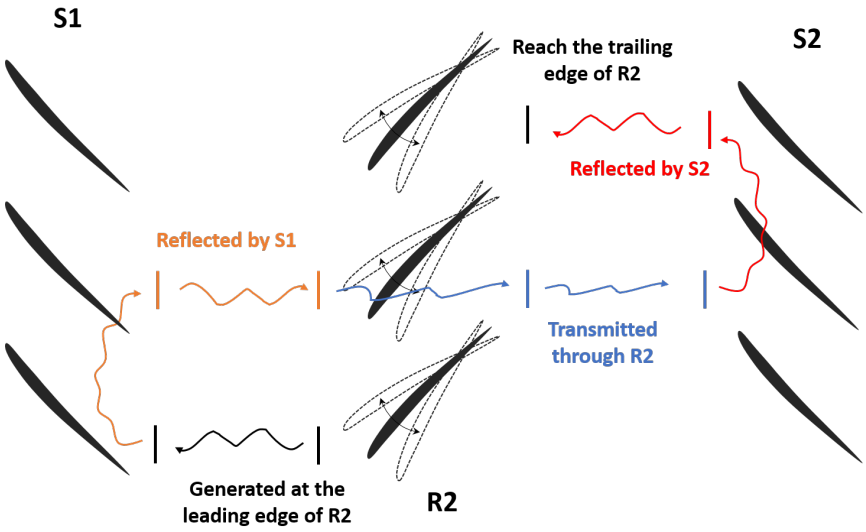


Figure 7.31: Transmission and reflection of acoustic waves through the embedded rotor.

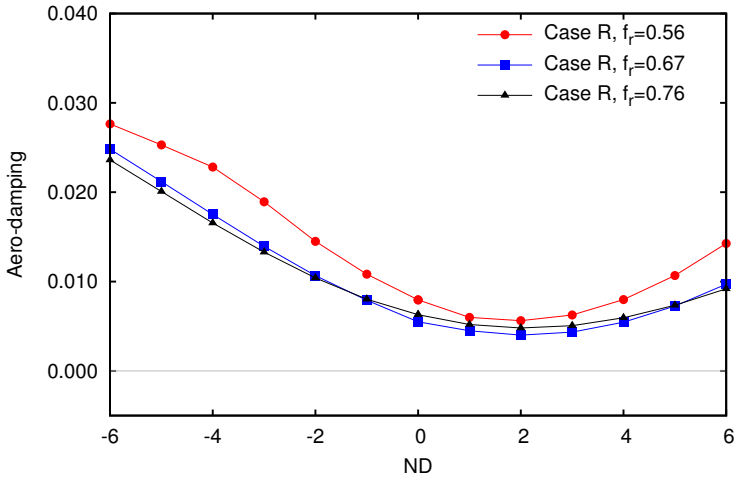


Figure 7.32: Aero-damping of R2 as a function of nodal diameter for different blade vibration frequency, *Case R*.

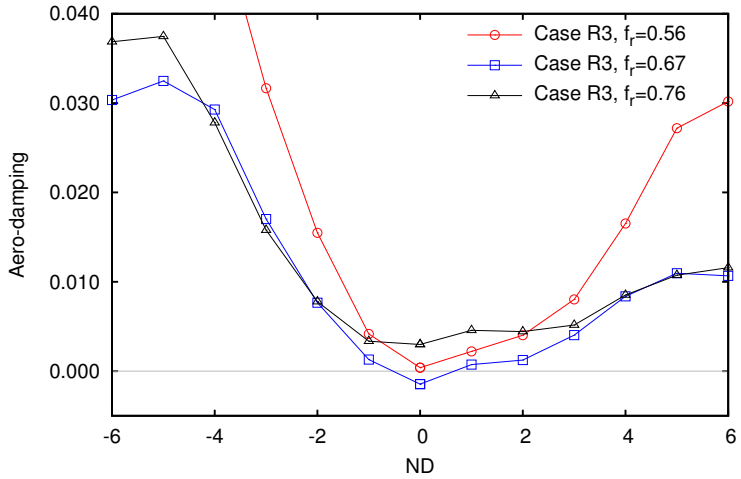


Figure 7.33: Aero-damping of R2 as a function of nodal diameter for different blade vibration frequency, *Case SRS*.

7.6.3 Effect of vibration frequency

Figure 7.32 shows the computed aerodynamic damping of R2 for various vibration frequencies as a function of nodal diameter. In this plot the results of the isolated *Case R* setup for three vibration frequencies $f_r = 0.56$, $f_r = 0.67$ and $f_r = 0.76$ are displayed (which are all cut-on between -1ND and 6ND !!CHECK!!). It can be seen from the plot that the change of blade vibration frequency (by about $\pm 15\%$) results in very limited changes of blade aero-damping for the isolated R2. This is believed to be the result of the acoustic fields upstream and downstream of the blade being cut-on for low inter-blade phase angle modes, where aero-damping of the blade experiences limited variation with the variation of vibration frequency. Among the three frequencies studied, the predicted aero-damping for the vibration frequency $f_r = 0.56$ shows a slightly higher value. Moreover, the blade is predicted to be stable for all the nodal diameter modes with the least damped mode being 2ND.

Figure 7.33 shows the computed aerodynamic damping of R2 for various vibration frequencies as a function of nodal diameter for the embedded *Case SRS* setup. By comparing to Figure 7.32, it can be seen from the plot that the the inclusion of adjacent stators changes the aero-damping of the embedded rotor significantly. Although the presence of S1 and S2 shows destabilising effects for modes in the vicinity of 0ND for all three

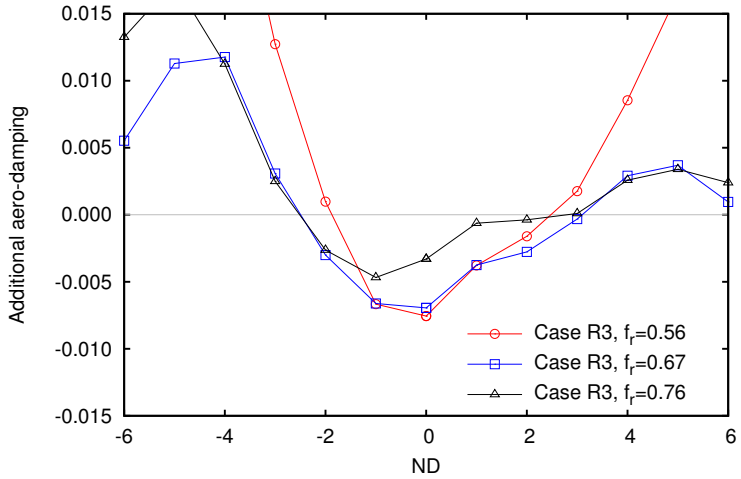


Figure 7.34: Additional aero-damping of R2 as a function of nodal diameter for different blade vibration frequency, *Case SRS*.

frequencies studied, it is seen that the only unstable mode predicted by the CFD analysis corresponds to the 0ND mode with the datum frequency $f_r = 0.67$. This observation corroborates the experimental observations that the flutter event occurred in a very narrow speed range (i.e. narrow frequency range). In order to examine the influence of the stators on flutter stability of the embedded R2, the additional aero-damping is calculated for each case by taking the difference between aero-damping obtained using the *Case SRS* setup and *Case R* setup.

Figure 7.34 shows the calculated additional aerodynamic damping for computations with the three vibration frequencies as a function of nodal diameter. It is clearly seen from the plot that for nodal diameter between -2ND and 2ND, the aero-damping of R2 shows a decrease with the presence of S1 and S2 irrespective of the vibration frequency studied. However, the destabilising effects due to acoustic reflections are more prominent for vibration frequencies $f_r = 0.56$ and $f_r = 0.67$ than $f_r = 0.76$. It is seen that for the case of $f_r = 0.67$, the relatively low blade aero-damping in the isolated setup combines with the destabilising effect due to acoustic reflections from both S1 and S2 to produce the flutter instability at 0ND. Moreover, the results shown in the plots above clearly confirms that the flutter instability of R2 is not caused by the flow-modeshape interactions (since the isolated rotor is always stable) or rotor-stator interaction (since they occur at differ-

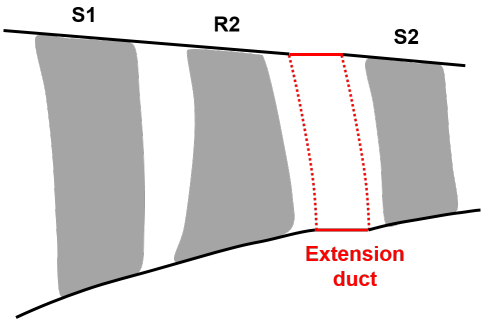


Figure 7.35: Illustration of extended the duct between R2 and S2.

ent frequencies from the vibration), but rather the reflections from adjacent blade rows due to acoustic perturbations generated by blade vibration. This conclusion will be further confirmed by the following analysis.

7.6.4 Effect of rotor-stator axial gap

In the next study, the axial gap between R2 and S2 is increased (by about 70% of R2 tip axial chord) by means of a straight extended duct, so that the phase of the reflected acoustic wave can be varied and its effect on the flutter stability of R2 is studied. This extension of duct between R2 and S2 is illustrated in Figure 7.35. It should be noted that the base steady flow on the rotor blade is kept roughly the same for the cases with and without the extension duct. Moreover, as demonstrated in Figure 7.25, the effect of flow on aero-damping of R2 is much smaller than that due to the acoustic effects, indicating that the extension of axial gap performed here is a viable approach.

Figure 7.36 shows the comparison of the computed aero-damping of R2 for the isolated *Case R*, the datum 3-row embedded *Case SRS* and the extended 3-row embedded *Case SRES* assemblies. It can be seen from the plot that the increase of R2-S2 axial gap results in positive effects for nodal diameters between -1ND and 3ND, whereas negligible effect can be seen for some other modes (e.g. -3ND to -2ND, and 3ND to 4ND). Moreover, the flutter at 0ND is avoided with the increase of the axial gap.

In order to understand the cause of aero-damping variation due to the increase of R2-S2 axial gap, the phase change of acoustic waves propagating through the duct between R2 and S2 is studied. In Figure 7.37 the calculated

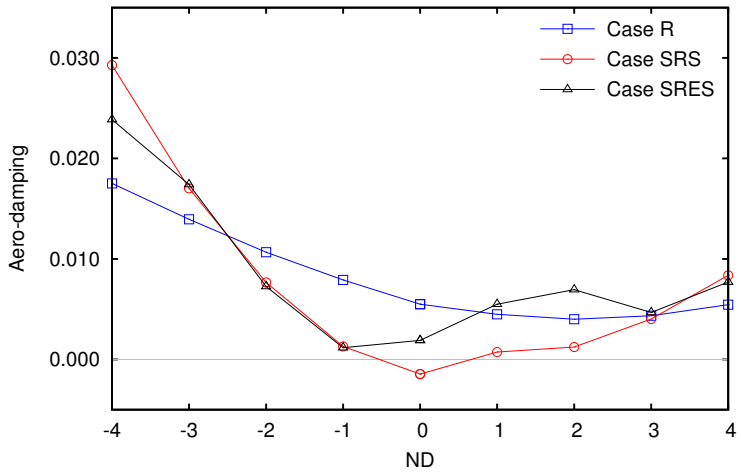


Figure 7.36: Aero-damping of R2 with increased R2-S2 axial gap.

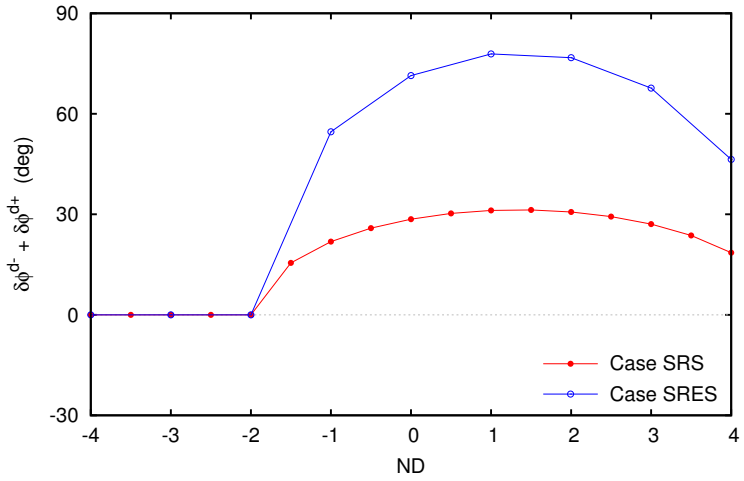


Figure 7.37: Phase variation of acoustic waves propagating in the duct between R2 and S2.

phase change between the trailing edge of R2 and the leading edge of S2 (based on the analytical method presented in Section 4.3) are displayed for the datum *Case SRS* and the extended *Case SRES*. It should be mentioned that the phase change shown in Figure 7.37 only accounts for the phase change of the acoustic waves propagating in the duct between the two blade rows (i.e. $\delta\phi^{d-}_{m,n} + \delta\phi^{d+}_{m,n}$ in Figure 4.13), and does not account for the phase change reflecting from the stator vanes (i.e. $\delta\phi^{dR}_{m,n}$ in Figure 4.13). It can be seen from the plot that, for acoustic modes that are cut-on (-1ND to 4ND), the increase in R2-S2 axial gap results in an increase in the phase change of acoustic waves propagating through the duct (by as much as about 50°). This additional phase change is believed to be the cause of the change in blade aero-damping shown in Figure 7.36 for the nodal diameter between -1ND and 3ND. Moreover, it is seen that the extension duct results in no variation in the phase change of cut-off waves propagating in the duct (i.e. -3ND to -2ND), which explains the negligible effects due to the duct extension observed for these nodal diameters in Figure 7.36.

In conclusion, the influence of acoustic reflections from blade rows and boundary conditions on flutter stability of an embedded rotor are clearly demonstrated in this chapter. It has been shown that flutter of such an embedded rotor in a multi-stage compressor is unlikely to occur by self-driven flow-modeshape interactions. For the case studied in this work, the pre-condition for such type of flutter requires acoustic reflections from blade rows on both the upstream and downstream sides to have destabilising contributions. Moreover, flutter is most likely to occur at inter-blade phase angles where the lowest aerodynamic damping due to the blade motion occurs (flow and modeshape driven). It is also found that by changing the reflection location, through either changing the location of reflecting flow boundaries or changing the rotor-stator axial gaps, the aerodynamic damping of the embedded rotor can be altered significantly. The observation highlights the need for careful selection of inter-row spacing in the design of a multi-stage compressor to avoid flutter of potentially problematic modes.

Based on the analyses performed using various assemblies of blade rows, it is concluded that for the case studied the most significant influence of acoustic reflection comes from blade rows immediately adjacent to the embedded rotor. This conclusion is likely to hold for typical compressor geometries and flows where the resultant amplitude of acoustic waves due to multiple

transmissions (through the neighbouring blade rows) becomes negligible. Moreover, it is concluded for the case studied that the effect due to the upstream stator and the downstream stator seem to be independent and can be analysed separately. This conclusion becomes invalid when the amplitude of reflection coefficient at both the adjacent blade rows and the amplitude of the transmission coefficient at the embedded rotor are high (this problem has been illustrated in Figure 7.31). However, these two aforementioned criteria cannot usually be satisfied simultaneously (at least for situations that are cut-on on both sides of the rotor) for typical turbomachinery applications. The observations indicate that an alternative strategy for flutter analysis for such an embedded blade row can be devised, where unsteady CFD computations using full annulus multi blade row models may not be required. Such an approach requires the acoustic reflections from these stators to be calculated in an analytical approach, based on which the obtained information for the reflected acoustic waves can be used to determine their influence on the flutter stability of the embedded rotor. The development and application of such an alternative strategy is presented in the next chapter.

8 An Alternative Strategy For Embedded Blade Row Flutter Analysis

8.1 Development of the Method

It wa shown in Chapter 7 that acoustic reflections from blade rows have a significant impact on the flutter stability of embedded rotor blades. Unsteady CFD flutter computations with the rotor treated in isolation cannot capture the effects of acoustic reflections from blade rows, which can lead to significant over-predictions of blade aerodynamic damping. In order to capture the effects of acoustic reflections from adjacent blade rows on flutter stability of an embedded rotor, computations must be performed with the presence of these blade rows in the CFD model. For time domain CFD solvers, the inclusion of the rotor and its adjacent stators would require unsteady computations performed in a full annulus approach. Furthermore, for numerical stability, the time step for unsteady computation has to be chosen such that blade passing frequencies are resolved, which can be an order of magnitude smaller than that needed for the vibration frequency. Consequently, the model size and time step constraints for such flutter computations are significantly more expensive than that for the isolated blade row analysis. For instance, the single passage isolated rotor model presented in Section 7.4 consists of about 0.3 million grid points which requires about 4 hours of computation time using 4 CPU cores, while the three blade row full annulus model *Case SRS* presented in Section 7.5 contains about 40 million grid points which requires roughly 80 hours of computation time using 60 CPU cores. The increase in model size and computational cost for these full annulus multi blade row models are a limiting factor for flutter analysis of embedded blade rows in early design stages of an engine. Alter-

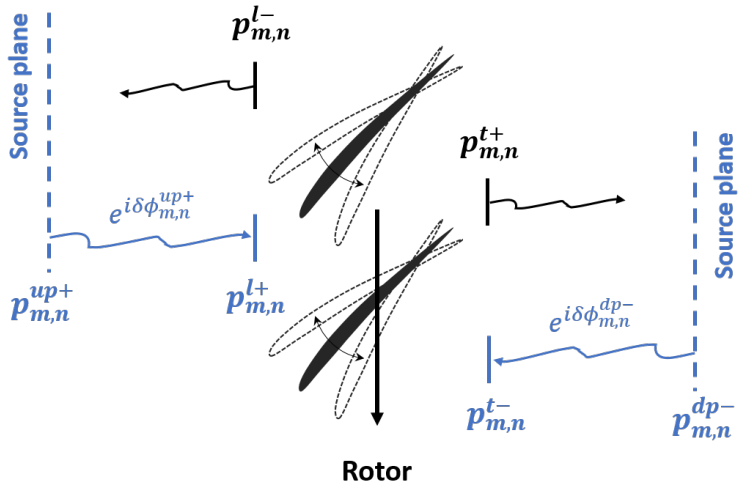


Figure 8.1: Imposing acoustic waves in the rotor domain using unsteady plane sources.

natively, if a low-fidelity method is developed so that the acoustic reflections from other blade rows can be modelled without the presence of these blade row geometries, unsteady CFD computations for the embedded rotor blade can be carried out using a single blade row and a single passage.

Therefore, the aim of this chapter is to develop a low-fidelity alternative strategy so that cost-efficient flutter analysis of an embedded rotor under the influence of acoustic reflections from other blade rows can be carried out in early design stages of an engine. The development of such a strategy is presented in this section and will be validated in the following sections by performing flutter computations for the Rotor 2 of the E3E compressor (the case studied in Chapter 7).

It has been shown in Chapter 4 that the transmission and reflection of acoustic waves at a blade row can be calculated analytically. Based on the obtained information (i.e. amplitude, phase and wavenumbers) of the reflected acoustic wave, unsteady CFD computations can be performed by imposing the calculated reflected acoustic waves in the domain of the embedded rotor without the presence of adjacent blade rows. This can be achieved numerically by introducing unsteady plane sources upstream and downstream of the rotor as illustrated in Figure 8.1. By using this strategy, unsteady CFD flutter computations for an embedded rotor blade can be

carried out in a single passage single blade row approach which will greatly reduce the model size and the computational time cost (compared with full annulus multi-row models).

The alternative strategy for flutter analysis of embedded rotors consists of six stages:

1. Determine the nodal diameter modes of interest for the embedded rotor so that flutter analysis can be performed for such modes.

2. Model the generation of acoustic waves due to blade vibration of the embedded rotor in such potentially problematic modes using single passage single blade row unsteady CFD computations.

3. Trace the propagation of the generated acoustic waves in the compressor duct between blade rows using an analytical approach.

4. Calculate the reflection of these propagating acoustic waves at blade rows (i.e. the stator vanes adjacent to the embedded rotor).

5. Impose the calculated reflected acoustic waves in the domain of the isolated rotor (upstream and downstream of the blade) using unsteady plane sources.

6. Perform unsteady CFD flutter computations for the embedded rotor in a single passage single blade row approach with the imposed sources.

For stage 1 of the above process, the choice usually goes to the least stable modes of the rotor (in the isolated setup without reflection) as acoustic reflection driven flutter is unlikely to occur when the aero-damping due to blade motion is high. Based on the past experience, the least stable modes for a typical rotor blade usually correspond to the low inter-blade phase angle forward travelling modes for the 1^{st} flapwise bending (1F) blade mode (as shown in the previous chapter), and nodal diameters corresponding to the inter-blade phase angle of around 90°for the 1^{st} torsion (1T) blade mode [3]. Moreover, as illustrated in the previous chapter, the pre-condition for acoustic reflection driven flutter of a rotor blade in multi-stage compressors normally requires the acoustic fields to be cut-on at the leading and trailing edges of the blade, which consequently further limits the nodal diameter modes of interest. Stage 2 of the above process can be performed

using single passage unsteady CFD computations for the isolated rotor in a cost-efficient manner, based on which the amplitude and phase of the generated acoustic waves can be obtained through a wave-splitting procedure. It has been shown in Chapter 4 that Stage 3 and 4 of the above process can be accomplished analytically, based on which the amplitude and phase of the reflected acoustic waves (with respect to the waves generated by the blade vibration obtained in Stage 2) can be evaluated without the need of unsteady CFD computations. The information can then be imposed as acoustic perturbations in Stage 5. This is achieved as follows: assuming negligible amplitude change from the source planes to the rotor, the unsteady pressure to be imposed on the source planes (for cut-on acoustic modes) can be obtained using

$$p^{up}_{m,n} = p^{l+}_{m,n} e^{-i\delta\phi^{up}_{m,n}} \tag{8.1}$$

$$p^{dp}_{m,n} = p^{t-}_{m,n} e^{-i\delta\phi^{dp}_{m,n}} \tag{8.2}$$

where

$$\delta\phi^{up}_{m,n} = \int^{L^{up}} k_{x^{+}_{m,n}} dx \tag{8.3}$$

$$\delta\phi^{dp}_{m,n} = \int^{L^{dp}} k_{x^{-}_{m,n}} dx \tag{8.4}$$

and L^{up} is the axial range between the upstream source plane and rotor leading edge, ,L^{dp} is the axial range between the downstream source plane and rotor trailing edge, $p^{l+}_{m,n}$ and $p^{t-}_{m,n}$ are the unsteady pressure for the calculated reflected acoustic waves at the leading and trailing edges of the rotor, and $p^{up}_{m,n}$ and $p^{dp}_{m,n}$ are the unsteady pressure for the acoustic waves at the upstream and downstream source planes. The acoustic perturbations are imposed inside the rotor domain (upstream and downstream of the blade) by means of characteristic variables for acoustic waves [46, 101]. Flutter computations can be subsequently performed in a single passage single blade row approach (Stage 6) using the aforementioned 3$^{\text{rd}}$ flutter computation strategy (Chapter 3.4).

Based on the proposed method, flutter analyses of the embedded R2 (Chapter 7) for forward travelling modes with low inter-blade phase angle (0ND to 4ND) in the 1F mode will be presented in this chapter, where each

stage of the aforementioned process is studied sequentially in the following sections.

8.2 Generated Acoustic Waves Near the Rotor

In the first step, the acoustic waves generated by the vibration of the Rotor 2 blades (Chapter 7) are modelled. This is achieved by conducting unsteady CFD computations for the isolated rotor using a single passage computation. Based on the fully developed unsteady CFD solutions, a wave-splitting procedure is performed to decompose the unsteady perturbations into acoustic waves. The properties of the generated acoustic waves obtained from wave-splitting, such as axial wavenumber and mode angle, are compared with calculations based on the analytical methods (Chapter 4). All the analytical calculations in this chapter are carried out based on the average flow field for the axial planes at the leading and trailing edges of the blade.

For the mean flow condition studied in this chapter, the rotor (and stators) operates at the peak efficiency operating condition, i.e. operating point E shown in Chapter 7, at which the occurrence of flutter in the 1F/0ND mode was measured in test and predicted by full annulus multi blade row unsteady CFD computations. For all the unsteady CFD computations performed in this work, non-reflecting boundary conditions are applied at the inflow and the outflow boundaries to minimise numerical reflections. The blade is excited in the 1F mode at a reduced frequency of 0.67. For all the unsteady computations performed in this section the blade motion is prescribed using the 3^{rd} flutter computation strategy (Section 3.4). The physical time step for unsteady computation is resolved as 200 time steps for one vibration cycle. This time step was obtained by performing a temporal convergence study.

Figure 8.2 shows the cut-on frequency range at the leading edge and the trailing edge of R2 calculated using Equation 4.21, which is displayed in this plot by the reduced frequency (in absolute frame of reference) as a function of circumferential order m (nodal diameter). It should be noted that in the plot shown here, the reduced frequency is a measure of angular frequency that characterises the rotational speed of travelling modes (i.e. $\omega + m\Omega$ similar to Equation 6.2), and thus can take both positive or negative values. In these plots the cut-on range for radial order $n = 0$ (shaded regions) and

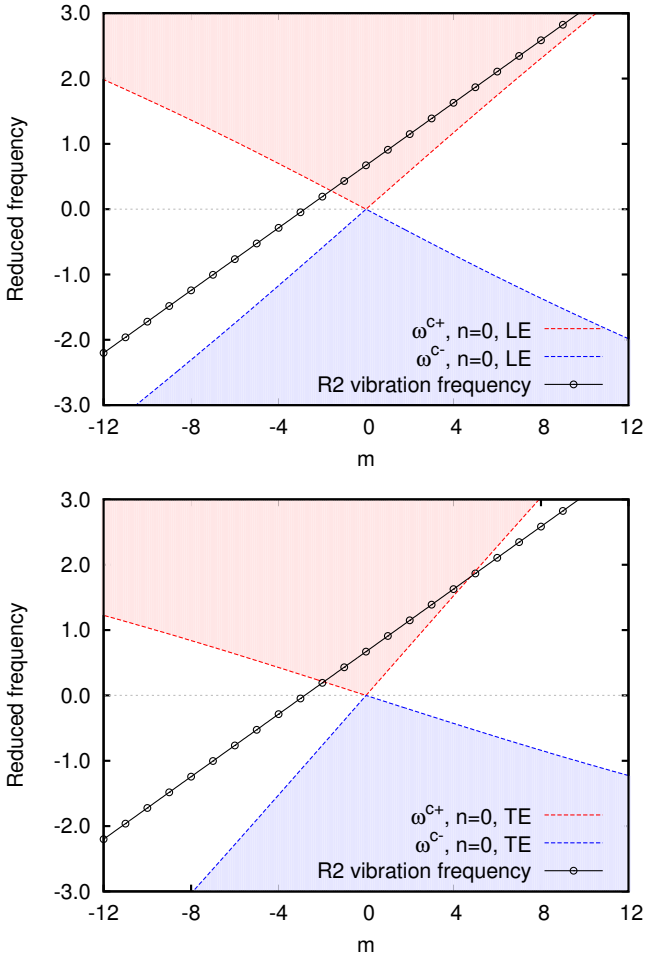


Figure 8.2: Cut-on frequency range (in absolute frame of reference) at (a) the leading edge and (b) the trailing edge of R2.

the blade vibration frequency in the stationary frame of reference (black line) are displayed.

By examining the plots shown in Figure 8.2, it is first noted that the cut-on region for acoustic waves can be divided into two separate regions (shaded red and blue regions), which correspond to the two cut-on criteria shown by Equation 4.21. The cut-on frequencies ω^{c+} and ω^{c-} calculated using Equation 4.21 are shown in this figure as the dashed red and blue lines respectively, where acoustic waves are cut-on for frequencies above ω^{c+}, i.e. shaded red area, and for frequencies below ω^{c-}, i.e. shaded blue area. The physical meanings of these two cut-on regions can be understood as follows: the physical criterion for cut-on (as given by Tyler and Sofrin [21]) states that acoustic modes become cut-on when their circumferential phase speed reaches a critical Mach number (which is $M = 1$ for the case of zero mean flow and on an infinitely thin annulus); in light of this criterion, acoustic waves associated with the forward travelling modes as well as the backward travelling modes can be cut-on when their angular velocities exceed the corresponding critical values; these cut-on conditions correspond to frequencies above ω^{c+} (i.e. high speed rotating modes in positive circumferential direction) and frequencies below ω^{c-} (i.e. high speed rotating modes in negative circumferential direction).

It is seen from Figure 8.2 that the cut-on criteria manifest as two triangular regions connected at the origin of zero frequency and zero circumferential order, which is obvious since the $(0, 0)$ mode is always cut-on. When the flow has zero swirl ($M_\theta = 0$), the triangular cut-on regions can be shown (by Equation 4.21) to be symmetrical about the axis of $m = 0$ and also about the axis of reduced frequency $f_r = 0$. With the increase of tangential flow velocity, the convection effects by the flow result in the 'rotation' of the triangular regions about the origin. This is clearly seen in this figure where the cut-on triangular regions corresponding to the flow solution at the trailing edge seem to be more 'tilted' than those corresponding to the flow solution at the leading edge, due to flow turning by the rotor. This phenomenon results in more acoustic modes being cut-on at the leading edge as the vibration frequency line cuts through the shaded red area in a wider range. Based on calculations using the analytical methods, acoustic modes are cut-on between -1ND and 14ND (not shown in this plot) at the leading edge, and between -2ND and 4ND at the trailing edge.

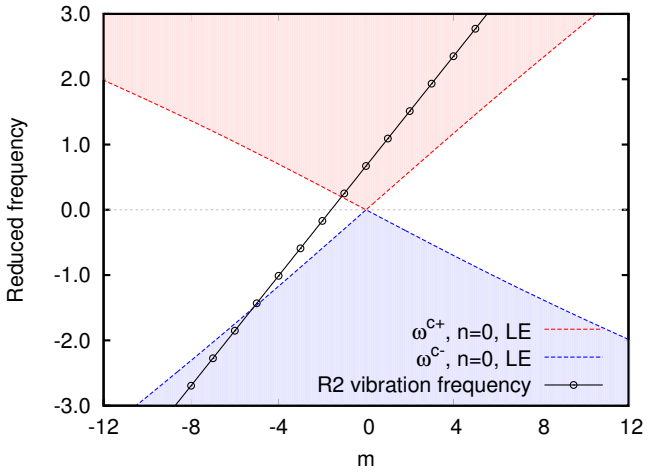


Figure 8.3: Cut-on frequency range (in absolute frame of reference) in the situation of low flow to shaft speed ratio.

It can be shown by studying Equation 4.21 that the boundaries for the two triangular regions (dashed lines) form two continuous straight lines. This is clearly illustrated in Figure 8.2. Based on an understanding of typical geometry and frequency of rotor blades and the flow conditions they operate in, the vibration frequency line (black line) usually has a shallower slope than the positively sloped boundaries of the cut-on regions (i.e the right side boundary of the shaded red region and the left side boundary of the shaded blue region), leading to cut-on modes occurring only at positive frequencies (as is for the rotor studied here). It is however theoretically possible to have a situation where the vibration frequency line crosses the shaded blue region at negative frequencies due to a steeper slope. An example of this is illustrated in Figure 8.3. In this situation the acoustic modes are cut-on for all circumferential orders except for the modes located between the shaded red and blue triangular regions (i.e. cut-on except for $-5 \leq m \leq -2$). However, this situation is unlikely to occur as it requires very low flow to shaft speed ratio, which is against the trend of modern turbomachinery designs (low-speed design).

Figure 8.4 shows the calculated axial wavenumber k_x (Equation 4.17) for the upstream propagating ([-]) and downstream propagating ([+]) acoustic waves at the leading edge and the trailing edge of R2 as a function of circumferential order m. In this plot the axial wavenumber calculated from

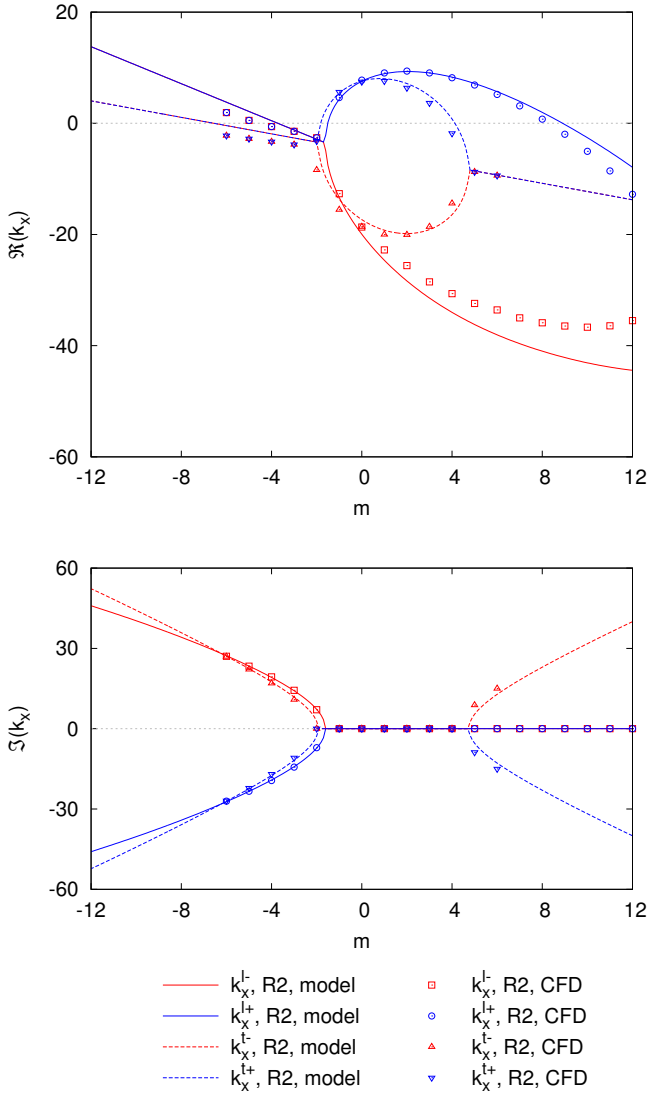


Figure 8.4: Axial wavenumber for upstream and downstream propagating acoustic waves at the leading and trailing edges of R2.

analytical theories (solid and dashed lines) are compared with the results obtained from wave-splitting of unsteady CFD solutions (symbols). The plots can be interpreted by considering the following:

- The criterion for cut-on/off of acoustic waves is a function of duct geometry, flow Mach number and mode order, and is independent of the direction of propagation. In simple words, for a certain circumferential mode order, the upstream propagating and downstream propagating acoustic waves can either be cut-on or cut-off at the same time.

- When an acoustic mode is cut-on, the imaginary component of axial wavenumber is zero. When the mode is cut-off, the imaginary component of axial wavenumber for the upstream propagating wave and the downstream propagating wave are equal but have opposite signs. This is clearly seen in the imaginary component plot of Figure 8.4.

- When an acoustic mode is cut-off, the real component of axial wavenumber for the upstream and downstream propagating waves are the same, and show a linear trend with the circumferential order (the 'backbone' straight lines in the real component plot of Figure 8.4). For cut-on acoustic modes, the real axial wavenumber for the upstream and downstream propagating waves are different, and deviate equally from the 'backbone' lines to form an oval-like pattern. Due to the turning of flow by the rotor, a wider range of cut-on modes can be seen at the leading edge than the trailing edge.

It is also seen from the plots that the axial wavenumbers calculated using the analytical method show good agreement in general with results obtained from wave-splitting of unsteady CFD solutions. A notable difference can be seen at high circumferential mode orders, where acoustic modes are calculated to be more cut-on than those obtained from CFD solutions using wave-splitting (which can be seen from the difference in the oval-like regions). This is believed to be the result of three-dimensional flow field in the CFD computations, which is not taken into account in the analytical method. Nevertheless, good agreement can be seen for low circumferential mode orders, where the blade aero-damping is low and for which the analysis is limited to.

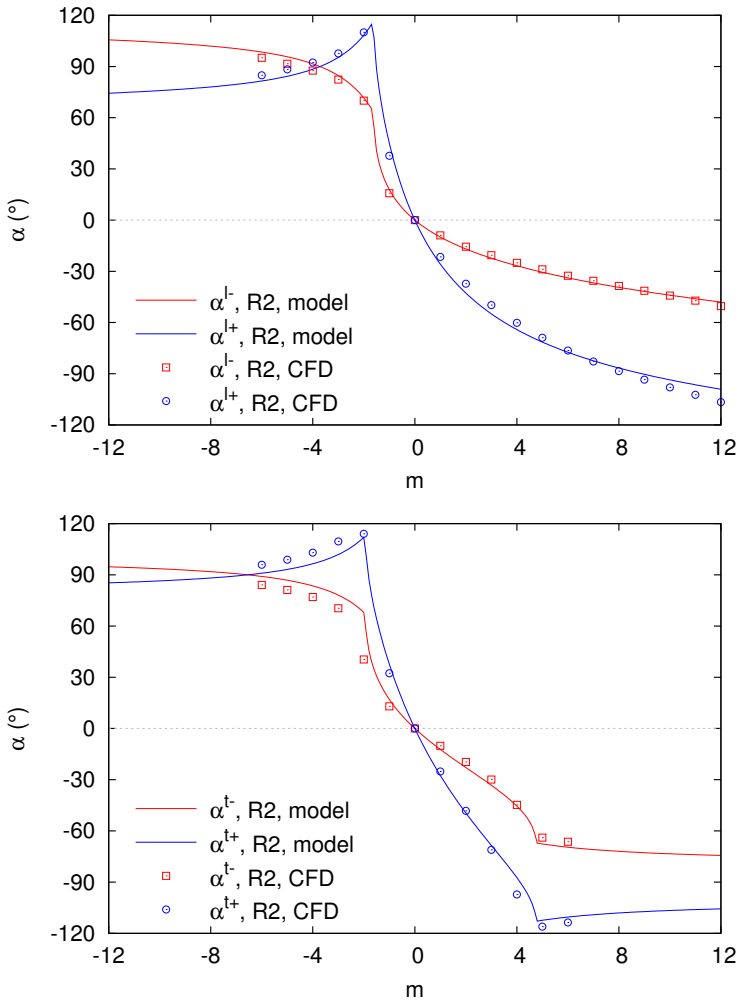


Figure 8.5: Mode angle for upstream and downstream propagating acoustic waves at the leading and the trailing edges of R2.

Figure 8.5 shows the calculated mode angle with respect to the engine axis for the upstream and downstream propagating acoustic waves as a function of circumferential order m. In the plot shown here the mode angles for radial order $n = 0$, calculated using analytical methods (Equation 4.23), are compared with the results obtained from wave-splitting of unsteady CFD solutions (computed from the obtained wavenumbers). It can be seen from the plots that the $(0, 0)$ mode, known as the 'plane wave' mode, has a mode angle of 0°. As acoustic modes approach cut-off (i.e. for higher nodal diameters), the mode angle tends to 90°and the mode phase velocities become purely circumferential. Moreover, it is noted that the angle between the wave front and the engine axis can become higher than 90°as the modes approach cut-off. It is also seen that, due to different flows, cut-on acoustic waves at the leading edge of the rotor have smaller mode angles than their counterparts at the trailing edge. In general, a good agreement can be seen between the analytical calculations and the results obtained from unsteady CFD solutions.

Figure 8.6 shows the amplitude and phase of the (outgoing) acoustic waves generated by blade vibration as a function of nodal diameter. The amplitude for each nodal diameter is normalised by the amplitude of acoustic pressure at the trailing edge, and the phase is relative to blade motion at zero displacement and the maximum positive velocity. In this plot the nodal diameters at which acoustic modes become cut-off are also highlighted by means of the dashed lines. The acoustic modes are cut-on at the trailing edge for nodal diameters between the two blue dashed lines, and cut-on at the leading edge for nodal diameters to the right of the dashed red line (which becomes cut-off at 14ND). It can be seen from the amplitude plot that, prior to cut-off at -2ND, acoustic modes at the leading edge of the blade experiences a resonance (peak of the red curve). Similarly, a resonance is seen at 5ND for acoustic waves at the trailing edge of the blade (manifests as the red curve being close zero). It can be seen from the phase plot that for acoustic modes that are cut-on at both the leading and trailing edges of the blade (i.e. -1ND to 4ND), the phase of the leading edge acoustic pressure and trailing edge acoustic pressure are nearly constant (with respect to ND) with a difference of about 180°. It is also noticed that as the trailing edge acoustic field becomes cut-off at -2ND, the phase of trailing edge acoustic pressure cycles through 360°so that it lags the leading edge

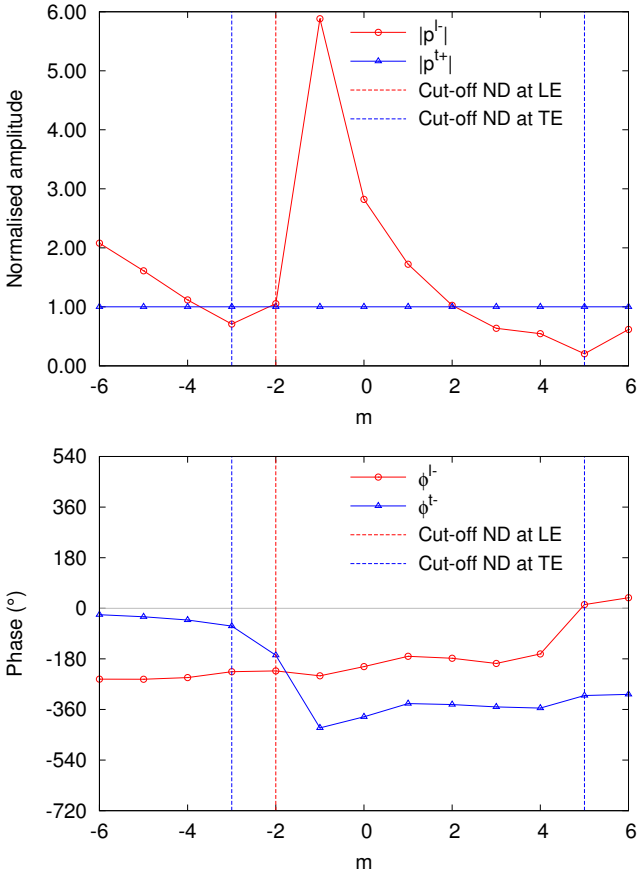


Figure 8.6: Amplitude and phase of the acoustic waves generated at the leading edge and the trailing edge of R2.

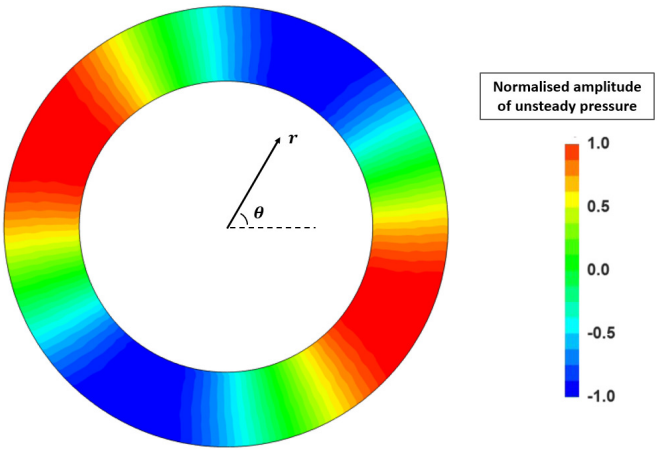


Figure 8.7: Unsteady pressure contour for an imposed $(2, 0)$ acoustic wave plotted in the cross-section view of a duct.

by about 180°.

It has been shown in this section that the properties of the generated acoustic waves, such as axial wavenumber and mode angle, can be calculated analytically with a good degree of accuracy. Combined with the amplitude and phase of the generated waves obtained using single passage unsteady CFD computations, analytical calculations can be carried out to obtain the amplitude and phase of the acoustic waves reflecting from the other blade rows. The analysis of transmission and reflection of acoustic waves at blade rows is presented in the next section.

8.3 Acoustic Reflection from a Blade Row

In the next step, transmission and reflection of acoustic waves at a blade row are studied. This is achieved by carrying out unsteady CFD computations for the blade row of interest with imposed acoustic perturbations using plane sources as illustrated by Figure 8.7 (similar to *Case G* in Chapter 5). A wave-splitting procedure is performed at the leading and trailing edges of the blade row to decompose the unsteady perturbations in the CFD solutions into propagating waves, based on which the amplitude ratio and phase change of the complex transmission and reflection coefficients are obtained. The obtained transmission and reflection coefficients are compared with the calculations based on the analytical method presented in Section 4.4. As

shown in Chapter 4, the analytical calculations require only the knowledge of the mean flow field, thus can be carried out without the need of unsteady CFD computations. The main objective of this section is to demonstrate that the transmission and reflection of acoustic waves at a blade row can be calculated using an analytical approach with good degree of accuracy without the need of unsteady CFD computations.

In the first part of the study, transmission and reflection of acoustic waves at a thin annulus blade row are studied. The geometry for the thin annulus blade rows in this study are identical to the cases studied in Chapter 5. The computations of the thin annulus blade rows allow one to study the effects of key parameters on the transmission and reflection of acoustic waves at bladed structures, such as incident mode angle, solidity, stagger, reduced frequency and camber.

In the second part of this work, the transmission and reflection of acoustic waves, generated by the vibration of Rotor 2 blades, at Stator 1 and Stator 2 (of the E3E HP compressor) are studied. The results obtained from wave-splitting of unsteady CFD solutions are compared with calculations using the analytical method (Section 4.4).

8.3.1 Thin annulus blade row

In the first part of this work, transmission and reflection of acoustic waves at thin annulus blade rows are studied. The computation domain consists of a high hub/tip ratio (0.965) stationary blade row inside a constant radius straight long duct, and the blades have identical aerofoil sections at all radial heights. The inflow and outflow boundaries of the duct are placed approximately 10 chords away from the blades. Computations are performed for blade rows with unloaded flat plates and cambered blades. The geometry and grid for all the blades studied in this work are identical to the thin annulus blade rows studied in Chapter 5.

The steady state flow solutions are obtained by imposing the physical boundary conditions at the farfield inflow and outflow boundaries. The mean flow angle is kept the same as the stagger for cases with flat plates. The mean flow field for cambered blades is the same as shown in Figure 5.14.

For unsteady time-accurate computations, non-reflecting boundary conditions are applied at the inflow and outflow boundaries to minimise numerical

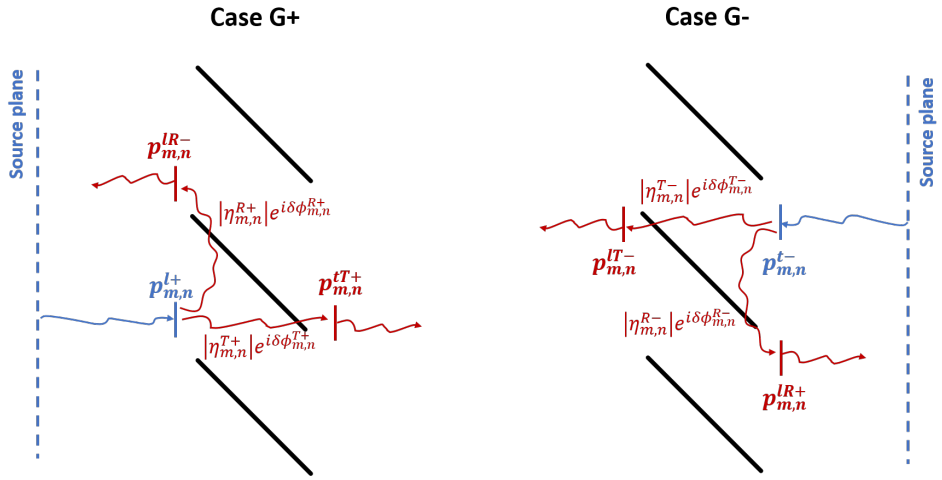


Figure 8.8: (a) *Case G+*: imposing a downstream propagating acoustic wave incident on the blade row; (b) *Case G-*: imposing an upstream propagating acoustic wave incident on the blade row.

reflections. The unsteady computations are performed using a full annulus approach. The physical time step for unsteady computations is resolved as 200 time steps per period.

The unsteady computations are performed by introducing acoustic perturbations which are incident on the blade row by means of unsteady plane sources. Figure 8.8 illustrates the unsteady pressure traces for two types of problem configurations: (1) *Case G-*: upstream propagating acoustic waves imposed in the downstream field of the blade row; (2) *Case G+*: downstream propagating acoustic waves imposed in the upstream field of the blade row. In order to obtain the (complex) transmission and reflection coefficient at the blade row, unsteady perturbations at the leading edge and the trailing edge are split into upstream and downstream propagating acoustic waves, based on which the amplitude ratio and phase change of the complex coefficients are calculated.

For the studies performed in this work, the effects of incident mode angle α, solidity c/s, blade stagger angle θ_s, chord length c and blade camber are investigated. These parameters are varied in this work as follows:

- The incident mode angle α (as shown in Figure 8.9) is varied by increasing the circumferential mode order m and frequency of the imposed waves ω simultaneously, which is intended to mimic the forward

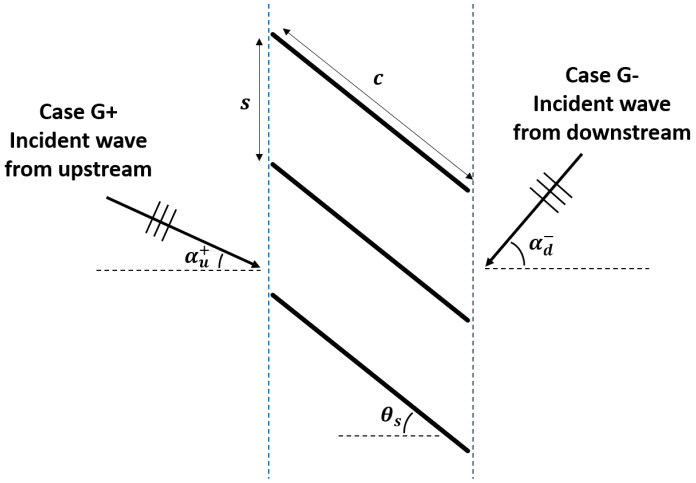


Figure 8.9: Illustration of blade row geometry and incident acoustic waves in this study.

and backward travelling acoustic waves generated by the vibration of Rotor 2. The relationship between the frequency of perturbation ω and the circumferential mode order m is kept as $\omega = \omega_0 + m\Omega_0$, where the vibration frequency ω_0 (corresponding to the reduced frequency of 0.67 of R2 at the peak efficiency operating point E) and the shaft speed Ω_0 (corresponding to 93.1% speed for R2) are fixed throughout this analysis. For the case studied here, only the forward travelling modes are considered (similar trends are expected for the backward travelling modes).

- The solidity c/s is varied by changing the blade count N_b for a fixed chord length c. For the case studied here, the solidity is calculated as $c/s = \frac{cN_b}{2\pi r_t}$ where r_t is the casing radius.
- The mean flow angle and the stagger angle are varied simultaneously for the blade row with flat plates so that zero loading is maintained.
- The chord length c is varied while keeping all other parameters fixed, including solidity c/s.

The effects of the above parameters are investigated by comparing the results obtained from wave-splitting of unsteady CFD solutions with the calculations using the analytical method (Section 4.4). Some selected results are presented and discussed below.

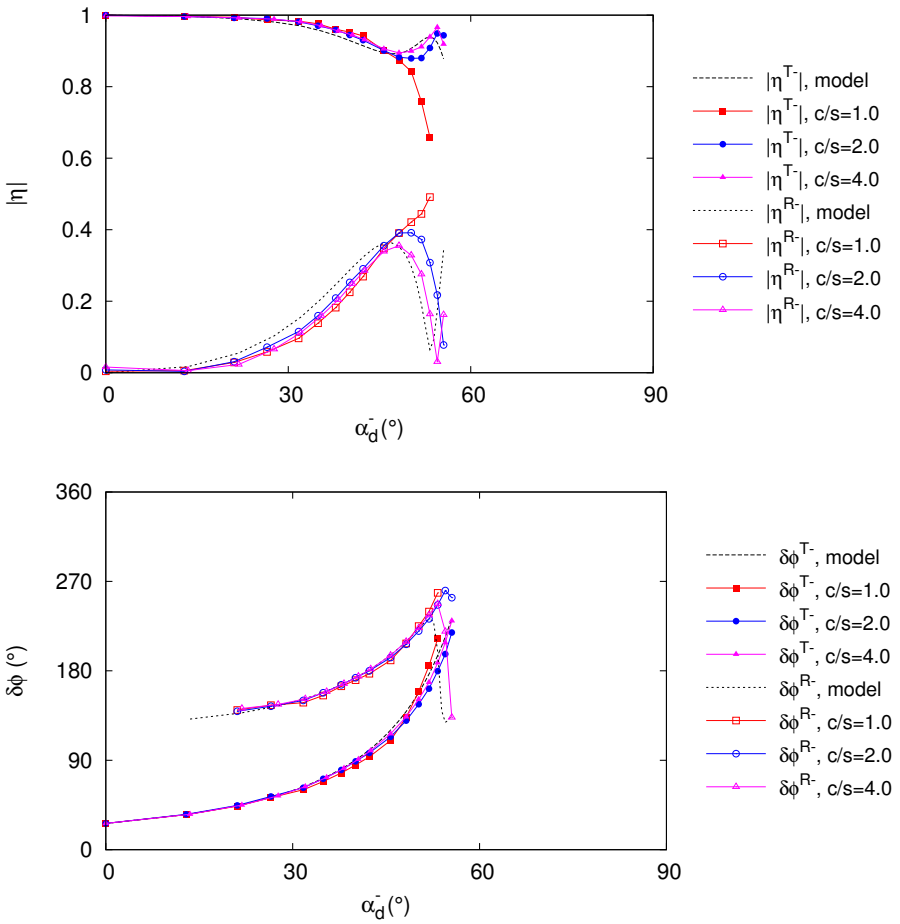


Figure 8.10: Effect of solidity on transmission and reflection coefficients, $\theta_s = 0°$, $M = 0.1$, *Case G-*.

Effects of solidity

Figure 8.10 and Figure 8.11 show the complex transmission and reflection coefficients as a function of incident mode angle for different solidities. The amplitude ratio $|\eta|$ and the phase change $\delta\phi$ for the complex transmission and reflection coefficients are defined in Equation 4.51 to 4.54. In these plots the results for incident acoustic waves impinging on the 0°stagger blade row (for *Case G-* and *Case G+*) with solidity of $c/s = 1.0$, $c/s = 2.0$ and $c/s = 4.0$ are displayed. In the plots shown here each incident mode angle of the coloured lines represents a full annulus unsteady CFD computation. It should be mentioned again that the horizontal axis of the plots corresponds

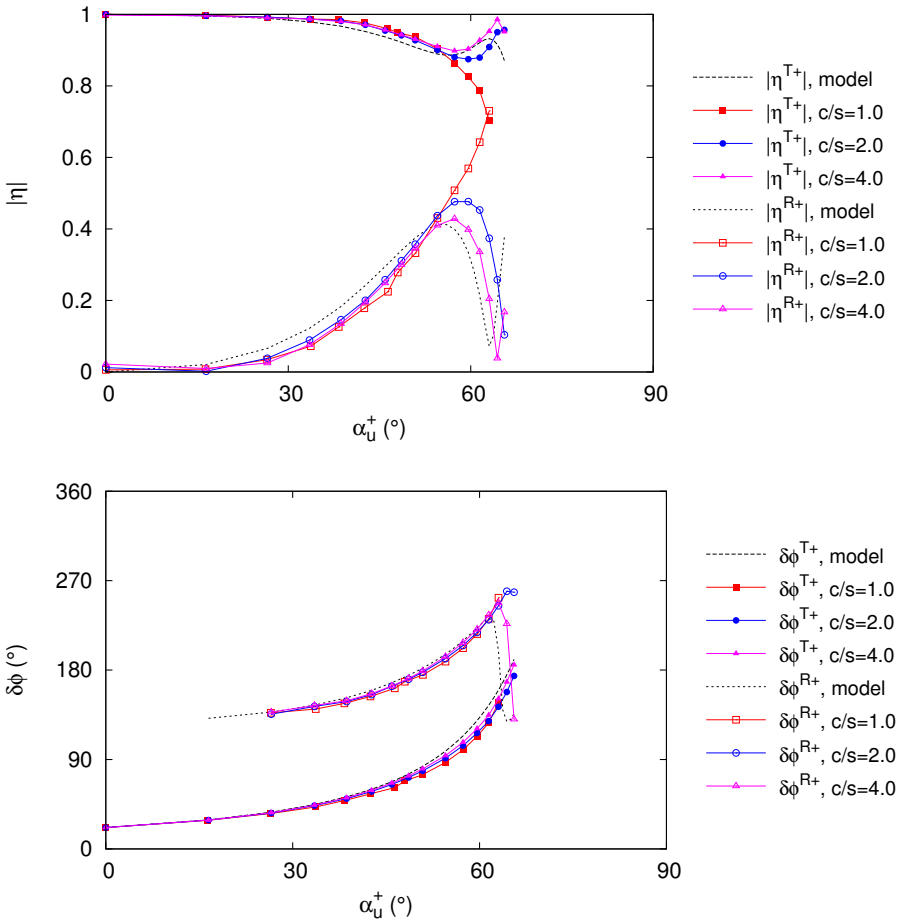


Figure 8.11: Effect of solidity on transmission and reflection coefficients, $\theta_s = 0°$, $M = 0.1$, *Case G+*.

to simultaneous increase in circumferential order m and frequency ω (and consequently the free stream wavenumber $k = \frac{\omega}{a}$). It can be seen from the plots that for an incident mode angle of 0°(i.e. the $(0, 0)$ plane wave mode), the acoustic waves transmits through the blade row unimpeded without the change in amplitude ($|\eta^T| = 1$ and $|\eta^R| = 0$). With the increase of incident mode angle, the amplitude of the transmitted wave decreases and the amplitude of the reflected wave increases. On the other hand, the phase change of the transmission coefficient and the reflection coefficient shows an increase with the increase of incident mode angle. Discrepancies between results for different solidities appear at high incident mode angles where modes are close to cut-off (around $\alpha = 50°$ for *Case G-* and $\alpha = 60°$ for *Case G+*). As the incident mode angle is further increased, the amplitude of reflection coefficient shows a decrease to (nearly) zero while the amplitude of transmission coefficient shows an increase to (nearly) unity. This observed trend is a result of the wavenumber parameter $kc = \pi$, which corresponds to the chord length being half of the wavelength. At this condition, the unsteady pressure at the leading edge is completely out of phase with that at the trailing edge, and the acoustic waves pass through the cascade undisturbed. This condition also holds for $kc = n\pi$ for integer n. Moreover, as the amplitude of reflection coefficient drops to zero (at about $\alpha = 55°$ for *Case G-* and $\alpha = 60°$ for *Case G+*), the phase of the reflection coefficient shows a shift of 180°. As the parameter kc approaches multiplies of π, the computations with solidity $c/s = 4.0$ and $c/s = 2.0$ are well approximated by the analytical model. However, this is not the case for computations with $c/s = 1.0$; this may be because the assumption of one-dimensional wave propagation in blade passages is no longer valid.

The general trends of transmission and reflection coefficients are well represented by the analytical calculations. With the increase of solidity, the results obtained from unsteady CFD solutions show a tendency of converging to the analytical calculations, which is devised based on the assumption of infinite solidity. Discrepancies can be seen at high incident mode angles ($\alpha > 50°$ which corresponds to $m > 10$ for the case studied) where acoustic waves are close to cut-off. Flutter analyses are however usually not focused on these conditions (near cut-off), since the aero-damping of the blade (for the isolated rotor in a long straight duct) is usually quite high and flutter is unlikely to occur.

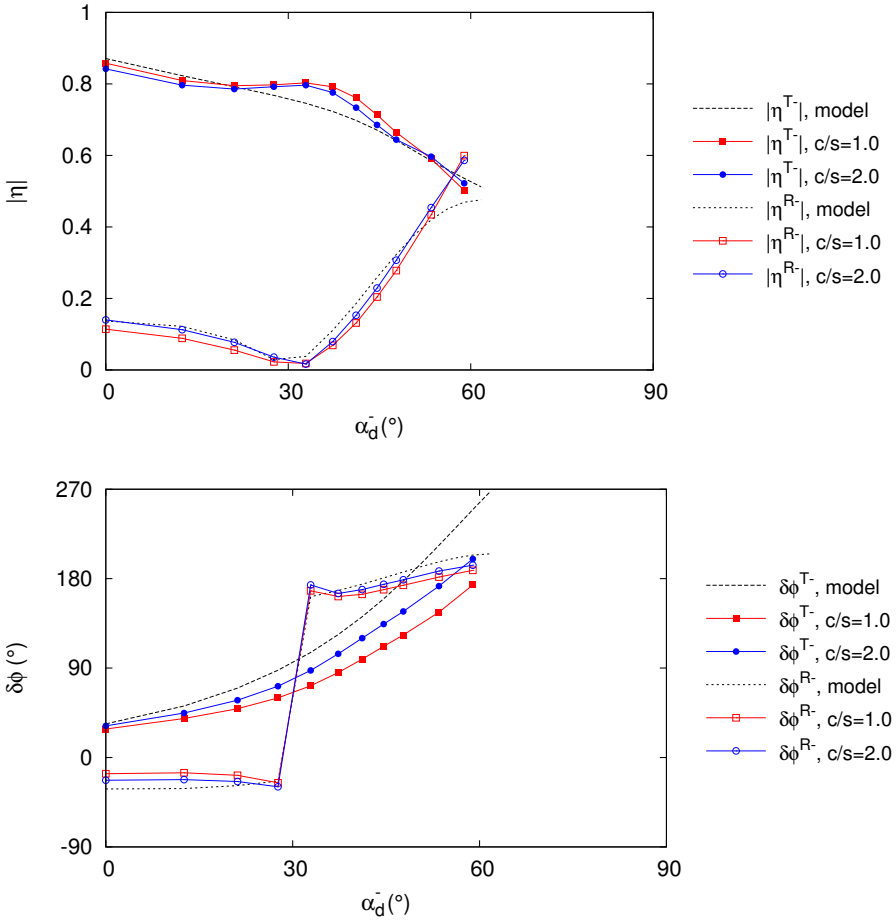


Figure 8.12: Effect of solidity on transmission and reflection coefficients, $\theta_s = 45°$, $M = 0.3$, *Case G-*.

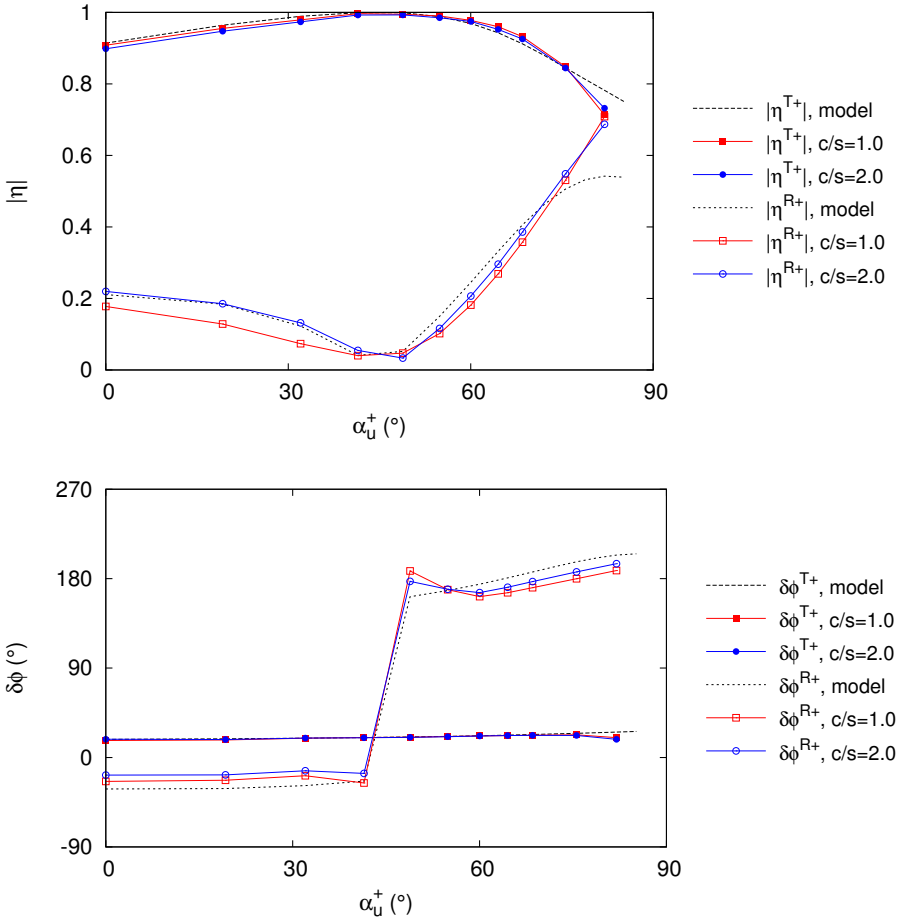


Figure 8.13: Effect of solidity on transmission and reflection coefficients, $\theta_s = 45°$, $M = 0.3$, *Case G+*.

Figure 8.12 and Figure 8.13 show the effect of solidity on the transmission and reflection of acoustic waves at a 45°stagger blade row with a Mach number of $M = 0.3$. In these plots the results for incident acoustic waves impinging on the blade row (*Case G-* and *Case G+*) with solidity of $c/s = 1.0$ and $c/s = 2.0$ are displayed. For incident acoustic waves impinging on the leading edge of the blade row (*Case G+*), unity transmission and zero reflection are seen when the incident mode angle aligns with the stagger angle of the blades (i.e. 45°in this case). On the other hand, for upstream propagating waves impinging from the downstream side (*Case G-*), it can be seen from the plots that the amplitude of the reflected waves drops to zero at about $\alpha = 30°$, which is due to the mode angle for the reflected acoustic wave being aligned with the stagger. Moreover, it is seen that when the reflection amplitude passes through zero, there is an accompanying phase change of about 180°. In general, the calculations based on the analytical method shows a good agreement with the results obtained from unsteady CFD solutions. A minor discrepancy is seen in Figure 8.12 for the calculated amplitude of transmitted waves at the incident mode angle of about $\alpha = 35°$, indicating that the actual mechanism of transmission is somewhat slightly different from that assumed in the analytical method. A larger discrepancy can be seen as modes approach cut-off ($\alpha > 50°$ for *Case G-* and $\alpha > 75°$ for *Case G+*), where the application of the analytical method is found to be inadequate.

Based on the observations from the plots, the major effect of solidity is seen in the transmission phase change for *Case G-*, where lower solidity leads to under-predictions of the transmission phase change. With the increase of solidity, the results obtained from unsteady CFD solutions converges to the analytical calculations ($c/s = \infty$), which indicates that the propagation characteristics of acoustic waves in the blade passages depends on the solidity of the blade row. Moreover, it is noticed that this trend is not present for the 0°stagger blade row shown in Figure 8.10 and Figure 8.11.

This phenomenon can be explained by the following analysis. Figure 8.14 illustrates the idealised propagation path in blade passages for an upstream propagating wave impinging on the trailing edge. Due to the presence of non-permeable metal blade surfaces, the incident acoustic waves are turned to propagate in the blade passages in the direction of stagger. The propagation of acoustic waves in blade passages can be assumed to be one-

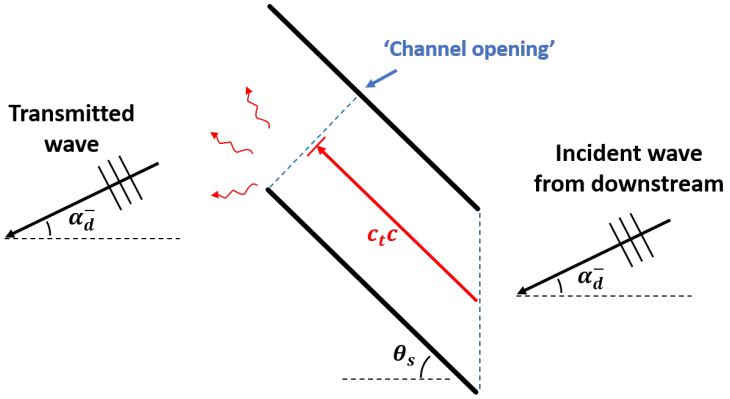


Figure 8.14: 'Covered passage' parameter c_t for upstream propagating acoustic waves (*Case G-*).

dimensional propagation in a 'channel' parallel to the blades. For a blade row consisting of staggered blades (as shown in the figure), acoustic waves propagating in the passage are able to escape (radiating outwards) at the location where one end-wall of the 'channel' terminates. In these situations the path of the transmitted acoustic waves do not cover the whole blade chord as assumed by the analytical model ($c/s = \infty$), thus resulting in a smaller phase change during the transmission process. On the other hand, as can be seen in Figure 8.11, this effect is much smaller for downstream propagating acoustic waves impinging from the upstream side (*Case G+*), which is the result of larger wavelength for the downstream propagating waves.

In order to represent this phenomenon in the analytical model, a coefficient called 'covered passage' c_t is introduced as

$$c_t = \max\left(0, \quad \frac{\frac{c}{s} - \frac{1}{2}\sin\theta_s}{\frac{c}{s}}\right) \tag{8.5}$$

which is a multiplier to the chord length of the blades when calculating the phase change of upstream propagating acoustic wave transmitting through a blade row. It is seen Equation 8.5 that the proposed covered passage parameter approaches 1 when the solidity tends to infinity or the stagger becomes zero, which can clearly model the trend of transmission phase change observed in the previous plots.

Figure 8.15 shows the phase change of an upstream propagating acoustic

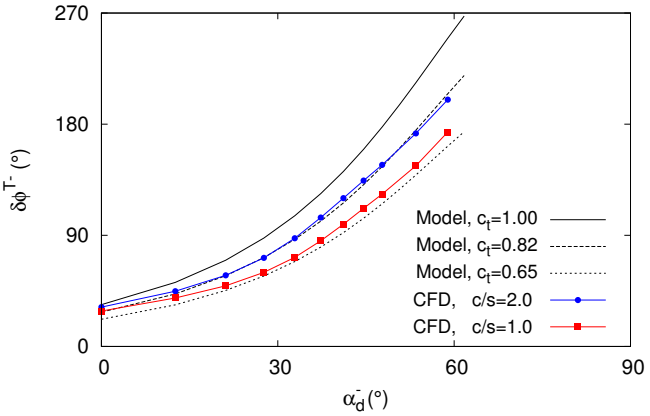


Figure 8.15: Effect of covered passage parameter c_t on transmission and reflection coefficients, $\theta_s = 45°$, $M = 0.3$, *Case G-*.

wave transmitting through the 45°stagger blade row (as previously shown in Figure 8.12). In this plot the analytical calculations based on the proposed 'covered passage' coefficient $c_t = 0.82$ (corresponding to $c/s = 2.0$) and $c_t = 0.65$ (corresponding to $c/s = 1.0$) are also displayed. It can be seen from the plot that with the introduction of the covered passage coefficient, the effect of solidity on the phase change of acoustic transmissions can be approximated with a good degree of accuracy.

Effects of chord length

Figure 8.16 shows the effect of chord length on the transmission and reflection coefficients for upstream propagating acoustic waves impinging on the 0°stagger blade row from the downstream side (*Case G-*). In these plots the results for chord length $c = 0.04m$ and $c = 0.08m$ are displayed. It can be seen from the plots that with the increase of chord length, the reduction of reflection amplitude due to the wavenumber parameter $kc = \pi$ (at about $\alpha = 50°$ for $c = 0.04m$) moves to a lower incident mode angle (at about $\alpha = 35°$ for $c = 0.08m$). This is obvious since the relation $kc = \pi$ is satisfied at a lower wavenumber k for higher chord length c (i.e. occurs at lower ω and hence lower α for the case studied). As the chord length is doubled, the time required for an acoustic wave to propagate through the blade passage and thus its phase change is doubled. The phase change of acoustic waves transmitting through the blade row doubles as the chord length is doubled

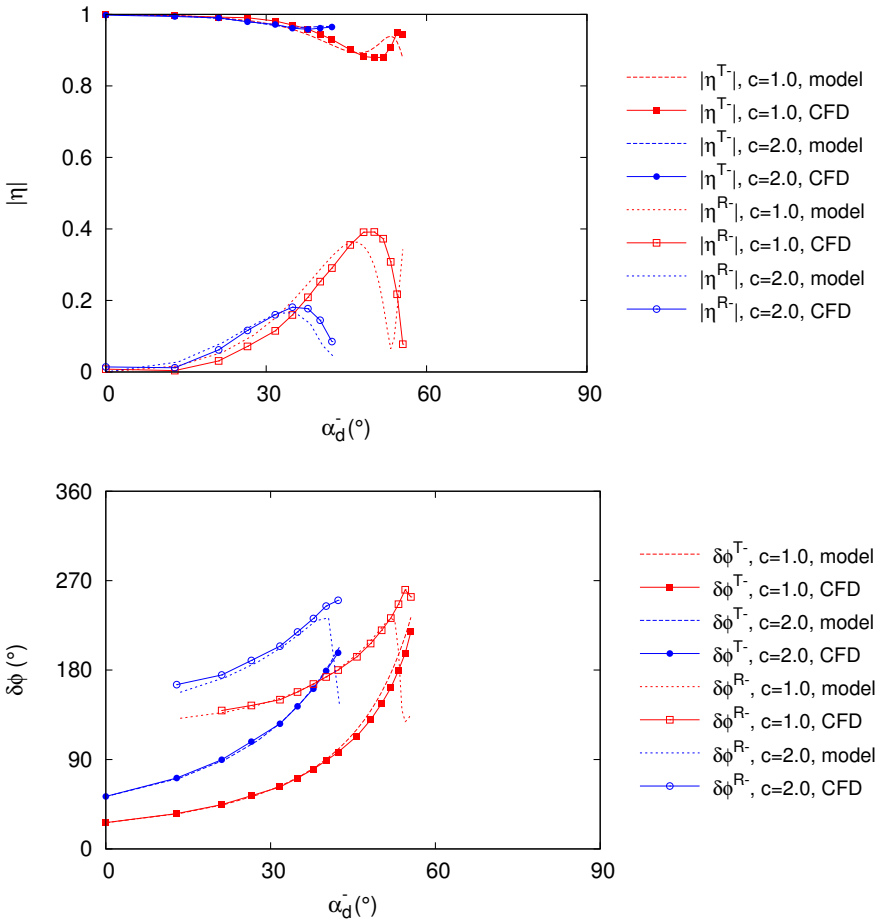


Figure 8.16: Effect of chord length on transmission and reflection coefficients, $\theta_s = 0°$, $M = 0.1$, $c/s = 2.0$, *Case G-*.

since the time required for acoustic waves to propagate through the blade passage is doubled.

The phase change of acoustic waves reflecting from the blade row also shows an increase with the increase of chord length, indicating that (at least) part of the reflection process occurs at the passage opening at the leading edge. It can be seen from the plots that the discussed trends are well captured by the analytical model except for discrepancies due to solidity close to cut-off.

Effects of camber

In order to investigate the accuracy of the devised analytical method in predicting the transmission and reflection coefficients of acoustic waves at a blade row consisting of loaded blades, unsteady CFD computations are performed for a thin annulus blade row consisting of cambered blades. The geometry and grid for the cambered blades are identical to that presented in Chapter 5, where the stagger of blades are 45°and the mean flow fields upstream and downstream of the blade row are illustrated in Figure 5.14.

Figure 8.17 shows the computed transmission and reflection coefficients as a function of incident mode angle. In these plots the results for the transmission and reflection of acoustic waves at a blade row of 45°stagger flat plates and 45°stagger cambered blades are displayed. It can be seen from the plots that the amplitude of reflected acoustic waves shows an increase with the introduction of camber (and thus blade loading) especially at higher incident mode angles. On the other hand, the amplitude of the transmitted waves show very limited changes due to the camber of blade. Moreover, it is seen that the condition corresponding to zero reflection amplitude (at about $\alpha = 30°$ for flat plates) no longer exists as a result of the introduction of camber. The phase of the reflection coefficient shows a continuous change (blue lines) instead of 180°step change (red lines) as shown in the bottom plot of Figure 8.17. The calculations based on the devised analytical method shows very good agreement with the results obtained from unsteady CFD solutions. Furthermore, the continuous phase change through the zero reflection amplitude region (at about $\alpha = 30°$) is accurately modelled by the devised analytical method. It will be shown in the next section for the computations of the loaded stator vanes that the

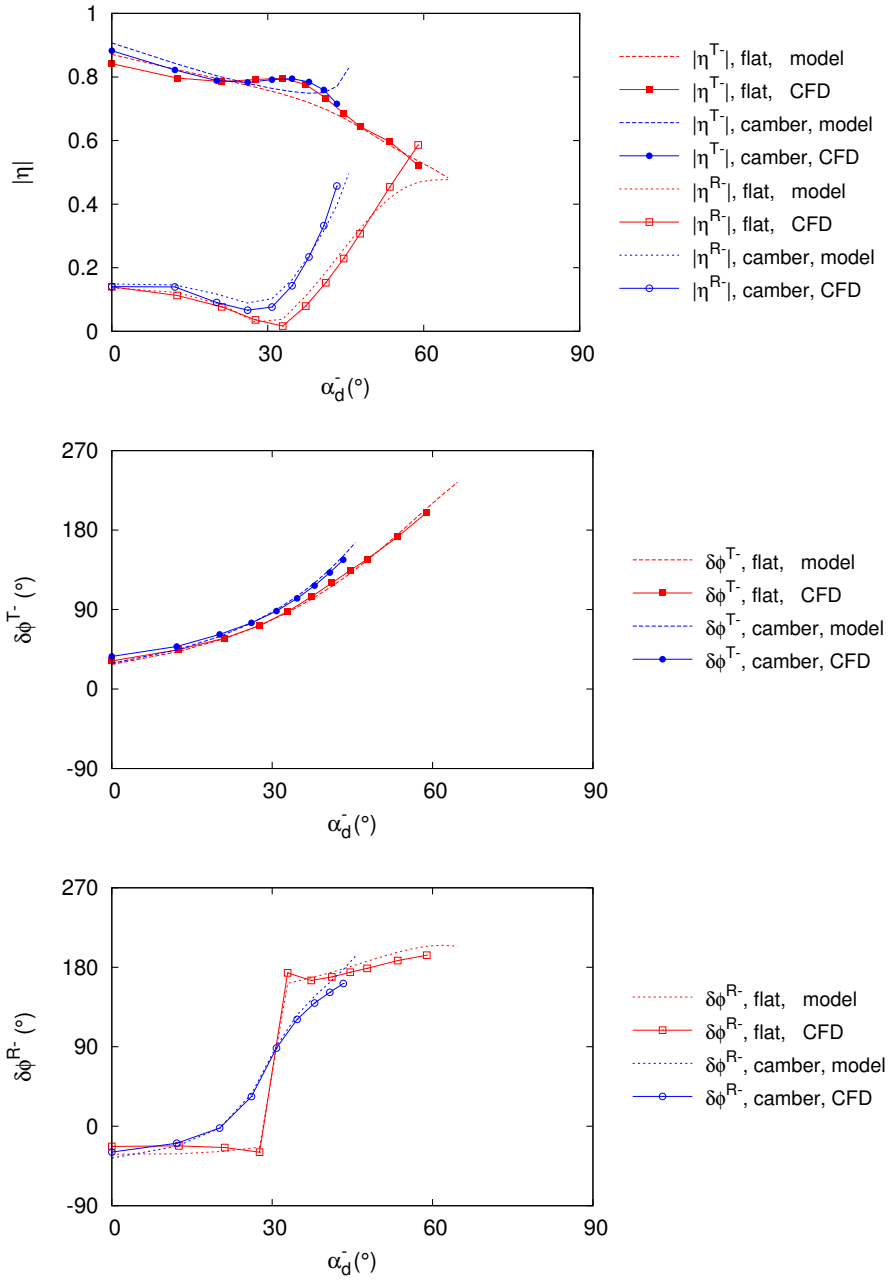


Figure 8.17: Effect of camber on transmission and reflection coefficients, $c/s = 2.0$, $c_t = 0.82$, *Case G-*.

ability to predict this continuous phase change is essential in predicting the phase of reflected acoustic waves in real turbomachinery applications.

It is clearly demonstrated in Figure 8.10 to Figure 8.17 that the devised analytical model is capable of analysing the transmission and reflection of acoustic waves at a thin annulus blade row. The main findings of the parametric study can be summaries as follows:

- The effect of solidity is relatively small for low incident mode angles. The effect becomes more pronounced for modes close to cut-off where the application of the analytical method is inadequate. Moreover, solidity was shown to have a noticeable impact on the phase change of upstream propagating acoustic waves transmitting through a blade row; this effect can be modelled with a reasonably good degree of accuracy with the proposed covered passage parameter.

- The increase in blade chord length (at a fixed solidity) results in an increase in the phase change of acoustic waves transmitting through and reflecting from a blade row, which is obvious since longer physical time is required for waves to propagate through the blade row. At the condition of $kc = n\pi$ for integer n, acoustic waves pass through the blade row undisturbed resulting in unity transmission and zero reflection.

- When the blades are cambered, the unity transmission and zero reflection conditions are no longer valid. The camber of blades, and thus the turning of flow, showed a significant impact on the reflection coefficient with a higher amplitude and a continuous phase change. The effect of camber on the transmission coefficient was found to be small.

The effects of key parameters such as incident mode angle, Mach number, stagger and chord length are captured well by the model. Moreover, the devised model shows clear improvements compared with the semi-actuator disk model in [27], where the effects of blade camber are not accounted for. Discrepancies are observed at high incident mode angles where acoustic waves are close to cut-off. However, analyses for acoustic reflection driven flutter usually do not focus on these conditions (near cut-off), since the

aero-damping of the isolated blade (in a long straight duct) is usually quite high and flutter is unlikely to occur.

8.3.2 Three-dimensional stator vanes

In the next step, transmission and reflection of acoustic waves at three-dimensional stator vanes (Stator 1 and Stator 2) of the E3E HP compressor are investigated. This is achieved (similar to the previous section) by performing unsteady CFD computations for the stator vanes of interest with incoming acoustic perturbations imposed using unsteady plane sources. Transmission and reflection coefficients of acoustic waves are obtained from wave-splitting of the unsteady CFD solutions, and are compared with calculations using the analytical method. The main objective of this section is to establish the applicability and accuracy of the devised analytical method (based on the cascade theory) on the prediction of the transmission and the reflection coefficients of acoustic waves at three-dimensional stator vanes.

The incident acoustic waves imposed in the CFD computations have the same properties (such as frequency, axial wavenumber and mode angle) with those generated by the vibration of Rotor 2 blades (as shown in Figure 8.4 and Figure 8.5). Unsteady CFD computations and analytical calculations are carried out for the upstream propagating acoustic waves impinging on the trailing edge of S1, and the downstream propagating acoustic waves impinging on the leading edge of S2. By using this approach, the amplitude and phase of the reflected acoustic waves propagating back towards the embedded Rotor 2 can be evaluated. For the analysis conducted here, acoustic reflections from blade rows further away (e.g. Rotor 1 and Rotor 3) are not considered since they were shown to have negligible influence on the flutter stability of Rotor 2 (Figure 7.26).

For the steady state flow studied in this section, the flow past the stators are fixed at the peak efficiency operating condition, i.e. operating point E shown in Chapter 7, at which flutter of R2 in the 1F/0ND mode is observed. For unsteady CFD computations, non-reflecting boundary conditions are applied at the inflow and outflow boundaries to minimise numerical reflections. The unsteady computations are performed using a full annulus approach. The physical time step for unsteady computations is resolved as 200 time steps per period. This time step was obtained by performing a

temporal convergence study.

In order to mimic the forward and backward travelling waves generated by the vibration of R2 blades, the frequency of perturbation in the stationary frame of reference is varied with the circumferential mode order (as the relationship shown by the black line in Figure 8.2). It is seen from Figure 7.5 that for the vibration mode studied the rotor blade experiences the maximum displacement at the tip, which usually corresponds to the region with the maximum (positive or negative) aerodynamic damping. Therefore, the investigations in this section concentrate on the behaviour of acoustic waves in the tip region. Analytical calculations are performed based on the radially averaged mean flow field, and are compared with the results obtained from wave-splitting of the unsteady CFD solutions on the casing surface. Furthermore, the analysis focuses on the low inter-blade phase angle modes corresponding to $-6 \leq m \leq 6$, since most of the cut-on acoustic modes are situated in this region and the aero-damping for the isolated rotor is at the minimum (Figure 7.25). This nodal diameter range is thus considered to be the most prone to acoustic reflection driven flutter. It is also worth noting that the accuracy of the post-processing wave-splitting procedure used deteriorates as modes become cut-off, which could lead to difficulties in the interpretation of results for highly cut-off modes.

Figure 8.18 shows the real and imaginary components of axial wavenumber for upstream and downstream propagating acoustic waves as a function of circumferential order m. In these plots the results obtained from wave-splitting of unsteady CFD solutions (symbols) are compared with the calculations based on the analytical method (solid and dashed curves) at the leading and trailing edges of the stators. Based on the knowledge gained from Figure 8.4, it can be seen from Figure 8.18 that acoustic modes are cut-on for a wider range of circumferential orders downstream of the stators (dashed curves have a wider range of zero imaginary components), which is a result of the reduction in swirl by the stator blades (i.e. M_θ is decreased). For the range of circumferential order shown in these plots, acoustic modes are predicted by the analytical method to be cut-on for $-1 \leq m \leq 5$ at the leading edge of S1 (solid curves in bottom left plot), for $-1 \leq m \leq 4$ at the leading edge of S2 (solid curves in bottom right plot), and for $-1 \leq m \leq 6$ at the trailing edge of both stators (dashed lines in the bottom plots). In general, a good agreement can be seen between the calculations based on

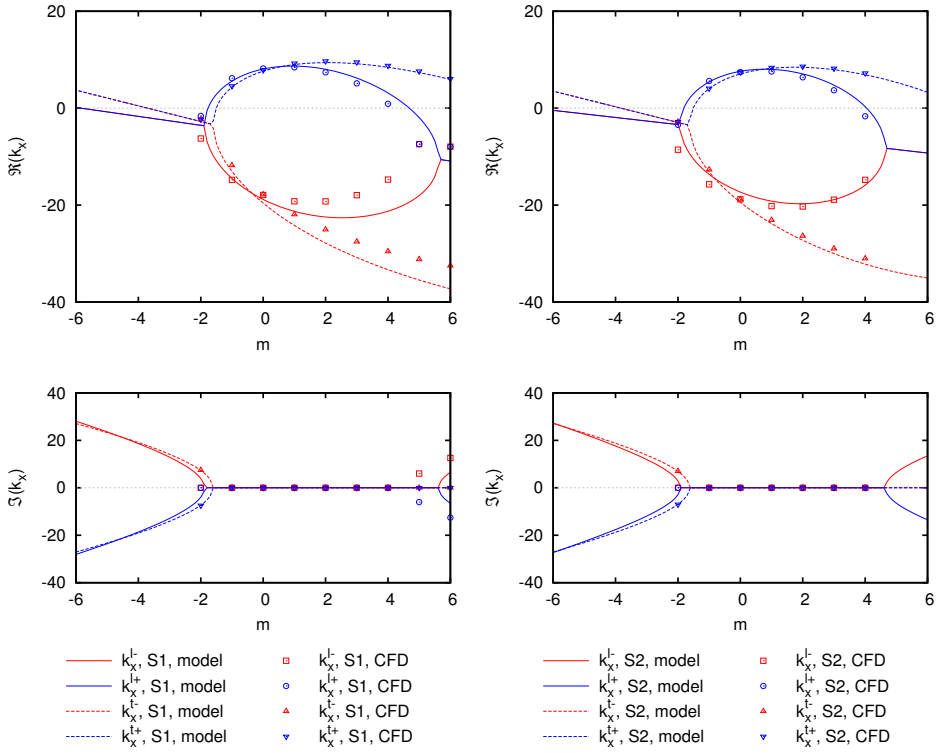


Figure 8.18: Real and imaginary components of axial wavenumber for upstream propagating ($-$) and downstream propagating ($+$) acoustic waves at the leading edge (l) and the trailing edge (t) of (a) S1 (left plots) and (b) S2 (right plots).

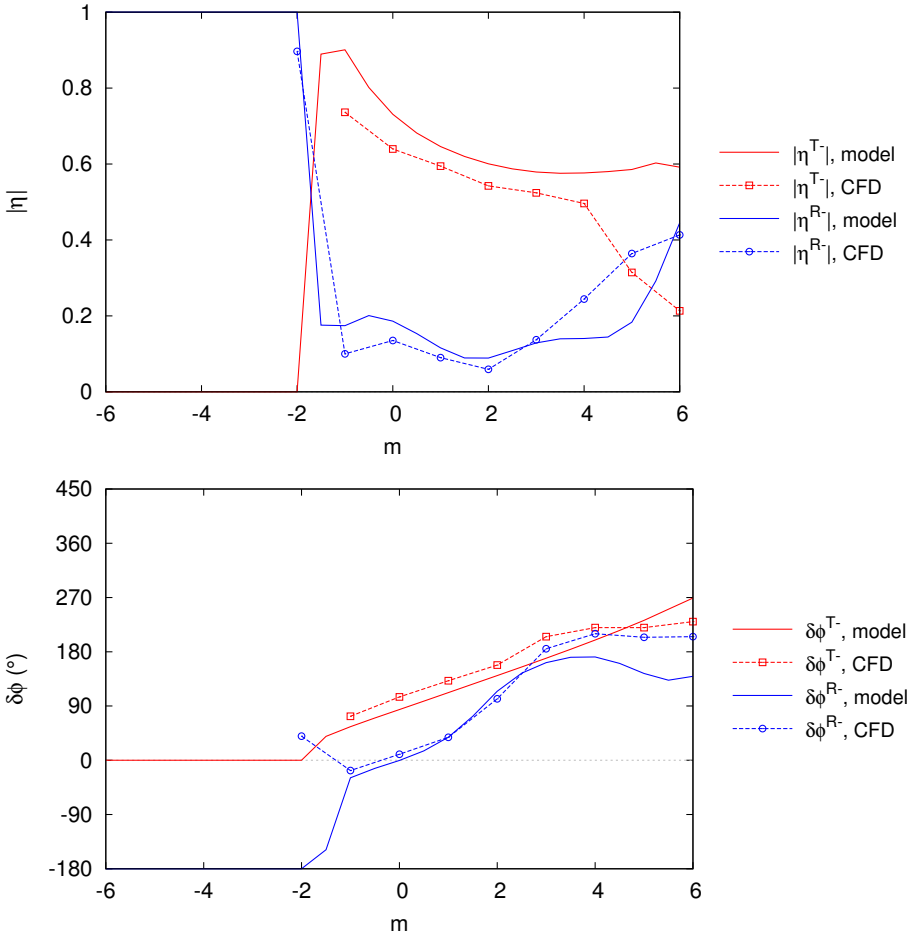


Figure 8.19: Transmission and reflection coefficients of upstream propagating acoustic waves generated by R2 vibration at S1, $c_t = 0.72$.

the analytical method and the results obtained from unsteady CFD solutions. A noticeable discrepancy can be seen at $m = -2$, where the mode is shown to be cut-on at the leading edge of both stators in CFD (zero imaginary component for square and circle symbols) and is predicted to be just cut-off by the analytical calculations (small non-zero imaginary component for solid curves). Moreover, the leading edge cut-on range is slightly over-predicted by the analytical method (bottom left plot), which indicates cut-off at $m = 6$ as opposed to $m = 5$ given by wave-splitting. This over-prediction also affects the calculated real components of axial wavenumber around $m = 5$, where discrepancies can be seen in the top left plot.

Figure 8.19 shows the computed complex transmission and reflection coefficients, due to acoustic waves impinging on S1, as a function of circumferential order m. In these plots the amplitude ratio and phase change of the coefficients obtained from wave-splitting of unsteady CFD computations are compared with the calculations based on the analytical method. It should be noted that the CFD results shown in these plots are for cut-on waves due to the difficulty in wave-splitting for cut-off modes. The results in this figure show a very similar trend to those in Figure 8.17 for the cambered blade. Moreover, as the incident acoustic wave becomes cut-off ($m < -2$), the transmission coefficient shows a rapid decrease to zero whereas the reflection coefficient goes up to near unity. As opposed to the unloaded flat blades, the condition for zero reflection amplitude is no longer present due to steady blade loading. As a result, the phase of the reflection coefficient shows a continuous transition (in the vicinity of $m = 2$) instead of a 180°step change (for instance shown in Figure 8.12).

It can be seen from the plots that the transmission and reflection coefficients between the results obtained from wave-splitting of unsteady CFD solutions and from analytical calculations show a reasonably good agreement (especially at low NDs which are cut-on). The discrepancy is seen to increase with the increase of the circumferential mode order, where the amplitude of transmission coefficient is over-predicted and the amplitude of reflection coefficient is under-predicted (at $m = 4, 5$). Moreover, the discrepancies in the phase of transmission and reflection coefficients also increase with the increase of m. The observed discrepancies are believed to be the result of acoustic modes becoming cut-off in the upstream field of S1 (cut-off when $m > 4$), leading to difficulties in both the analytical calculations and the wave-splitting procedure. Moreover, the analytical calculations are based on the radially averaged flow field, which represent an approximated two-dimensional solution to a three-dimensional geometry and flow field. Nevertheless, the phase of the reflected acoustic waves, which is the most important parameter for acoustic reflection driven flutter, is calculated with a good degree of accuracy using the devised analytical model for low NDs which are of interest for flutter in the 1F mode.

Figure 8.20 shows the computed complex transmission and reflection coefficients, due to acoustic waves impinging on S2, as a function of circumferential order m. It can be seen from the plots that the amplitude of

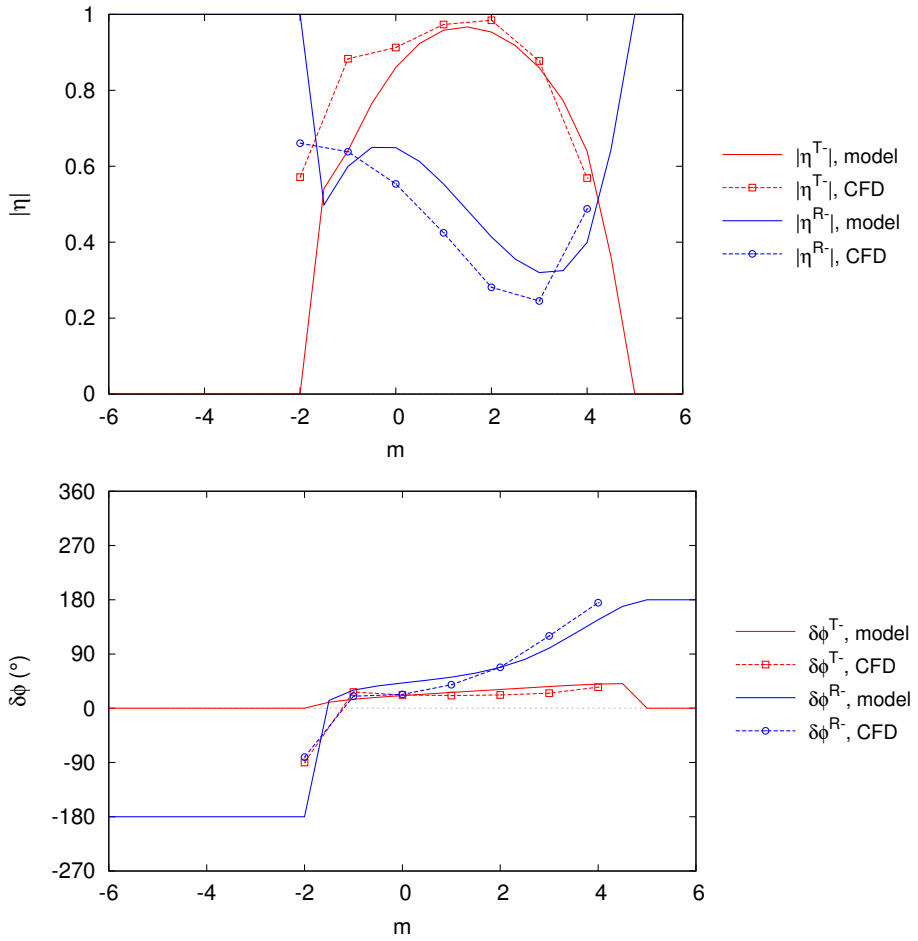


Figure 8.20: Transmission and reflection coefficients of downstream propagating acoustic waves generated by R2 vibration at S2.

transmission coefficient reaches a maximum value of nearly unity around $m = 2$, which is the result of the incident mode angle (about $\alpha = 50°$ as shown in Figure 8.5) in alignment with the stagger of S2 (about 45°). Contrary to the transmission and reflection of acoustic waves at flat plates, the amplitude of the reflection coefficient at this condition is significantly higher than zero as a result of non-negligible steady blade loading. As the incident wave becomes cut-off ($m < -2$ or $m > 4$), it is again seen from the plots that the amplitude of transmission coefficient decreases and the amplitude of reflection coefficient increases. Moreover, it is seen that for the flow condition studied, the amplitude of reflection coefficient due to the incident downstream propagating acoustic waves impinging on S2 is significantly higher than that due to the upstream propagating acoustic waves reflecting from S1. It is clearly seen that the transmission and reflection coefficients calculated using the devised analytical model show good agreement with the results obtained from wave-splitting of unsteady CFD solutions.

It has been shown in this section that the devised analytical model is capable of predicting the complex transmission and reflection coefficients of acoustic waves at a blade row with loaded blades. The analytical calculations based on the radially averaged flow field are in good agreement with the results on the casing surface obtained from wave-splitting of unsteady CFD solutions. The accuracy of the analytical calculations deteriorates as acoustic modes approach cut-off (for high circumferential mode orders). The discrepancies are believed to come from three origins: (1) the simplifications in the development of the analytical model (for instance the effect of solidity is not accounted for as demonstrated in Figure 8.12); (2) the limitations of the two-dimensional cascade model when applied to three-dimensional geometries and flows, since the cut-on/off of acoustic modes in such a three-dimensional duct is dependent on the radial distribution of the mean flow field instead of the average; (3) the difficulty in modelling the transmission and reflection of acoustic waves in the situation of cut-on/off transition across a blade row (i.e. the condition which can lead to acoustic resonance), for instant at $m = 6$ in Figure 8.19. Nevertheless, a good agreement has be observed for cut-on acoustic modes with low circumferential order m (i.e. low inter-blade phase angle modes), where the blade aerodynamic damping (for the 1F mode) for the isolated rotor is at the minimum.

8.4 Flutter Computations Using the Simplified Approach

It has been demonstrated in the previous section that the transmission and reflection coefficients of acoustic waves at a blade row can be calculated analytically with a reasonable degree of accuracy without the need of unsteady CFD computations. Based on the information obtained, the calculated reflected acoustic waves are imposed inside the domain of the embedded rotor using unsteady plane sources (as demonstrated in Section 5.4), which allows unsteady CFD computations to be performed in a single passage single blade row fashion. This section presents the application of the proposed method on the embedded Rotor 2 of the E3E HP compressor (Chapter 7). The results obtained by using the proposed method are compared with those based on high-fidelity full annulus multi-row models (presented in Chapter 7).

For the steady state flow studied in this section, the operating condition for the rotor is fixed at the peak efficiency operating point E (Section 7.5). at which flutter of R2 in the 1F/0ND mode is observed.

The blade vibration is initiated at a reduced frequency of 0.67 at which flutter of the 1F/0ND mode was measured in test and predicted by full annulus multi-row unsteady CFD computations. Aerodynamic work at each blade stream section is calculated through integration of unsteady pressure and blade motion (Section 3.4). For the flutter analyses conducted in this section, the cut-on low inter blade phase angle forward travelling modes (0ND to 4ND) are only considered. The physical time step for flutter computations is resolved as 200 time steps per vibration cycle. This time step was obtained by performing a temporal convergence study.

Three configurations of the problem are studied in this work:

- *Case GR*: rotor with imposed acoustic gust from the upstream field, which represents partially embedded Rotor 2 with acoustic reflections from Stator 1.

- *Case RG*: rotor with imposed acoustic gust from the downstream field, which represents partially embedded Rotor 2 with acoustic reflections from Stator 2.

- *Case GRG*: rotor with imposed acoustic gust from the upstream and

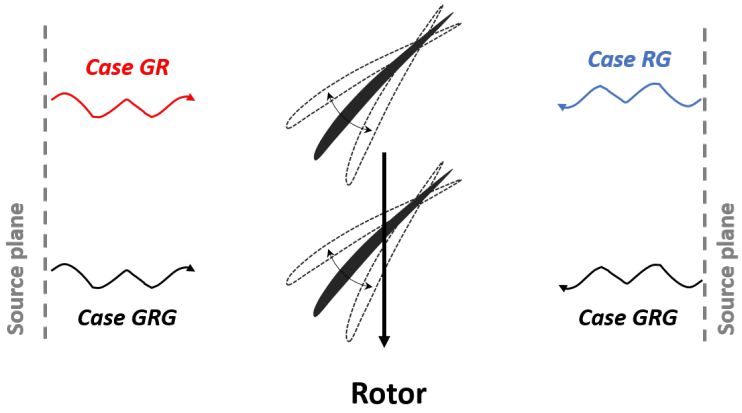


Figure 8.21: Imposing acoustic waves in the rotor domain using unsteady plane sources.

downstream fields simultaneously, which represents embedded Rotor 2 with acoustic reflections from both Stator 1 and Stator 2.

The above configurations are illustrated schematically in Figure 8.21.

Figure 8.22 shows the computed aero-damping of R2 in the partially embedded environment as a function of nodal diameter. In this plot the aero-damping obtained from full annulus multi-row unsteady CFD computations, namely *Case SR* and *Case RS* (solid red and black curves), are compared with the aero-damping obtained using the simple approach, namely *Case GR* and *Case RG* (dashed red and black curves). Also shown in this plot as a reference is the aero-damping for the isolated *Case R* obtained from full annulus unsteady CFD computation. The aero-damping computed using the simple approach for nodal diameters 0ND to 4ND (cut-on on both upstream and downstream sides of R2) are shown in this plot. A similar trend can be seen between the aero-damping predicted using the simple approach and the aero-damping obtained from full annulus multi-row computations, indicating that the phase of the reflected waves is adequately predicted by the model. It is seen that the effects of Stator 2 for 1ND and 2ND are under-predicted, whereas the effects of Stator 1 is under-predicted at 0ND and 4ND and over-predicted at 1ND. These over- and under-predictions of aero-damping are likely to be the result of the discrepancies in the calculated amplitude and phase of the reflected acoustic waves.

Figure 8.23 shows the computed aero-damping of R2 in the embedded

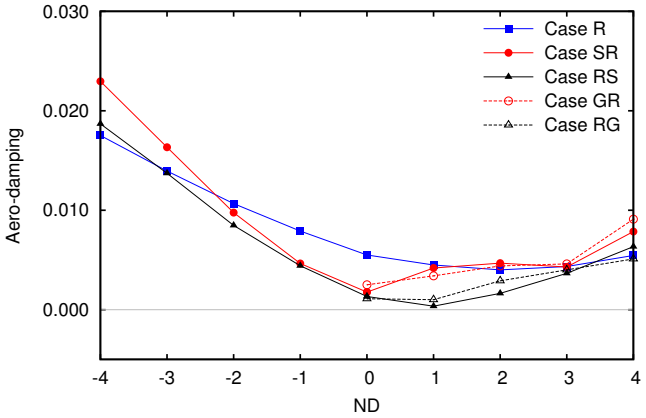


Figure 8.22: Aero-damping of R2 in the partially embedded S1/R2 and R2/S2 environments.

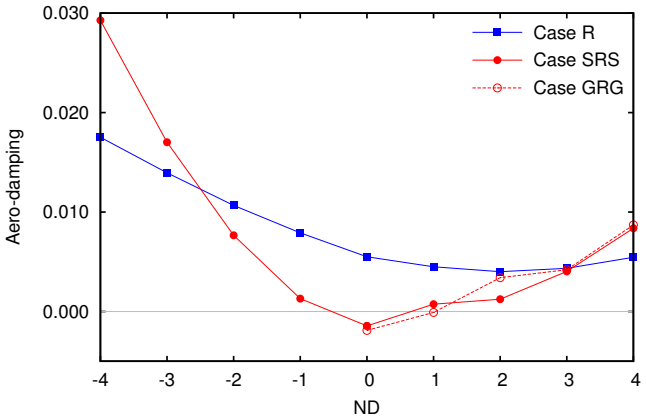


Figure 8.23: Aero-damping of R2 in the embedded S1/R2/S2 environment.

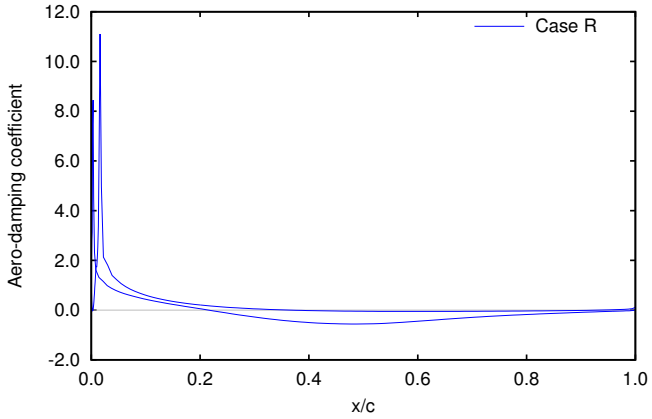


Figure 8.24: Aero-damping coefficient at 90% span of R2 (0ND).

environment as a function of nodal diameter. In this plot the aero-damping obtained from full-annulus multi-row unsteady CFD computations, namely *Case 3R* (solid red curve), is compared with the aero-damping obtained using the simple approach, namely *Case GRG* (dashed red curve). Also shown in this plot for reference is the aero-damping for the isolated *Case R* obtained from full annulus unsteady CFD computation. Again, the aero-damping computation computed using the simple approach for nodal diameters 0ND to 4ND (cut-on on both upstream and downstream sides of R2) are shown in this plot. In general, the trend of aero-damping obtained from the simple approach shows a reasonably good agreement with that obtained from the full annulus multi-row computations. A notable discrepancy is seen at 2ND where the effect of adjacent stators is under-predicted. Nevertheless, flutter is predicted at 0ND using the simple approach, which confirms its applicability on the case studied.

In order to further verify the predictions using the simple approach, aerodynamic work coefficient and the aero-damping coefficient at various R2 spans are calculated. Figure 8.24 and Figure 8.25 show the calculated aero-damping coefficient at 90% span of R2 as a function of normalised axial chord (x/c) for the 0ND mode for the isolated and 3-row analysis.

It is seen in Figure 8.24 (*Case R*) that at this radial height, the leading edge of Rotor 2 in this study is responsible for providing the main source of positive aero-damping, whereas the mid-chord region is the main source of negative aero-damping. In order to show the change in aero-damping due

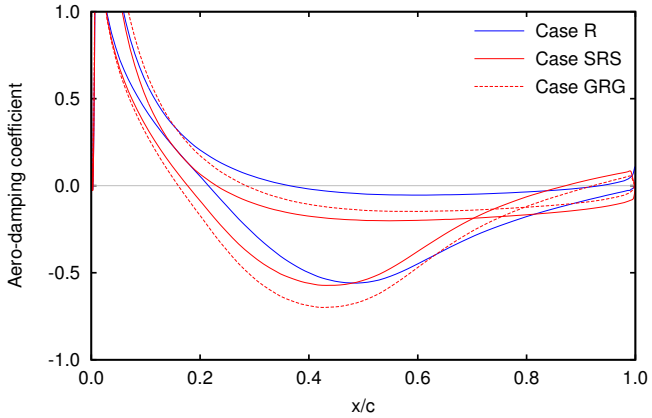


Figure 8.25: Aero-damping coefficient at 90% span of R2 (0ND).

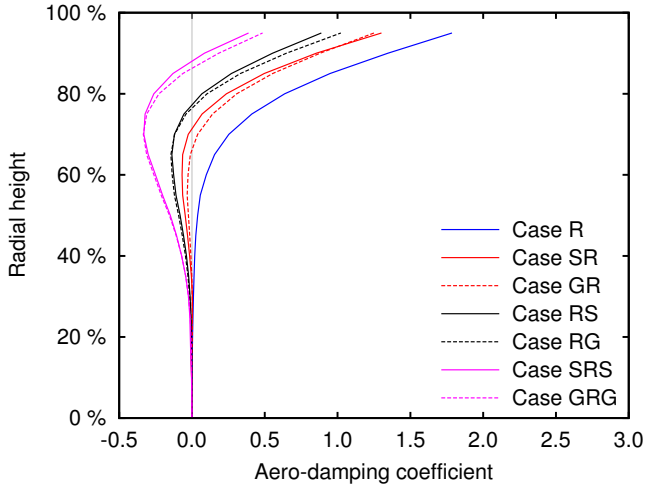


Figure 8.26: Aero-damping coefficient at a function of R2 span (0ND).

to acoustic reflections from the adjacent stators more clearly (i.e. ignore the leading edge peak), the range of the y axis is restricted to the same order as that near the mid-chord, i.e. -1 to 1. It can be seen from Figure 8.25 that the presence of acoustic reflections from the adjacent stators induce more negative aero-damping in the mid-chord region of the blade. The leading edge aero-damping is not changed significantly due to the presence of acoustic reflections from the stators, indicating that the the positive aero-damping at the leading edge is dominated by the unsteady loading effect induced by the blade motion. The aero-damping obtained using the simple approach shows a reasonable agreement with that obtained from the full annulus multi-row analysis. Importantly, the trend of aero-damping is captured adequately by the simplified approach. By further comparing the radial distribution of the calculated aero-damping coefficient, shown in Figure 8.26 as a function of R2 span, it is seen that the radial aero-damping distribution is also captured by the simple approach with reasonable accuracy, where similar trends can be identified between the results obtained using the two approaches. It is also seen that the major contribution to aero-damping comes from the outer span of the blade (60% to 100%). The simple approach achieves an overall reduction of computational cost of around 360 times for the case studied compared with the full annulus multi-row approach.

In conclusion, the proposed low-fidelity alternative strategy is intended for evaluating the influence of acoustic reflection on flutter stability of embedded rotors at a reduced cost compared with full annulus multi-row unsteady CFD computations. Although computational techniques for multi-row interactions, such as partial assembly for time-domain methods and the capability for single passage multi-row unsteady computations for frequency-domain methods (limited to selected frequencies), can be adopted to reduce the computation cost while retaining reasonably high fidelity, these approaches focus on the numerical aspects of the problem and do not provide physical explanations as for why and how the interaction occurs. Conversely, the devised new strategy, although of lower fidelity, allows one to analyse the mechanisms behind the acoustic reflection driven flutter and investigate the influence of key parameters with relative ease. In light of the understandings gained through the process, physical insights can be drawn regarding ways to prevent such flutter events for embedded rotors, which cannot be easily achieved by means of full annulus multi-row CFD compu-

tations. Therefore, the proposed alternative strategy provides a useful tool in early design stages of an engine when the susceptibility of an embedded blade row to acoustic reflection driven flutter is to be investigated.

9 Conclusion and Further Work

Modern gas turbine design continues to drive towards improved performance, reduced weight and reduced cost. This trend of aero-engine design results in thinned blade aerofoils which are more susceptible to flutter. Moreover, the use of Titanium blade-integrated-disks (blisks) is becoming more common in modern aeroengine designs. Such structures have very low mechanical damping in contrast to traditional bladed-disk assemblies. For such structures, the main source of damping to the blade comes from the air flow, which highlights the importance of accurate prediction of blade damping contribution due to aerodynamic forces. Recent rig tests and CFD predictions have shown that reflections of the acoustic waves generated by blade vibration can play an important part on flutter stability of embedded blades in multi-stage compressors. Therefore, accurate prediction of blade aerodynamic damping in a multi-row environment becomes vital. However, research on the interactions between the blade vibration, the resulting reflected acoustic waves and flutter is limited, and the physical understanding of such interactions is poor. Therefore, this thesis presented a detailed investigation into the flutter of fans and embedded rotors in the core compressors of modern axial flow aero-engines driven by acoustic reflections from the intake and the adjacent blade rows, with the aim of developing a new strategy for the flutter analysis of such embedded blades which can be used at early design stages of an engine. This chapter presents the main findings of this thesis and concludes with a series of recommendations for future work.

9.1 Concluding Remarks

This thesis addressed the impact of the interactions between acoustic reflections and flutter of embedded blades, where the term embedded refers to blades that are surrounded by structures such as other blade rows or engine intakes. It was shown that such interactions are driven by the re-

flection of perturbations generated by the blade vibration, which occurs at the frequency of vibration rather than the blade passing frequencies. For the present work the study concentrated on the flutter of blades in the 1st flapwise bending (1F) mode with the interest in the low inter-blade phase angles (the least stable modes for the 1F mode).

Objective 1

Propose and devise a method to model the generation, propagation and reflection of acoustic waves due to blade vibration.

With the aim of understanding the fundamental mechanisms behind the acoustic reflection driven flutter of embedded blade rows, an analytical method was devised to calculate the transmission and reflection of acoustic waves at a blade row consisting of cambered blades, which is capable of providing more accurate amplitude and phase changes of acoustic waves in such situations over the existing analytical methods based on unloaded flat plates. Based on the established theories and the methods devised, a model was constructed to calculate the complete reflection process of an acoustic wave, whereby the amplitude and phase relations between the outgoing acoustic waves generated by blade vibration and the resulting reflected acoustic waves can be obtained without the need of unsteady CFD computations.

Armed with the analytical model developed, in-depth analyses were carried out to study the acoustic reflection driven flutter in a fan and intake system and an embedded environment for a rotor blade in a multi-stage compressor. Analytical calculations based on the devised method showed good agreement with the results obtained from wave-splitting of full annulus unsteady CFD solutions, indicating that the acoustic reflection from the intake and blade rows can be evaluated analytically with a good degree of accuracy without the need of unsteady CFD computations.

Objective 2

Study the influence of acoustic reflection from adjacent blade rows on flutter stability of the rotor blades in core compressors.

The fundamental behaviour of blade vibration and its interaction with duct acoustics was studied first by performing flutter computations of a

thin annulus blade row. It was shown that for blade vibration in a flap mode, the aero-damping contribution for the twist vibration driven by the unsteady moment (induced by both the plunge and twist motions) is negligible, whereas the unsteady lift induced by the plunge motion is always positively damped and the unsteady lift induced by the twist motion is always negatively damped. The effect of incoming acoustic gusts (at the same frequency with the blade vibration) on the near blade unsteady pressure field and the resulting blade aero-damping was also investigated. It was shown that the incoming acoustic gust can induce significant changes of unsteady pressure, and consequently marked changes in the amplitude and phase of the unsteady blade loading, resulting in beneficial or detrimental effects on the blade aero-damping. The effect of the incoming gust on blade flutter stability was more pronounced for the plunge vibration than the twist vibration, and the most detrimental condition was observed when the unsteady loading contribution induced by the incoming acoustic gust is in phase with the plunge velocity. The analysis concluded that the effects on blade aero-damping due to the blade motion and the incoming acoustic gust are independent and can be analysed separately.

The influence of acoustic reflections from adjacent blade rows on flutter stability of an embedded rotor in a multi-stage compressor was studied next. Acoustic reflections were demonstrated to have a significant impact on the flutter stability of embedded rotor blades. Flutter of the embedded blades in this study occurs at a flow condition well away from stall, and at a reduced frequency significantly higher than the typical critical flutter frequencies. It was shown that this type of flutter requires the acoustic waves produced by the blade vibration to to be cut-on on both upstream and downstream sides of the blade. Reflection of these generated acoustic waves from the two neighbouring stators were shown to have the largest influence on the flutter stability of the embedded rotor, where the effect of reflections from blade rows farther away was found to be negligible for the case studied. It was demonstrated that flutter is most likely to occur when the minimum aero-damping contribution due to the blade motion and the most detrimental effect due to the acoustic reflections coincide. Moreover, for such rotor blades embedded in a multi-stage compressor, the variation of vibration frequency showed limited impact on the aero-damping contribution due to the blade motion. On the other hand, blade vibration

frequency and rotor-stator axial gap were found to be the key parameters for the acoustic reflection driven flutter of such embedded blades.

Objective 3

Study the effects of acoustic reflection from the intake on flutter stability of the fan blades.

Flutter bite of fan blades was demonstrated to occur at part speed operating conditions near the stall boundary driven by the acoustic reflections from the intake. It was shown that acoustic reflections can play an important part in fan flutter, and should be taken into account during the design of a new engine. This type of flutter requires the acoustic waves generated by the blade vibration to to be cut-on on the upstream side of the blade and cut-off on the downstream side of the blade. Reflection of the cut-on acoustic waves from the intake changes the aero-damping of the blade by modifying the phase and amplitude of unsteady pressure at the leading edge of the blade. By conducting flutter computations using different intake geometries and subsequent post-processing analysis based on a wave-splitting procedure, it was shown that the aero-damping contribution due to the blade motion and the acoustic reflection from the intake are independent and can be analyses separately, therefore the design of a new intake can be assessed on its own for the same fan set. Intake length, Mach number and vibration frequency were found to be the key parameters which determine the timing and phasing of the reflected acoustic wave, which can result in beneficial or detrimental effects to the overall stability of the fan and intake system.

The analysis revealed a relationship between the phase difference between the reflected and outgoing acoustic waves at the leading edge of the blade and the aero-damping contribution due to the acoustic reflections from intake. The most destabilising case occurs when the outgoing wave lags the reflected wave by 90°. Furthermore, by performing flutter computations at different fan speeds and with different intake length, it was found that the increase in intake length moves the flutter bite to a lower speed.

Objective 4

Based on the understanding gained, develop a new low-fidelity method which is capable of predicting the possibility of flutter of compressor blades (or fan) due to acoustic reflections.

A novel simple analytical model was proposed to evaluate the susceptibility of fan blades to acoustic reflection driven flutter. The model calculates the propagation of acoustic waves in the intake duct and their reflections at the intake opening, from which the amplitude and phase relation between the outgoing and the reflected acoustic waves can be obtained. A parameter called 'flutter index' was proposed to characterise the effects of acoustic reflections on flutter stability of fan blades. The proposed index is a function of the amplitude of reflection coefficient at the intake opening, and the phase difference between the outgoing and the reflected acoustic waves at the leading edge of the blade. The calculated 'flutter index' showed good agreement with the aero-damping contribution due to acoustic reflections from the intake which were obtained from unsteady CFD computations. The model was applied to a real intake and showed a good agreement with the flutter bite speed for three rig fan blades measured.

In addition, a new alternative strategy for the flutter analysis of embedded blade rows in multi-stage compressors was proposed. The method works by modelling the propagation and reflection of acoustic waves at the adjacent blade rows using an analytical approach, whereby flutter computations of the embedded rotor can be performed in a single passage fashion by imposing the calculated reflected waves as unsteady plane sources. Using the low-fidelity approach, aero-damping of the (embedded) rotor blade was computed and showed similar trend with the aero-damping obtained from full annulus multi-row computations. The proposed method differs from the existing approaches, such as full annulus multi-row unsteady CFD computations, in that it provides the physical explanations as for why and how the interaction between flutter and acoustic reflections occurs. Moreover, the method allows one to efficiently analyse the effect of key parameters that are influential to the acoustic reflection driven flutter, based on which physical insights can be drawn regarding ways to prevent the occurrence of such flutter events for embedded rotors. It was shown that computations using the proposed model leads to two orders of magnitude reduction

in computational cost compared with time domain full annulus multi-row computations.

9.2 Recommendations for Future Work

The effectiveness of the analytical methods in analysing the flutter of embedded blades due to acoustic reflections is clearly demonstrated in this thesis. The following aspects associated with the analytical methods can be improved:

- Sound generation due to the blade vibration is currently modelled using unsteady CFD computations. Established analytical methods concerning this subject ignore the steady loading and the camber of the blades. This issue becomes more predominant for the flutter bite of fan blades where the pre-condition for flutter requires the upstream side of the blade to be cut-on and the downstream side of the blade to be cut-off. These existing analytical methods which use blade rows with no mean pressure rise are therefore incapable of reproducing the unsteady pressure field required, and are thus unsuitable for the analysis of acoustic reflection driven flutter. Improvements of the analytical methods to include the effects of steady loading would allow the modelling of sound generation to be conducted in an analytical approach, which would lead to further cost reductions of the proposed model.

- The transmission and reflection of acoustic waves at a blade row is modelled using the cascade method with a good degree of success. Improvements of the current method can be sought to extend the existing model to three dimensions, which can become useful for applications with significant radial variation of blade geometry and flow field. Moreover, the extended three dimensional model would allow the capabilities of analysing the reflection of acoustic waves with higher radial orders (i.e. $n > 0$).

- The (complex) reflection coefficients from the intake opening calculated using the existing approach show a reasonably good agreement with the results obtained from wave-splitting of unsteady CFD solutions. It was shown in Section 6.7 that the effect of intake lip geometry

has a significant impact on the amplitude of the reflected waves. This effect is not modelled by the existing analytical approach. Further in-depth studies can be performed to explore the physics behind this phenomenon and seek for possible improvements for the existing analytical method.

- The low-fidelity flutter analysis method presented in Section 5.5 was shown to be very effective in determining the most destabilising condition due to the effect of incoming acoustic gusts. Further analysis can be performed to obtained a more rigorous analytical relationship between the unsteady lift and the blade leading and trailing edge unsteady pressure field, so that the magnitude of the aero-damping contributions can be evaluated without the need of unsteady CFD computations.

This thesis focuses on the flutter of embedded blades due to acoustic reflections from other structures. There are known cases where the upstream propagating acoustic wave generated by the blade vibration can be reflected into a downstream propagating vortical wave, and the downstream propagating vortical wave generated by the blade vibration can be reflected into an upstream propagating acoustic wave. In order to investigate the influence of these effects, computations can be performed to study the generation of vortical waves due to the blade vibration, and the effect on blade aero-damping due to incoming vortical gusts. Both of these studies require further developments of the post-processing wave-splitting procedure, where the splitting of unsteady disturbances into vortical waves is known to be difficult.

Finally, methods to prevent such acoustic reflection driven flutter can be sought. Acoustic liners can be incorporated into the model as they are typically used in intakes to reduce community noise levels. The liners work by attenuating the acoustic waves at community noise frequencies. The model can be extended to include the effects of the acoustic liner on the propagation and reflection of acoustic waves in the intake at flutter freqiencies. Moreover, casing treatments and flow injection at the blade tip are used to enhance the aerodynamic stability of the blade. These methods modify the geometry of the duct and create genuinely unsteady circulatory flows near the tip of the blade, both of which are expected to have a non-negligible

effect on the generation and propagation of acoustic waves. Further studies regarding the behaviour of acoustic waves in these regions could provide viable solutions for the prevention of the acoustic reflection driven flutter.

Bibliography

[1] Garrick, I. E., and Reed, W. H., 1981. "Historical Development of Aircraft Flutter". *J. Aircr.,* ***18***(11), pp. 897–912.

[2] Hansen, M. H., 2007. "Aeroelastic instability problems for wind turbines". *Wind Energy,* ***10***(6), pp. 551–577.

[3] Srinivasan, a. V., 1997. "Flutter and Resonant Vibration Characteristics of Engine Blades". *J. Eng. Gas Turbines Power,* ***119***(4), p. 742.

[4] Klinger, H., Lazik, W., and Wunderlich, T., 2008. "The Engine 3E Core Engine". In ASME Turbo Expo 2008 Power Land, Sea, Air Vol. 1 Aircr. Engine; Ceram. Coal, Biomass Altern. Fuels; Manuf. Mater. Metall. Microturbines Small Turbomach., pp. 93–102.

[5] Laxalde, D., Gibert, C., and Thouverez, F., 2008. "Experimental and Numerical Investigations of Friction Rings Damping of Blisks". In Vol. 5 Struct. Dyn. Parts A B, ASME, pp. 469–479.

[6] Vahdati, M., and Imregun, M., 1996. "A Non-Linear Aeroelasticity Analysis of a Fan Blade Using Unstructured Dynamic Meshes". *Proc. Inst. Mech. Eng. Part C J. Mech. Eng. Sci.,* ***210***(6), nov, pp. 549–564.

[7] Isomura, K., and Giles, M. B., 1998. "A Numerical Study of Flutter in a Transonic Fan". *J. Turbomach.,* ***120***(3), p. 500.

[8] Srivastava, R., Bakhle, M. A., and Keith, T. G., 2003. "Numerical Simulation of Aerodynamic Damping for Flutter Analysis of Turbomachinery Blade Rows". *J. Propuls. Power,* ***19***(2), mar, pp. 260–267.

[9] Chi, R. M., and Srinivasan, A. V., 1985. "Some Recent Advances in the Understanding and Prediction of Turbomachine Subsonic Stall Flutter". *J. Eng. Gas Turbines Power,* ***107***(2), p. 408.

[10] Vahdati, M., Smith, N. H. S., and Zhao, F., 2015. "Influence of Intake on Fan Blade Flutter". *J. Turbomach.,* ***137***(8), p. 081002.

[11] Vahdati, M., and Cumpsty, N., 2015. "Aeroelastic Instability in Transonic Fans". *J. Eng. Gas Turbines Power,* ***138***(2), sep, p. 022604.

[12] Vahdati, M., Simpson, G., and Imregun, M., 2011. "Mechanisms for Wide-Chord Fan Blade Flutter". *J. Turbomach.,* ***133***(4), p. 041029.

[13] Lane, F., 1956. "System Mode Shapes in the Flutter of Compressor Blade Rows". *J. Aeronaut. Sci.,* ***23***(616), pp. 54–66.

[14] Whitehead, D., 1962. "Force and moment coefficients for vibrating aerofoils in cascade". *Gt. Britain ARC R&M,* ***3254***(3254).

[15] Chiang, H.-W. D., and Kielb, R. E., 1993. "An Analysis System for Blade Forced Response". *J. Turbomach.,* ***115***(4), pp. 762–770.

[16] Campbell, W., 1924. "The Protection of Steam-Turbine Disk Wheels From Axial Vibration - Part II - Exposition of the Nature and Theory of Vibration in Turbine Wheels". *Gen. Electr. Rev.,* ***27***(7), pp. 459–484.

[17] Fung, Y. C., 2002. *An introduction to the theory of aeroelasticity.* Courier Corporation.

[18] Kielb, R. E., Barter, J. W., Thomas, J. P., and Hall, K. C., 2003. "Blade Excitation by Aerodynamic Instabilities: A Compressor Blade Study". In Vol. 4 Turbo Expo 2003, ASME, pp. 399–406.

[19] Dodds, J., and Vahdati, M., 2015. "Rotating Stall Observations in a High Speed CompressorPart I: Experimental Study". *J. Turbomach.,* ***137***(5), may, p. 051002.

[20] Snyder, L. E., and Burns, D. W., 1988. *Forced vibration and flutter design methodology.* North Atlantic Treaty Organization, Advisory Group for Aerospace Research and Development, jun.

[21] Tyler, J., and Sofrin, G., 1962. Axial Flow Compressor Noise Studies. Tech. rep., jan.

[22] Whitehead, D., 1972. "Vibration and Sound Generation in a Cascade of Flat Plates in Subsonic Flow". *Gt. Britain ARC R&M*(3685).

[23] Smith, S. N., 1973. "Discrete Frequency Sound Generation in Axial Flow Turbomachines". *Gt. Britain ARC R&M*(3709), pp. 1–58.

[24] Parker, R., 1966. "Resonance effects in wake shedding from parallel plates: Some experimental observations". *J. Sound Vib.,* ***4***(1), pp. 62–72.

[25] Parker, R., and Griffiths, W., 1968. "Low frequency resonance effects in wake shedding from parallel plates". *J. Sound Vib.,* ***7***(3), pp. 371–379.

[26] Parker, R., 1984. "Acoustic Resonances Axial Flow and Blade Vibration in". *J. Sound Vib.,* ***92***, pp. 529–539.

[27] Kaji, S., and Okazaki, T., 1970. "Propagation of sound waves through a blade row. II. Analysis based on the acceleration potential method". *J. Sound Vib.,* ***11***(3), pp. 355–IN1.

[28] Cooper, A. J., and Peake, N., 2000. "Trapped acoustic modes in aeroengine intakes with swirling flow". *J. Fluid Mech.,* ***419***, pp. 151–175.

[29] Hellmich, B., and Seume, J., 2008. "Causes of Acoustic Resonance in a High-Speed Axial Compressor". *J. Turbomach.,* ***130***(3), pp. 031003–1–9.

[30] Koch, W., 2009. "Acoustic resonances and trapped modes in annular plate cascades". *J. Fluid Mech.,* ***628***, p. 155.

[31] Buffum, D. H., 1995. "Blade Row Interaction Effects on Flutter and Forced Response". *J. Propuls. Power,* ***11***(2), mar, pp. 205–212.

[32] Silkowski, P. D., 1996. "A coupled mode method for multistage aeroelastic and aeroacoustic analysis of turbomachinery". PhD thesis.

[33] Hall, K. C., and Silkowski, P. D., 1997. "The Influence of Neighboring Blade Rows on the Unsteady Aerodynamic Response of Cascades". *J. Turbomach.,* ***119***(1), jun, p. 85.

[34] Silkowski, P. D., and Hall, K. C., 1998. "A Coupled Mode Analysis of Unsteady Multistage Flows in Turbomachinery". *J. Turbomach.,* ***120***(3), pp. 410–421.

[35] Whitehead, D. S., 1987. "Classical Two-Dimensional Methods". In *AGARD Man. Aeroelasticity Axial Flow Turbomachines, Vol. 1, Unsteady Turbomach. Aerodyn.*

[36] Hall, K. C., and Ekici, K., 2005. "Multistage Coupling for Unsteady Flows in Turbomachinery". *AIAA J.,* ***43***(3), mar, pp. 624–632.

[37] Namba, M., Yamasaki, N., and Nishimura, S., 2000. "Unsteady Aerodynamic Force on Oscillating Blades of Contra-Rotating Annular Cascades". In Proc. 9th Int. Symp. Unsteady Aerodyn. Aeroacoustics Aeroelasticity Turbomachines.

[38] Ekici, K., and Hall, K. C., 2007. "Nonlinear Analysis of Unsteady Flows in Multistage Turbomachines Using Harmonic Balance". *AIAA J.,* ***45***(5), pp. 1047–1057.

[39] Li, H. D., and He, L., 2005. "Blade Aerodynamic Damping Variation With Rotor-Stator Gap: A Computational Study Using Single-Passage Approach". *J. Turbomach.,* ***127***(3), p. 573.

[40] Huang, X. Q., He, L., and Bell, D. L., 2006. "Influence of Upstream Stator on Rotor Flutter Stability in a Low Pressure Steam Turbine Stage". *Proc. Inst. Mech. Eng. Part A J. Power Energy,* ***220***(1), jan, pp. 25–35.

[41] Rahmati, M. T., He, L., Wang, D. X., Li, Y. S., Wells, R. G., and Krishnababu, S. K., 2013. "Nonlinear Time and Frequency Domain Methods for Multirow Aeromechanical Analysis". *J. Turbomach.,* ***136***(4), sep, p. 041010.

[42] Fransson, T., and Vogt, D., 2011. "FUTURE Flutter-Free Turbomachinery Blades". In Aero Days 2011, Madrid, pp. 1–35.

[43] Hsu, K., Hoyniak, D., and Anand, M. S., 2012. "Full-Annulus Multi-Row Flutter Analyses". *Proc. ASME Turbo Expo 2012*, p. 1453.

[44] Sharland, I. J., 1964. "Sources of Noise in Axial Flow Fans". *J. Sound Vib.,* ***1***(3), pp. 302–322.

[45] Mani, R., 1970. "Discrete frequency noise generation from an axial flow fan blade row". *J. Basic Eng.,* ***92***(1), pp. 37–43.

[46] Giles, M. B., 1990. "Nonreflecting boundary conditions for Euler equation calculations". *AIAA J.,* ***28***(12), dec, pp. 2050–2058.

[47] Morfey, C., 1964. "Rotating pressure patterns in ducts: Their generation and transmission". *J. Sound Vib.,* ***1***(1), pp. 60–87.

[48] Kaji, S., and Okazaki, T., 1970. "Propagation of sound waves through a blade row. I. Analysis based on the semi-actuator disk theory". *J. Sound Vib.,* ***11***(3), pp. 339–353.

[49] Mani, R., and Horvay, G., 1970. "Sound transmission through blade". *J. Sound Vib.,* ***12***(1), pp. 59–83.

[50] Wiener, N., and Hopf, E., 1931. "Über eine Klasse singulärer Integralgleichungen". *Sem-Ber. Preuss. Akad. Wiss. Berlin.,* ***30/32***, pp. 696–706.

[51] Amiet, R., and Sears, W. R., 1969. Reflection and transmission of oblique sound waves by a blade row. Tech. rep.

[52] Lane, F., and Friedman, M., 1958. Theoretical investigation of subsonic oscillatory blade-row aerodynamics. Tech. rep.

[53] Rienstra, S., 1984. "Acoustic radiation from a semi-infinite annular duct in a uniform subsonic mean flow". *J. Sound Vib.,* ***94***(2), pp. 267–288.

[54] Ovenden, N., Eversman, W., and Rienstra, S., 2004. "Cut-on Cut-off Transition in Flow Ducts: Comparing Multiple-scales and Finite-element Solutions". *10th AIAA/CEAS Aeroacoustics Conf.*, p. 2945.

[55] Marshall, J., and Imregun, M., 1996. "A Review of Aeroelasticity Methods With Emphasis on Turbomachinery Applications". *J. Fluids Struct.,* ***10***(3), pp. 237–267.

[56] Whitehead, D. S., 1959. "Vibration of cascade blades treated by actuator disc methods". *Arch. Proc. Inst. Mech. Eng. 1847-1982 (vols 1-196),* ***173***(1959), jun, pp. 555–574.

[57] Tanida, Y., and Okazaki, T., 1963. "Stall-Flutter in Cascade : 1st Report, Translatory Vibration of Cascade Blades as Treated by Semi-Actuator Disc Method, Part 1". *Bull. JSME,* ***6***(24), pp. 744–752.

[58] Tanida, Y., and Okazaki, T., 1963. "Stall-Flutter in Cascade : 2nd Report, Translatory Vibration of Cascade Blades as Treated by Semi-Actuator Disc Method, Part 2". *Bull. JSME,* ***6***(24), pp. 753–757.

[59] Adamczyk, J. J., 1978. Analysis of Supersonic Stall Bending Flutter in Axial-Flow Compressor by Actuator Disk Theory. Tech. rep.

[60] Adamczyk, J. J., Stevans, W., and Jutras, R., 1982. "Supersonic Stall Flutter of High-Speed Fans". *J. Eng. Power,* ***104***(3), p. 675.

[61] Bendiksen, O. O., and Friedmann, P. P., 1982. "The Effect of Bending-Torsion Coupling on Fan and Compressor Blade Flutter". *J. Eng. Power,* ***104***(3), p. 617.

[62] Srinivasan, A. V., and Fabunmi, J. A., 1984. "Cascade Flutter Analysis of Cantilevered Blades". *J. Eng. Gas Turbines Power,* ***106***(1), p. 34.

[63] Bendiksen, O. O., 1986. "Role of shocks in transonic/supersonic compressor rotor flutter". *AIAA J.,* ***24***(7), jul, pp. 1179–1186.

[64] Kielb, R. E., and Kaza, K. R. V., 1985. "Flutter of Swept Fan Blades". *J. Eng. Gas Turbines Power,* ***107***(2), p. 394.

[65] Kielb, R. E., and Ramsey, J. K., 1989. "Flutter of a Fan Blade in Supersonic Axial Flow". *J. Turbomach.,* ***111***(4), p. 462.

[66] Imregun, M., 1995. "Prediction of flutter stability using aeroelastic FRF". *J. Fluids Struct.,* ***9***(9), may, pp. 419–434.

[67] Bendiksen, O. O., 1991. "A new approach to computational aeroelasticity". In 32nd Struct. Struct. Dyn. Mater. Conf., Vol. AIAA-91-09, American Institute of Aeronautics and Astronautics, pp. 1712–1727.

[68] Guruswamy, P., and Yang, T. Y., 1981. "Aeroelastic time response analysis of thin airfoils by transonic code LTRAN2". *Comput. Fluids,* ***9***(4), dec, pp. 409–425.

[69] Berry, H. M., Batina, J. T., and Yang, T. Y., 1986. "Viscous effects on transonic airfoil stability and response". *J. Aircr.,* ***23***(5), may, pp. 361–369.

[70] Bendiksen, O. O., 1987. "Transonic flutter analysis using the Euler equations". In 28th Struct. Struct. Dyn. Mater. Conf., no. 87, American Institute of Aeronautics and Astronautics.

[71] Cunningham, H. J., Batina, J. T., and Bennett, R. M., 1988. "Modern wing flutter analysis by computational fluid dynamics methods". *J. Aircr.,* ***25***(10), oct, pp. 962–968.

[72] Yang, Z., and Zhao, L., 1988. "Analysis of limit cycle flutter of an airfoil in incompressible flow". *J. Sound Vib.,* ***123***(1), may, pp. 1–13.

[73] Tatum, K. E., and Giles, G., 1988. "Integrating nonlinear aerodynamic and structural analysis for a complete fighter configuration". *J. Aircr.,* ***25***(12), dec, pp. 1150–1156.

[74] Srivastava, R., Huff, D. L., Sankar, L. N., and Reddy, T. S. R., 1991. "Application of an efficient hybrid scheme for aeroelastic analysis of advanced propellers". *J. Propuls. Power,* ***7***(5), sep, pp. 767–775.

[75] Yamamoto, O., and August, R., 1992. "Structural and aerodynamic analysis of a large-scale advanced propeller blade". *J. Propuls. Power,* ***8***(2), mar, pp. 367–373.

[76] He, L., 1994. "Integration of 2-D Fluid/Structure Coupled System for Calculations of Turbomachinery Aerodynamic/ Aeroelastic Instabilities". *Int. J. Comut. Fluid Dyn.,* ***3***(3-4), dec, pp. 217–231.

[77] He, L., and Denton, J. D., 1994. "Three-Dimensional Time-Marching Inviscid and Viscous Solutions for Unsteady Flows Around Vibrating Blades". *J. Turbomach.,* ***116***(3), p. 469.

[78] Ji, S., and Liu, F., 1999. "Flutter computation of turbomachinery cascades using a parallel unsteady Navier-Stokes code". *AIAA J.,* ***37***(3), mar, pp. 320–327.

[79] Yao, J., Jameson, A., Alonso, J. J., and Liu, F., 2001. "Development and Validation of a Massively Parallel Flow Solver for Turbomachinery Flows". *J. Propuls. Power,* ***17***(3), may, pp. 659–668.

[80] Doi, H., and Alonso, J. J., 2002. "Fluid/Structure Coupled Aeroelastic Computations for Transonic Flows in Turbomachinery". In Vol. 4 Turbo Expo 2002, Parts A B, no. August, ASME, pp. 787–794.

[81] Adamczyk, A. J., 1984. Modeling Equations for Simulating Flows in Multistage Turbomachinery. Tech. rep.

[82] Verdon, J. M., and Caspar, J. R., 1984. "A linearized unsteady aerodynamic analysis for transonic cascades". *J. Fluid Mech.,* ***149***, dec, p. 403.

[83] Giles, M., 1992. "An Approach for Multi-Stage Calculations Incorporating Unsteadiness". In ASME 1992 Int. Gas Turbine Aeroengine Congr. Expo. Vol. 1 Turbomach., ASME, p. V001T01A092.

[84] Hall, K. C., and Clark, W. S., 1993. "Linearized euler predictions of unsteady aerodynamic loads in cascades". *AIAA J.,* ***31***(3), mar, pp. 540–550.

[85] He, L., and Ning, W., 1998. "Efficient approach for analysis of unsteady viscous flows in turbomachines". *AIAA J.,* ***36***(11), nov, pp. 2005–2012.

[86] Clark, W. S., and Hall, K. C., 2000. "A Time-Linearized NavierStokes Analysis of Stall Flutter". *J. Turbomach.,* ***122***(3), p. 467.

[87] Petrie-Repar, P., 2004. "Development of an Efficient Linearised Navier-Stokes Flow Solver for Turbomachinery Applications". In *New Results Numer. Exp. Fluid Mech. IV*. Springer-Verlag Berlin Heidelberg, pp. 286–293.

[88] Ning, W., and He, L., 1997. "Computation of Unsteady Flows Around Oscillating Blades Using Linear and Nonlinear Harmonic Euler Methods". *ASME 1998 Int. Gas Turbine Aeroengine Congr. Exhib.,* ***120***(3), p. 8.

[89] Hall, K. C., Thomas, J. P., and Clark, W. S., 2002. "Computation of Unsteady Nonlinear Flows in Cascades Using a Harmonic Balance Technique". *AIAA J.,* ***40***(5), may, pp. 879–886.

[90] Thomas, J., Custer, C., Dowell, E., and Hall, K., 2009. "Unsteady Flow Computation Using a Harmonic Balance Approach Implemented About the OVERFLOW 2 Flow Solver". In 19th AIAA Comput. Fluid Dyn., American Institute of Aeronautics and Astronautics.

[91] Yao, W., and Marques, S., 2014. "An Aeroelastic Harmonic Balance Solver Using High-Order CFD". In R. Aeronaut. Soc. Bienn. Appl. Aerodyn. Res. Conf. 2014.

[92] Olausson, M., and Eriksson, L.-E., 2009. "An absorbing inlet buffer layer for rotor wake/stator time domain computations". In Proc. ASME Turbo Expo 2009, pp. 709–718.

[93] Petrie-Repar, P. J., 2010. "Three-Dimensional Non-Reflecting Boundary Condition for Linearized Flow Solvers". In Vol. 6 Struct. Dyn. Parts A B, ASME, pp. 1247–1252.

[94] Sayma, A. I., Vahdati, M., Sbardella, L., and Imregun, M., 2000. "Modeling of Three-Dimensional Viscous Compressible Turbomachinery Flows Using Unstructured Hybrid Grids". *AIAA J.,* ***38***(6), jun, pp. 945–954.

[95] Spalart, P., and Allmaras, S., 1992. "A one-equation turbulence model for aerodynamic flows". In 30th Aerosp. Sci. Meet. Exhib., American Institute of Aeronautics and Astronautics.

[96] Swanson, R., and Turkel, E., 1992. "On central-difference and upwind schemes". *J. Comput. Phys.,* ***101***(2), aug, pp. 292–306.

[97] Choi, M., Smith, N. H. S., and Vahdati, M., 2013. "Validation of Numerical Simulation for Rotating Stall in a Transonic Fan". *J. Turbomach.,* ***135***(2), p. 021004.

[98] Dodds, J., and Vahdati, M., 2015. "Rotating Stall Observations in a High Speed CompressorPart II: Numerical Study". *J. Turbomach.,* ***137***(5), p. 51003.

[99] Newmark, N., 1959. "A Method of Computation for Structural Dynamics". *J. Eng. Mech.,* ***85***(7), pp. 67–94.

[100] Batina, J. T., 1991. "Unsteady Euler algorithm with unstructured dynamic mesh for complex-aircraft aerodynamic analysis". *AIAA J.,* ***29***(3), mar, pp. 327–333.

[101] Hirsch, C., 2007. *Numerical Computation of Internal and External Flows*. Butterworth-Heinemann; 2 edition.

[102] Toro, E. F., 2009. *Riemann Solvers and Numerical Methods for Fluid Dynamics*. Springer Berlin Heidelberg, Berlin, Heidelberg.

[103] Vahdati, M., Sayma, A. I., Freeman, C., and Imregun, M., 2005. "On the Use of Atmospheric Boundary Conditions for Axial-Flow Compressor Stall Simulations". *J. Turbomach.,* ***127***(2), p. 349.

[104] Denton, J., and Singh, U., eds., 1979. Time marching methods for turbomachinery flow calculation.

[105] Moinier, P., and Giles, M. B., 2005. "Eigenmode Analysis for Turbomachinery Applications". *J. Propuls. Power,* ***21***(6), nov, pp. 973–978.

[106] Rice, E., Heidmann, M., and Sofrin, T., 1979. "Modal propagation angles in a cylindrical duct with flow and their relation to sound radiation". In 17th Aerosp. Sci. Meet., American Institute of Aeronautics and Astronautics.

[107] Rienstra, S. W., 1999. "Sound transmission in slowly varying circular and annular lined ducts with flow". *J. Fluid Mech.,* ***380***, pp. 279–296.

[108] Cooper, A. J., and Peake, N., 2001. "Propagation of unsteady disturbances in a slowly varying duct with mean swirling flow". *J. Fluid Mech.,* ***445***, pp. 207–234.

[109] Atassi, H., and Akai, T. J., 1978. "Aerodynamic Force and Moment on Oscillating Airfoils in Cascade". In ASME 1978 Int. Gas Turbine Conf. Prod. Show Vol. 1B Gen., ASME, p. V01BT02A080.

[110] Zhao, F., Smith, N., and Vahdati, M., 2016. "A Simple Model for Identifying the Flutter Bite' of Fan Blades". In Vol. 7B Struct. Dyn., ASME, p. V07BT34A004.

[111] Zhao, F., Nipkau, J., and Vahdati, M., 2016. "Influence of acoustic reflections on flutter stability of an embedded blade row". *Proc. Inst. Mech. Eng. Part A J. Power Energy,* ***230***(1), pp. 29–43.

[112] Zhao, F., Nipkau, J., and Vahdati, M., 2015. "A Simple Low-Fidelity Model for Embedded Blade Row Flutter Prediction". In Vol. 7B Struct. Dyn., ASME, p. V07BT34A002.

[113] Klinger, H., Bake, S., Vogt, H.-F., Knieschke, D., and Schober, P., 2011. "Altitude Testing of the E3E Core Engine". In Vol. 1 Aircr. Engine; Ceram. Coal, Biomass Altern. Fuels; Wind Turbine Technol., ASME, pp. 223–232.

Appendix I: Eigenmode Decomposition in Inviscid Flow

The compressible Euler equations in convective form can be expressed as

$$\frac{\mathrm{D}\rho}{\mathrm{D}t} + \rho\nabla\cdot\mathbf{u} = 0 \tag{9.1}$$

$$\rho\frac{\mathrm{D}\mathbf{u}}{\mathrm{D}t} + \nabla p = 0 \tag{9.2}$$

$$\rho\frac{\mathrm{D}E}{\mathrm{D}t} + \nabla\cdot(p\mathbf{u}) = 0 \tag{9.3}$$

where the variables have their usual meaning.

In cylindrical coordinate system (x, r, θ) the above equations can be written as

$$\frac{\partial\rho}{\partial t} + \rho\frac{\partial u_x}{\partial x} + \rho\frac{\partial u_r}{\partial r} + \frac{\rho}{r}\left(\frac{\partial u_\theta}{\partial\theta} + u_r\right) + u_x\frac{\partial\rho}{\partial x} + u_r\frac{\partial\rho}{\partial r} + \frac{u_\theta}{r}\frac{\partial\rho}{\partial\theta} = 0 \tag{9.4}$$

$$\rho\frac{\partial u_x}{\partial t} + \rho u_x\frac{\partial u_x}{\partial x} + \rho u_r\frac{\partial u_x}{\partial r} + \rho\frac{u_\theta}{r}\frac{\partial u_x}{\partial\theta} + \frac{\partial p}{\partial x} = 0 \tag{9.5}$$

$$\rho\frac{\partial u_r}{\partial t} + \rho u_x\frac{\partial u_r}{\partial x} + \rho u_r\frac{\partial u_r}{\partial r} + \rho\frac{u_\theta}{r}\frac{\partial u_r}{\partial\theta} - \rho u_\theta\frac{u_\theta}{r} + \frac{\partial p}{\partial r} = 0 \tag{9.6}$$

$$\rho\frac{\partial u_\theta}{\partial t} + \rho u_x\frac{\partial u_\theta}{\partial x} + \rho u_r\frac{\partial u_\theta}{\partial r} + \rho\frac{u_\theta}{r}\frac{\partial u_\theta}{\partial\theta} + \rho u_r\frac{u_\theta}{r} + \frac{1}{r}\frac{\partial p}{\partial\theta} = 0 \tag{9.7}$$

$$\frac{\partial p}{\partial t} + u_x\frac{\partial p}{\partial x} + u_r\frac{\partial p}{\partial r} + \frac{u_\theta}{r}\frac{\partial p}{\partial\theta} + \gamma p\left(\frac{\partial u_x}{\partial x} + \frac{\partial u_r}{\partial r} + \frac{u_r}{r} + \frac{1}{r}\frac{\partial u_\theta}{\partial\theta}\right) = 0 \tag{9.8}$$

Assume small amplitude perturbations

$$\rho = \rho^0 + \rho' \tag{9.9}$$

$$u_x = u_x^0 + u_x' \tag{9.10}$$

$$u_r = u_r^0 + u_r' \tag{9.11}$$

$$u_\theta = u_\theta^0 + u_\theta' \tag{9.12}$$

$$p = p^0 + p' \tag{9.13}$$

where superscript 0 denotes the mean flow field and $'$ denotes the perturbed field.

Substitute Equation 9.9 to 9.13 into Equation 9.4 to 9.8, consider only the first order terms and ignore steady flow gradients (uniform flow assumption), one obtains the linearised Euler equations

$$\frac{\partial \rho'}{\partial t} + \rho^0 \frac{\partial u'_x}{\partial x} + \rho^0 \frac{\partial u'_r}{\partial r} + \frac{\rho^0}{r}\frac{\partial u'_\theta}{\partial \theta} + \frac{\rho^0 u'_r}{r} + \frac{\rho' u^0_r}{r} + u^0_x \frac{\partial \rho'}{\partial x} + u^0_r \frac{\partial \rho'}{\partial r} + \frac{u^0_\theta}{r}\frac{\partial \rho'}{\partial \theta} = 0 \tag{9.14}$$

$$\rho^0 \frac{\partial u'_x}{\partial t} + \rho^0 u^0_x \frac{\partial u'_x}{\partial x} + \rho^0 u^0_r \frac{\partial u'_x}{\partial r} + \frac{\rho^0 u^0_\theta}{r}\frac{\partial u'_x}{\partial \theta} + \frac{\partial p'}{\partial x} = 0 \tag{9.15}$$

$$\rho^0 \frac{\partial u'_r}{\partial t} + \rho^0 u^0_x \frac{\partial u'_r}{\partial x} + \rho^0 u^0_r \frac{\partial u'_r}{\partial r} + \frac{\rho^0 u^0_\theta}{r}\frac{\partial u'_r}{\partial \theta} - \frac{2\rho^0 u'_\theta u^0_\theta}{r} - \frac{\rho' u^0_\theta u^0_\theta}{r} + \frac{\partial p'}{\partial r} = 0 \tag{9.16}$$

$$\rho^0 \frac{\partial u'_\theta}{\partial t} + \rho^0 u^0_x \frac{\partial u'_\theta}{\partial x} + \rho^0 u^0_r \frac{\partial u'_\theta}{\partial r} + \frac{\rho^0 u^0_\theta}{r}\frac{\partial u'_\theta}{\partial \theta} + \frac{\rho' u^0_r u^0_\theta}{r} + \frac{\rho^0 u'_r u^0_\theta}{r} + \frac{\rho^0 u^0_r u'_\theta}{r} + \frac{1}{r}\frac{\partial p'}{\partial \theta} = 0 \tag{9.17}$$

$$\frac{\partial p'}{\partial t} + u^0_x \frac{\partial p'}{\partial x} + u^0_r \frac{\partial p'}{\partial r} + \frac{u^0_\theta}{r}\frac{\partial p'}{\partial \theta} + \gamma p^0 \left(\frac{\partial u'_x}{\partial x} + \frac{\partial u'_r}{\partial r} + \frac{u'_r}{r} + \frac{1}{r}\frac{\partial u'_\theta}{\partial \theta} \right) + \frac{\gamma p' u^0_r}{r} = 0 \tag{9.18}$$

The above equations can be written in a matrix form as

$$\mathbf{I}\frac{\partial \mathbf{U}}{\partial t} + \mathbf{A_x}\frac{\partial \mathbf{U}}{\partial x} + \mathbf{A_r}\frac{\partial \mathbf{U}}{\partial r} + \frac{\mathbf{A}_\theta}{r}\frac{\partial \mathbf{U}}{\partial \theta} + \frac{\mathbf{A_s}}{r}\mathbf{U} = 0 \tag{9.19}$$

where

$$\mathbf{U} = \begin{pmatrix} \rho' \\ u'_x \\ u'_r \\ u'_\theta \\ p' \end{pmatrix} \tag{9.20}$$

$$\mathbf{A_x} = \begin{pmatrix} u^0_x & \rho^0 & 0 & 0 & 0 \\ 0 & u^0_x & 0 & 0 & \frac{1}{\rho^0} \\ 0 & 0 & u^0_x & 0 & 0 \\ 0 & 0 & 0 & u^0_x & 0 \\ 0 & \gamma p^0 & 0 & 0 & u^0_x \end{pmatrix} \tag{9.21}$$

$$\mathbf{A_r} = \begin{pmatrix} u_r^0 & 0 & \rho^0 & 0 & 0 \\ 0 & u_r^0 & 0 & 0 & 0 \\ 0 & 0 & u_r^0 & 0 & \frac{1}{\rho^0} \\ 0 & 0 & 0 & u_r^0 & 0 \\ 0 & 0 & \gamma p^0 & 0 & u_r^0 \end{pmatrix} \tag{9.22}$$

$$\mathbf{A}_\theta = \begin{pmatrix} u_\theta^0 & 0 & 0 & \rho^0 & 0 \\ 0 & u_\theta^0 & 0 & 0 & 0 \\ 0 & 0 & u_\theta^0 & 0 & 0 \\ 0 & 0 & 0 & u_\theta^0 & \frac{1}{\rho^0} \\ 0 & 0 & 0 & \gamma p^0 & u_\theta^0 \end{pmatrix} \tag{9.23}$$

$$\mathbf{A_s} = \begin{pmatrix} u_r^0 & 0 & \rho^0 & 0 & 0 \\ 0 & 0 & 0 & 0 & 0 \\ -\left(u_\theta^0\right)^2 & 0 & 0 & -2\rho^0 u_\theta^0 & 0 \\ u_r^0 u_\theta^0 & 0 & \rho^0 u_\theta^0 & \rho^0 u_r^0 & 0 \\ 0 & 0 & \gamma p^0 & 0 & \gamma u_r^0 \end{pmatrix} \tag{9.24}$$

Assume $\mathbf{U}$ has a separable wave-like solution in time, and axial and circumferential space, such that

$$\mathbf{U} = \tilde{\mathbf{U}}(r) e^{-\mathrm{i}\omega t + \mathrm{i}k_x x + \mathrm{i}m\theta} \tag{9.25}$$

where ω is the angular frequency, k_x is the axial wavenumber, m is the circumferential wavenumber (order) and $\tilde{\mathbf{U}}(r)$ is the eigenfunction in the radial direction.

Pre-multiply Equation 9.19 by $\mathbf{A_x}^{-1}$ to make k_x the eigenvalue of this system, one can write

$$-\mathrm{i}\omega \mathbf{A_x}^{-1}\mathbf{U} + \mathrm{i}k_x \mathbf{U} + \mathbf{A_x}^{-1}\mathbf{A_r}\frac{\partial \mathbf{U}}{\partial r} + \frac{\mathrm{i}m}{r}\mathbf{A_x}^{-1}\mathbf{A}_\theta \mathbf{U} + \frac{1}{r}\mathbf{A_x}^{-1}\mathbf{A_s}\mathbf{U} = 0 \tag{9.26}$$

or

$$\omega \mathbf{B_t}\mathbf{U} - k_x \mathbf{U} + \mathrm{i}\mathbf{B_r}\frac{\partial \mathbf{U}}{\partial r} - \frac{m}{r}\mathbf{B}_\theta \mathbf{U} + \frac{\mathrm{i}}{r}\mathbf{B_s}\mathbf{U} = 0 \tag{9.27}$$

where

$$\mathbf{B_t} = \mathbf{A_x}^{-1} \tag{9.28}$$

$$\mathbf{B_r} = \mathbf{A_x}^{-1}\mathbf{A_r} \tag{9.29}$$

$$\mathbf{B}_\theta = \mathbf{A_x}^{-1}\mathbf{A}_\theta \tag{9.30}$$

$$\mathbf{B_s} = \mathbf{A_x}^{-1}\mathbf{A_s} \tag{9.31}$$

Equation 9.27 can be solved by forming a general eigenvalue problem, and through discretisation on N levels of radial grid

$$(\omega\hat{\mathbf{B}}_\mathbf{t} + \mathrm{i}\hat{\mathbf{B}}_\mathbf{r} - \frac{m}{r}\hat{\mathbf{B}}_\theta + \frac{\mathrm{i}}{r}\hat{\mathbf{B}}_\mathbf{s})\hat{\mathbf{U}} = k_x\hat{\mathbf{U}} \tag{9.32}$$

where $\hat{\mathbf{B}}_\mathbf{t}$, $\hat{\mathbf{B}}_\mathbf{r}$, $\hat{\mathbf{B}}_\theta$ and $\hat{\mathbf{B}}_\mathbf{s}$ are matrices of the discretised field of dimension $5N \times 5N$, and $\hat{\mathbf{U}}$ is a vector of length $5N$.

The above eigenvalue problem can be solved numerically using a central difference scheme with artificial dissipation, along with appropriate boundary conditions at the duct end-walls. The solution to this problem contains eigenvalues as the axial wavenumber k_x, and right eigenvectors as the eigenfunction $\tilde{\mathbf{U}}(r)$.

Appendix II: Solution of Acoustic Transmission and Reflection at a Blade Row

As described in Section 4.4, the simultaneous equations to be solved for the transmission and reflection of acoustic waves at a cascade of cambered blades (two flat plate section) are as follows:

$$(M_u - \frac{\cos\alpha_u^-}{\cos\theta_u})p_1 = [(1+M_u)p_5^l - (1-M_u)p_4^l] \tag{9.33}$$

$$[1 - M_u\cos(\theta_u - \alpha_u^-)]p_1 = [(1+M_u)p_5^l + (1-M_u)p_4^l] \tag{9.34}$$

$$-\cos\theta_d p_4^t + \cos\theta_d p_5^t = -\cos\alpha_d^- p_0 + \cos\alpha_d^+ p_2 + a_d R_d u_3 \tag{9.35}$$

$$-\sin\theta_d p_4^t + \sin\theta_d p_5^t = -\sin\alpha_d^- p_0 - \sin\alpha_d^+ p_2 + a_d R_d v_3 \tag{9.36}$$

$$p_4^t + p_5^t = p_0 + p_2 \tag{9.37}$$

$$(1+M_u)p_5^{ml} - (1-M_u)p_4^{ml} = \frac{a_u\cos\theta_d}{a_d\cos\theta_u}[(1+M_d)p_5^{mt} - (1-M_d)p_4^{mt}] \tag{9.38}$$

$$(1+M_u)p_5^{ml} + (1-M_u)p_4^{ml} = \frac{R_u}{R_d}[(1+M_d)p_5^{mt} + (1-M_d)p_4^{mt}] \tag{9.39}$$

where the mode angle α, blade stagger angle θ, mean flow density R, mean flow Mach number M and speed of sound a can be obtained based on the solution of the mean flow field. The mean flow field is readily available at the design stage which can be obtained based on the design intent or an analytical/numerical solution.

The above set of equations contain 13 unknown perturbations: p_0, p_1, p_2, p_4^l, p_4^{ml}, p_4^{mt}, p_4^t, p_5^l, p_5^{ml}, p_5^{mt}, p_5^t, u_3 and v_3. In order to obtain an expression for the transmission coefficient $\eta^T = \frac{p_1}{p_0}$ or the reflection coefficient $\eta^R = \frac{p_2}{p_0}$, one needs 5 additional equations to eliminate the other unknown perturbations.

For simplicity of solution, let's assume that the blade camber is small, and that the chord length of the front section and the rear section are identical and equal to $\frac{c}{2}$, where c is the chord length of the cambered blade. It should be noted that this can be easily modified to accommodate a more accurate geometry representation.

Therefore, based on the assumption of one-dimensional wave propagation in the blade passages, one obtains

$$\frac{p_4^{ml}}{p_4^l} = e^{ik_4^l \frac{c}{2}} \tag{9.40}$$

$$\frac{p_5^{ml}}{p_5^l} = e^{ik_5^l \frac{c}{2}} \tag{9.41}$$

$$\frac{p_4^t}{p_4^{mt}} = e^{ik_4^t \frac{c}{2}} \tag{9.42}$$

$$\frac{p_5^t}{p_5^{mt}} = e^{ik_5^t \frac{c}{2}} \tag{9.43}$$

where k denotes the wavenumber of acoustic waves.

Assembling Equation 9.33 to 9.43 and Equation 4.42, one obtains 12 equations for the aforementioned 13 unknowns. Rearrange and eliminate the unknown perturbations, the transmission coefficient $\eta^T = \frac{p_1}{p_0}$ and the reflection coefficient $\eta^R = \frac{p_2}{p_0}$ can be expressed as

$$\frac{p_1}{p_0} = \frac{C - B_d}{(C - A_d)Q_1 + (C + A_d)Q_2} \tag{9.44}$$

$$\frac{p_2}{p_0} = \frac{(A_d - B_d)Q_1 - (A_d + B_d)Q_2}{(C - A_d)Q_1 + (C + A_d)Q_2} \tag{9.45}$$

where

$$Q_1 = \frac{(A_u - B_u)(S_2 - S_1)}{4S_1S_2(1 + M_d)} e^{i(k_4^l + k_5^t)\frac{c}{2}} + \frac{(A_u + B_u)(S_2 + S_1)}{4S_1S_2(1 + M_d)} e^{i(k_5^l + k_5^t)\frac{c}{2}} \tag{9.46}$$

$$Q_2 = \frac{(A_u - B_u)(S_2 + S_1)}{4S_1S_2(1 - M_d)} e^{i(k_4^l + k_4^t)\frac{c}{2}} - \frac{(A_u + B_u)(S_2 - S_1)}{4S_1S_2(1 - M_d)} e^{i(k_4^t + k_5^l)\frac{c}{2}} \tag{9.47}$$

$$A_u = 1 - M_u \cos(\theta_u - \alpha_u^-) \tag{9.48}$$

$$A_d = 1 - M_d \cos(\theta_d - \alpha_d^-) \tag{9.49}$$

$$B_u = M_u - \frac{\cos \alpha_u^-}{\cos \theta_u} \tag{9.50}$$

$$B_d = M_d - \frac{\cos \alpha_d^-}{\cos \theta_d} \tag{9.51}$$

$$C = \frac{\cos \alpha_d^+}{\cos \theta_d} - M_d \cos(\alpha_d^- + \alpha_d^+) \tag{9.52}$$

$$S_1 = \frac{a_u \cos \theta_d}{a_d \cos \theta_u} \tag{9.53}$$

$$S_2 = \frac{R_u}{R_d} \tag{9.54}$$

Rearrange Equation 9.44 and one obtains the complex transmission coefficient

$$\frac{p_1}{p_0} = \frac{1}{H_1 e^{i(k_4^l + k_5^t)\frac{c}{2}} + H_2 e^{i(k_5^l + k_5^t)\frac{c}{2}} + H_3 e^{i(k_4^l + k_4^t)\frac{c}{2}} + H_4 e^{i(k_5^l + k_4^t)\frac{c}{2}}} \tag{9.55}$$

where

$$H_1 = \frac{(C - A_d)(B_u - A_u)(S_2 - S_1)}{4S_1 S_2 (1 + M_d)(C - B_d)} \tag{9.56}$$

$$H_2 = \frac{(C - A_d)(B_u + A_u)(S_2 + S_1)}{4S_1 S_2 (1 + M_d)(C - B_d)} \tag{9.57}$$

$$H_3 = -\frac{(C + A_d)(B_u - A_u)(S_2 + S_1)}{4S_1 S_2 (1 - M_d)(C - B_d)} \tag{9.58}$$

$$H_4 = -\frac{(C + A_d)(B_u + A_u)(S_2 - S_1)}{4S_1 S_2 (1 - M_d)(C - B_d)} \tag{9.59}$$

Hence the amplitude ratio and the phase change of the transmission coefficient can be obtained respectively as

$$\left|\frac{p_1}{p_0}\right| = \sqrt{\frac{1}{H}} \tag{9.60}$$

$$\begin{aligned} \arg \frac{p_1}{p_0} = -\text{atan2} \left(H_1 \sin(G_1) + H_2 \sin(G_2) + H_3 \sin(G_3) + H_4 \sin(G_4) \right., \\ \left. H_1 \cos(G_1) + H_2 \cos(G_2) + H_3 \cos(G_3) + H_4 \cos(G_4) \right) \end{aligned} \tag{9.61}$$

where

$$H = H_1^2+H_2^2+H_1^3+H_4^2+(2H_1H_2+2H_3H_4)\cos D_1+(2H_1H_3+2H_2H_4)\cos D_2 + 2H_1H_4\cos(D_1-D_2)+2H_2H_3\cos(D_1+D_2) \quad (9.62)$$

$$G_1 = (\frac{k_u}{1-M_u} - \frac{k_d}{1+M_d})\frac{c}{2} \quad (9.63)$$

$$G_2 = (-\frac{k_u}{1+M_u} - \frac{k_d}{1+M_d})\frac{c}{2} \quad (9.64)$$

$$G_3 = (\frac{k_u}{1-M_u} + \frac{k_d}{1-M_d})\frac{c}{2} \quad (9.65)$$

$$G_4 = (-\frac{k_u}{1+M_u} + \frac{k_d}{1-M_d})\frac{c}{2} \quad (9.66)$$

$$D_1 = -\frac{1}{1-M_u^2}k_u c \quad (9.67)$$

$$D_2 = -\frac{1}{1-M_d^2}k_d c \quad (9.68)$$

Similarly, rearrange Equation 9.45 and one obtains the complex reflection coefficient

$$\frac{p_2}{p_0} = \frac{T_1 e^{i(k_4^l+k_5^t)\frac{c}{2}} + T_2 e^{i(k_5^l+k_5^t)\frac{c}{2}} + T_3 e^{i(k_4^l+k_4^t)\frac{c}{2}} + T_4 e^{i(k_5^l+k_4^t)\frac{c}{2}}}{Z_1 e^{i(k_4^l+k_5^t)\frac{c}{2}} + Z_2 e^{i(k_5^l+k_5^t)\frac{c}{2}} + Z_3 e^{i(k_4^l+k_4^t)\frac{c}{2}} + Z_4 e^{i(k_5^l+k_4^t)\frac{c}{2}}} \quad (9.69)$$

where

$$T_1 = \frac{(A_d-B_d)(B_u-A_u)(S_2-S_1)}{1+M_d} \quad (9.70)$$

$$T_2 = \frac{(A_d-B_d)(B_u+A_u)(S_2+S_1)}{1+M_d} \quad (9.71)$$

$$T_3 = \frac{(A_d+B_d)(B_u-A_u)(S_2+S_1)}{1-M_d} \quad (9.72)$$

$$T_4 = \frac{(A_d+B_d)(B_u+A_u)(S_2-S_1)}{1-M_d} \quad (9.73)$$

$$Z_1 = \frac{(C - A_d)(B_u - A_u)(S_2 - S_1)}{1 + M_d} \tag{9.74}$$

$$Z_2 = \frac{(C - A_d)(B_u + A_u)(S_2 + S_1)}{1 + M_d} \tag{9.75}$$

$$Z_3 = -\frac{(C + A_d)(B_u - A_u)(S_2 + S_1)}{1 - M_d} \tag{9.76}$$

$$Z_4 = -\frac{(C + A_d)(B_u + A_u)(S_2 - S_1)}{1 - M_d} \tag{9.77}$$

Hence the amplitude ratio and the phase change of the reflection coefficient can be obtained respectively as

$$|\frac{p_2}{p_0}| = \sqrt{\frac{T}{Z}} \tag{9.78}$$

$$\begin{aligned}\arg \frac{p_2}{p_0} = \operatorname{atan2}\left(T_1 \sin(G_1) + T_2 \sin(G_2) + T_3 \sin(G_3) + T_4 \sin(G_4)\right., \\ T_1 \cos(G_1) + T_2 \cos(G_2) + T_3 \cos(G_3) + T_4 \cos(G_4)) \\ + \operatorname{atan2}\left(T_1 \sin(G_1) + T_2 \sin(G_2) + T_3 \sin(G_3) + T_4 \sin(G_4)\right., \\ T_1 \cos(G_1) + T_2 \cos(G_2) + T_3 \cos(G_3) + T_4 \cos(G_4))\end{aligned} \tag{9.79}$$

where

$$\begin{aligned}T = T_1^2 + T_2^2 + T_1^3 + T_4^2 + (2T_1T_2 + 2T_3T_4)\cos D_1 + (2T_1T_3 + 2T_2T_4)\cos D_2 \\ + 2T_1T_4 \cos(D_1 - D_2) + 2T_2T_3 \cos(D_1 + D_2)\end{aligned} \tag{9.80}$$

$$\begin{aligned}Z = Z_1^2 + Z_2^2 + Z_1^3 + Z_4^2 + (2Z_1Z_2 + 2Z_3Z_4)\cos D_1 + (2Z_1Z_3 + 2Z_2Z_4)\cos D_2 \\ + 2Z_1Z_4 \cos(D_1 - D_2) + 2Z_2Z_3 \cos(D_1 + D_2)\end{aligned} \tag{9.81}$$

Appendix III: Extract Letter

E-theses letter: request to reproduce an extract from a third party's published work

23/08/2016

Dear Rolls-Royce plc,

I am completing my PhD thesis at Imperial College London entitled 'Embedded Blade Row Flutter'.

I seek your permission to reprint, in my thesis an extract from:

1. M. Vahdati, N. Smith and F. Zhao, "Influence of intake on fan blade flutter," in Proceedings of ASME Turbo Expo 2014, Dusseldorf, Germany, 2014, Paper No. GT2014-25859.
2. F. Zhao, J. Nipkau and M. Vahdati, "Influence of acoustic reflection on flutter stability of an embedded blade row," in 11th European Turbomachinary Conference, Madrid, Spain, 2015, Paper No. ETC2015-34.
3. F. Zhao, J. Nipkau and M. Vahdati, "A simple low-fidelity model for embedded blade row flutter prediction," in Proceedings of ASME Turbo Expo 2015, Montreal, Canada, 2015, Paper No. GT2015-42173.
4. F. Zhao, N. Smith and M. Vahdati, "A simple model for identifying the 'flutter bite' of fan blades" in Proceedings of ASME Turbo Expo 2016, Seoul, Korea, 2016, Paper No. GT2016-56336.

I would like to include the extract in my thesis which will be added to Spiral, Imperial's institutional repository http://spiral.imperial.ac.uk/ and made available to the public under a Creative Commons Attribution-NonCommercial-NoDerivs licence.

If you are happy to grant me all the permissions requested, please return a signed copy of this letter. If you wish to grant only some of the permissions requested, please list these and then sign.

Yours sincerely,

Fanzhou Zhao

Permission granted for the use requested above:

I confirm that I am the copyright holder of the extract above and hereby give permission to include it in your thesis which will be made available, via the internet, for non-commercial purposes under the terms of the user licence.

Signed:

Name: Alan Kestin

Organisation: Rolls-Royce plc

Job title: Chief of VEDS